

# **Strong Spin-Orbit Interaction, Helical Hole States, and Spin Qubits in Nanowires and Quantum Dots**

**Inauguraldissertation**

ZUR

Erlangung der Würde eines Doktors der Philosophie

vorgelegt der

Philosophisch-Naturwissenschaftlichen Fakultät

der Universität Basel

VON

**Christoph Klöffel**

aus Nüdlingen, Deutschland

Basel, 2014

Originaldokument gespeichert auf dem Dokumentenserver der Universität Basel  
**edoc.unibas.ch**



Dieses Werk ist unter dem Vertrag „Creative Commons Namensnennung-Keine kommerzielle Nutzung-Keine Bearbeitung 3.0 Schweiz“ (CC BY-NC-ND 3.0 CH) lizenziert.

Die vollständige Lizenz kann unter  
**[creativecommons.org/licenses/by-nc-nd/3.0/ch/](https://creativecommons.org/licenses/by-nc-nd/3.0/ch/)**  
eingesehen werden.



**Namensnennung-Keine kommerzielle Nutzung-Keine Bearbeitung 3.0 Schweiz**  
(CC BY-NC-ND 3.0 CH)

**Sie dürfen:** **Teilen** — den Inhalt kopieren, verbreiten und zugänglich machen

**Unter den folgenden Bedingungen:**



**Namensnennung** — Sie müssen den Namen des Autors/Rechteinhabers in der von ihm festgelegten Weise nennen.



**Keine kommerzielle Nutzung** — Sie dürfen diesen Inhalt nicht für kommerzielle Zwecke nutzen.



**Keine Bearbeitung erlaubt** — Sie dürfen diesen Inhalt nicht bearbeiten, abwandeln oder in anderer Weise verändern.

**Wobei gilt:**

- **Verzichtserklärung** — Jede der vorgenannten Bedingungen kann **aufgehoben** werden, sofern Sie die ausdrückliche Einwilligung des Rechteinhabers dazu erhalten.
- **Public Domain (gemeinfreie oder nicht-schützbare Inhalte)** — Soweit das Werk, der Inhalt oder irgendein Teil davon zur Public Domain der jeweiligen Rechtsordnung gehört, wird dieser Status von der Lizenz in keiner Weise berührt.
- **Sonstige Rechte** — Die Lizenz hat keinerlei Einfluss auf die folgenden Rechte:
  - Die Rechte, die jedermann wegen der Schranken des Urheberrechts oder aufgrund gesetzlicher Erlaubnisse zustehen (in einigen Ländern als grundsätzliche Doktrin des **fair use** bekannt);
  - Die **Persönlichkeitsrechte** des Urhebers;
  - Rechte anderer Personen, entweder am Lizenzgegenstand selber oder bezüglich seiner Verwendung, zum Beispiel für **Werbung** oder Privatsphärenschutz.
- **Hinweis** — Bei jeder Nutzung oder Verbreitung müssen Sie anderen alle Lizenzbedingungen mitteilen, die für diesen Inhalt gelten. Am einfachsten ist es, an entsprechender Stelle einen Link auf diese Seite einzubinden.

Genehmigt von der Philosophisch-Naturwissenschaftlichen Fakultät auf Antrag von

Prof. Dr. Daniel Loss

Prof. Dr. Guido Burkard

Basel, den 20.5.2014

Prof. Dr. Jörg Schibler  
Dekan



# Acknowledgments

First and foremost I would like to thank my supervisor Prof. Daniel Loss for accepting me as a PhD student and for his advice, help, and support throughout my time in his group. His knowledge and passion about physics are highly impressive. Despite his busy schedule and his large research group, he was always willing and able to help, even regarding the tiny details, and his suggestions for new research projects always turned out to be well thought through with rigor and foresight. I appreciate his respectful and supportive attitude and am proud to be a part of his team.

Second, I wish to thank Prof. Guido Burkard for co-refereeing my thesis. His willingness to read and referee my work is a great honor.

I am particularly grateful to Prof. Richard Warburton for his great support both at the Heriot-Watt University in Edinburgh and at the University of Basel. I owe a lot to him, and I am glad that we had a fruitful collaboration that became a part of this thesis. I also want to thank him for chairing the PhD defense.

During the first year of my PhD program, I was fortunate to collaborate very closely with Dr. Mircea Trif, who introduced me to the new and interesting topics that we had started working on. I benefitted a lot from his expertise and want to thank him for this valuable collaboration. I am also grateful to my office mates Prof. Suhas Gangadharaiah, Dr. Silas Hoffman, Dr. Peter Stano, Dr. Pawel Szumniak, and Dr. Robert Zak, all of whom I truly enjoyed working with. In particular, I want to thank Dr. Peter Stano for countless interesting and helpful discussions that notably contributed to the results of this thesis. Moreover, I had the pleasure of sharing one project each with Viktoriia Kornich and Franziska Maier, both of whom I thank for their great work that led to the success of these projects.

The experimental data in this thesis, taken in Prof. Richard Warburton's and Prof. Brian Gerardot's laboratories at Heriot-Watt University, were obtained with rather unusual circumstances. After Dr. Paul Dalgarno and I had carried out some first preparatory measurements in the absence of magnetic fields, the project was about to end because Dr. Dalgarno had a new position at the University of St. Andrews and I was going to start the PhD program in Basel soon. However, the project was too interesting to just abandon it, and so we all decided that I would return to Edinburgh a few weeks later in order to carry out the experiments at nonzero magnetic fields, given a limited time frame of less than 20 days in total. Successfully obtaining all this data on my own and in this short amount of time would have been impossible without Dr. Dalgarno, who very patiently had taught me a lot about working in the lab. I want to cordially thank him for his help throughout this project. Many thanks also to Prof. Brian Gerardot for useful advice and for allowing me to use some of his equipment, and to Dr. Daniel Brunner for his kind assistance, e.g., during helium refills and with the installation of the magnet.

There are many people whom I would like to thank for useful discussions, in fact, too many to be listed here completely. Besides the ones already mentioned above, I want to express my gratitude to Prof. Hendrik Bluhm, Dr. Bernd Braunecker, Prof. Bill Coish, Prof. Carlos Egues, Dr. Jan Fischer, Prof. Vitaly Golovach, Dr. Yongjie Hu, Dr. Georgios Katsaros, Prof. Ferdinand Kuemmeth, Prof. Charles Marcus, Dr. Karl Petersson, Prof. Jason Petta, Prof. Martino Poggio, Dr. Beat Röthlisberger, Prof. Manuel Schmidt, Prof. Dimitrije Stepanenko, Prof. Alexander Tartakovskii, Prof. Yaroslav Tserkovnyak, Dr. Oleksandr Tsypliyatyev, Dr. Bernhard Urbaszek, Prof. Roland Winkler, Dr. James Wootton, Prof. Amir Yacoby, and, of course, to all my present and former colleagues in the Condensed Matter Theory Group!

Due to my role as webmaster of the Department of Physics, I had the pleasure of working with essentially all staff and faculty members of the department. Among many others, I want to acknowledge Prof. Stefan Antusch, Prof. Christoph Bruder, Francois Erkadoo, Beat Glatz, Bernd Heimann, Dr. Barbara Hellermann, Astrid Kalt, Barbara Kammermann, Prof. Patrick Maletinsky, Sascha Martin, Prof. Ernst Meyer, Prof. Thomas Rauscher, Dr. Peter Reimann, Dr. Monica Schönenberger, Michael Steinacher, Roland Steiner, Prof. Philipp Treutlein, and Germaine Weaver. In particular, I want to thank the manager of the website, Prof. Dominik Zumbühl, for the good collaboration and his always friendly and respectful attitude.

I am glad that the research topics discussed in this thesis attracted considerable funding, and being involved in writing research reports and proposals as well as attending project review meetings were very useful experiences. For financial support I want to acknowledge the Swiss NF, NCCRs Nanoscience and QSIT, S<sup>3</sup>NANO, DARPA, IARPA, and SiSPIN.

It is hard to imagine life without friends. Remarkably, some of my fellow students in Würzburg have accompanied me throughout my studies of physics literally since the very first day. Among others, I want to thank Arne Buchter, Thomas Keitzl, Peter Kiefel, Christian Kramer, Dr. Andreas Kuhlmann, Jonathan Prechtel, Sebastian Riecker, Jan Salomon, the friends from my hometown and the friends I met in Basel. I learned a lot from all of them and want to thank them for their support.

Finally, I want to thank my parents Thekla and Werner, my brother Philipp, and my whole family for always being there for me and for their unconditional support throughout my life.

# Summary

Semiconducting nanowires (NWs) and quantum dots (QDs) are promising platforms for spintronics and quantum computation. Great experimental and theoretical efforts have been made to continuously improve their performances, which is evident from the large variety of setups, material combinations, and operation schemes under investigation. With the work summarized in this PhD thesis, we want to contribute to a better understanding of some of these systems.

The main result of our work is the discovery of a novel spin-orbit interaction (SOI) of Rashba type that arises for holes in NWs in the presence of an electric field. In contrast to conventional Rashba and Dresselhaus SOI, this mechanism is not suppressed by the fundamental band gap and therefore unusually strong. As a consequence, we find that Ge/Si core/shell NWs can host helical hole states with remarkably large spin-orbit energies on the order of millielectronvolts. Furthermore, we propose a setup for universal and electrically controlled quantum information processing with hole-spin qubits in Ge/Si NW QDs. Single-qubit gates can be performed on a subnanosecond timescale; two-qubit gates can be controlled independently and over long distances; idle qubits are well protected against electrical noise and lattice vibrations (phonons).

Another key result follows from our analysis of the phonon-mediated decay of singlet-triplet qubits in lateral GaAs double quantum dots (DQDs). We find that two-phonon processes lead to strong dephasing when the DQDs are biased, and the predicted temperature dependence provides a possible explanation for recent experimental data. When the DQDs are unbiased, the dephasing is highly suppressed and the decoherence times of the qubits are by orders of magnitude longer than those for biased DQDs.

In the last part of the thesis, we present a technique for manipulating the emission polarization and the nuclear spins of a single self-assembled QD. Our scheme exploits a natural cycle in which an electron spin is repeatedly created with resonant optical excitation when the QD is tunnel coupled to a Fermi sea. Among other things, we find that the nuclear spin polarization and the effective electron  $g$  factor can be changed continuously from negative to positive via the laser wavelength, with a region of bistability near a particular detuning. An analogous behavior is observed for the average polarization of the spontaneously emitted photons. Our experimental results, some of which are counterintuitive, are very well reproduced with a quantitative model.

The thesis is organized as follows. In Chapter 1, we review experimental and theoretical progress toward quantum computation with spins in QDs, with particular focus on NW QDs, lateral QDs, and self-assembled QDs. In Chapter 2, we study the low-energy hole states of Ge/Si NWs in the presence of electric and magnetic fields. We also consider the shell-induced strain, which strongly affects the NW and QD spectra. In Chapter 3, hole-spin qubits in Ge/Si NW QDs are investigated. We find a highly anisotropic and electrically tunable  $g$  factor and analyze the qubit lifetimes due to phonon-mediated decay. A setup for quantum information processing with these qubits is proposed in Chapter 4, where we also present surprisingly simple formulas for the effective Hamiltonian of the qubits. A detailed analysis of the static strain and the low-energy phonons in core/shell NWs is provided in Chapter 5, completing the part on NWs and NW QDs. In Chapter 6, we investigate the phonon-mediated decay of singlet-triplet qubits in lateral DQDs. The developed technique for controlling the emission polarization and the nuclear spins of optically active QDs is discussed in Chapter 7. Supplementary information to Chapters 2–7 is appended.





# Contents

<b>Acknowledgments</b>	<b>i</b>
<b>Summary</b>	<b>iii</b>
<b>Contents</b>	<b>v</b>
<b>PART I: Introduction (Review)</b>	<b>1</b>
<b>1 Prospects for Spin-Based Quantum Computing in Quantum Dots</b>	<b>3</b>
1.1 Introduction . . . . .	4
1.2 Promising Quantum Dot Structures, Definition of Lifetimes, and Essential Requirements . . . . .	5
1.3 Spin-Orbit Interaction and Nuclear Spins in Quantum Dots . . . . .	6
1.3.1 Spin-Orbit Interaction . . . . .	6
1.3.2 Nuclear Spins . . . . .	9
1.4 Recent Progress in Quantum Dot Systems . . . . .	13
1.4.1 Self-Assembled Quantum Dots . . . . .	14
1.4.2 Lateral Quantum Dots . . . . .	15
1.4.3 Quantum Dots in Nanowires . . . . .	18
1.4.4 Overview . . . . .	20
1.5 Proposals for Long-Distance Spin-Spin Coupling . . . . .	20
1.6 Outlook . . . . .	23
References . . . . .	27
<b>PART II: Direct Rashba Spin-Orbit Interaction, Helical Hole States, and Spin Qubits in Nanowires and Nanowire Quantum Dots in the Presence of Phonons, Strain, and Control Fields (Theory)</b>	<b>37</b>
<b>2 Strong Spin-Orbit Interaction and Helical Hole States in Ge/Si Nanowires</b>	<b>39</b>
2.1 Introduction . . . . .	40
2.2 Model Hamiltonian and Numerical Solution . . . . .	41
2.3 Effective 1D Hamiltonian . . . . .	42
2.4 Static Strain . . . . .	43
2.5 Quantum Dot Spectrum . . . . .	43
2.6 Direct Rashba Spin-Orbit Interaction and Helical Hole States . . . . .	44
2.7 Magnetic Field Effects . . . . .	46
2.8 Discussion . . . . .	47
References . . . . .	49
<b>3 Tunable g Factor and Phonon-Mediated Hole Spin Relaxation in Ge/Si Nanowire Quantum Dots</b>	<b>51</b>
3.1 Introduction . . . . .	52
3.2 Theoretical Model . . . . .	53
3.2.1 Effective 1D Hamiltonian for Holes in Ge/Si Nanowires . . . . .	53

3.2.2	Effective 1D Hamiltonian for Hole-Phonon Interaction . . . . .	53
3.2.3	Harmonic Confinement and Quantum Dot Hamiltonian . . . . .	54
3.3	Large Anisotropy and Electrical Tunability of Hole-Spin $g$ Factor . . . . .	54
3.4	Phonon-Mediated Decay of Hole-Spin Qubits . . . . .	55
3.4.1	Effective Qubit Hamiltonian and Bloch-Redfield Theory . . . . .	55
3.4.2	Decay Rates for Various Setup Geometries . . . . .	56
3.5	Conclusions . . . . .	57
	References . . . . .	59
<b>4</b>	<b>Circuit QED with Hole-Spin Qubits in Ge/Si Nanowire Quantum Dots</b>	<b>63</b>
4.1	Introduction . . . . .	64
4.2	Setup and Model Hamiltonian . . . . .	64
4.3	Effective Hamiltonian for the Hole-Spin Qubit . . . . .	65
4.4	Ultrafast Single-Qubit Gates and Tunable $g$ Factors . . . . .	66
4.5	Two-Qubit Gates via Circuit QED . . . . .	67
4.6	Qubit Lifetimes and Gate Fidelities . . . . .	68
4.7	Results for Different Setups . . . . .	69
	References . . . . .	71
<b>5</b>	<b>Acoustic Phonons and Strain in Core/Shell Nanowires</b>	<b>75</b>
5.1	Introduction . . . . .	76
5.2	Linear Elasticity Theory . . . . .	77
5.3	Static Strain in Core/Shell Nanowires . . . . .	78
5.3.1	Boundary Conditions . . . . .	79
5.3.2	Analytical Results . . . . .	80
5.3.3	Results for Ge/Si Core/Shell Nanowires . . . . .	82
5.4	Phonons in Homogeneous Nanowires . . . . .	84
5.4.1	Equation of Motion, Ansatz, and Boundary Conditions . . . . .	84
5.4.2	Torsional Mode . . . . .	86
5.4.3	Longitudinal Mode . . . . .	87
5.4.4	Flexural Modes . . . . .	88
5.4.5	Normalization . . . . .	89
5.5	Phonons in Core/Shell Nanowires . . . . .	90
5.5.1	Ansatz and Boundary Conditions . . . . .	90
5.5.2	Torsional Mode . . . . .	91
5.5.3	Longitudinal Mode . . . . .	93
5.5.4	Flexural Modes . . . . .	95
5.5.5	Normalization . . . . .	97
5.5.6	Limits of Vanishing and Infinite Shell . . . . .	98
5.6	Conclusions . . . . .	98
	References . . . . .	99
<b>PART III: Lifetimes of Singlet-Triplet Qubits in Lateral Double Quantum Dots With and Without Detuning (Theory)</b>		<b>103</b>
<b>6</b>	<b>Phonon-Mediated Decay of Singlet-Triplet Qubits in Double Quantum Dots</b>	<b>105</b>
6.1	Introduction . . . . .	106
6.2	System, Hamiltonian, and Basis States . . . . .	106

6.3	Regime of Large Detuning . . . . .	108
6.3.1	Effective Hamiltonian and Bloch-Redfield Theory . . . . .	108
6.3.2	Input Parameters . . . . .	109
6.3.3	Temperature Dependence . . . . .	110
6.3.4	Origin of Strong Dephasing . . . . .	112
6.3.5	Angular Dependence . . . . .	113
6.4	Regime of Small Detuning . . . . .	114
6.5	Conclusions and Outlook . . . . .	115
	References . . . . .	117
<b>PART IV: Optical and Electrical Control of the Nuclear Spin Polarization and the Photoluminescence of a Self-Assembled Quantum Dot (Experiment &amp; Theory)</b>		<b>121</b>
<b>7</b>	<b>Controlling the Interaction of Electron and Nuclear Spins in a Tunnel-Coupled Quantum Dot</b>	<b>123</b>
7.1	Introduction . . . . .	124
7.2	Setup . . . . .	124
7.3	Natural Cycle in the Hybridization Region . . . . .	124
7.4	Control of Emission Polarization and Overhauser Field . . . . .	125
7.5	Quantitative Model . . . . .	127
7.6	Outlook . . . . .	129
	References . . . . .	131
<b>APPENDIX</b>		<b>133</b>
<b>A</b>	<b>Supplementary Information to Chapter 2</b>	
	<b>“Strong Spin-Orbit Interaction and Helical Hole States in Ge/Si Nanowires”</b>	<b>135</b>
A.1	Representation of Spin Matrices . . . . .	136
A.2	Basis States for the Effective 1D Hamiltonian . . . . .	136
A.3	Bir-Pikus Hamiltonian . . . . .	137
A.4	Quantum Dot Spectrum . . . . .	137
A.5	Spin-Orbit Energy in InAs Nanowires . . . . .	138
A.6	Standard Rashba SOI and Rashba Coefficient . . . . .	138
A.7	Coupling to Magnetic Fields . . . . .	139
	References . . . . .	141
<b>B</b>	<b>Supplementary Information to Chapter 3</b>	
	<b>“Tunable <math>g</math> Factor and Phonon-Mediated Hole Spin Relaxation in Ge/Si Nanowire Quantum Dots”</b>	<b>143</b>
B.1	Effective 1D Hamiltonian for Holes . . . . .	144
B.2	Effective 1D Hamiltonian for Hole-Phonon Interaction . . . . .	145
<b>C</b>	<b>Supplementary Information to Chapter 4</b>	
	<b>“Circuit QED with Hole-Spin Qubits in Ge/Si Nanowire Quantum Dots”</b>	<b>147</b>
C.1	Effective 1D Hamiltonian . . . . .	148
C.1.1	Basis States . . . . .	148
C.1.2	Effective 1D Hamiltonian . . . . .	148
C.2	Quantum Dot: Perturbative Analysis . . . . .	150
C.2.1	Hamiltonian . . . . .	150

C.2.2	Step 1	151
C.2.3	Step 2	151
C.2.4	Step 3	152
C.2.5	Step 4	153
C.2.6	Step 5	154
C.2.7	Step 6	155
C.2.8	Remarks	155
C.3	Quantum Dot: Numerical Analysis	155
C.3.1	Basis States	155
C.3.2	Algorithm 1	156
C.3.3	Algorithm 2	156
C.3.4	Remarks	157
C.4	Parameter Range and Validity of Results	157
C.4.1	Effective 1D Hamiltonian	157
C.4.2	Qubit Hamiltonian	158
C.4.3	Remarks	158
C.5	Cavity-Based Interactions	158
C.5.1	Electric Cavity Field	158
C.5.2	Qubit-Cavity Coupling	159
C.5.3	Qubit-Qubit Coupling	160
C.5.4	Two-Qubit Gates	161
C.6	Charge Noise	163
C.6.1	Perturbation due to Electric Field Fluctuations	163
C.6.2	Relaxation and Dephasing at Maximal Transverse Coupling	163
C.6.3	Numerical Estimates	165
C.6.4	Remarks	165
C.7	Results from Effective Model	166
	References	169

## D Supplementary Information to Chapter 5

	<b>“Acoustic Phonons and Strain in Core/Shell Nanowires”</b>	<b>171</b>
D.1	Parameters for Ge/Si Core/Shell Nanowires	172
D.2	Coordinate Systems for Stress and Strain	172
D.2.1	Cartesian and Cylindrical Coordinates	172
D.2.2	Transformation of Second Rank Tensors	173
D.2.3	Strain in Cylindrical Coordinates	174
D.3	Phonons in Bulk	175
D.3.1	Plane Waves and Classical Lattice Vibrations	175
D.3.2	Hamiltonian	176
D.3.3	Quantization	177
D.4	Phonon Quantization in Core/Shell and Core/Multishell Wires	180
	References	183

## E Supplementary Information to Chapter 6

	<b>“Phonon-Mediated Decay of Singlet-Triplet Qubits in Double Quantum Dots”</b>	<b>185</b>
E.1	Basis States	186
E.2	Hamiltonian	188
E.2.1	Hamiltonian $H_0$	189

E.2.2	Coulomb Repulsion . . . . .	189
E.2.3	Zeeman Term . . . . .	189
E.2.4	Spin-Orbit Interaction . . . . .	189
E.2.5	Hyperfine Interaction . . . . .	190
E.2.6	Electron-Phonon Coupling . . . . .	191
E.2.7	Phonon Bath . . . . .	195
E.3	Model Hamiltonian at Small Detuning . . . . .	195
E.3.1	Exchange Energy and Orbital Level Spacing . . . . .	195
E.3.2	Matrix Representation . . . . .	196
E.4	Model Hamiltonian at Large Detuning . . . . .	197
E.5	Bloch-Redfield Theory . . . . .	197
E.6	Continuum Limit . . . . .	199
E.7	Simple Model for Dephasing at Large Detuning . . . . .	199
E.8	Dephasing via Singlet States at Small Detuning . . . . .	202
E.9	Summary of Input Parameters . . . . .	203
	References . . . . .	205

**F Supplementary Information to Chapter 7**

**“Controlling the Interaction of Electron and Nuclear Spins in a Tunnel-Coupled Quantum Dot”**

		<b>207</b>
F.1	Outline . . . . .	208
F.2	Coherent Evolution of Five-Level System . . . . .	208
F.3	Flip-Flop of Electron and Nuclear Spin . . . . .	210
F.4	Nuclear Spin Dynamics and Stable Solutions . . . . .	211
F.5	Calculation of Nuclear Spin Distribution Width . . . . .	212
F.6	Input Parameters . . . . .	212
F.7	Flip-Flop Term in an Effective Two-Level System . . . . .	214
F.7.1	Strong Correlation . . . . .	214
F.7.2	No Correlation . . . . .	215
	References . . . . .	217

**Curriculum Vitae** **219**

**List of Publications** **221**



# **PART I**

## **Introduction**

(Review)





# Chapter 1

## Prospects for Spin-Based Quantum Computing in Quantum Dots

**Adapted from:**

Christoph Kloeffel and Daniel Loss,  
*Annu. Rev. Condens. Matter Phys.* **4**, 51 (2013).

Experimental and theoretical progress toward quantum computation with spins in quantum dots (QDs) is reviewed, with particular focus on QDs formed in GaAs heterostructures, on nanowire-based QDs, and on self-assembled QDs. We report on a remarkable evolution of the field, where decoherence – one of the main challenges for realizing quantum computers – no longer seems to be the stumbling block it had originally been considered. General concepts, relevant quantities, and basic requirements for spin-based quantum computing are explained; opportunities and challenges of spin-orbit interaction and nuclear spins are reviewed. We discuss recent achievements, present current theoretical proposals, and make several suggestions for further experiments.

## 1.1 Introduction

The concept of entanglement and nonlocality [1], one of the most striking features of quantum mechanics, has been heavily debated since the early days of the field [2]. By now, there is abundant experimental evidence [3] that Nature indeed does possess nonlocal aspects, in stark contrast to our everyday-life experience.

But it was only relatively recently [4], when Richard Feynman [5, 6], David Deutsch [7], and other researchers in the 1980s, envisioned the idea of exploiting the quantum degrees of freedom for a novel way of information processing. The central questions then were whether and how it is possible to efficiently simulate any finite physical system with a man-made machine. Deutsch argued that such a simulation is not possible perfectly within the classical computational framework that had been developed for decades [7]. Instead, the universal computing machine should be of a quantum nature, i.e., a quantum computer.

Since then, progress in different areas of research and industry tremendously influenced the advent of quantum computing. First, the booming computer industry led to major progress in semiconductor, nano-, and laser technology, a prerequisite for the fabrication, addressing, and manipulation of single quantum systems needed in an experimental realization. Second, several algorithms have been developed, such as those by Deutsch [7, 8], Grover [9], and Shor [10, 11], which clearly illustrate that quantum computers, exploiting the existence of entanglement, can solve problems much faster than classical computers. A recent review on using quantum computers for quantum simulations can be found in Ref. [12]. In addition, the theories of quantum complexity and entanglement are currently being established, a process that is still far from complete. The emerging fields of nano- and quantum information science have inspired and motivated each other in various ways.

Shortly after the first quantum algorithms were developed, setups were suggested to turn quantum computing into reality. These ideas, among others, are based on quantum dots (QDs) [13, 14], cold trapped ions [15], cavity quantum electrodynamics (QED) [14, 16], bulk nuclear magnetic resonance [17], low-capacitance Josephson junctions [18], donor atoms [19, 20], linear optics [21], molecular magnets [22], spin clusters [23], or color centers in diamond [24–26]. Many interesting results have followed, some of which are reviewed here.

In 1997, encoding quantum information in the spin states of QDs was proposed [13]. The tunnel barrier between neighboring dots, which can be varied via gates (see Fig. 1.1), induces time-dependent electron-electron interactions and affects the spin states via the Heisenberg exchange coupling. The proposal demonstrates theoretically that such a setup allows for universal and scalable quantum computing, controllable by purely electrical means at ultrahigh clock speed. Here, we particularly focus on the experimental and theoretical achievements following Ref. [13] because substantial progress in this field has been made within the past few years. An overview on recent results in other setups can be found in, e.g., Ref. [27], where different qubit platforms are also compared to each other. For previous reviews, see Refs. [4, 28, 29].

The review is organized as follows. In Sec. 1.2 we introduce the three QD systems discussed in this review: self-assembled QDs, lateral QDs, and nanowire-based QDs. We also comment on basic requirements for quantum computation and define the spin lifetimes  $T_1$ ,  $T_2$ , and  $T_2^*$ . Spin-orbit interaction and nuclear spins are covered in Sec. 1.3. These present an undesired (noise) source of relaxation and decoherence for the spin qubits on the one hand, but on the other hand allow for all-electrical spin manipulation via electric-dipole-induced spin resonance or for strong (effective) magnetic field gradients. In Sec. 1.4, recent progress in these QD systems is summarized, compared, and discussed. Newly proposed architectures for long-distance qubit-qubit coupling are reviewed in Sec. 1.5, followed by our summary and final remarks in Sec. 1.6.

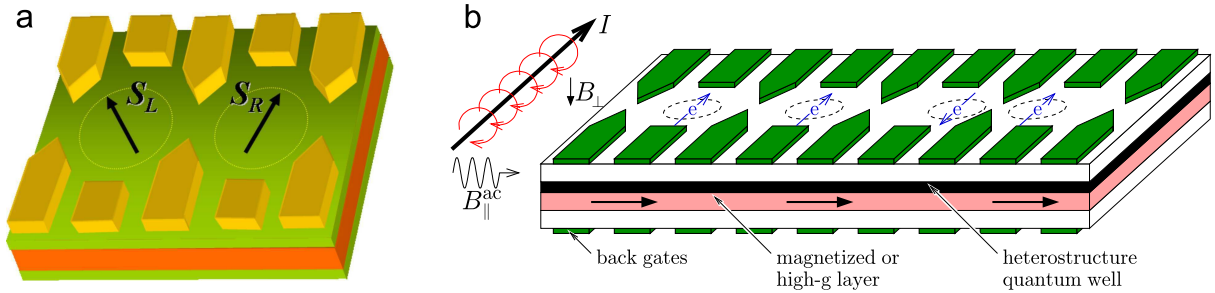


Figure 1.1. Basic scheme for the physical implementation of a quantum computer as proposed in Ref. [13]. (a) The qubits are encoded in the single-electron spin states of quantum dots (QDs), where the barrier between adjacent QDs is controllable via electric gates. When the barrier is reduced, the electron wave functions overlap and the spins  $\mathbf{S}_L$  and  $\mathbf{S}_R$  (here in units of  $\hbar$ ) interact via the Heisenberg exchange coupling  $J(t)\mathbf{S}_L \cdot \mathbf{S}_R$ , where  $J(t)$  is a function of gate voltage and corresponds to the energy splitting of the spin singlet and triplet states. This allows for electrically controlled two-qubit gates with fast operation times [13]. (b) A QD array based on panel a, where the qubits in the two right dots are coupled while the others are decoupled. Rotations of individual spins may be achieved by pulling the desired electron down into a region of high magnetization or high  $g$  factor via back gates, such that the Zeeman splitting and, hence, the resonance condition changes for this electron in the presence of a static magnetic field  $B_{\perp}$ . A resonantly applied oscillating magnetic field pulse  $B_{\parallel}^{\text{ac}}$  then rotates the addressed qubit (electron spin resonance, ESR), while all others remain unaffected due to off-resonance. Exploiting spin-orbit interaction, the rotations may also be driven fully electrically via electric-dipole-induced spin resonance (EDSR). For details on ESR and EDSR, see Sec. 1.3.1.1. Alternatively, fast single-qubit gates may be implemented via exchange-controlled spin rotations [13, 198]. The combination of single- and two-qubit gates results in a universal set of quantum gates, so that the proposed schemes allow for fast and purely electrically controlled quantum computation with electron spins in QDs [13]. *The pictures were used with permission of Daniel Loss.*

## 1.2 Promising Quantum Dot Structures, Definition of Lifetimes, and Essential Requirements

QDs confine electrons or holes (missing valence band electrons) in all three dimensions, on length scales which are comparable to the wavelengths of the particles, i.e., typically  $\sim 10$ – $100$  nm in each spatial direction. There are many possibilities to realize such confinement, which is evident from the variety of systems under study. In this report, we mainly focus on three of them. The first category is self-assembled QDs. These form naturally during growth, where InGaAs dots within a GaAs matrix are commonly used examples. When InGaAs is grown on GaAs (Stranski-Krastanov mode), islands form spontaneously, due to the mismatch in the lattice constants, after a small critical thickness of only a few monolayers is reached. These may then be covered with further layers of GaAs. Such QDs are typically lens shaped, with heights of  $\sim 5$  nm (growth direction) and diameters  $\sim 20$  nm, and confinement results from the difference in the conduction and valence band edges of the involved materials. Alternatively, interface fluctuation QDs arise from monolayer fluctuations in thin quantum wells, typically resulting in GaAs dots within AlGaAs [30]. The second category, lateral QDs, is based on two-dimensional electron gases (2DEGs) and two-dimensional hole gases (2DHGs), which exist in heterostructures from materials with suitable band properties and additional dopants. For instance, AlGaAs/GaAs heterostructures are routinely used to form 2DEGs and 2DHGs within GaAs, which are strongly confined along the growth direction. Lithographically defined gate electrodes on the sample surface also allow confinement in the transverse directions, leading to quasi-2D QDs of  $\sim 100$  nm in diameter. The orbital parts of the wave functions play an important role for lateral QDs and have been studied in great detail in Refs. [31, 32]. Finally, semiconductor nanowires naturally provide confinement in two dimensions, due to their small diameters of  $\sim 10$ – $100$  nm, and repulsive forces along the wire may again be added via nearby gates or additional layers of barrier material. We note that several other QD implementations exist, which, however, for space reasons we do not discuss. Prominent examples are colloidal QDs [33, 34] and QDs

in carbon-based systems, like graphene [35] or carbon nanotubes [36, 37], which are highly attractive for implementing spin qubits.

Any setup considered for quantum computation should fulfill a list of essential criteria, such as scalability and the ability to initialize the system in a fiducial state [38]. For quantum error correction schemes to be applicable, it is important that the lifetimes are much longer than the gate operation times. A decade ago, this was considered a very serious challenge, but to a great extent, this problem has now been overcome in QDs as discussed in Sec. 1.4. Three timescales are of interest in this context, which we illustrate in terms of the electron spin qubit states  $|\uparrow\rangle$  and  $|\downarrow\rangle$ , assuming that these are eigenstates of the Pauli operator  $\sigma_z$  with energy difference  $\Delta$ . First, the relaxation time  $T_1$  describes transitions  $|\uparrow\rangle \rightarrow |\downarrow\rangle$  due to interactions with the environment, such as the lattice, which leads to relaxation from the excited  $|\uparrow\rangle$  to the ground state  $|\downarrow\rangle$ . A typical measure for  $T_1$  is  $\langle\sigma_z\rangle(t)$  with initial state  $|\uparrow\rangle$ . Second, the decoherence time  $T_2$  quantifies the decay of quantum mechanical superpositions and accounts for transitions of type  $|\uparrow\rangle + |\downarrow\rangle \rightarrow \{|\downarrow\rangle, |\uparrow\rangle\}$  induced by the environment (Fig. 1.2, inset). When the state is initially  $(|\uparrow\rangle + |\downarrow\rangle)/\sqrt{2}$ , an eigenstate of  $\sigma_x$ , a typical measure for  $T_2$  is the envelope function of  $\langle\sigma_x\rangle(t)$ . We note that  $\langle\sigma_x\rangle(t)$  oscillates between  $\pm 1$  at angular frequency  $\Delta/\hbar$  for a perfectly isolated system, but decays to 0 as the state turns into either  $|\uparrow\rangle$  or  $|\downarrow\rangle$  because  $\langle\uparrow|\sigma_x|\uparrow\rangle = 0 = \langle\downarrow|\sigma_x|\downarrow\rangle$ . The envelope function itself may be referred to as  $|\langle\sigma_+\rangle|(t) = |\langle\sigma_x\rangle(t) + i\langle\sigma_y\rangle(t)|$ . Finally, in practice it is generally required to average over an ensemble, rather than to measure a single system only. The averaged  $|\langle\sigma_+\rangle|(t)$  often decays faster than in each individual case because the oscillation frequencies may be slightly different from system to system (i.e., small deviations in  $\Delta$ ), which leads to destructive interference and additional damping. The so-called dephasing time obtained from an ensemble measurement is therefore labeled  $T_2^*$ . The three timescales  $T_1$ ,  $T_2$ , and  $T_2^*$  are not completely unrelated. For spin qubits in QDs, where decoherence predominantly results from spin-orbit interaction ( $T_2 = 2T_1$  [39, 40]; Sec. 1.3.1.2) and hyperfine coupling to nuclear spins ( $T_2 \ll T_1$ ; Sec. 1.3.2), one finds that  $T_2 \leq 2T_1$  and usually  $T_2^* < T_2$  and  $T_2 \ll T_1$  in practice. Commenting on the terminology, the relaxation ( $T_1$ ), decoherence ( $T_2$ ), and dephasing ( $T_2^*$ ) times are only well defined when  $\langle\sigma_z\rangle$  or  $|\langle\sigma_+\rangle|$ , respectively, decay exponentially, which is the assumed behavior in most quantum error correction schemes. Strictly speaking, one should therefore avoid these terms when the longitudinal or transverse decay is of a nonexponential form. We note, however, that the introduced nomenclature is often used to characterize any decaying behavior for convenience.

A key criterion for building quantum computers, the one which actually justifies their name, is the presence of a universal set of quantum gates. This may fortunately be realized with one- and two-body interactions only, because any operation can be carried out as a sequence of one- and two-qubit gates. In fact, the implementation of single-qubit rotations for each element, along with only one type of entangling two-qubit gates, e.g.,  $\sqrt{\text{SWAP}}$  or CNOT, between neighboring qubits would be sufficient for universal quantum computation [38, 41]. We note in passing that entanglement of spin qubits can be created in many different ways and over long distances, for instance, by extracting and separating Cooper pairs from an s-wave superconductor as proposed in Ref. [42] and experimentally investigated recently in Refs. [43–46]. Nuclear spins and spin-orbit interaction, which present an undesired source of decoherence on the one hand, may prove useful for implementing qubit gates on the other hand, and both mechanisms are analyzed in more detail in the next section.

## 1.3 Spin-Orbit Interaction and Nuclear Spins in Quantum Dots

### 1.3.1 Spin-Orbit Interaction

Spin-orbit interaction (SOI) couples the orbital motion of a particle to its spin. Prime examples are relativistic effects of type  $\mathbf{l} \cdot \mathbf{s}$ , which can be derived from the Dirac equation, where  $\mathbf{l}$  and  $\mathbf{s} = \hbar\boldsymbol{\sigma}/2$  correspond to the orbital and spin angular momentum of the electron, respectively [47]. The operator  $\mathbf{l} \cdot \mathbf{s}$

is invariant under time reversal and parity transformations (spatial inversion) and commutes with both  $(\mathbf{l} + \mathbf{s})^2$  and  $l_z + s_z$ . As a consequence, due to Bloch functions of  $p$ - as opposed to  $s$ -type, SOI leads to interesting properties in the topmost valence band, which can be described mathematically in terms of an effective spin 3/2 [48, 49]. In the presence of inversion asymmetry, additional terms that do not conserve parity arise for the envelope function of electron and hole states. Based on the type of asymmetry, two important SOI mechanisms can be distinguished here. Rashba SOI results from structural inversion asymmetry and, for electrons, is typically of the form  $H_R \propto \mathbf{E}_{\text{eff}} \cdot (\boldsymbol{\sigma} \times \mathbf{p})$ , where the components  $\sigma_i$  are the Pauli matrices for spin 1/2,  $\mathbf{p}$  is the momentum operator, and  $\mathbf{E}_{\text{eff}}$  is an effective electric field determined by the system structure [48, 50]. Dresselhaus SOI is present in materials that lack bulk inversion symmetry, such as InAs or GaAs, and is of the form  $H_D \propto p_{x'}(p_{y'}^2 - p_{z'}^2)\sigma_{x'} + p_{y'}(p_{z'}^2 - p_{x'}^2)\sigma_{y'} + p_{z'}(p_{x'}^2 - p_{y'}^2)\sigma_{z'}$ , where  $x'$ ,  $y'$ , and  $z'$  correspond to the crystallographic directions [100], [010], and [001], respectively [48, 51].

For quasi-2D systems, the Hamiltonians  $H_R$  and  $H_D$  can be reduced further. For strong confinement along the  $z$  direction, the Rashba term simplifies to  $H_R = \alpha(p_x\sigma_y - p_y\sigma_x)$  with Rashba parameter  $\alpha$ . The resulting form of the Dresselhaus term strongly depends on the growth direction. For the  $z$  axis chosen along the confinement direction, one can substitute  $p_z \rightarrow \langle p_z \rangle = 0$ ,  $p_z^2 \rightarrow \langle p_z^2 \rangle$ , and all other terms can be neglected because of their smallness compared to terms  $\propto \langle p_z^2 \rangle$  [52]. For example, for  $z \parallel [100]$  one obtains  $H_D = \beta(p_y\sigma_y - p_x\sigma_x)$ , while for  $z \parallel [110]$  the spin projection along the confinement direction is conserved,  $H_D \propto p_x\sigma_z$ . Both these Hamiltonians vary under rotations of the coordinate system about the  $z$  axis, so that their exact form is determined by the relative orientation of coordinate and crystal axes. This is different for  $z \parallel [111]$ , where the effective Dresselhaus term is  $H_D \propto p_x\sigma_y - p_y\sigma_x$ , which moreover corresponds exactly to the form of the Rashba term. Therefore, Rashba and Dresselhaus SOI can cancel in lowest order for growth along the [111] direction [53].

We note that the presence of SOI results in small, but finite, anisotropic corrections to the Heisenberg exchange interaction of electron spins, thus affecting the fidelity of quantum gates based on isotropic exchange. Fortunately, strategies have been developed with which the SOI-induced gate errors can be strongly suppressed [54–56]. In general, gate errors can be reduced from first to second (or higher) order in SOI when the coupling strength  $J(t)$  is varied symmetrically in time, followed by additional qubit rotations [54, 56]. In particular, the anisotropic corrections can be cancelled completely in the CNOT gate construction of Ref. [13] when the system is pulsed such that the anisotropic terms are linear in  $J(t)$  [55]. Additional errors caused by dipole-dipole interactions were found to be negligible for CNOT (in typical situations) [55].

### 1.3.1.1 Electric-Dipole-Induced Spin Resonance

A rather useful technique for electrically controlled qubit rotations is electric-dipole-induced spin resonance (EDSR). It is closely related to the well-known electron spin resonance (ESR), which we therefore review first. For this, let us consider an electron in a QD in the presence of magnetic fields. The Hamiltonian  $H = H_0 + H_Z$  consists of a spin-independent part  $H_0 = p^2/(2m^*) + V(\mathbf{r})$ , where the first (second) term corresponds to the kinetic (potential) energy, and the Zeeman part  $H_Z = g\mu_B \mathbf{B} \cdot \boldsymbol{\sigma}/2$ , which couples the magnetic field  $\mathbf{B}$  to the spin. In the following, we assume that a constant magnetic field  $B_z$  is applied along the  $z$  axis, while a small oscillating field  $B_x(t) = B_\perp \cos(\omega t)$ ,  $B_\perp < B_z$ , is applied along the  $x$  axis. For any fixed orbital state  $|n\rangle$ , with  $H_0|n\rangle = E_n|n\rangle$ , the time evolution of the spin is described by the

(von Neumann) master equation for the density matrix  $\rho$ ,

$$\frac{d}{dt}\rho = -\frac{i}{\hbar}[E_n + H_Z, \rho] = -\frac{i}{\hbar}[H_Z, \rho], \quad (1.1)$$

$$H_Z = \frac{\hbar\omega_z}{2} \begin{pmatrix} 1 & 0 \\ 0 & -1 \end{pmatrix} + \frac{\hbar\omega_{\perp}}{4} \begin{pmatrix} 0 & e^{-i\omega t} \\ e^{i\omega t} & 0 \end{pmatrix} + \frac{\hbar\omega_{\perp}}{4} \begin{pmatrix} 0 & e^{i\omega t} \\ e^{-i\omega t} & 0 \end{pmatrix}, \quad (1.2)$$

where we defined  $\hbar\omega_z \equiv g\mu_B B_z$ ,  $\hbar\omega_{\perp} \equiv g\mu_B B_{\perp}$ , and the states of the matrices correspond to  $\{|n, \uparrow\rangle, |n, \downarrow\rangle\} \equiv \{|\uparrow\rangle, |\downarrow\rangle\}$ . When  $\omega \approx \omega_z$ , the final term of the chosen representation of  $\sigma_x \cos(\omega t)$ , Eq. (1.2), can be omitted because it only superimposes a fast and negligibly small oscillation to the dynamics. Within this rotating wave approximation, the resulting set of differential equations is exactly solvable. When the spin is originally in the  $|\uparrow\rangle$  state and the oscillating field is applied for  $t \geq 0$ , the probability  $p_{\downarrow}$  of a spin flip oscillates according to

$$p_{\downarrow} = \frac{\omega_{\perp}^2}{\omega_{\perp}^2 + 4\delta^2} \sin^2 \left( \frac{t}{4} \sqrt{\omega_{\perp}^2 + 4\delta^2} \right), \quad (1.3)$$

where  $\delta \equiv \omega - \omega_z$  is the detuning from the resonance condition  $\omega = \omega_z$ , and  $4\pi/\sqrt{\omega_{\perp}^2 + 4\delta^2}$  is the cycle duration. We note that the resulting spin-flip probability is completely equivalent to Eq. (1.3) when the spin is initially down.

Remarkably, in the presence of SOI one finds that an oscillating electric field  $\mathbf{E}(t) = \mathbf{E}_0 \cos(\omega t)$  leads to an effective magnetic field  $\mathbf{b}_0 \cos(\omega t)$  with, in general, nonzero components perpendicular to the static magnetic field. Hence, spin rotations can efficiently be driven by purely electrical means (EDSR). This may be achieved by applying ac voltages to nearby gates, at frequencies that are in resonance with the Zeeman splitting, as recently exploited in experiments on nanowire-based InAs and InSb QDs [57–60]. Explicit expressions for  $\mathbf{b}_0$  are lengthy, and in the following we therefore comment on important properties found in an analysis for lateral QDs with growth axis  $z \parallel [100]$  and harmonic confinement in the  $x$ - $y$  plane [61]. First, in contrast to ESR, the EDSR arises from coupling to other orbital states and therefore depends on the level spacing. This can easily be seen, because  $\langle \uparrow | x | \downarrow \rangle$ ,  $\langle \uparrow | y | \downarrow \rangle$ ,  $\langle n | p_x | n \rangle$ , and  $\langle n | p_y | n \rangle$  vanish, so that neither the dipolar term  $e\mathbf{E}(t) \cdot \mathbf{r}$  nor  $H_R$  or  $H_D$  couples the spin states in lowest order. A unitary Schrieffer-Wolff transformation shows that the leading term for EDSR is a combination of Zeeman coupling and SOI. More precisely, the effective magnetic field in the ground state is  $\propto \mathbf{B}_0 \times \mathbf{\Omega}(t)$ , where  $\mathbf{B}_0$  is the static magnetic field and  $\mathbf{\Omega}(t) = \mathbf{\Omega}_0 \cos(\omega t)$  depends linearly on the electric field components in the  $x$ - $y$  plane and the parameters  $\alpha$  and  $\beta$  [61]. We note that the resulting magnetic field is fully transverse and therefore most efficient. It can be quenched if  $\mathbf{B}_0 \parallel \mathbf{\Omega}_0$ . For typical GaAs QDs, EDSR allows spin manipulation on a timescale of 10 ns with the current experimental setups [61]. Numerical studies based on single electrons in 1D double quantum dots (DQDs) revealed rather unexpected spin dynamics at large driving field amplitudes, such as incomplete spin flips and surprisingly long cycle durations at resonance, pointing out possible challenges for future applications of EDSR in DQDs [62]. An analysis for heavy-hole (HH) QDs can be found in Ref. [63].

### 1.3.1.2 Relaxation and Decoherence

SOI and hyperfine interaction (Sec. 1.3.2) are the dominant decay channels for spin qubits. In particular, Rashba and Dresselhaus SOI lead to spin relaxation in combination with the phonon field, whereas other relaxation processes are usually negligible [39, 40, 64–67]. For electrons in [100]-grown 2D QDs it has been calculated that this phonon-mediated mechanism results in relaxation times  $T_1 \propto (\hbar\omega_0)^4 / (g\mu_B B)^5$  at low temperatures, where  $g\mu_B B$  is the Zeeman splitting induced by a magnetic field  $B$ , and  $\hbar\omega_0$  is the orbital level spacing [64]. For moderate magnetic fields, this dependence agrees very well with experimental results [52, 68–70]. As the magnetic fields become very large, the wavelengths of the phonons with energy  $g\mu_B B$  eventually become much smaller than the size of the QD; i.e., the phonon-induced effects

average out when integrating over the electron wave function and  $T_1$  increases rather than decreases [39]. Maximal relaxation rates are usually observed when the phonon wavelength matches the dot size [52]. In the other limit, for very small magnetic fields, the derived expression for  $T_1$  diverges. This is because the above theory focuses on single-phonon processes, so that only phonons in resonance with the Zeeman transition can contribute. Kramers' theorem forbids SOI-induced spin relaxation in the absence of a magnetic field [52, 64], which is also the reason why EDSR requires the presence of a finite magnetic field. When two-phonon processes are included,  $T_1$  converges to a finite value [64, 71, 72].

Holes are an attractive alternative to electrons because of the suppressed contact hyperfine interaction with nuclear spins (see subsection below). Phonon-mediated spin relaxation has also been analyzed in detail for flat [100]-grown HH QDs with magnetic fields along the confinement axis [40]. For low magnetic fields, one finds  $T_1 \propto B^{-5}$  due to Dresselhaus SOI, which is the same dependence as in the electron case, while the contribution due to Rashba SOI is  $T_1 \propto B^{-9}$ . The analysis shows that the spin relaxation time for HHs can be comparable to or even longer than that for electrons when the QD is strongly 2D, illustrating that holes are very sensitive to confinement [40]. For instance,  $T_1 > 0.2$  ms has been measured for HHs in self-assembled InGaAs QDs [73–75]. In the limit  $B \rightarrow 0$ , the relaxation times are determined by two-phonon processes. These have been included theoretically [72], suggesting times  $T_1$  on the order of milliseconds, in good agreement with values observed in experiments [74, 75].

Notably, the upper limit  $T_2 = 2T_1$  is fulfilled in both the electron [39] and the hole [40] cases discussed above, in contrast to the naively expected relation  $T_2 \ll T_1$ . Furthermore, theory predicts that electron spin relaxation is drastically suppressed for a certain magnetic field direction when  $|\alpha| = |\beta|$  in [100]-grown QDs [39]. (In passing we note that in this special limit, a new symmetry in spin space emerges giving rise to interesting spintronics effects in quasi-2D systems [76, 77].) Tuning the Rashba coefficient via electric fields, this effect should be observable in an experiment with a vector magnet. The analysis of SOI-mediated relaxation has been extended to QDs with two electrons, forming spin singlet and triplet states, where magnetic field orientations with strongly suppressed spin relaxation were found to exist for arbitrary Rashba and Dresselhaus coefficients [67]. The (relative) strengths of  $\alpha$  and  $\beta$  may be found via the singlet-triplet anticrossings for magnetic fields applied in growth direction, or by measuring the magic angles at which the singlet-triplet anticrossings and thus the corresponding singlet-triplet relaxations vanish in leading order of the SOI [67, 78]. Recently, a formula has been derived for lateral DQDs, which quantifies the level splitting at the singlet-triplet anticrossing in terms of various parameters [79]. This formula should allow the extraction of both the spin-orbit parameters and also the hyperfine coupling from transport or charge-sensing experiments in such DQDs [79]. Effects of hyperfine interaction are discussed below.

### 1.3.2 Nuclear Spins

A QD typically consists of  $10^4$ – $10^6$  atoms, so that an electron or hole confined to the QD overlaps with a large number of nuclear spins. The nuclear spin bath itself reveals large lifetimes, indicated by the long dipole-dipole correlation time among nuclear spins,  $\sim 0.1$  ms in GaAs [80, 81]. (Since the dipole-dipole interaction, resulting from the finite magnetic dipole moments of the nuclei, does not conserve spin, the dipole-dipole correlation time can be interpreted as the time it takes for a nuclear spin to flip in the mean field of the surrounding ones.) Despite its long lifetimes, the nuclear spin ensemble presents the main source of electron and hole spin decoherence. This is due to the hyperfine interaction among electron and nuclear spins, for which three different mechanisms can be derived from the Dirac equation [82]. The first one is the (isotropic) contact hyperfine interaction, which is the most relevant mechanism for conduction band electrons. For holes, where the Bloch functions are  $p$ - as opposed to  $s$ -type, the anisotropic hyperfine interaction and coupling to the orbital angular momentum become dominant. Below we summarize the effects and opportunities of a nuclear spin bath in more detail, beginning with a theoretical investigation

in Secs. 1.3.2.1–1.3.2.2 and ending with a brief overview on experimental achievements in Sec. 1.3.2.3.

### 1.3.2.1 Electron Spin Decoherence

When we assume that the external magnetic field, if present, is oriented along the  $z$  axis, the Hamiltonian of an electron spin  $\hbar\boldsymbol{\sigma}/2$  coupled to a bath of nuclear spins  $\hbar\mathbf{I}_k$  reads

$$\frac{1}{2}g\mu_B B_z \sigma_z + \frac{1}{2} \sum_k A_k \mathbf{I}_k \cdot \boldsymbol{\sigma} = \frac{1}{2} \left( g\mu_B B_z + \sum_k A_k I_k^z \right) \sigma_z + \frac{1}{4} \sum_k A_k (I_k^+ \sigma_- + I_k^- \sigma_+), \quad (1.4)$$

where  $\boldsymbol{\sigma} = (\sigma_x, \sigma_y, \sigma_z)$  is the vector of spin-1/2 Pauli matrices,  $g$  is the effective electron  $g$  factor,  $B_z$  is the external magnetic field, the  $A_k$  (positive for In, Ga, As) are the contact hyperfine coupling coefficients, and  $I_k^\pm = I_k^x \pm iI_k^y$  and  $\sigma_\pm = \sigma_x \pm i\sigma_y$  are the raising and lowering operators for nuclear and electron spin, respectively [82, 83]. The effects of the nuclear spins on an electron spin in a QD can thus be described in terms of an effective magnetic field  $\sum_k A_k \mathbf{I}_k / (g\mu_B)$ , referred to as the Overhauser field. Its component  $B_n^z$  along the  $z$  axis changes the total Zeeman splitting by the Overhauser shift, while transverse components couple the spin states  $|\uparrow\rangle$  and  $|\downarrow\rangle$  through electron-nuclear-spin flip-flop processes [83]. To avoid confusion, we mention that the term Overhauser field is often used for both the 3D effective nuclear magnetic field and its component  $B_n^z$ . The largest possible value for  $|B_n^z|$ , obtained for a fully polarized bath, is  $B_n^{\max} = IA/(|g\mu_B|)$ , where  $A$  is the averaged effective hyperfine coupling constant and  $I$  is the (average) quantum number for the nuclear spin. For GaAs,  $A \approx 90 \mu\text{eV}$  and  $I = 3/2$ , thus  $B_n^{\max} \approx 5 \text{ T}$  for the bulk  $g$  factor  $-0.44$ , and we note that  $B_n^{\max}$  is independent of the dot size [82, 83]. Without further preparation, the  $N$  nuclear spins inside a QD are in a superposition of states with different fields  $B_n^z$ , statistically distributed around a mean value  $pB_n^{\max}$ , where  $-1 \leq p \leq 1$  is the nuclear spin polarization along the  $z$  axis. Unless  $|p| \rightarrow 1$ , the width of this distribution is on the order of  $B_n^{\max}/\sqrt{N}$ , i.e., a few (tens of) millitesla for typical GaAs QDs of  $\sim 10^4$ – $10^6$  nuclear spins [84–86]. These internal fluctuations lead to dephasing and reduce the electron spin coherence time in GaAs dots to a few nanoseconds only [81–86]. The associated decay of the transverse spin is Gaussian and the decay time scales  $\propto \sqrt{N}/(A\sqrt{1-p^2})$  when  $I = 1/2$  and homogeneous coupling are assumed for simplicity [81]. One possibility for prolonging the lifetimes, apart from increasing the dot size, is therefore to polarize the nuclear spins [31, 81, 84, 85], which is discussed in more detail in Sec. 1.3.2.3. However, referring to the factor  $\sqrt{1-p^2}$  obtained for  $I = 1/2$ ,  $|p| > 0.99$  is required to reduce the decoherence by a factor of ten.

A second, attractive approach that has been theoretically proposed [81] for lifetime prolongation is to narrow the intrinsic distribution for  $|p| < 1$ . When the nuclear spin bath is initially in a less noisy, narrowed state, the electron spin decoherence induced by the finite width of possible  $B_n^z$  is suppressed. In particular, this dephasing mechanism is overcome when the system is initially in an eigenstate to a field  $B_n^z$ . In this case, the decoherence time is no longer  $\propto \sqrt{N}$ , but  $\propto N$ , so that the coherence times can be increased by several orders of magnitude [81–85, 87, 88]. The decay dynamics clearly differ from the Gaussian behavior that results from internal dephasing. In fact, an entire zoo of decoherence laws has been found, with a time decay that can proceed through several different stages (see Fig. 1.2) [89]. The reason for this feature is a rather long bath correlation time of order  $\hbar N/A$  [82–85]. The dynamics of the isolated electron spin interacting with the nuclear bath are therefore history-dependent (non-Markovian), and a Markov approximation, for which the longitudinal and transverse spin components decay exponentially, is typically invalid. On timescales  $< 0.1 \text{ ms}$ , where the dipolar coupling among nuclear spins can be ignored, this non-Markovian decay has been analyzed in great detail, and we list a few key results below. Assuming that the externally induced Zeeman splitting is large, such that  $|g\mu_B B_z| > A$  for  $I$  of order unity, i.e.,  $|B_z| \gtrsim 3.5 \text{ T}$  for GaAs, direct electron spin flips are energetically forbidden, which gives rise to pure dephasing of the electron spin [87]. Under these conditions (perturbative approach possible), the various stages that the transverse electron spin dynamics pass through have been calculated with



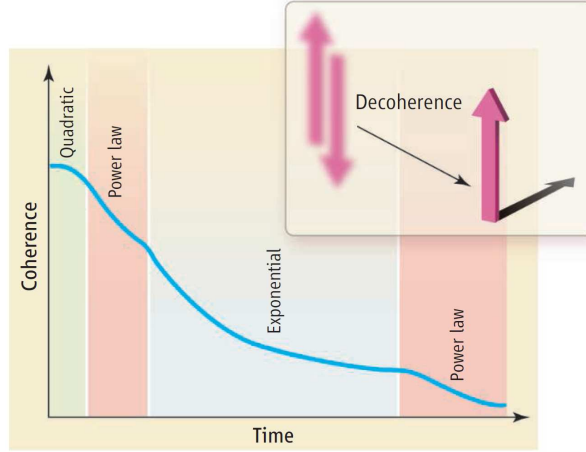


Figure 1.2. Schematic decay of  $|\langle\sigma_+\rangle(t)|$  for a quantum dot electron with large Zeeman splitting, assuming that the nuclear spin bath has been prepared in a narrowed state and that echo pulses are absent. The sketch illustrates the variety of decay laws that the system proceeds through. We note that the initial quadratic decay occurs on an ultrashort timescale, while an additional quadratic shoulder appears at the transition from the power law to the exponential loss of coherence. Details can be found in Refs. [81–83, 87–89]. (Inset) Decoherence corresponds to the decay of quantum mechanical superpositions due to interaction with the environment. For the prominent example of an electron spin qubit with eigenstates  $|\uparrow\rangle, |\downarrow\rangle$ , decoherence refers to transitions of type “ $|\uparrow\rangle$  and  $|\downarrow\rangle$ ”  $\rightarrow$  “either  $|\uparrow\rangle$  or  $|\downarrow\rangle$ ” and can be quantified by the time decay of the transverse spin  $|\langle\sigma_+\rangle(t)|$  as described in Sec. 1.2. *The picture was taken from Ref. [89] and is property of Science Magazine (<http://www.sciencemag.org>).*

one unified and systematic method based on expansion of a generalized master equation [81–83, 87, 88]. These stages include an ultrashort quadratic decay and an initial (partial) power-law decay, followed by a quadratic shoulder, a dominant exponential decay, and a long-time power-law decay. However, the exact behavior depends on various parameters, such as the QD dimensionality [83, 87]. The Markovian regime, which gives rise to the exponential decay, is reached for sufficiently large  $B_z$ , and analytic expressions for the decoherence time  $T_2 \propto NB_z^2$  have been found [82, 87, 88, 90]. This analysis was also of interest from a technical point of view, because it verified that calculations based on high-order expansions of a leading-order effective Hamiltonian can have limited validity. In particular, a notable modulation of the decay envelope found at long times cannot be obtained with an effective Hamiltonian (see Ref. [87] and references therein). Observing these additional oscillations experimentally would be a desirable confirmation of the theory. At low magnetic fields, an expansion of the generalized master equation is not possible, and the spin dynamics still are not understood in detail. A list of available approaches allowing for some insight into the low-field regime can be found in Refs. [83, 91]. For instance, the system is exactly solvable in the special case when the nuclear spin bath is initially fully aligned [84, 85]. Independently of  $B_z$ , it turns out that both  $\langle\sigma_z\rangle(t)$  and  $|\langle\sigma_+\rangle(t)|$  first perform small oscillations owing to coherent exchange with the nuclear spin bath. After the bath correlation time of order  $\hbar N/A$ , electron spin coherence is irreversibly lost and the spin components converge to constant values, slightly below the initial values only, where the system remains until dipole-dipole interactions among the nuclear spins become relevant [84, 85]. For  $B_z = 0$ , assuming a Gaussian envelope wave function, this asymptotic time decay evolves according to  $\ln^{-3/2}(t')$  and  $\ln^{-1}(t')$  for 3D and 2D QDs, respectively, where  $t' \propto tA/N$ . At large  $B_z$ , this decay is  $\propto (t')^{-3/2}$  and  $\propto (t')^{-1}$  in 3D and 2D dots, respectively, in agreement with the systematic solutions of the generalized master equation [81, 84, 85].

### 1.3.2.2 Hole Spin Decoherence

The spin dynamics have also been investigated for HHs in quasi-2D QDs [82, 92–94]. Assuming the strong confinement along the  $z$  axis, we recall that the states can be classified according to their angular momenta (effective spins)  $|J, m_J\rangle$ , where  $J$  quantifies the size and  $m_J \in \{-J, -J+1, \dots, J\}$  is the  $z$ -projection in units of  $\hbar$ . This results from the strong SOI in the valence band, coupling the electron spin to the  $p$ -type Bloch functions. HHs have  $|3/2, \pm 3/2\rangle$ , whereas light-hole (LH) states have  $|3/2, \pm 1/2\rangle$ , and the two bands are energetically well separated in 2D-like QDs. Even though the contact hyperfine term is absent, the remaining mechanisms, i.e., anisotropic hyperfine interaction and coupling to the orbital angular momentum, turn out to be rather strong – in typical III-V compounds, they are only one order of magnitude weaker than the contact hyperfine interaction for electrons [92, 95–98]. Remarkably, the coupling of the HH to the nuclear spin bath takes on a simple Ising form in leading order,  $\sum_k A_k^h I_k^z s_z$ , where  $A_k^h$  is the coupling to the  $k$ th nucleus,  $I_k^z$  denotes the  $z$  component of the  $k$ th nuclear spin in units of  $\hbar$ , and  $s_z$  is the HH pseudospin operator with eigenvalues  $s_z = \pm 1/2$  for  $m_J = \pm 3/2$  [92, 94]. This clearly differs from the Heisenberg-type contact hyperfine interaction  $\sum_k A_k \mathbf{I}_k \cdot \boldsymbol{\sigma}/2$  [Eq. (1.4)] because transverse components are basically absent in the case of holes.

As for electrons, one can distinguish between different initial configurations. In the case of an unprepared, inhomogeneously broadened nuclear spin bath, the transverse hole spin decay depends on the orientation of the external magnetic field  $\mathbf{B}$ . For zero field or  $\mathbf{B} \parallel z$ , dephasing results in a Gaussian time decay, as for electrons, with timescales of typically a few tens of nanoseconds [92]. However, due to the Ising-type rather than Heisenberg-type HH-nuclear-spin interaction, the situation changes drastically for an in-plane magnetic field  $\mathbf{B} \parallel x$ . Because the hyperfine fluctuations are now purely perpendicular to the applied field, the decay is no longer Gaussian and one finds instead that the transverse hole spin decays  $\propto \sqrt{\hbar E_{Z,x} / (\langle E_{n,z}^2 \rangle t)}$  at long times in the limit  $E_{Z,x}^2 \gg \langle E_{n,z}^2 \rangle$ , where  $E_{Z,x} = |g_x \mu_B B|$  is the externally induced Zeeman splitting,  $g_x$  is the in-plane HH  $g$  factor, and  $\langle E_{n,z}^2 \rangle$  is the variance of the nuclear field  $\sum_k A_k^h I_k^z$  [82, 92]. For typical GaAs QDs and magnetic fields of a few Tesla, the associated decay times are long, around tens of microseconds [92]. Only a few months after these calculations were published, an experiment on self-assembled InGaAs QDs with  $\mathbf{B} \parallel x$  confirmed that HH spins in 2D-like QDs are highly coherent, with  $T_2^* > 0.1 \mu\text{s}$  ( $T_2^* > 1 \mu\text{s}$  with  $\sim 40\%$  probability) reported for the setup under study [75, 99].

For applications that require large Zeeman splittings, an in-plane magnetic field may be inconvenient because  $g_x$  is usually much smaller than the HH  $g$  factor  $g_z$  along the axis of strong confinement. Long coherence times for  $\mathbf{B} \parallel z$  can be achieved as well, namely by preparing the nuclear spin bath in a narrowed state [93, 94]. When the nuclear spins are initially in an eigenstate of  $\sum_k A_k^h I_k^z$ , with  $\mathbf{B} \parallel z$ , decoherence can only result from additional transverse terms in the HH-nuclear-spin coupling which then allow for flip-flop processes. These additional terms mainly arise from coupling to neighboring bands, i.e., the conduction band, LH band, and split-off band, and are about one to two orders of magnitude weaker than the dominant Ising term [93, 94]. It turns out that the time decay of the transverse spin due to band hybridization is purely exponential and that the decoherence time  $T_2$  can be tuned over several orders of magnitude via the applied magnetic field. In fact, decoherence due to nuclear spins can be so strongly suppressed that other mechanisms, such as the dipole-dipole interaction or the coupling to the phonon bath, may take over as the dominant sources of transverse spin decay [93, 94]. Calculations on self-assembled QDs showed that the Ising-like form of the hyperfine coupling is preserved for realistic strain distributions [94]. The strain considerably affects the hyperfine-induced hole spin decoherence, largely through coupling to the conduction band, allowing tuning of  $T_2$  by an order of magnitude for fixed Zeeman splittings [94].

### 1.3.2.3 Distribution Narrowing and Dynamic Nuclear Polarization

As summarized above, the electron and hole spin decoherence induced by nuclear spins can be strongly suppressed when the nuclear spin bath is initialized in a narrowed state. Moreover, the effective nuclear magnetic field, up to  $\sim \pm 5$  T for electrons in GaAs QDs, allows the realization of large magnetic field gradients among neighboring QDs [100] and tuning the resonance energies in optically active QDs over several tens of microelectronvolts [101–104]. Therefore, nuclear spins are more and more considered a source of opportunity rather than trouble, leading to enormous experimental efforts in this field. Dynamic nuclear polarization (DNP) schemes are usually based on the isotropic contact hyperfine interaction among electron spin and nuclear spins. As illustrated in Sec. 1.3.2.1, Eq. (1.4), the transverse components of the Overhauser field allow the polarization of the nuclei via electron-nuclear-spin flip-flop processes, building up a large nuclear field  $\sum_k A_k I_k^z$  with maximum Overhauser shift  $|g| \mu_B B_n^{\max} = AI$ . An example for DNP via the hole spin can be found in Ref. [105].

DNP has been achieved experimentally by multiple forms of optical [101–112], electrical [100, 113–117], and magnetic [118, 119] driving, although it is impossible to completely list the large variety of approaches. Polarizations  $50\% < |p| < 70\%$  have been reported so far [106–108]; however, achieving  $|p| > 90\%$  remains a very challenging task. Interestingly, many DNP schemes feature an intrinsic feedback mechanism that drives the system toward fixed, stable nuclear field values, so that the width of the nuclear field distribution is narrowed at the same time [103–105, 118, 119]. Similar effects have been demonstrated using pulsed optical excitation on an ensemble of QDs [120, 121], and it has been shown that efficient feedback loops may also be included intentionally [113]. Further promising approaches for the preparation of narrowed states are based on indirect measurement [122–125].

We note that all decay properties described earlier in this section correspond to the free-induction decay, i.e., the case where the system evolves in the absence of externally applied control sequences. The dephasing due to inhomogeneous broadening can be undone to a large extent by applying spin-echo pulses, which notably increases the spin coherence times [126–132]. In parallel, an alternative trend is to bypass the interaction with nuclear spins completely by switching to host materials such as Ge and Si, which can be grown nuclear-spin-free. Examples for both approaches are discussed in the next section, where we review recent progress toward quantum computation with spins in QDs. Finally, we note that an alternative route to reduce the nuclear spin noise (besides narrowing and DNP) would be to polarize the nuclear spins by freezing them out, either by applying a sufficiently strong magnetic field on the order of 15 T at a few millikelvin [133] or by inducing an ordering transition of the nuclear spin system due to Ruderman-Kittel-Kasuya-Yosida (RKKY) interactions. The latter phenomenon has attracted a lot of interest in recent years, and we refer the interested reader to the literature [134–137].

## 1.4 Recent Progress in Quantum Dot Systems

Since the first proposals in the 1990s, researchers worldwide have been working hard toward the ambitious goal of implementing a quantum computer. In QDs, seminal progress has been made within the past few years. In this section, we summarize and discuss some of the key results, where we distinguish between self-assembled, lateral, and nanowire-based QDs. Table 1.1 in Sec. 1.4.4 summarizes relevant information, such as the measured lifetimes, and compares  $T_2$  to reported operation times as commented below.

Quantum systems are sensitive, and errors inevitably occur in any realistic device. Therefore, schemes for fault-tolerant quantum computing have been developed, where errors can automatically be corrected as long as they occur with low enough probability. The latter condition can usually be quantified in terms of a threshold rate [138–140]. For instance, standard error correction schemes require that at least  $\sim 10^4$  gate operations can be carried out within the decoherence time of a qubit [138–143]. A few years ago, a novel scheme derived from the toric code [144] was presented, referred to as the planar code or

surface code [145–149]. The logical qubits are encoded within several physical qubits each, all of which are arranged in a 2D lattice with nearest neighbor interactions. Logical single- and two-qubit gates are then performed via a series of projective measurements. This code is probably the most powerful quantum computing scheme presently known, with a remarkably large error threshold around 1% [145–149], so that  $\sim 10^2$  operations per decoherence time may already be sufficient. When errors for readout become negligible, error correction in the surface code is even possible up to a threshold rate of currently 18.5% [150]. The viability of topological error correction has recently been demonstrated in a first proof-of-principle experiment [151]. For further information on fault-tolerant quantum computation with the surface code we refer to Refs. [145–151]. A general overview on fault-tolerance is provided in Ref. [149].

### 1.4.1 Self-Assembled Quantum Dots

As opposed to gate-defined QDs, the confinement in self-assembled dots purely arises from the conduction and valence band offsets of the involved materials, leading to strong confinement on a very small scale in all three dimensions. Therefore, self-assembled QDs are typically operational at 4 K, the boiling temperature of  $^4\text{He}$ . Moreover, they are optically active and feature strong interband transitions with almost hard selection rules [30, 75, 102]. Exploiting this property, self-assembled QDs are primarily studied using optical means, and heterostructures have been designed that allow precise control over the charge states [152, 153].

For a qubit with basis  $|1\rangle$  and  $|0\rangle$ , the general qubit state can be written as  $|\psi\rangle = \cos(\theta/2)|1\rangle + e^{i\phi}\sin(\theta/2)|0\rangle$ , neglecting global phases, where  $0 \leq \theta \leq \pi$  and  $0 \leq \phi < 2\pi$  correspond to the polar and azimuthal angles, respectively, of a point on the Bloch sphere. Prerequisites for the implementation of a quantum computer are the abilities to initialize, to control, and to read out such a qubit state. All of this has been achieved now. First, the spins of both electrons [154] and holes [74, 155] can be initialized with  $\geq 99\%$  fidelity. Second, ultrashort optical pulses, combined with an externally induced Zeeman splitting, have allowed for complete quantum control, i.e., arbitrary rotations on the Bloch sphere, with operation times on the order of only a few picoseconds. Again, this has successfully been demonstrated on both single electrons [129, 156, 157] and single holes [158–160]. Recently, initialization and coherent control have also been reported for two-particle qubits defined by the spin singlet and triplet states of electrons [161] and holes [159] in vertically stacked QDs. The latter, also referred to as QD molecules, form naturally during growth when a second layer of QDs is grown on top of a first layer. Even though the position of the dots in the first layer is arbitrary, the QDs in the second layer will form right on top of the first ones due to strain in the tunnel barrier grown in between. Finally, several methods have been developed to read out the spin states. These include time-averaged readout via Faraday rotations [162], Kerr rotations [163], and resonance fluorescence [164]. In addition, time-resolved Kerr rotation spectroscopy has been reported [156, 165], and it has been shown that QD molecules allow measurement of the spin state of a single electron in real time via the resonance fluorescence [166]. In the latter case, the presence of a second dot enables the use of different optical transitions (laser energies) for the initialization and readout steps [166, 167].

Dephasing and decoherence times have been measured. For single-electron spin qubits, dephasing results in  $T_2^* \simeq 1\text{--}10$  ns [120, 129, 156, 163, 165, 168] depending on the exact system, whereas the observed decoherence times are  $T_2 \simeq 3$   $\mu\text{s}$  [120, 129]. However, it has been verified already that  $T_2^*$  can be significantly prolonged by narrowing the distribution of the nuclear field [105, 120, 121]. For single holes, the reported  $T_2^* = 2\text{--}21$  ns [158–160] and  $T_2 = 1.1$   $\mu\text{s}$  [158] are similar to those for electrons, hence shorter than initially expected, which is attributed to electrical noise [158, 159, 169]. Measurements based on coherent population trapping, i.e., in the frequency domain as opposed to the time domain, have revealed a much longer hole-spin dephasing time of  $> 0.1$   $\mu\text{s}$  [75, 99]. Electrical noise is also the reason for the short  $T_2^* = 0.4\text{--}0.7$  ns [161] and  $T_2^* \leq 0.6$  ns [159] observed for singlet-triplet qubits from

electrons and holes, respectively. When the QD molecule is operated in a regime where the singlet-triplet splitting is less sensitive to fluctuating electric fields,  $T_2^*$  can be increased by several orders of magnitude, and dephasing times up to 200 ns have recently been measured for coupled electrons [170]. Importantly, comparing the listed  $T_2$  to the notably short operation times of a few (tens of) picoseconds illustrates that the threshold factor of  $\sim 10^4$  for standard quantum error correction schemes has already been exceeded in both electron and hole systems. For reported spin relaxation times  $T_1$ , see Table 1.1.

The optical properties make self-assembled QDs highly promising candidates for applications as single-photon sources, and designs for enhanced extraction efficiencies are being developed [171]. Moreover, they may present an interface between stationary and flying qubits. Recently, interference of single photons from two separate QDs was demonstrated [172, 173], which is a promising approach for generating entanglement and implementing two-qubit gates between distant spins. Because different QDs, unlike atoms, have different resonance energies, implementing such a two-qubit gate requires that the level structure of a dot be tunable so that the photon energies can be made to match. Such fine tuning may be achieved via strain [172, 174], via the Stark effect [173, 175], or by polarizing the nuclear spins up to a desired (Overhauser) nuclear magnetic field. DNP in single self-assembled QDs has been studied in detail [101–112]. For instance, schemes exist both for high [103] and low [104] external magnetic fields that allow for continuous, bidirectional tuning of the Overhauser field, fully controlled by the laser wavelength. Both schemes are also capable of narrowing the width of the nuclear field distribution [103, 104].

As an alternative to the widely studied III-V compounds, self-assembled QDs can also be grown from group IV materials. A prominent example is self-assembled Ge QDs on Si substrates. Due to the indirect band gap of Ge and Si, these dots are not as optically active as typical III-V QDs [176]. Self-assembled Ge/Si QDs are subject to great experimental efforts, and detailed knowledge about growth and their electrical and optical properties has been gained [176–178].

## 1.4.2 Lateral Quantum Dots

Substantial progress has been made on implementing gate-controlled qubits within the 2DEG of a heterostructure. Experiments have predominantly been carried out on GaAs QDs within AlGaAs/GaAs heterostructures, which should be considered the host material in the following discussion unless stated otherwise. Mainly, two different approaches for encoding the qubit have emerged. The first scheme follows the original proposal [13], using the spin eigenstates  $|\uparrow\rangle$  and  $|\downarrow\rangle$  of single electrons. The second scheme uses the singlet  $|S\rangle = (|\uparrow\downarrow\rangle - |\downarrow\uparrow\rangle)/\sqrt{2}$  and triplet  $|T_0\rangle = (|\uparrow\downarrow\rangle + |\downarrow\uparrow\rangle)/\sqrt{2}$  states of two electron spins, forming an  $S$ - $T_0$  qubit [179–181]. We summarize below the results for both approaches.  $S$ - $T_+$  qubits [182] and qubits from three-spin states [183–186] are currently under investigation.

### 1.4.2.1 Single-Spin Qubits

The two eigenstates of a single electron in a QD,  $|\uparrow\rangle$  and  $|\downarrow\rangle$ , are split by an effective Zeeman energy via coupling to external and internal (Overhauser) magnetic fields. This energy difference gives rise to coherent single-qubit rotations  $(|\uparrow\rangle + |\downarrow\rangle)/\sqrt{2} \leftrightarrow (|\uparrow\rangle - |\downarrow\rangle)/\sqrt{2}$ . Rotations about the second axis of the Bloch sphere,  $|\uparrow\rangle \leftrightarrow |\downarrow\rangle$ , can be driven by means of E(D)SR, which we introduced in Sec. 1.3. Finally, two-qubit gates such as  $\sqrt{\text{SWAP}}$  and SWAP gates can be implemented by controlling the overlap of the wave functions and, hence, the exchange energy for neighboring electrons. Thirteen years after publication of the original proposal [13], the elementary unit of an all-electrical spin-qubit processor has now been implemented for the first time, demonstrating independently controllable single-spin rotations combined with interdot spin exchange in a DQD [187]. An important part of the setup in Ref. [187] is a micromagnet at the sample surface, whose stray field provides a time-independent magnetic field gradient at the QDs. This gradient is useful for two reasons. First, it allows for efficient and electrically driven ESR; an oscillating electric field slightly shifts the position of the electron in the QD, so that the electron

effectively feels an oscillating magnetic field of the same frequency without the need for SOI [187, 188]. Second, it leads to shifted resonance frequencies in adjacent QDs via a difference in the Zeeman energies, so that neighboring qubits can be addressed individually [116, 117, 187–189].

When quantum information is processed with the spin states of single electrons in QDs, qubit states can be read out via so-called spin-to-charge conversion as originally proposed in Ref. [13]. In this scheme, the system is electrically tuned to a regime where the electron of interest, depending on its energy and, thus, its spin state, does or does not tunnel into, e.g., a neighboring ancilla dot or a reservoir. The presence or absence of an electron can be detected with a nearby quantum point contact (QPC), whose conductance de-/increases due to the electric field provided by the electron charge [190, 191]. Single-shot readout of individual spins via spin-to-charge conversion has successfully been demonstrated experimentally, and furthermore this approach also allows for efficient qubit initialization when the QD is tunnel-coupled to a reservoir [52, 192, 193].

Performance of the implemented spin-qubit processor [187] was tested via a time-averaged readout scheme, using a QPC to measure the average charge configuration when the system is tuned to the Pauli spin blockade regime (see also  $S$ - $T_0$  qubits, Sec. 1.4.2.2). A fully operational unit for quantum computation requires precise initialization and single-shot readout of the individual qubit states, which therefore still needs to be included. Latest developments are promising [52, 189, 192–194], and an independent single-shot measurement of two electron spins in a DQD, with fidelities close to 90%, has recently been reported [193]. In the experiments described in Ref. [193], a time around 1 ms was required for spin readout and initialization to  $|\uparrow\rangle$ , slightly shorter than the measured spin relaxation time of  $\sim 4$ –5 ms. The latter strongly depends on the regime of operation, i.e., the applied gate voltages, and can take values  $T_1 > 1$  s [70]. The decoherence times  $T_2$  can be assumed to be much longer than a microsecond. For a single echo pulse and a magnetic field of 70 mT only, a decay time near 1  $\mu$ s has been measured, and clearly longer coherence times can be expected at higher magnetic fields and more sophisticated pulse sequences [127].

Comparing  $T_2$  to the typical operation times, we find that the threshold rates of proposed (standard) error correction protocols have already come within reach, as summarized below. Two-qubit gates are fast. For instance, SWAP operations  $|\uparrow\downarrow\rangle \rightarrow |\downarrow\uparrow\rangle$  require a time of order  $h/(2J)$ , where  $h$  is Planck’s constant and  $J$  is the exchange energy. They are routinely carried out within  $\lesssim 10$  ns [187, 195], and SWAP times  $< 0.5$  ns have been demonstrated [126]. Furthermore, single-qubit rotations induced by the Zeeman splitting typically occur on a subnanosecond timescale. Using the bulk  $g$  factor  $-0.44$  for GaAs and  $B_z = 1$  T (often chosen in-plane to avoid orbital effects) as the magnetic field that defines the quantization axis, the  $\pi$ -rotation  $(|\uparrow\rangle + |\downarrow\rangle)/\sqrt{2} \rightarrow (|\uparrow\rangle - |\downarrow\rangle)/\sqrt{2}$  requires a time of order  $h/|2g\mu_B B_z| \simeq 0.1$  ns. The efficiency of the universal set of qubit gates is therefore limited by the operation time  $\sim h/|g\mu_B B_\perp|$  for coherently driven spin flips  $|\uparrow\rangle \rightarrow |\downarrow\rangle$ , where  $B_\perp$  is the amplitude of the oscillating magnetic field perpendicular to  $B_z$  (see also Sec. 1.3.1.1). Recently reported spin-flip times are on the order of several tens of nanoseconds, for both magnetically [80, 127, 196] and electrically [188, 197] driven rotations, corresponding to  $B_\perp \approx 1$ –10 mT. The efficiency of electrically controlled rotations may, among other things, be improved by increasing the magnetic field gradient [188] or even, in a brute-force approach, by switching to host materials with stronger SOI [197] and larger  $g$  factors. Alternatively, coherent single-spin rotations about an arbitrary axis may be implemented using an auxiliary spin in a nearby QD with a different Zeeman field, which enables a purely exchange-based control without the need for SOI or oscillating fields [13, 198]. Such exchange-controlled single-qubit gates have not yet been realized experimentally; theoretical results, however, are promising and point toward high fidelities, with gating times of  $\sim 1$  ns [198].

### 1.4.2.2 Two-Spin Qubits ( $S$ - $T_0$ )

In the  $S$ - $T_0$  approach, every qubit is formed by two electrons in two adjacent QDs, where the charge configuration and the overlap of the electron wave functions depend on the shape of the confining potential, which in turn is determined by the applied gate voltages. Within the frame of this review it is sufficient to distinguish the two charge configurations (1,1) and (0,2), which denotes that the electrons are found either in different dots or both in the right QD, respectively. Coherent rotations  $|S\rangle \leftrightarrow |T_0\rangle$  are induced by a magnetic field gradient between the two QDs, typically achieved by dynamic polarization of the nuclear spins [100, 113, 115] or by a nearby positioned micromagnet [116, 117, 187–189]. When the barrier is reduced such that the wave functions strongly overlap, the finite exchange energy gives rise to coherent rotations  $|\uparrow\downarrow\rangle \leftrightarrow |\downarrow\uparrow\rangle$ , i.e.,  $(|T_0\rangle + |S\rangle)/\sqrt{2} \leftrightarrow (|T_0\rangle - |S\rangle)/\sqrt{2}$ , thus allowing for arbitrary rotations on the Bloch sphere [100]. These single-qubit operations can be carried out within a few nanoseconds only, and even subnanosecond operation times have been achieved already (see Table 1.1) [100, 126]. Two-qubit gates may be implemented by capacitive coupling, where the charge configuration in one DQD affects the exchange energy and, hence, the precession frequency in the other DQD [181, 195, 199]. Charge-conditional phase flips of an  $S$ - $T_0$  qubit have recently been demonstrated in four-dot systems [195, 199], and it was verified experimentally that the resulting CPHASE gate between two  $S$ - $T_0$  qubits is entangling [199]. Alternatively, as proposed theoretically in Ref. [200], CNOT gates may be implemented using the exchange interaction between adjacent QDs as the only time-dependent control parameter. The proposal shows that SOI and local magnetic field gradients allow for perfect CNOT operations, which are fast (a few nanoseconds) and, moreover, protected against charge noise.

For initialization, the potential energy in one of the dots is reduced such that both electrons tend to occupy the ground state of the same QD. This sets the qubit in the singlet state because the symmetric orbital part of the two-electron wave function requires an antisymmetric contribution of the spin. After operation in the (1,1) regime, the same idea also allows for a spin-to-charge conversion and therefore presents a popular basis for readout schemes. Having reduced the potential energy in one QD, the system changes to (0,2) for  $|S\rangle$ , but remains in (1,1) for  $|T_0\rangle$  due to Pauli exclusion. As described in Sec. 1.4.2.1, these charge states can be observed via nearby QPCs [126, 190, 191], which may furthermore be embedded in radio-frequency (rf) impedance matching circuits to allow for faster readout [125, 201, 202]. However, the quality of the outcome (readout visibility, see also Sec. 1.4.4) strongly depends on the triplet relaxation time at the measurement point, which may be clearly reduced in the presence of large magnetic field gradients [115], and implementing schemes for fast and reliable single-shot readout therefore remains an important task. Recently, single-shot measurements with measurement times down to 100 ns have been reported, using an rf sensor QD that is much more sensitive than standard QPCs [194]. As an alternative approach, dispersive readout of spin singlet and triplet states has been demonstrated with an rf resonant circuit coupled to a DQD [203]. Also, readout via spin-dependent tunnel rates has been achieved for the singlet and triplet states in a single QD [52, 204, 205].

Even though the random distribution of the nuclear spins leads to rapid dephasing within  $\sim 10$  ns [113, 126, 206], two-electron spin states feature very long coherence times. A single echo pulse increases the dephasing time to a few microseconds [126, 130–132], and more sophisticated pulse sequences have demonstrated coherence times on the order of 100  $\mu$ s [130–132], where 276  $\mu$ s currently corresponds to the largest value reported so far [131]. Assuming that the two-qubit gates can be operated on a similar timescale (nanoseconds) as the single-qubit gates, the threshold value of  $\sim 10^4$  operations per decoherence time is reached. As summarized above (Sec. 1.4.2.1), this similarly holds for the approach where qubits are formed by the spin states of single electrons.

### 1.4.2.3 Dynamic Nuclear Polarization and Alternative Host Materials

For both qubit encoding schemes, control over the nuclear spin bath is of great benefit. Various methods for DNP have been developed and demonstrated [100, 113–119], all of which may be used to generate large magnetic field gradients between neighboring QDs. Such gradients can be measured quantitatively via the cycle duration of oscillations  $|S\rangle \leftrightarrow |T_0\rangle$  [100, 113, 115], and differences  $> 200$  mT in the Overhauser field have been induced and subsequently exploited for coherent rotations on the Bloch sphere [100]. In addition, schemes exist to reduce the width of the nuclear field distribution [113, 118, 119], allowing for substantial prolongation of the dephasing times [113].

Besides GaAs QDs, other promising host materials are under investigation. In particular, rapid progress has been made on Si QDs within Si/SiGe heterostructures [207–212]. For instance, slow electron spin relaxation  $T_1 > 1$  s has recently been observed in this material via single-shot readout [210]. Also, single-shot measurements have allowed the extraction of relaxation times  $T_1 \sim 10$  ms for  $S$ - $T_0$  qubits operated near the (1,1)-(0,2) charge state transition [211]. Moreover, a hyperfine-induced dephasing time  $T_2^* = 360$  ns has been deduced from ensemble-averaged measurements on an  $S$ - $T_0$  qubit [212], which is nearly two orders of magnitude longer than the dephasing times measured in GaAs.

As opposed to self-assembled QDs, gate-defined systems cannot confine electrons and holes at the same time and are therefore optically inactive [30]. Currently, experiments are almost exclusively carried out on gated 2DEGs, and new experimental challenges may be encountered when 2DHGs are used instead [213]. However, considering the long lifetimes predicted for HHs in QDs [40, 92, 93] and the fact that strong magnetic field gradients may be induced via micromagnets [116, 117, 187–189], we think that hole spins can present a valuable alternative to electron spins.

### 1.4.3 Quantum Dots in Nanowires

Semiconducting nanowires attracted a lot of interest as promising platforms for Majorana fermions [214–216], field effect transistors [217], programmable circuits [218], single-photon sources [219], lasers [220, 221], and others. QDs therein form when the confinement in the transverse directions, provided by the wire geometry, is supplemented with an additional confinement in the longitudinal direction, which can be achieved both via electric gates and via structured growth of materials with suitable band offsets. In the first case, coupling between neighboring QDs is easily controllable via the gate voltages, while the second case is highly attractive for optical processes because electrons and holes can be stored at the same time (see also self-assembled QDs). Nanowires are thus versatile and may present a valuable link between stationary and flying qubits. For instance, similar to self-assembled QDs [30, 75, 102, 153], voltage-controlled charging and spin-dependent selection rules have been demonstrated on optically active InAsP QDs embedded in InP wires [222–224].

Nanowires have been grown from a variety of materials, all of which feature different properties and advantages. A prominent host material is InAs, which is known for its strong SOI and large  $g$  factors. Experiments on electrons in InAs nanowire QDs revealed a spin-orbit length  $l_{\text{SO}} \simeq 130$  nm, i.e., a spin-orbit energy  $E_{\text{SO}} \simeq 100$   $\mu\text{eV}$  [78], along with  $g$  factors  $|g| \simeq 7$ – $10$  [57–59, 78]. These features allow for fast spin rotations via EDSR [57–59], and spin-flip times  $< 10$  ns have already been demonstrated on single-spin qubits [57, 59]. However, the coherence time observed in Ref. [57] turned out to be rather short, only 50 ns for a single echo pulse and  $< 200$  ns for several pulses, which is considered to be attributable to the large nuclear spin  $9/2$  of In. The relaxation times in this experiment clearly exceeded the measurement range, i.e., the microsecond timescale [57], consistent with the theoretically predicted  $T_1$  of several microseconds to milliseconds [225]. Experiments with singlet-triplet states in an InAs nanowire DQD in the multi-electron regime showed that spin relaxation may be suppressed via tuning of the interdot coupling [226]. Besides InAs, InSb has also recently attracted a lot of attention, where EDSR



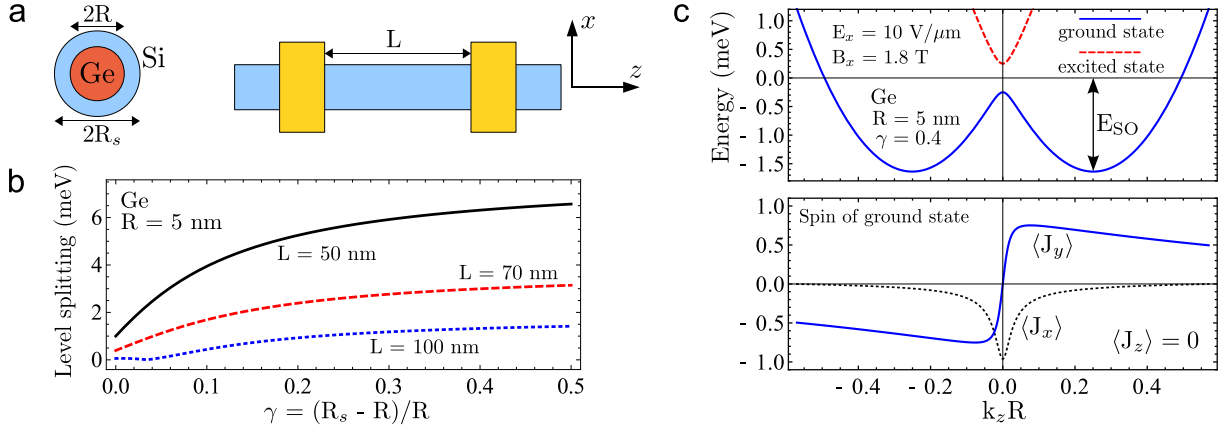


Figure 1.3. Calculated low-energy properties of hole states in Ge/Si core/shell nanowires, following Ref. [233]. (a) Holes accumulate in the Ge core of radius  $R$ , surrounded by a Si shell of thickness  $R_s - R$  leading to static strain. When the nanowire is supplemented with confinement along the wire axis  $z$ , a quantum dot of radius  $R$  and (effective) length  $L$  forms. (b) Energy gap between the two lowest Kramer's doublets in a longitudinal Ge quantum dot of  $R = 5$  nm and different lengths  $L$  as a function of relative shell thickness  $\gamma = (R_s - R)/R$ . The Si shell allows changing of the level splitting by several millielectronvolts, which is particularly useful for implementing spin qubits. (c, top) Hole spectrum as a function of longitudinal wave number  $k_z$  for a typical Ge/Si wire of  $R = 5$  nm and  $R_s = 7$  nm in the presence of an electric field  $E_x = 10$  V/ $\mu\text{m}$  and a magnetic field  $B_x = 1.8$  T along  $x$  (see panel a), illustrating strong spin-orbit interaction and sensitivity to magnetic fields, which are prerequisites for efficient qubit manipulation. The spin-orbit energy  $E_{\text{SO}} > 1.5$  meV, resulting from direct, dipolar coupling to  $E_x$ , is more than 15 times greater than the reported value for InAs [78]. At  $k_z = 0$ ,  $B_x$  opens a Zeeman gap of 0.5 meV, corresponding to  $|g| \sim 5$ . (c, bottom) Expectation value of the effective hole spin components  $J_x$ ,  $J_y$ , and  $J_z$  for the ground state plotted above. When the Fermi level is set within the gap at  $k_z = 0$ , the wire transports opposite spins in opposite directions, the characteristic feature of a helical mode. Therefore, Ge/Si nanowires also provide a promising basis for spin filters and Majorana fermions [214–216, 229, 233].

spectroscopy on the two-electron states of a gate-defined nanowire DQD revealed  $l_{\text{SO}} \simeq 200\text{--}300$  nm and very large  $g$  factors  $|g| \gtrsim 30$  [60].

A promising alternative to the III-V compounds are Ge/Si core/shell nanowires, which can be grown nuclear-spin-free. The valence band offset at the Ge/Si interface is large,  $\sim 0.5$  eV, so that holes accumulate naturally in the Ge core without the need for dopants [227, 228]. High mobilities [217] and long mean free paths [227] have been observed, along with a highly coherent charge transport seen through proximity-induced superconductivity [229]. Progress has also been made on gate-controlled Ge/Si nanowire QDs, even though the single-hole regime has not quite been reached yet [230–232]. Experiments on such a DQD have recently revealed spin relaxation times near 1 ms [232]. Furthermore, as illustrated in Fig. 1.3b, the relative thickness of the Si shell allows for varying the QD level splitting by several millielectronvolts via the static strain [233]. Remarkably, Ge/Si nanowires were also found to feature strong SOI: theoretical studies of the low-energy hole states showed that direct, dipolar coupling to an electric field gives rise to a SOI of Rashba type (“direct Rashba spin-orbit interaction”) which exceeds the standard Rashba SOI by one to two orders of magnitude [233]. Figure 1.3c (top) plots the ground-state spectrum for a typical nanowire of 5 nm core radius and 2 nm shell thickness in a moderate electric field of 10 V/ $\mu\text{m}$  perpendicular to the wire. The corresponding spin-orbit energy is  $E_{\text{SO}} > 1.5$  meV, more than 15 times greater than the reported value for InAs [78]. The additional magnetic field in Fig. 1.3c (top) along the electric field axis opens a gap in the spectrum ( $|g| \simeq 5$  at  $k_z = 0$ ), illustrating sensitivity to magnetic fields, a prerequisite for efficient qubit manipulation. The hole  $g$  factors in Ge/Si nanowire QDs are tunable via both the confinement and the magnetic field orientation [231, 233]. All these properties should allow for electrically controlled qubits with long lifetimes and short operation times. Furthermore, Ge/Si nanowires present an outstanding platform for helical hole states and Majorana fermions [214–216, 229, 233]. Finally, we mention that helical states [37, 234] and Majorana fermions [235] can alternatively be realized

in armchair carbon nanotubes without the need for a magnetic field, allowing for purely electrical setups. The required field, on the order of 1 V/nm [37, 234, 235], is stronger than in the case of Ge/Si wires, but still below experimentally achievable limits.

#### 1.4.4 Overview

Table 1.1 summarizes important information about the systems covered in this section, such as the longest measured lifetimes and shortest reported operation times. We would like to point out that, even though we studied the literature carefully, the provided summary is not intended to be complete, as further improvements might already have been achieved that we were not aware of when completing this review. The table also lists established initialization and readout schemes for each system, along with a ratio of the observed decoherence and gating times. The latter illustrates that decoherence no longer presents a massive stumbling block.

Typical values for characterizing readout schemes are the measurement fidelities  $F$  and the visibilities  $V$ . We note that these are not exactly equivalent. When  $e_{0 \rightarrow 1}$  denotes the error probability that the qubit state  $|0\rangle$  is incorrectly read as  $|1\rangle$ , the measurement fidelity for state  $|0\rangle$  is  $F_0 = 1 - e_{0 \rightarrow 1}$  [125, 192, 204]. Analogously, the measurement fidelity for the qubit state  $|1\rangle$  is  $F_1 = 1 - e_{1 \rightarrow 0}$ . One may define the readout fidelity for a particular experiment as  $F = p_0 F_0 + p_1 F_1 = 1 - p_0 e_{0 \rightarrow 1} - p_1 e_{1 \rightarrow 0}$ , where  $p_0$  ( $p_1$ ) is the probability that the system is initially in  $|0\rangle$  ( $|1\rangle$ ) [166]. Weighting  $|0\rangle$  and  $|1\rangle$  equally, this results in  $F = 1 - (e_{0 \rightarrow 1} + e_{1 \rightarrow 0})/2$  [52, 205]. A more general quantity is the visibility  $V = 1 - e_{0 \rightarrow 1} - e_{1 \rightarrow 0}$ , which is independent of  $p_0$  and  $p_1$  and presents a lower bound for the readout fidelity in a system [52, 125, 192, 204]. We note that readout may also be characterized by the measurement efficiency defined in Ref. [236], where various readout schemes have been analyzed theoretically.

##### *Description of Table 1.1:*

For each of the systems discussed in the text, the table summarizes the longest lifetimes, the shortest operation times, the highest readout fidelities (visibilities), and the highest initialization fidelities reported so far in experiments. Information on established schemes for readout and initialization is provided, along with a rating on scalability. All single-qubit operation times correspond to rotations of  $\pi$  (about the  $z$  and  $x$  axis, respectively) on the Bloch sphere. For a qubit with eigenstates  $|0\rangle$  and  $|1\rangle$ ,  $\tau_Z$  refers to operations of type  $(|0\rangle + |1\rangle)/\sqrt{2} \rightarrow (|0\rangle - |1\rangle)/\sqrt{2}$ , whereas  $\tau_X$  refers to rotations of type  $|0\rangle \rightarrow |1\rangle$ . Two-qubit gates are characterized by the SWAP time  $\tau_{\text{SW}}$ , describing operations of type  $|01\rangle \rightarrow |10\rangle$ . The ratio  $T_2/\tau_{\text{op}}$ , where  $\tau_{\text{op}}$  is the longest of the three operation times, gives an estimate for the number of qubit gates the system can be passed through before coherence is lost. Referring to standard error correction schemes, this value should exceed  $\sim 10^4$  for fault-tolerant quantum computation to be implementable. Using the surface code, values above  $\sim 10^2$  may already be sufficient. Experiments on self-assembled QDs have predominantly been carried out in (In)GaAs. Unless stated otherwise, GaAs has been the host material for gate-defined QDs in two-dimensional electron gases (2DEGs). The results listed for nanowire QDs have been achieved in InAs (electrons) and Ge/Si core/shell (holes) nanowires. We note that the experimental conditions, such as externally applied magnetic fields, clearly differ for some of the listed values and schemes. Finally, we wish to emphasize that further improvements might already have been achieved that we were not aware of when writing this review.

## 1.5 Proposals for Long-Distance Spin-Spin Coupling

Recently, pairwise control of the exchange interaction via electric gates has been demonstrated in a triple quantum dot [185, 186]. Such control is an essential requirement for most quantum computer architectures (see Fig. 1.1b), so the experiments of Ref. [185] present an important proof of scalability. Large-scale quantum computers, however, must be capable of reaching a system size of several thousands

Table 1.1. Overview of the state of the art for quantum computing with spins in quantum dots (QDs), with references in footnotes. For details, see the description in Sec. 1.4.4. Abbreviation: n.a., not yet available.

	Self-Assembled QDs		Lateral QDs in 2DEGs		QDs in Nanowires	
	Electrons	Holes	Single Spins	$S$ - $T_0$ Qubits	Electrons	Holes
Lifetimes	$T_1 > 20$ ms <sup>a</sup> $T_2 : 3$ $\mu$ s <sup>b</sup> $T_2^* \gtrsim 0.1$ $\mu$ s <sup>c</sup>	$T_1 : 0.5$ ms <sup>d</sup> $T_2 : 1.1$ $\mu$ s <sup>e</sup> $T_2^* > 0.1$ $\mu$ s <sup>f</sup>	$T_1 > 1$ s <sup>g</sup> $T_2 : 0.44$ $\mu$ s <sup>h</sup> $T_2^* : 37$ ns <sup>h</sup> $T_1^{\text{Si}} > 1$ s <sup>i</sup>	$T_1 : 5$ ms <sup>j</sup> $T_2 : 276$ $\mu$ s <sup>k</sup> $T_2^* : 94$ ns <sup>l</sup> $T_1^{\text{Si}} \sim 10$ ms <sup>m</sup> $T_2^{*,\text{Si}} : 360$ ns <sup>n</sup>	$T_1 \gg 1$ $\mu$ s <sup>o</sup> $T_2 : 0.16$ $\mu$ s <sup>o</sup> $T_2^* : 8$ ns <sup>o</sup>	$T_1 : 0.6$ ms <sup>p</sup> $T_2 : \text{n.a.}$ $T_2^* : \text{n.a.}$
Operation times	$\tau_Z : 8.1$ ps <sup>q</sup> $\tau_X : 4$ ps <sup>r</sup> $\tau_{\text{SW}} : 17$ ps <sup>s</sup>	$\tau_Z : 17$ ps <sup>e</sup> $\tau_X : 4$ ps <sup>e</sup> $\tau_{\text{SW}} : 25$ ps <sup>t</sup>	$\tau_Z : \text{n.a.}$ <sup>u</sup> $\tau_X : 20$ ns <sup>v</sup> $\tau_{\text{SW}} : 350$ ps <sup>w</sup>	$\tau_Z : 350$ ps <sup>w</sup> $\tau_X : 0.39$ ns <sup>x</sup> $\tau_{\text{ccpf}} : 30$ ns <sup>y</sup>	$\tau_Z : \text{n.a.}$ <sup>z</sup> $\tau_X : 8.5$ ns <sup>A</sup> $\tau_{\text{SW}} : \text{n.a.}$	n.a.
$T_2/\tau_{\text{op}}$	$1.8 \times 10^5$	$4.4 \times 10^4$	22	$9.2 \times 10^3$	n.a.	n.a.
Readout schemes and visibilities $V$ (fidelities $F$ )	$F = 96\%$ <sup>B</sup> Resonance fluorescence in a QD molecule  Other: Faraday <sup>C</sup> and Kerr <sup>D</sup> rotation spectroscopy, resonance fluorescence <sup>E</sup>	Absorption <sup>F</sup> and emission <sup>G</sup> spectroscopy (selection rules)	$V = 65\%$ <sup>H</sup> $V^{\text{Si}} = 88\%$ <sup>i</sup> Spin-selective tunneling  $F = 86\%$ <sup>I</sup> Spin-selective tunneling (two spins)  Other: Photon-assisted tunneling <sup>J</sup>	$V = 90\%$ <sup>K</sup> $F = 97\%$ <sup>L</sup> Spin-dependent charge distribution (rf-QPC <sup>K</sup> , rf-SQD <sup>L</sup> )  $V = 81\%$ <sup>M</sup> Spin-dependent tunneling rates  Other: Dispersive readout <sup>N</sup>	$F = 70\%$ – $80\%$ <sup>O</sup> Pauli spin blockade  Other: Dispersive readout <sup>P</sup>	Spin-dependent charge distribution (sensor dot coupled via floating gate) <sup>Q</sup>
Initialization schemes and fidelities $F_{\text{in}}$	$F_{\text{in}} > 99\%$ <sup>R</sup> Optical pumping	$F_{\text{in}} = 99\%$ <sup>S</sup> Optical pumping $F_{\text{in}} > 99\%$ <sup>T</sup> Exciton ionization	Spin-selective tunneling, <sup>U</sup> adiabatic ramping to ground state of nuclear field <sup>V</sup>	Pauli exclusion <sup>w</sup>	Pauli spin blockade <sup>O</sup>	n.a. (single-hole regime not yet reached)
Scalability	Scaling seems challenging		Seems scalable <sup>W</sup> (e.g., via floating gates <sup>X</sup> )		Seems scalable (e.g., via floating gates <sup>X</sup> )	

<sup>a</sup>[68]; <sup>b</sup>[120, 129];

<sup>c</sup>Measured for single electrons in a narrowed nuclear spin bath [105] and for two-electron states in quantum dot molecules with reduced sensitivity to electrical noise [170], both via coherent population trapping. Without preparation,  $T_2^* \sim 0.5$ – $10$  ns (see Sec. 1.4.1).;

<sup>d</sup>[73, 74]; <sup>e</sup>[158];

<sup>f</sup>[99]. Measured through coherent population trapping. Other experiments revealed  $T_2^* = 2$ – $21$  ns attributed to electrical noise [158, 159].;

<sup>g</sup>[70]; <sup>h</sup>[127]; <sup>i</sup>[210]; <sup>j</sup>[204, 206]; <sup>k</sup>[131];

<sup>l</sup>[113]. Achieved by narrowing the nuclear spin bath. Without narrowing,  $T_2^* \sim 10$  ns [113, 126, 206].;

<sup>m</sup>[211];

<sup>n</sup>[212]. Hyperfine-induced.;

<sup>o</sup>[57]; <sup>p</sup>[232]; <sup>q</sup>[129]; <sup>r</sup>[129, 157]; <sup>s</sup>[161]; <sup>t</sup>[159];

<sup>u</sup>While Ref. [127] gets close, we are currently not aware of a Ramsey-type experiment where coherent rotations about the Bloch sphere  $z$  axis have explicitly been demonstrated as a function of time. Thus no value is listed. However,  $\tau_Z$  should be short, on the order of  $0.1$  ns assuming a magnetic field of  $1$  T and  $g = -0.44$  as in bulk GaAs.;

<sup>v</sup>[188]; <sup>w</sup>[126]; <sup>x</sup>[100];

<sup>y</sup>[195]. SWAP gates for  $S$ - $T_0$  qubits have not yet been implemented. We therefore list the duration  $\tau_{\text{ccpf}}$  of a charge-state conditional phase flip.;

<sup>z</sup>In Ref. [57], rotations about an arbitrary axis in the  $x$ - $y$  plane of the Bloch sphere are reported instead, controlled via the phase of the applied microwave pulse.;

<sup>A</sup>[57, 59]; <sup>B</sup>[166]; <sup>C</sup>[162]; <sup>D</sup>[156, 163, 165]; <sup>E</sup>[164]; <sup>F</sup>[74, 159]; <sup>G</sup>[73, 158]; <sup>H</sup>[192]; <sup>I</sup>[193]; <sup>J</sup>[189];

<sup>K</sup>[125]. rf-QPC: radio-frequency quantum point contact [201, 202].;

<sup>L</sup>[199]. rf-SQD: radio-frequency sensor quantum dot [194].;

<sup>M</sup>[204]. The paper demonstrates readout of the singlet and triplet states in a single quantum dot.;

<sup>N</sup>[203]. A radio-frequency resonant circuit is coupled to a double quantum dot.;

<sup>O</sup>[57]. The readout and initialization schemes in this experiment only determine whether two spins in neighboring qubits are equally or oppositely oriented.;

<sup>P</sup>[59]. A superconducting transmission line resonator is coupled to a double quantum dot.;

<sup>Q</sup>[232]. The scheme, operated in the multihole regime, distinguishes the spin triplet states from the spin singlet.;

<sup>R</sup>[154]; <sup>S</sup>[74]; <sup>T</sup>[155]; <sup>U</sup>[192, 193, 210];

<sup>V</sup>[126]. Information about the nuclear field is required for the electronic ground state to be known.;

<sup>W</sup>[185]; <sup>X</sup>[237].

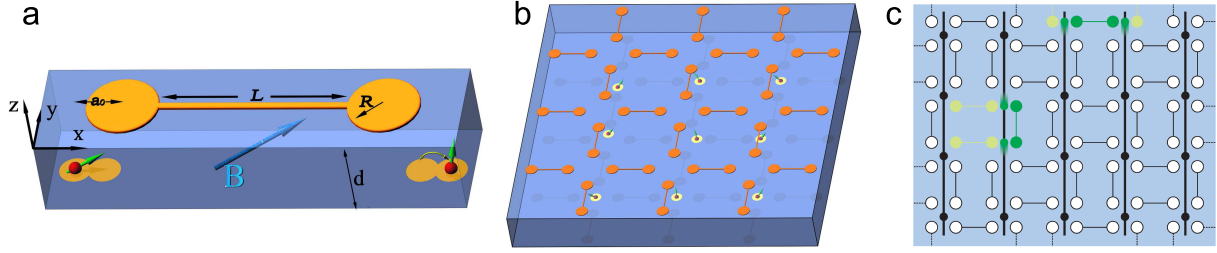


Figure 1.4. Long-distance qubit-qubit coupling via floating gates, allowing individual qubits to be separated by large distances [237]. (a) Schematic setup for two spins in separated double quantum dots coupled capacitively via a floating gate (here: simple, symmetric “dog bone” geometry). In the presence of a magnetic field and spin-orbit coupling, the electrostatic interaction of the charges results in an effective spin-spin coupling. Depending on the actual system and the gate geometry, remarkably strong qubit-qubit interactions of 1–100  $\mu\text{eV}$  can be reached [237]. (b) Scalable quantum computer architecture using metallic floating gates on top of a 2D electron gas. (c) An alternative architecture with qubits (black dots) implemented in nanowires (vertical black lines). In both b and c, qubit-qubit interactions can be switched on (off) via gates by moving the qubits close to (away from) the corresponding metal discs. The architectures provide a platform for the powerful surface code [145–151]. *All pictures were taken from Ref. [237] and are property of the American Physical Society (<http://www.aps.org>).*

of qubits. This poses serious architectural challenges to the exchange-based QD scheme from Ref. [13] (see Fig. 1.1) because the large amount of wires and metallic gates needs to be installed and operated on a very small scale. A promising strategy to meet this challenge has recently been proposed [237]; long-distance spin-spin coupling can be achieved capacitively via floating gates, allowing the (D)QDs to be moved far apart. The effective qubit-qubit coupling  $J'$  via floating gates can take remarkably large values  $J' \sim 1\text{--}100 \mu\text{eV}$  [237]. These are comparable to the achievable exchange energies  $J \sim 10\text{--}100 \mu\text{eV}$  in typical GaAs DQDs [13, 52, 237], where we note that  $J$  close to  $10 \mu\text{eV}$  has already been realized [126]. The floating gates may be positioned on top of the sample, as sketched in Fig. 1.4a, or may even be defined within the 2DEG. Qubit-qubit coupling can be switched on and off by changing the relative positions of the QDs (charges) with respect to the gates, allowing for all-electrical control [237]. Proposed, scalable architectures for a quantum computer with floating gates are shown in Figs. 1.4b and 1.4c. A key feature of the architectures suggested in Ref. [237] is that they all consist of a 2D lattice of spin qubits with nearest neighbor qubit-qubit interactions. Therefore, they all allow for the implementation of the surface code with its strikingly large error threshold around 1% (see also Sec. 1.4 and Refs. [145–151] for further information).

Another scheme for long-distance coupling between spins uses the photon field of a cavity. The original idea goes back to a proposal from 1999, which suggests that laser-induced Raman transitions can be used to couple the electron spin states of distant QDs when embedded in an optical cavity [14]. A few years later, as an alternative to the standard cavity QED, 1D superconducting transmission line resonators, which operate as on-chip microwave cavities, have been introduced and have launched the field of circuit QED [238, 239]. Since then, several proposals for long-range spin-spin coupling via circuit QED have been made [225, 240–244]. The direct coupling of a single spin to the magnetic component of the cavity electromagnetic field, however, is weak, and achieving strong interactions between a spin qubit and a cavity thus requires other mechanisms, resulting in a variety of suggested approaches. These, for instance, are based on Raman-type transitions among single-electron states in DQDs [240], on  $S\text{--}T_0$  qubits in QD molecules with (nuclear) magnetic field gradients [241, 242], or on the single-electron states in DQDs contacted to ferromagnetic insulators [243]. Relatively recently, using electron spins in InAs nanowire QDs was proposed [225]. InAs nanowire QDs feature a strong SOI and, thus, enable efficient coupling between the qubits and the electric component of the cavity field. Investigated architectures are shown in Fig. 1.5, where nanowires with strong longitudinal (transverse) QD confinement are placed parallel (perpendicular) to the transmission line in panel a (b). Rotations of individual qubits can be

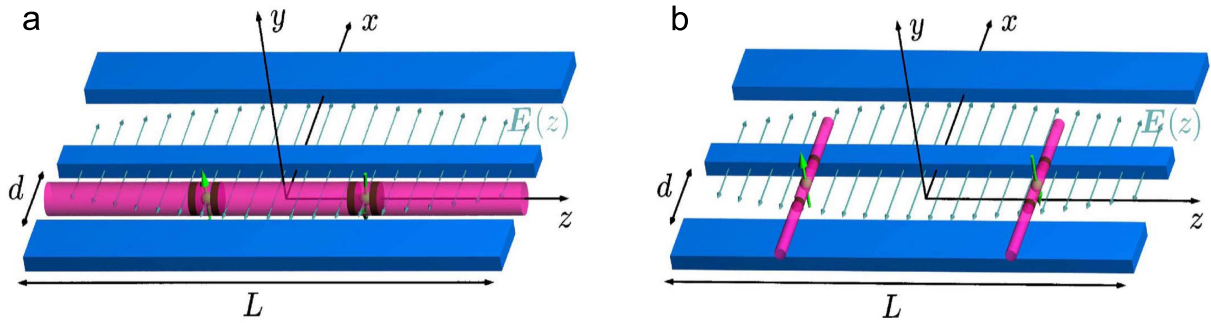


Figure 1.5. Architectures for long-range qubit-qubit coupling via microwave cavities as studied in Ref. [225]. The superconducting transmission line resonator is sketched in blue, assuming that the center conductor of length  $L$  is separated from the neighboring ground planes by a distance  $d$ . Electron spin states (thick green arrows) in InAs nanowire quantum dots (QDs) serve as qubits. The QD confinement, illustrated by brown discs within the nanowires (pink cylinders), can be realized with a suitable barrier material, such as InP, or with electric gates. (a) A large-diameter nanowire is oriented parallel to the transmission line and hosts QDs with strong longitudinal confinement. (b) Small-diameter nanowires, each hosting a QD with strong transverse confinement, are placed perpendicular to the transmission line. An insulating material separates the wires from the superconducting resonator to prevent a current flow. In both setups, the spin-orbit interaction enables all-electrical operation along with strong long-range interactions mediated by the photon field of the cavity [225]. For the system in panel b, the time to coherently swap two spins was estimated to be around 20 ns, and further improvement seems clearly possible. *The pictures were taken from Ref. [225] and are property of the American Physical Society (<http://www.aps.org>).*

driven through EDSR [57–61], and two-qubit interactions can be turned on and off by changing the QD confinements with nearby gates, allowing for all-electrical control [225]. For the setup shown in Fig. 1.5b, an operation time around 20 ns was estimated for swapping two spins coherently, and further optimization seems clearly possible. Recent experiments [59] following Ref. [225] have led to very encouraging results. They demonstrate that spin-cavity coupling strengths on the order of 1 MHz (several nanoelectronvolts) are experimentally feasible, exceeding the coupling of the spin to the magnetic component of the cavity field by several orders of magnitude and anticipating that the strong coupling regime for spin qubits can be reached [59]. Notably, it has been shown theoretically that circuit QED also allows for long-range coupling between certain types of molecular magnets [245]. A discussion of relaxation and decoherence in those systems can be found in Ref. [246].

## 1.6 Outlook

When electron spins in QDs were proposed for quantum computation, the experimental situation was not encouraging. Gate-controlled QDs within 2DEGs were limited to around 30 or more confined electrons each, and techniques for single-qubit manipulation and readout were not available [247]. Furthermore, decoherence from interactions with the environment was considered an almost insurmountable obstacle. Within the past decade, the situation has changed dramatically, owing to continuous experimental and theoretical progress. QDs are now routinely controlled down to the last electron (hole), owing to a clever gate design based on plunger gates [52, 247, 248], and various schemes have been applied for both qubit initialization and readout. Reducing the occupation number of QDs to the minimum is desirable for high-fidelity quantum computation [249]; however, larger fillings with a well-defined spin-1/2 ground state are also useful [23]. In addition, efficient single- and two-qubit gates have been demonstrated, allowing for universal quantum computing when combined. The achieved gating times are much shorter than measured lifetimes, and it seems that one will soon be able to overcome decoherence to the required extent. This is a major step toward the realization of a quantum computer.

While the field is very advanced for the workhorse systems such as lateral GaAs QDs or self-assembled

(In)GaAs QDs, rapid progress is also being made in the quest for alternative systems with further optimized performance. First, this includes switching to different host materials. For instance, Ge and Si can be grown nuclear-spin-free, and required gradients in the Zeeman field may be induced via micromagnets. Second, both electron- and hole-spin qubits are under investigation, exploiting the different properties of conduction and valence bands, respectively. Finally, promising results are obtained from new system geometries, particularly nanowire QDs.

Future tasks can probably be divided into three categories. The first one consists of studying new quantum computing protocols (such as the surface code), which put very low requirements on the physical qubits. The second category refers to further optimization of the individual components listed in Table 1.1. For instance, longer lifetimes are certainly desired, as are high-quality qubit gates with even shorter operation times. However, as decoherence no longer seems to present the limiting issue, particular focus should also be put on implementing schemes for highly reliable, fast, and scalable qubit readout (initialization) in each of the systems. Finally, because the results in Table 1.1 are usually based on different experimental conditions, the third category consists of merging all required elements into one scalable device, without the need for excellent performance. Such a complete spin-qubit processor should combine individual single-qubit rotations about arbitrary axes, a controlled (entangling) two-qubit operation, initialization into a precisely known state, and single-shot readout of each qubit. While Ref. [187] presents an important step toward this unit, prototypes of a complete spin-qubit processor could present the basis for continuous optimization.

In summary, considering the impressive progress achieved within the past decade, one may be cautiously optimistic that a large-scale quantum computer can indeed be realized.

### Summary Points:

- The experimental situation has dramatically changed since 1998, when the original proposal for quantum computation with quantum dots [13] was published. Quantum dots are now precisely controlled down to the last spin. Single-qubit rotations around different axes, two-qubit operations, and various initialization and readout schemes have successfully been demonstrated (Table 1.1).
- Overcoming decoherence to the required extent should soon be possible, which is a big step toward the implementation of a quantum computer.
- Nuclear spins and spin-orbit interaction, on the one hand, present a source of decoherence and relaxation. On the other hand, they can generate large Overhauser fields and are useful for realizing quantum gates. Schemes exist to narrow the width of the nuclear field distribution.
- Several quantum dot systems are currently under investigation, including host materials with or without nuclear spins, operation in the conduction or valence band, and different geometries. Holes in Ge/Si-nanowire-based quantum dots are promising examples [230–233].
- Electrically pulsed, pairwise control of the exchange interaction has been demonstrated in a triple quantum dot [185]; i.e., the scalability of exchange-based schemes for quantum computing [13] has now been verified experimentally.
- Long-distance spin-spin coupling via floating gates may be used to overcome architectural challenges of a large-scale quantum computer, and several 2D architectures have been proposed [237]. Alternatively, distant spins may be coupled via the photon field of a cavity [14, 59, 225, 240–245].
- Recent development toward quantum computation with quantum dots has been very positive, and one can be curious about the progress to be made in the next few years.

### **Future Issues:**

- The surface code is a powerful protocol for fault-tolerant quantum computing [144–151]. Can the requirements on the physical qubits be reduced further?
- Can longer lifetimes and more efficient qubit gates be reported? In particular, can schemes for fast and highly reliable single-shot readout and initialization be implemented in each of the discussed systems?
- Schemes for exchange-controlled single-spin rotations (about arbitrary axes) have been proposed as an efficient alternative to rotations driven by oscillating fields [13, 198]. Can this be realized experimentally?
- Electrically controlled single-qubit and two-qubit operations were demonstrated in the setup of Ref. [187]. Can a complete spin-qubit processor be reported soon?

### **Disclosure Statement**

The authors are not aware of any affiliations, memberships, funding, or financial holdings that might be perceived as affecting the objectivity of this review.

### **Acknowledgments**

We thank J. R. Wootton for useful comments and critical reading of the manuscript. We also thank S. Gangadharaiah, F. Maier, P. Stano, D. Stepanenko, M. Trif, and R. J. Warburton for helpful discussions and acknowledge support from the Swiss NF, NCCRs Nanoscience and QSIT, DARPA, and IARPA.





# References

- [1] Schrödinger E. 1935. *Naturwissenschaften* 23:823–28
- [2] Einstein A, Podolsky B, Rosen N. 1935. *Phys. Rev.* 47:777–80
- [3] Aspect A, Grangier P, Roger G. 1982. *Phys. Rev. Lett.* 49:91–94
- [4] Žak RA, Röthlisberger B, Chesi S, Loss D. 2010. *Riv. Nuovo Cim.* 33:345–99
- [5] Feynman RP. 1982. *Int. J. Theor. Phys.* 21:467–88
- [6] Feynman RP. 1985. *Opt. News* 11:11–20
- [7] Deutsch D. 1985. *Proc. R. Soc. Lond. A* 400:97–117
- [8] Deutsch D, Jozsa R. 1992. *Proc. R. Soc. Lond. A* 439:553–58
- [9] Grover LK. 1997. *Phys. Rev. Lett.* 79:325–28
- [10] Shor PW. 1994. Algorithms for quantum computation: discrete logarithms and factoring. *Proc. 35th Annu. Symp. Found. Comput. Sci., Santa Fe, NM*, pp. 124–34. Los Alamitos, CA: IEEE Comput. Soc. Press
- [11] Shor PW. 1997. *SIAM J. Comput.* 26:1484–509
- [12] Brown KL, Munro WJ, Kendon VM. 2010. *Entropy* 12:2268–307
- [13] **Loss D, DiVincenzo DP. 1998. *Phys. Rev. A* 57:120–26**  
**Proposed that spins in quantum dots can be used for quantum computation and can be operated by purely electrical means at ultrahigh clock speed**
- [14] Imamoglu A, Awschalom DD, Burkard G, DiVincenzo DP, Loss D, et al. 1999. *Phys. Rev. Lett.* 83:4204–07
- [15] Cirac JI, Zoller P. 1995. *Phys. Rev. Lett.* 74:4091–94
- [16] Turchette QA, Hood CJ, Lange W, Mabuchi H, Kimble HJ. 1995. *Phys. Rev. Lett.* 75:4710–13
- [17] Gershenfeld NA, Chuang IL. 1997. *Science* 275:350–56
- [18] Shnirman A, Schön G, Hermon Z. 1997. *Phys. Rev. Lett.* 79:2371–74
- [19] Kane BE. 1998. *Nature (London)* 393:133–37
- [20] Vrijen R, Yablonovitch E, Wang KL, Jiang HW, Balandin AA, et al. 2000. *Phys. Rev. A* 62:012306
- [21] Knill E, Laflamme R, Milburn GJ. 2001. *Nature (London)* 409:46–52
- [22] Leuenberger MN, Loss D. 2001. *Nature (London)* 410:789–93
- [23] Meier F, Levy J, Loss D. 2003. *Phys. Rev. Lett.* 90:047901
- [24] Jelezko F, Wrachtrup J. 2006. *Phys. Status Solidi A* 203:3207–25

- [25] Hanson R, Awschalom DD. 2008. *Nature (London)* 453:1043–49
- [26] Maletinsky P, Hong S, Grinolds MS, Hausmann B, Lukin MD, et al. 2012. *Nat. Nanotechnol.* 7:320–24
- [27] Ladd TD, Jelezko F, Laflamme R, Nakamura Y, Monroe C, O’Brien JL. 2010. *Nature (London)* 464:45–53
- [28] Burkard G, Engel HA, Loss D. 2000. *Fortschr. Phys.* 48:965–86
- [29] Cerletti V, Coish WA, Gywat O, Loss D. 2005. *Nanotechnology* 16:R27–49
- [30] Gywat O, Krenner HJ, Berezovsky J. 2010. *Spins in Optically Active Quantum Dots*. Weinheim: Wiley-VCH
- [31] Burkard G, Loss D, DiVincenzo DP. 1999. *Phys. Rev. B* 59:2070–78
- [32] Schliemann J, Loss D, MacDonald AH. 2001. *Phys. Rev. B* 63:085311
- [33] Gupta JA, Awschalom DD, Peng X, Alivisatos AP. 1999. *Phys. Rev. B* 59:R10421–24
- [34] Gupta JA, Awschalom DD, Efros AL, Rodina AV. 2002. *Phys. Rev. B* 66:125307
- [35] Trauzettel B, Bulaev DV, Loss D, Burkard G. 2007. *Nat. Phys.* 3:192–96
- [36] Bulaev DV, Trauzettel B, Loss D. 2008. *Phys. Rev. B* 77:235301
- [37] Klinovaja J, Schmidt MJ, Braunecker B, Loss D. 2011. *Phys. Rev. B* 84:085452
- [38] DiVincenzo DP. 2000. *Fortschr. Phys.* 48:771–83
- [39] Golovach VN, Khaetskii AV, Loss D. 2004. *Phys. Rev. Lett.* 93:016601
- [40] Bulaev DV, Loss D. 2005. *Phys. Rev. Lett.* 95:076805
- [41] Barenco A, Bennett CH, Cleve R, DiVincenzo DP, Margolus N, et al. 1995. *Phys. Rev. A* 52:3457–67
- [42] Recher P, Sukhorukov EV, Loss D. 2001. *Phys. Rev. B* 63:165314
- [43] Hofstetter L, Csonka S, Nygård J, Schönberger C. 2009. *Nature (London)* 461:960–63
- [44] Herrmann LG, Portier F, Roche P, Levy Yeyati A, Kontos T, Strunk C. 2010. *Phys. Rev. Lett.* 104:026801
- [45] Schindele J, Baumgartner A, Schönberger C. 2012. *Phys. Rev. Lett.* 109:157002
- [46] Das A, Ronen Y, Heiblum M, Mahalu D, Kretinin AV, Shtrikman H. 2012. *Nat. Commun.* 3:1165
- [47] Nolting W, Ramakanth A. 2009. *Quantum Theory of Magnetism*. Berlin: Springer
- [48] Winkler R. 2003. *Spin-Orbit Coupling Effects in Two-Dimensional Electron and Hole Systems*. Berlin: Springer
- [49] Luttinger JM. 1956. *Phys. Rev.* 102:1030–41
- [50] Bychkov YA, Rashba EI. 1984. *J. Phys. C: Solid State Phys.* 17:6039–45
- [51] Dresselhaus G. 1955. *Phys. Rev.* 100:580–86
- [52] Hanson R, Kouwenhoven LP, Petta JR, Tarucha S, Vandersypen LMK. 2007. *Rev. Mod. Phys.* 79:1217–65

- [53] Balocchi A, Duong QH, Renucci P, Liu BL, Fontaine C, et al. 2011. *Phys. Rev. Lett.* 107:136604
- [54] Bonesteel NE, Stepanenko D, DiVincenzo DP. 2001. *Phys. Rev. Lett.* 87:207901
- [55] Burkard G, Loss D. 2002. *Phys. Rev. Lett.* 88:047903
- [56] Stepanenko D, Bonesteel NE, DiVincenzo DP, Burkard G, Loss D. 2003. *Phys. Rev. B* 68:115306
- [57] Nadj-Perge S, Frolov SM, Bakkers EPAM, Kouwenhoven LP. 2010. *Nature (London)* 468:1084–87
- [58] Schroer MD, Petersson KD, Jung M, Petta JR. 2011. *Phys. Rev. Lett.* 107:176811
- [59] Petersson KD, McFaul LW, Schroer MD, Jung M, Taylor JM, et al. 2012. *Nature (London)* 490:380–83
- [60] Nadj-Perge S, Pribiag VS, van den Berg JWG, Zuo K, Plissard SR, et al. 2012. *Phys. Rev. Lett.* 108:166801
- [61] Golovach VN, Borhani M, Loss D. 2006. *Phys. Rev. B* 74:165319
- [62] Khomitsky DV, Gulyaev LV, Sherman EY. 2012. *Phys. Rev. B* 85:125312
- [63] Bulaev DV, Loss D. 2007. *Phys. Rev. Lett.* 98:097202
- [64] Khaetskii AV, Nazarov YV. 2001. *Phys. Rev. B* 64:125316
- [65] Erlingsson SI, Nazarov YV. 2002. *Phys. Rev. B* 66:155327
- [66] Bulaev DV, Loss D. 2005. *Phys. Rev. B* 71:205324
- [67] Golovach VN, Khaetskii A, Loss D. 2008. *Phys. Rev. B* 77:045328
- [68] Kroutvar M, Ducommun Y, Heiss D, Bichler M, Schuh D, et al. 2004. *Nature (London)* 432:81–84
- [69] Dreiser J, Atatüre M, Galland C, Müller T, Badolato A, Imamoglu A. 2008. *Phys. Rev. B* 77:075317
- [70] Amasha S, MacLean K, Radu IP, Zumbühl DM, Kastner MA, et al. 2008. *Phys. Rev. Lett.* 100:046803
- [71] Abrahams E. 1957. *Phys. Rev.* 107:491–96
- [72] Trif M, Simon P, Loss D. 2009. *Phys. Rev. Lett.* 103:106601
- [73] Heiss D, Schaeck S, Huebl H, Bichler M, Abstreiter G, et al. 2007. *Phys. Rev. B* 76:241306(R)
- [74] Gerardot BD, Brunner D, Dalgarno PA, Öhberg P, Seidl S. 2008. *Nature (London)* 451:441–44
- [75] Gerardot BD, Warburton RJ. 2012. Studies of the hole spin in self-assembled quantum dots using optical techniques. In *Quantum Dots: Optics, Electron Transport and Future Applications*, ed. AI Tartakovskii, pp. 63–85. Cambridge: Cambridge Univ. Press
- [76] Schliemann J, Egues JC, Loss D. 2003. *Phys. Rev. Lett.* 90:146801
- [77] Duckheim M, Maslov DL, Loss D. 2009. *Phys. Rev. B* 80:235327
- [78] Fasth C, Fuhrer A, Samuelson L, Golovach VN, Loss D. 2007. *Phys. Rev. Lett.* 98:266801
- [79] Stepanenko D, Rudner M, Halperin BI, Loss D. 2012. *Phys. Rev. B* 85:075416
- [80] Koppens FHL, Klauser D, Coish WA, Nowack KC, Kouwenhoven LP, et al. 2007. *Phys. Rev. Lett.* 99:106803

- [81] Coish WA, Loss D. 2004. *Phys. Rev. B* 70:195340
- [82] Fischer J, Trif M, Coish WA, Loss D. 2009. *Solid State Commun.* 149:1443–50
- [83] Coish WA, Baugh J. 2009. *Phys. Status Solidi B* 246:2203–15
- [84] Khaetskii AV, Loss D, Glazman L. 2002. *Phys. Rev. Lett.* 88:186802
- [85] Khaetskii AV, Loss D, Glazman L. 2003. *Phys. Rev. B* 67:195329
- [86] Merkulov IA, Efros AL, Rosen M. 2002. *Phys. Rev. B* 65:205309
- [87] Coish WA, Fischer J, Loss D. 2010. *Phys. Rev. B* 81:165315
- [88] Coish WA, Fischer J, Loss D. 2008. *Phys. Rev. B* 77:125329
- [89] Fischer J, Loss D. 2009. *Science* 324:1277–78
- [90] Cywiński L, Witzel WM, Das Sarma S. 2009. *Phys. Rev. B* 79:245314
- [91] Liu RB, Yao W, Sham LJ. 2010. *Adv. Phys.* 59:703–802
- [92] Fischer J, Coish WA, Bulaev DV, Loss D. 2008. *Phys. Rev. B* 78:155329
- [93] Fischer J, Loss D. 2010. *Phys. Rev. Lett.* 105:266603
- [94] Maier F, Loss D. 2012. *Phys. Rev. B* 85:195323
- [95] Eble B, Testelin C, Desfonds P, Bernardot F, Balocchi A, et al. 2009. *Phys. Rev. Lett.* 102:146601
- [96] Testelin C, Bernardot F, Eble B, Chamarro M. 2009. *Phys. Rev. B* 79:195440
- [97] Fallahi P, Yilmaz ST, Imamoglu A. 2010. *Phys. Rev. Lett.* 105:257402
- [98] Chekhovich EA, Krysa AB, Skolnick MS, Tartakovskii AI. 2011. *Phys. Rev. Lett.* 106:027402
- [99] Brunner D, Gerardot BD, Dalgarno PA, Wüst G, Karrai K, et al. 2009. *Science* 325:70–72
- [100] Foletti S, Bluhm H, Mahalu D, Umansky V, Yacoby A. 2009. *Nat. Phys.* 5:903–08
- [101] Urbaszek B, Eble B, Amand T, Marie X. 2012. Nuclear spin effects in quantum dot optics. In *Quantum Dots: Optics, Electron Transport and Future Applications*, ed. AI Tartakovskii, pp. 237–52. Cambridge: Cambridge Univ. Press
- [102] Urbaszek B, Marie X, Amand T, Krebs O, Voisin P, et al. 2013. *Rev. Mod. Phys.* 85:79–133
- [103] Latta C, Högele A, Zhao Y, Vamivakas AN, Maletinsky P, et al. 2009. *Nat. Phys.* 5:758–63
- [104] Kloeffel C, Dalgarno PA, Urbaszek B, Gerardot BD, Brunner D, et al. 2011. *Phys. Rev. Lett.* 106:046802  
See Chapter 7
- [105] Xu X, Yao W, Sun B, Steel DG, Bracker AS, et al. 2009. *Nature (London)* 459:1105–09
- [106] Bracker AS, Stinaff EA, Gammon D, Ware ME, Tischler JG, et al. 2005. *Phys. Rev. Lett.* 94:047402
- [107] Chekhovich EA, Makhonin MN, Kavokin KV, Krysa AB, Skolnick MS, Tartakovskii AI. 2010. *Phys. Rev. Lett.* 104:066804
- [108] Klotz F, Jovanov V, Kierig J, Clark EC, Bichler M, et al. 2010. *Phys. Rev. B* 82:121307(R)

- [109] Tartakovskii AI, Wright T, Russell A, Fal'ko VI, Van'kov AB, et al. 2007. *Phys. Rev. Lett.* 98:026806
- [110] Maletinsky P, Badolato A, Imamoglu A. 2007. *Phys. Rev. Lett.* 99:056804
- [111] Makhonin MN, Tartakovskii AI, Ebbens A, Skolnick MS, Russell A, et al. 2008. *Appl. Phys. Lett.* 93:073113
- [112] Belhadj T, Simon CM, Amand T, Renucci P, Chatel B, et al. 2009. *Phys. Rev. Lett.* 103:086601
- [113] Bluhm H, Foletti S, Mahalu D, Umansky V, Yacoby A. 2010. *Phys. Rev. Lett.* 105:216803
- [114] Petta JR, Taylor JM, Johnson AC, Yacoby A, Lukin MD, et al. 2008. *Phys. Rev. Lett.* 100:067601
- [115] Barthel C, Medford J, Bluhm H, Yacoby A, Marcus CM, et al. 2012. *Phys. Rev. B* 85:035306
- [116] Laird EA, Barthel C, Rashba EI, Marcus CM, Hanson MP, Gossard AC. 2007. *Phys. Rev. Lett.* 99:246601
- [117] Laird EA, Barthel C, Rashba EI, Marcus CM, Hanson MP, Gossard AC. 2009. *Semicond. Sci. Technol.* 24:064004
- [118] Danon J, Vink IT, Koppens FHL, Nowack KC, Vandersypen LMK, Nazarov YV. 2009. *Phys. Rev. Lett.* 103:046601
- [119] Vink IT, Nowack KC, Koppens FHL, Danon J, Nazarov YV, Vandersypen LMK. 2009. *Nat. Phys.* 5:764–68
- [120] Greilich A, Yakovlev DR, Shabaev A, Efros AL, Yugova IA, et al. 2006. *Science* 313:341–45
- [121] Greilich A, Shabaev A, Yakovlev DR, Efros AL, Yugova IA, et al. 2007. *Science* 317:1896–99
- [122] Stepanenko D, Burkard G, Giedke G, Imamoglu A. 2006. *Phys. Rev. Lett.* 96:136401
- [123] Klauser D, Coish WA, Loss D. 2006. *Phys. Rev. B* 73:205302
- [124] Giedke G, Taylor JM, D'Alessandro D, Lukin MD, Imamoglu A. 2006. *Phys. Rev. A* 74:032316
- [125] Barthel C, Reilly DJ, Marcus CM, Hanson MP, Gossard AC. 2009. *Phys. Rev. Lett.* 103:160503
- [126] Petta JR, Johnson AC, Taylor JM, Laird EA, Yacoby A, et al. 2005. *Science* 309:2180–84
- [127] Koppens FHL, Nowack KC, Vandersypen LMK. 2008. *Phys. Rev. Lett.* 100:236802
- [128] Greilich A, Economou SE, Spatzek S, Yakovlev DR, Reuter D, et al. 2009. *Nat. Phys.* 5:262–66
- [129] Press D, De Greve K, McMahon PL, Ladd TD, Friess B, et al. 2010. *Nat. Photon.* 4:367–70
- [130] Barthel C, Medford J, Marcus CM, Hanson MP, Gossard AC. 2010. *Phys. Rev. Lett.* 105:266808
- [131] **Bluhm H, Foletti S, Neder I, Rudner MS, Mahalu D, et al. 2011. *Nat. Phys.* 7:109–13**  
**Observed a long coherence time above 0.2 ms for spin qubits in quantum dots**
- [132] Medford J, Cywiński L, Barthel C, Marcus CM, Hanson MP, Gossard AC. 2012. *Phys. Rev. Lett.* 108:086802
- [133] Chesil S, Loss D. 2008. *Phys. Rev. Lett.* 101:146803
- [134] Simon P, Loss D. 2007. *Phys. Rev. Lett.* 98:156401
- [135] Braunecker B, Simon P, Loss D. 2009. *Phys. Rev. B* 80:165119

- [136] Żak RA, Maslov DL, Loss D. 2012. *Phys. Rev. B* 85:115424
- [137] Governale M, Zülicke U. 2012. *Physics* 5:34
- [138] Aharonov D, Ben-Or M. 1997. Fault-tolerant quantum computation with constant error. *Proc. 29th Annu. ACM Symp. Theory Comput., El Paso, TX*, pp. 176–88. New York, NY: ACM
- [139] Knill E, Laflamme R, Zurek WH. 1998. *Science* 279:342–45
- [140] Preskill J. 1998. *Proc. R. Soc. Lond. A* 454:385–410
- [141] Awschalom DD, Loss D, Samarth N, eds. 2002. *Semiconductor Spintronics and Quantum Computation*. Berlin: Springer
- [142] Steane AM. 2003. *Phys. Rev. A* 68:042322
- [143] Aliferis P, Preskill J. 2008. *Phys. Rev. A* 78:052331
- [144] Kitaev AY. 2003. *Ann. Phys. (NY)* 303:2–30
- [145] Raussendorf R, Harrington J. 2007. *Phys. Rev. Lett.* 98:190504
- [146] Raussendorf R, Harrington J, Goyal K. 2007. *New J. Phys.* 9:199
- [147] Fowler AG, Stephens AM, Groszkowski P. 2009. *Phys. Rev. A* 80:052312
- [148] **Wang DS, Fowler AG, Hollenberg LCL. 2011. *Phys. Rev. A* 83:020302(R)**  
**Found that the error threshold exceeds 1% for quantum computation based on the surface code**
- [149] DiVincenzo DP. 2009. *Phys. Scr.* T137:014020
- [150] Wootton JR, Loss D. 2012. *Phys. Rev. Lett.* 109:160503
- [151] Yao XC, Wang TX, Chen HZ, Gao WB, Fowler AG, et al. 2012. *Nature (London)* 482:489–94
- [152] Drexler H, Leonard D, Hansen W, Kotthaus JP, Petroff PM. 1994. *Phys. Rev. Lett.* 73:2252–55
- [153] Warburton RJ, Schäfflein C, Haft D, Bickel F, Lorke A, et al. 2000. *Nature (London)* 405:926–29
- [154] Atatüre M, Dreiser J, Badolato A, Högele A, Karrai K, Imamoglu A. 2006. *Science* 312:551–53
- [155] Godden TM, Boyle SJ, Ramsay AJ, Fox AM, Skolnick MS. 2010. *Appl. Phys. Lett.* 97:061113
- [156] Berezovsky J, Mikkelsen MH, Stoltz NG, Coldren LA, Awschalom DD. 2008. *Science* 320:349–52
- [157] Press D, Ladd TD, Zhang B, Yamamoto Y. 2008. *Nature (London)* 456:218–21
- [158] De Greve K, McMahon PL, Press D, Ladd TD, Bisping D, et al. 2011. *Nat. Phys.* 7:872–78
- [159] Grelich A, Carter SG, Kim D, Bracker AS, Gammon D. 2011. *Nat. Photon.* 5:702–08
- [160] Godden TM, Quilter JH, Ramsay AJ, Wu Y, Brereton P, et al. 2012. *Phys. Rev. Lett.* 108:017402
- [161] Kim D, Carter SG, Grelich A, Bracker AS, Gammon D. 2011. *Nat. Phys.* 7:223–29
- [162] Atatüre M, Dreiser J, Badolato A, Imamoglu A. 2007. *Nat. Phys.* 3:101–05
- [163] Berezovsky J, Mikkelsen MH, Gywat O, Stoltz NG, Coldren LA, Awschalom DD. 2006. *Science* 314:1916–20

- [164] Vamivakas AN, Zhao Y, Lu CY, Atatüre M. 2009. *Nat. Phys.* 5:198–202
- [165] Mikkelsen MH, Berezovsky J, Stoltz NG, Coldren LA, Awschalom DD. 2007. *Nat. Phys.* 3:770–73
- [166] Vamivakas AN, Lu CY, Matthiesen C, Zhao Y, Fält S, et al. 2010. *Nature (London)* 467:297–300
- [167] Kim D, Economou SE, Badescu SC, Scheibner M, Bracker AS, et al. 2008. *Phys. Rev. Lett.* 101:236804
- [168] Xu X, Sun B, Berman PR, Steel DG, Bracker AS, et al. 2008. *Nat. Phys.* 4:692–95
- [169] Houel J, Kuhlmann AV, Greuter L, Xue F, Poggio M, et al. 2012. *Phys. Rev. Lett.* 108:107401
- [170] Weiss KM, Elzerman JM, Delley YL, Miguel-Sanchez J, Imamoglu A. 2012. *Phys. Rev. Lett.* 109:107401
- [171] Claudon J, Bleuse J, Malik NS, Bazin M, Jaffrennou P, et al. 2010. *Nat. Photon.* 4:174–77
- [172] Flagg EB, Muller A, Polyakov SV, Ling A, Migdall A, Solomon GS. 2010. *Phys. Rev. Lett.* 104:137401
- [173] Patel RB, Bennett AJ, Farrer I, Nicoll CA, Ritchie DA, Shields AJ. 2010. *Nat. Photon.* 4:632–35
- [174] Kuklewicz CE, Malein RNE, Petroff PM, Gerardot BD. 2012. *Nano Lett.* 12:3761–65
- [175] Kistner C, Heindel T, Schneider C, Rahimi-Iman A, Reitzenstein S, et al. 2008. *Opt. Express* 16:15006–12
- [176] Wang KL, Cha D, Liu J, Chen C. 2007. *Proc. IEEE* 95:1866–83
- [177] Katsaros G, Spathis P, Stoffel M, Fournel F, Mongillo M, et al. 2010. *Nat. Nanotechnol.* 5:458–64
- [178] Katsaros G, Golovach VN, Spathis P, Ares N, Stoffel M, et al. 2011. *Phys. Rev. Lett.* 107:246601
- [179] Levy J. 2002. *Phys. Rev. Lett.* 89:147902
- [180] Benjamin SC. 2001. *Phys. Rev. A* 64:054303
- [181] Taylor JM, Engel HA, Dür W, Yacoby A, Marcus CM, et al. 2005. *Nat. Phys.* 1:177–83
- [182] Petta JR, Lu H, Gossard AC. 2010. *Science* 327:669–72
- [183] DiVincenzo DP, Bacon D, Kempe J, Burkard G, Whaley KB. 2000. *Nature (London)* 408:339–42
- [184] Laird EA, Taylor JM, DiVincenzo DP, Marcus CM, Hanson MP, Gossard AC. 2010. *Phys. Rev. B* 82:075403
- [185] **Gaudreau L, Granger G, Kam A, Aers GC, Studenikin SA, et al. 2012. *Nat. Phys.* 8:54–58**  
**Proved the scalability of exchange-based quantum computing schemes [13] through electrical and pairwise control of the exchange interaction in a triple quantum dot**
- [186] Koppens FHL. 2012. *Nat. Phys.* 8:5–6
- [187] **Brunner R, Shin YS, Obata T, Pioro-Ladrière M, Kubo T, et al. 2011. *Phys. Rev. Lett.* 107:146801**  
**Demonstrated two-qubit interactions and individual single-qubit rotations through experimental realization of a spin-qubit processor following Ref. [13]**

- [188] Pioro-Ladrière M, Obata T, Tokura Y, Shin YS, Kubo T, et al. 2008. *Nat. Phys.* 4:776–79
- [189] Shin YS, Obata T, Tokura Y, Pioro-Ladrière M, Brunner R, et al. 2010. *Phys. Rev. Lett.* 104:046802
- [190] Field M, Smith CG, Pepper M, Ritchie DA, Frost JEF, et al. 1993. *Phys. Rev. Lett.* 70:1311–14
- [191] Elzerman JM, Hanson R, Greidanus JS, Willems van Beveren LH, De Franceschi S, et al. 2003. *Phys. Rev. B* 67:161308(R)
- [192] Elzerman JM, Hanson R, Willems van Beveren LH, Witkamp B, Vandersypen LMK, Kouwenhoven LP. 2004. *Nature (London)* 430:431–35
- [193] Nowack KC, Shafiei M, Laforest M, Prawiroatmodjo GEDK, Schreiber LR, et al. 2011. *Science* 333:1269–72
- [194] Barthel C, Kjaergaard M, Medford J, Stopa M, Marcus CM, et al. 2010. *Phys. Rev. B* 81:161308(R)
- [195] van Weperen I, Armstrong BD, Laird EA, Medford J, Marcus CM, et al. 2011. *Phys. Rev. Lett.* 107:030506
- [196] Koppens FHL, Buizert C, Tielrooij KJ, Vink IT, Nowack KC, et al. 2006. *Nature (London)* 442:766–71
- [197] Nowack KC, Koppens FHL, Nazarov YV, Vandersypen LMK. 2007. *Science* 318:1430–33
- [198] Coish WA, Loss D. 2007. *Phys. Rev. B* 75:161302(R)
- [199] Shulman MD, Dial OE, Harvey SP, Bluhm H, Umansky V, Yacoby A. 2012. *Science* 336:202–05
- [200] Klinovaja J, Stepanenko D, Halperin BI, Loss D. 2012. *Phys. Rev. B* 86:085423
- [201] Reilly DJ, Marcus CM, Hanson MP, Gossard AC. 2007. *Appl. Phys. Lett.* 91:162101
- [202] Cassidy MC, Dzurak AS, Clark RG, Petersson KD, Farrer I, et al. 2007. *Appl. Phys. Lett.* 91:222104
- [203] Petersson KD, Smith CG, Anderson D, Atkinson P, Jones GAC, Ritchie DA. 2010. *Nano Lett.* 10:2789–93
- [204] Hanson R, Willems van Beveren LH, Vink IT, Elzerman JM, Naber WJM, et al. 2005. *Phys. Rev. Lett.* 94:196802
- [205] Meunier T, Vink IT, Willems van Beveren LH, Koppens FHL, Tranitz HP, et al. 2006. *Phys. Rev. B* 74:195303
- [206] Johnson AC, Petta JR, Taylor JM, Yacoby A, Lukin MD, et al. 2005. *Nature (London)* 435:925–28
- [207] Borselli MG, Eng K, Croke ET, Maune BM, Huang B, et al. 2011. *Appl. Phys. Lett.* 99:063109
- [208] Thalakulam M, Simmons CB, Rosemeyer BM, Savage DE, Lagally MG, et al. 2010. *Appl. Phys. Lett.* 96:183104
- [209] Shi Z, Simmons CB, Prance JR, Gamble JK, Friesen M, et al. 2011. *Appl. Phys. Lett.* 99:233108
- [210] Simmons CB, Prance JR, Van Bael BJ, Koh TS, Shi Z, et al. 2011. *Phys. Rev. Lett.* 106:156804
- [211] Prance JR, Shi Z, Simmons CB, Savage DE, Lagally MG, et al. 2012. *Phys. Rev. Lett.* 108:046808
- [212] Maune BM, Borselli MG, Huang B, Ladd TD, Deelman PW, et al. 2012. *Nature (London)* 481:344–47



- [213] Grbić B, Leturcq R, Ensslin K, Reuter D, Wieck AD. 2005. *Appl. Phys. Lett.* 87:232108
- [214] Sau JD, Tewari S, Lutchyn RM, Stanescu TD, Das Sarma S. 2010. *Phys. Rev. B* 82:214509
- [215] Oreg Y, Refael G, von Oppen F. 2010. *Phys. Rev. Lett.* 105:177002
- [216] Gangadharaiyah S, Braunecker B, Simon P, Loss D. 2011. *Phys. Rev. Lett.* 107:036801
- [217] Xiang J, Lu W, Hu Y, Wu Y, Yan H, Lieber CM. 2006. *Nature (London)* 441:489–93
- [218] Yan H, Choe HS, Nam SW, Hu Y, Das S, et al. 2011. *Nature (London)* 470:240–44
- [219] Reimer ME, van Kouwen MP, Barkelid M, Hocevar M, van Weert MHM, et al. 2011. *J. Nanophoton.* 5:053502
- [220] Yan R, Gargas D, Yang P. 2009. *Nat. Photon.* 3:569–76
- [221] Chu S, Wang G, Zhou W, Lin Y, Chernyak L, et al. 2011. *Nat. Nanotechnol.* 6:506–10
- [222] van Weert MHM, Akopian N, Perinetti U, van Kouwen MP, Algra RE, et al. 2009. *Nano Lett.* 9:1989–93
- [223] van Weert MHM, den Heijer M, van Kouwen MP, Algra RE, Bakkers EPAM, et al. 2010. *Appl. Phys. Lett.* 96:233112
- [224] van Kouwen MP, Reimer ME, Hidma AW, van Weert MHM, Algra RE, et al. 2010. *Nano Lett.* 10:1817–22
- [225] Trif M, Golovach VN, Loss D. 2008. *Phys. Rev. B* 77:045434
- [226] Pfund A, Shorubalko I, Ensslin K, Leturcq R. 2007. *Phys. Rev. Lett.* 99:036801
- [227] Lu W, Xiang J, Timko BP, Wu Y, Lieber CM. 2005. *Proc. Natl. Acad. Sci. USA* 102:10046–51
- [228] Park JS, Ryu B, Moon CY, Chang KJ. 2010. *Nano Lett.* 10:116–21
- [229] Xiang J, Vidan A, Tinkham M, Westervelt RM, Lieber CM. 2006. *Nat. Nanotechnol.* 1:208–13
- [230] Hu Y, Churchill HOH, Reilly DJ, Xiang J, Lieber CM, Marcus CM. 2007. *Nat. Nanotechnol.* 2:622–25
- [231] Roddaro S, Fuhrer A, Brusheim P, Fasth C, Xu HQ, et al. 2008. *Phys. Rev. Lett.* 101:186802
- [232] Hu Y, Kuemmeth F, Lieber CM, Marcus CM. 2012. *Nat. Nanotechnol.* 7:47–50
- [233] **Kloeffel C, Trif M, Loss D. 2011. *Phys. Rev. B* 84:195314**  
**Predicted direct Rashba spin-orbit interaction and other attractive features for holes in Ge/Si nanowires**  
 See Chapter 2
- [234] Klinovaja J, Schmidt MJ, Braunecker B, Loss D. 2011. *Phys. Rev. Lett.* 106:156809
- [235] Klinovaja J, Gangadharaiyah S, Loss D. 2012. *Phys. Rev. Lett.* 108:196804
- [236] Engel HA, Golovach VN, Loss D, Vandersypen LMK, Elzerman JM, et al. 2004. *Phys. Rev. Lett.* 93:106804
- [237] **Trifunovic L, Dial O, Trif M, Wootton JR, Abebe R, et al. 2012. *Phys. Rev. X* 2:011006**  
**Showed that architectural challenges of large-scale quantum computers may be overcome via floating gates**

- [238] Blais A, Huang RS, Wallraff A, Girvin SM, Schoelkopf R.J. 2004. *Phys. Rev. A* 69:062320
- [239] Wallraff A, Schuster DI, Blais A, Frunzio L, Huang RS, et al. 2004. *Nature (London)* 431:162–67
- [240] Childress L, Sørensen AS, Lukin MD. 2004. *Phys. Rev. A* 69:042302
- [241] Burkard G, Imamoglu A. 2006. *Phys. Rev. B* 74:041307(R)
- [242] Taylor JM, Lukin MD. 2006. arXiv:cond-mat/0605144
- [243] Cottet A, Kontos T. 2010. *Phys. Rev. Lett.* 105:160502
- [244] Hu X, Liu Y, Nori F. 2012. *Phys. Rev. B* 86:035314
- [245] Trif M, Troiani F, Stepanenko D, Loss D. 2008. *Phys. Rev. Lett.* 101:217201
- [246] Prokof'ev NV, Stamp PCE. 2000. *Rep. Prog. Phys.* 63:669–726
- [247] Sachrajda A. 2011. *Physics* 4:75
- [248] Ciorga M, Sachrajda AS, Hawrylak P, Gould C, Zawadzki P, et al. 2000. *Phys. Rev. B* 61:R16315–18
- [249] Hu X, Das Sarma S. 2001. *Phys. Rev. A* 64:042312

#### **RELATED RESOURCES**

- [250] Nielsen MA, Chuang IL. 2000. *Quantum Computation and Quantum Information*. Cambridge: Cambridge Univ. Press
- [251] Mermin ND. 2007. *Quantum Computer Science: An Introduction*. Cambridge: Cambridge Univ. Press
- [252] Deutsch D. 1998. *The Fabric of Reality*. London: Penguin

## **PART II**

# **Direct Rashba Spin-Orbit Interaction, Helical Hole States, and Spin Qubits in Nanowires and Nanowire Quantum Dots in the Presence of Phonons, Strain, and Control Fields**

(Theory)



## Chapter 2

# Strong Spin-Orbit Interaction and Helical Hole States in Ge/Si Nanowires

**Adapted from:**

Christoph Kloeffel, Mircea Trif, and Daniel Loss,  
Phys. Rev. B **84**, 195314 (2011).

We study theoretically the low-energy hole states of Ge/Si core/shell nanowires. The low-energy valence band is quasidegenerate, formed by two doublets of different orbital angular momenta, and can be controlled via the relative shell thickness and via external fields. We find that direct (dipolar) coupling to a moderate electric field leads to an unusually large spin-orbit interaction of Rashba type on the order of meV which gives rise to pronounced helical states enabling electrical spin control. The system allows for quantum dots and spin qubits with energy levels that can vary from nearly zero to several meV, depending on the relative shell thickness.

## 2.1 Introduction

Semiconducting nanowires are subject to intense experimental effort as promising candidates for single-photon sources [1], field-effect transistors [2], and programmable circuits [3]. Progress is being made with both group-IV materials [2–5] and III-V compounds, particularly InAs, where single-electron quantum dots (QDs) [6, 7] and universal spin-qubit control [8] have been implemented. Proximity-induced superconductivity was demonstrated in these systems [9, 10], forming a platform for Majorana fermions [11–16].

The nanowires are operated in both the electron (conduction band, CB) [6–9] and hole (valence band, VB) [2–5, 10, 17] regimes. While these regimes are similar in the charge sector, holes can have many advantages in the spin sector. Due to strong spin-orbit interaction (SOI) on an atomic level, the electron spin is replaced by an effective spin  $J = 3/2$ , and even in systems that are inversion symmetric, the spin and momentum are strongly coupled, enabling efficient hole spin manipulation by purely electrical means. Holes, moreover, are very sensitive to confinement, which strongly prolongs their spin lifetimes [18–23]. Also, VBs possess only one valley at the  $\Gamma$  point, in contrast to the CBs of Ge and Si, which is particularly useful for spintronics devices such as spin filters [24] and spin qubits [25]. Most recently, spin-selective hole tunneling in SiGe nanocrystals was achieved [26].

In this chapter, we analyze the hole spectrum of Ge/Si core/shell nanowires, which combine several useful features. The holes are subject to strong confinement in two dimensions and can be confined down to zero dimension (0D) in QDs [4, 27, 28]. Ge and Si can be grown nuclear-spin-free, and mean free paths around  $0.5 \mu\text{m}$  have been reported [5]. During growth, the core diameter ( $\sim 5\text{--}100 \text{ nm}$ ) and shell thickness ( $\sim 1\text{--}10 \text{ nm}$ ) can be controlled individually. The VB offset at the interface is large,  $\sim 0.5 \text{ eV}$ , so that holes accumulate naturally in the core [5, 29]. Lack of dopants underpins the high mobilities [2] and the charge coherence seen in proximity-induced superconductivity [10].

We find that the low-energy spectrum in Ge/Si nanowires is quasidegenerate, in contrast to typical CBs. Static strain, adjustable via the relative shell thickness, allows lifting of this quasidegeneracy, providing a high degree of control. We also calculate the spectrum in longitudinal QDs, where this feature remains pronounced, which is essential for spin-qubit implementation. The nanowires are sensitive to external magnetic fields, with  $g$  factors that depend on both the field orientation and the hole momentum. In particular, we find an additional SOI of Rashba type (referred to as direct Rashba SOI, DRSOI), which results from a direct dipolar coupling to an external electric field. This term arises in first order of the multiband perturbation theory, and thus is 10–100 times larger than the known Rashba SOI (RSOI) for holes which is a third-order effect [30]. Moreover, the DRSOI scales linearly in the core diameter  $R$  (while the RSOI is proportional to  $R^{-1}$ ), so that spin-orbit interaction remains strong even in large nanowires. Similarly to the conventional Rashba SOI [11–17, 24, 31, 32], the DRSOI induces helical ground states, but with much larger spin-orbit energies (meV range) than in other known semiconductors.

The chapter is organized as follows. In Sec. 2.2 we introduce the unperturbed Hamiltonian for holes inside the Ge core and provide its exact, numerical solution. The system is very well described by an effective 1D Hamiltonian, which we derive in Sec. 2.3. In Sec. 2.4 we include the static strain and find a strong dependence of the nanowire spectrum on the relative shell thickness. The spectrum of Ge/Si-nanowire-based QDs is discussed subsequently (Sec. 2.5). In the main section, Sec. 2.6, we analyze the hole coupling to electric fields and compare the DRSOI to the standard RSOI. In this context, we also show that Ge/Si nanowires present an outstanding platform for helical hole states and Majorana fermions. Magnetic field effects are discussed in Sec. 2.7, followed by our summary and final remarks, Sec. 2.8. Technical details and additional information are appended, see Appendix A.

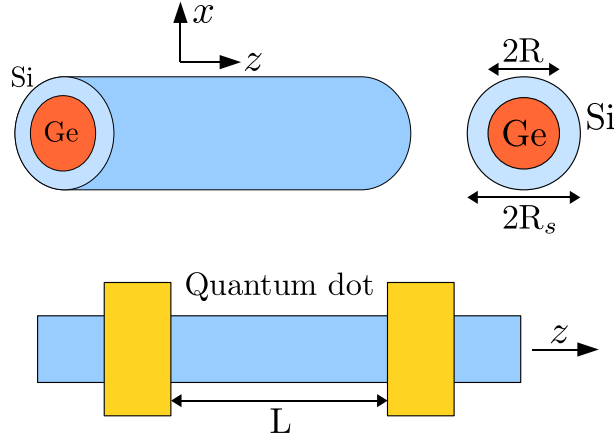


Figure 2.1. Schematic drawing of the systems studied in this chapter. Top: Excerpt of a Ge/Si nanowire with core radius  $R$  and shell thickness  $R_s - R$ , where the  $z$  axis corresponds to the axis along the wire. The nanowires are typically several micrometers in length and can therefore be considered infinitely extended, hosting a 1D hole gas inside their cores. The surrounding Si shell influences the hole spectrum through static strain. Bottom: Quantum dots of (effective) length  $L$  form when the holes are subject to additional confinement in the  $z$  direction. This can be realized via gates [4, 27, 28] or, in principle, by surrounding the Ge with layers of barrier material during growth [43].

## 2.2 Model Hamiltonian and Numerical Solution

In cubic semiconductors, the VB states are well described by the Luttinger-Kohn (LK) Hamiltonian [33, 34],

$$H_{\text{LK}} = \frac{\hbar^2}{2m} \left[ \left( \gamma_1 + \frac{5}{2} \gamma_s \right) k^2 - 2\gamma_s (\mathbf{k} \cdot \mathbf{J})^2 \right], \quad (2.1)$$

where  $J_{x,y,z}$  (in units of  $\hbar$ ) are the three components of the effective electron spin in the VB,  $m$  is the bare electron mass,  $\hbar\mathbf{k}$  is the momentum operator, and  $\gamma_1$  and  $\gamma_s \equiv (2\gamma_2 + 3\gamma_3)/5$  are the Luttinger parameters in spherical approximation, which is well applicable for Ge ( $\gamma_1 = 13.35$ ,  $\gamma_s = 5.11$ ) [35]. In studying nanowires [Fig. 2.1 (top)], the LK Hamiltonian must be supplemented with the confinement in the transverse directions ( $x$ - $y$  plane), perpendicular to the wire axis  $z$ . Since we are interested in the low-energy states, we can add two more simplifications at this stage. First, since the low-energy states are located near the core center, we can assume a potential with cylindrical symmetry even though the real system is not perfectly symmetric. Second, due to the large VB offset, the confinement can be treated as a hard wall,

$$V(r) = \begin{cases} 0, & r < R, \\ \infty, & r > R, \end{cases} \quad (2.2)$$

with  $R$  as the core radius. Given this confinement, the total Hamiltonian  $H_{\text{LK}} + V$  commutes with the operator  $F_z = L_z + J_z$ , where  $L_z = -i\partial_\phi$  is the orbital angular momentum along the wire axis, so that  $F_z$  is a good quantum number and the states can be classified accordingly [36, 37]. The system is also time-reversal symmetric (Kramers doublets), and due to cylindrical symmetry one obtains the same spectrum for the same  $|F_z|$ . This is valid for any circular confinement and does not require the assumption of a hard wall. We note that, again in clear contrast to the CB case,  $L_z$  is not conserved in the VB.

The Hamiltonian separates into  $4 \times 4$  blocks corresponding to given  $F_z$ . By solving  $H_{\text{LK}} + V$  numerically, using an ansatz analogous to those in Refs. [36, 37], we find that the low-energy spectrum in the Ge core is formed by two quasidegenerate bands, with  $F_z = \pm 1/2$  each, where the ground (excited) states at  $k_z = 0$  are of  $L_z \approx 0$  ( $|L_z| = 1$ ) type. These four (in total) bands are well separated from higher bands, and the quasidegeneracy indicates that one can project the problem onto this subspace. A plot of the spectrum is shown in Fig. 2.2 (bottom).

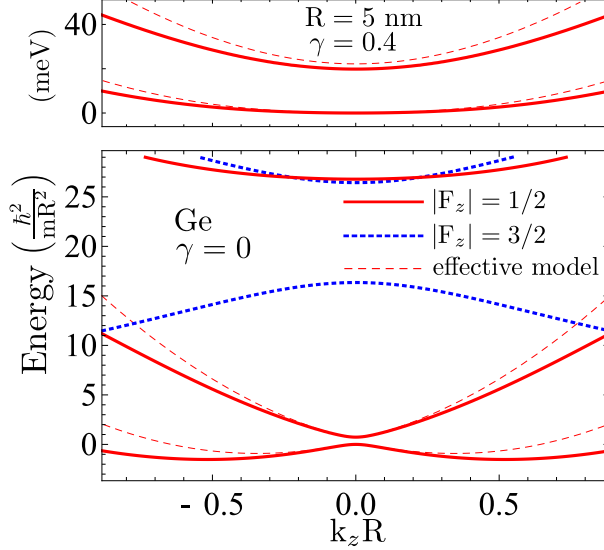


Figure 2.2. Low-energy hole spectrum of a Ge nanowire as a function of the longitudinal wave number  $k_z$ . In the unstrained case,  $\gamma = 0$ , the plot is independent of  $R$ , with  $\hbar^2/(mR^2) \simeq 0.76$  meV for  $R = 10$  nm. Due to time-reversal invariance and cylindrical symmetry, each line is a twofold degeneracy, where red (blue) indicates quantum numbers  $F_z = \pm 1/2$  ( $F_z = \pm 3/2$ ). At  $k_z = 0$  the spectrum is quasidegenerate, with the lowest states having  $L_z \approx 0$  (ground states) and  $|L_z| = 1$  (excited states) character. Dashed red lines result from the effective 1D model for the lowest subspace, where  $k_z$  is treated perturbatively. The top figure is a plot of the low-energy sector of a strained system,  $\gamma = 40\%$ , illustrating strong dependence on the Si shell thickness.

## 2.3 Effective 1D Hamiltonian

The present analysis does not, however, allow us to derive an effective 1D Hamiltonian describing the lowest-energy states. For this, we integrate out the transverse motion and treat  $k_z$  in perturbation theory ( $|k_z R| < 1$ ). The four eigenstates  $g_{\mp}$  and  $e_{\pm}$ , corresponding to ground and excited states for  $F_z = \pm 1/2$  at  $k_z = 0$ , serve as the basis states in the effective 1D Hamiltonian. The subscript refers to the sign of the contained spin state  $|\pm 3/2\rangle$ , since the system at  $k_z = 0$  can be separated into two  $2 \times 2$  spin blocks [37]; details of the calculation are described in Appendix A.2. Knowledge of  $g_{\pm}$  and  $e_{\pm}$ , with eigenenergies  $E_g \equiv 0$  and  $E_e \equiv \Delta_{\text{LK}}$ , allows us to include the  $k_z$ -dependent terms of the LK Hamiltonian. The diagonal matrix elements take on the form  $\langle g_{\pm} | H_{\text{LK}} | g_{\pm} \rangle = \hbar^2 k_z^2 / (2m_g)$ ,  $\langle e_{\pm} | H_{\text{LK}} | e_{\pm} \rangle = \hbar^2 k_z^2 / (2m_e) + \Delta_{\text{LK}}$ , and the nonzero off-diagonal terms are of type  $\langle e_{\pm} | H_{\text{LK}} | g_{\mp} \rangle = iCk_z$ , with  $C$  as a real-valued coupling constant [38]. Summarized in matrix notation, this yields

$$H_{\text{LK}}^{\text{eff}} = A_+ + A_- \tau_z + Ck_z \tau_y \sigma_x, \quad (2.3)$$

where  $A_{\pm} = \hbar^2 k_z^2 (m_g^{-1} \pm m_e^{-1}) / 4 \pm \Delta_{\text{LK}} / 2$ , and  $\tau_i$ ,  $\sigma_i$  are the Pauli matrices acting on  $\{g, e\}$ ,  $\{+, -\}$  (see also Appendix A.1). For Ge, the values are  $\Delta_{\text{LK}} = 0.73 \hbar^2 / (mR^2)$ ,  $C = 7.26 \hbar^2 / (mR)$ ,  $m_g \simeq m / (\gamma_1 + 2\gamma_s) = 0.043 m$ , and  $m_e = m / (\gamma_1 + \gamma_s) = 0.054 m$ . The eigenspectrum

$$E_{g,e}(k_z) = A_{\mp} \mp \sqrt{A_{\pm}^2 + C^2 k_z^2} \quad (2.4)$$

nicely reproduces all the key features of the exact solution and is added to Fig. 2.2 for comparison, with good agreement for  $|k_z R| < 1$ .



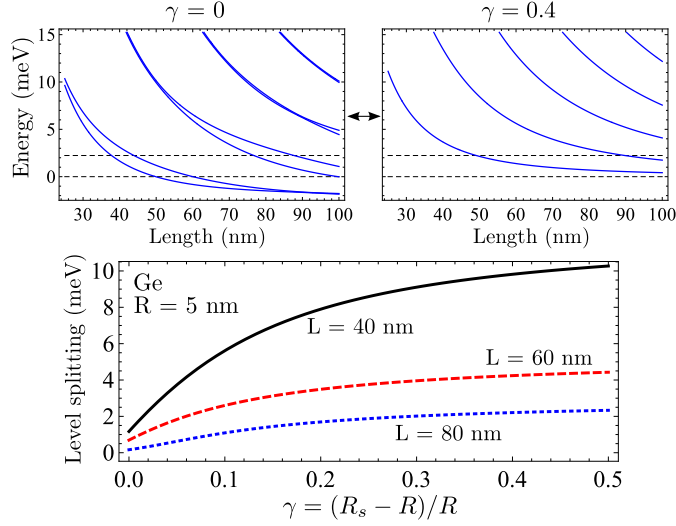


Figure 2.3. Top: Hole energy spectrum in a nanowire-based QD (Ge/Si core/shell,  $R = 5$  nm), for both a thin and a thick shell, as a function of confinement length  $L$ . Each line corresponds to a Kramers pair, and dashed lines represent  $\Delta_{\text{LK}}$  for comparison. Bottom: Level splitting of the two lowest Kramers doublets as a function of relative shell thickness  $\gamma$  and for different lengths  $L$ . Static strain, induced via the shell, allows continuous tuning of the energy gap over several meV, an attractive feature for spin qubit applications. For details, see Appendix A.4.

## 2.4 Static Strain

To the above model one needs to add the effects of static strain, since the Si shell (radius  $R_s$ ) tends to compress the Ge lattice. A detailed analysis of the strain field in Ge/Si core/shell nanowires can be found in Chapter 5; here we just quote the results needed to calculate the hole spectrum. The coupling is described by the Bir-Pikus Hamiltonian  $H_{\text{BP}}$  [Eq. (A.11) in Appendix A.3], which for Ge (the spherical approximation applies) is of the same form as Eq. (2.1), with  $k_i k_j$  replaced by the strain tensor elements  $\epsilon_{ij}$  [39]. Assuming a stress-free wire surface and continuous displacement and stress at the interface, symmetry considerations and Newton's second law require  $\epsilon_{xx} = \epsilon_{yy}$  and  $\epsilon_{xy} = \epsilon_{xz} = \epsilon_{yz} = 0$  within the core, so that only terms proportional to  $J_z^2$  contribute. Hence,  $F_z$  remains a good quantum number,  $[H_{\text{LK}} + V + H_{\text{BP}}, F_z] = 0$ , which allows us to solve the system exactly even in the presence of strain, following the same steps as described in Sec. 2.2. It is important that these exact spectra show that the low-energy states [Fig. 2.2 (bottom)] separate even further from the higher bands when the Ge core is strained by a Si shell, so that the low-energy sector remains energetically well isolated and projection onto this subspace is always valid.

In the 1D model, strain leads to a simple rescaling of the energy splitting  $\Delta_{\text{LK}} \rightarrow \Delta_{\text{LK}} + \Delta_{\text{BP}}(\gamma)$ , where  $0 \leq \Delta_{\text{BP}}(\gamma) \lesssim 30$  meV for  $0 \leq \gamma < \infty$ , with  $\gamma \equiv (R_s - R)/R$  as the relative shell thickness. Hence,  $\Delta_{\text{BP}}$  is independent of the core radius, while  $\Delta_{\text{LK}} \propto R^{-2}$ . We note that  $\Delta_{\text{LK}} \simeq 0.6$  meV for a wire of  $R = 10$  nm, which makes this energy scale very small. Therefore the splitting can be changed not only via  $R$ , but also via  $R_s$ . In fact, the system can be varied from the quasidegenerate to an electronlike regime [Fig. 2.2 (top)], where the  $L_z \simeq 0$  and  $|L_z| \simeq 1$  states are parabolas.

## 2.5 Quantum Dot Spectrum

We analyze this feature in more detail by calculating the eigenenergies of Ge/Si-nanowire-based QDs [Fig. 2.1 (bottom)]. All steps of this calculation are carefully explained in Appendix A.4. Remarkably, the variability with  $R_s$  also transfers to the QD levels. Figure 2.3 shows the spectrum as a function of confinement length for a wire with both thin and thick shells and plots the energy splitting of the lowest

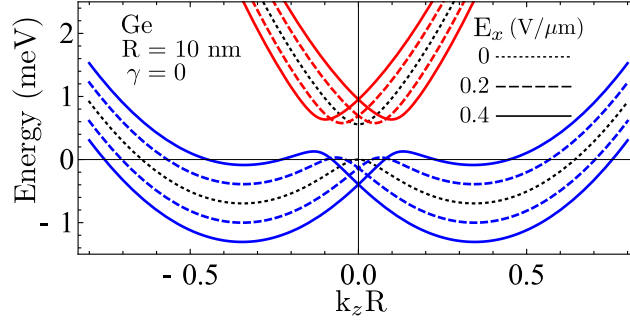


Figure 2.4. Dispersion relation for holes in a Ge nanowire of  $R = 10$  nm, negligible shell, and an applied electric field  $E_x$  along  $x$ , calculated from  $H_{\text{LK}}^{\text{eff}} + H_{\text{DR}}$ , Eqs. (2.3) and (2.6), with  $H_{\text{DR}}$  as the DRSOI Hamiltonian. Hole bands of lower (higher) energy are plotted blue (red). The RSOI is about 100 times smaller than the DRSOI and thus negligible. Note that the DRSOI shows qualitatively similar features to the standard Rashba SOI with dispersion curves shifted along  $k_z$  against each other.

Kramers doublets as a function of  $\gamma$ . For a negligible shell, the states lie so close in energy that additional degeneracies may even be observed. With increasing  $R_s$ , the QD spectrum changes monotonically from the quasidegenerate regime to gaps of several meV, which should, in particular, be useful for implementing spin qubits.

## 2.6 Direct Rashba Spin-Orbit Interaction and Helical Hole States

An electric field  $E_x$  applied along  $x$  couples directly to the charge of the hole via the dipole term

$$H_{\text{ed}} = -eE_x x, \quad (2.5)$$

with  $x = r \cos \phi$  as the carrier position in field direction. For holes in the Ge core we expect this energy gradient to have sizable effects compared to electron systems, since the low-energy band is made of quasidegenerate states of different  $L_z$  character. Moreover,  $E_x$  will also couple directly to the spins due to the SOI in the VB. Projection of  $H_{\text{ed}}$  onto the subspace yields the effective SOI Hamiltonian

$$H_{\text{DR}} = H_{\text{ed}}^{\text{eff}} = eE_x U \tau_x \sigma_z, \quad (2.6)$$

referred to as direct Rashba SOI (DRSOI), characterized by the coupling constant  $U = \langle g_+ | (-x) | e_+ \rangle$ . The form of Eq. (2.6) still resembles that in the CB case, where dipolar coupling cannot modify the spins. However, the additional  $k_z \tau_y \sigma_x$  term in  $H_{\text{LK}}^{\text{eff}}$  makes the key difference to the CB and accounts for the SOI featured in the LK Hamiltonian. Indeed, by diagonalizing  $H_{\text{LK}}^{\text{eff}} + H_{\text{DR}}$  we find that the DRSOI lifts the twofold degeneracy, as plotted in Fig. 2.4. Surprisingly, the effects closely resemble a standard RSOI for holes in a transverse electric field (see discussion below). [Again, this is not the case for the CB, where  $H_{\text{ed}}$  does not lift the degeneracy since spin and orbit are decoupled (in leading order).]

As a consequence, when analyzing the eigenstates of  $H_{\text{LK}}^{\text{eff}} + H_{\text{DR}}$  for their spin properties, we find that an electric field generates helical ground states, i.e., holes of opposite spin move in opposite directions. Figure 2.5 (top) shows the splitting of the lowest band when  $E_x = 6$  V/ $\mu\text{m}$  is applied to a typical Ge/Si nanowire of 5 nm core radius and 1.5 nm shell thickness. Even though RSOI is absent, the result resembles the typical CB spectra considered in previous studies, where Rashba SOI for electrons leads to two horizontally shifted parabolas in the  $E$ - $k$  diagram [12–14, 17, 24, 31]. Moreover, the analogy also holds for the spins, which are twisted toward the  $y$  direction, perpendicular to both the propagation axis  $z$  and the field direction  $x$ . As Fig. 2.5 (bottom) illustrates,  $\langle J_y \rangle$  in the ground state is an antisymmetric

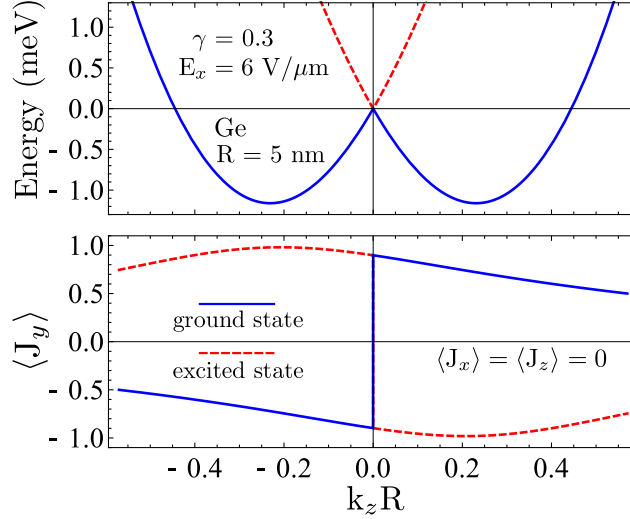


Figure 2.5. Top: Splitting of the lowest valence band when an electric field  $E_x = 6 \text{ V}/\mu\text{m}$  is applied to a Ge/Si nanowire of  $R = 5 \text{ nm}$  and  $R_s = 6.5 \text{ nm}$ . Ground (excited) hole states are plotted blue (red).  $E_{\text{SO}} > 1.0 \text{ meV}$ , a large value compared to that for InAs [6, 40], and the degeneracy at  $k_z = 0$  may be lifted via a magnetic field (see Fig. 2.6). The conventional RSOI for holes is negligible. Bottom: Plot of  $\langle J_y \rangle$  for the above system, where  $\langle J_x \rangle$  and  $\langle J_z \rangle$  are zero throughout. In the ground state, the nanowire carries opposite spins in opposite directions with  $|\langle J_y \rangle| \geq 1/2$ .

function of  $k_z$ , the characteristic feature of a helical mode. We note that  $\langle J_x \rangle = \langle J_z \rangle = 0$  throughout, so that the spins are indeed oppositely oriented. The values of  $|J_y|$  around the band minima are  $\geq 1/2$ , while the spin-orbit (SO) energy, i.e., the difference between band minimum and degeneracy at  $k_z = 0$ , is  $E_{\text{SO}} > 1.0 \text{ meV}$ . This value exceeds the reported  $100 \mu\text{eV}$  in InAs nanowires by a factor of 10 (see also Appendix A.5) [6, 40], and further optimization is definitely possible via both the gate voltage and the shell thickness.

We can understand the qualitative similarity of the DRSOI, Eq. (2.6), and RSOI [30],

$$H_{\text{SO}} = \alpha E_x (k_y J_z - k_z J_y), \quad (2.7)$$

by projecting the latter onto the low-energy subspace, which yields

$$H_{\text{R}} = H_{\text{SO}}^{\text{eff}} \simeq \alpha E_x S \tau_x \sigma_z \quad (2.8)$$

for  $|k_z R| < 1$ , with  $S = \langle g_+ | k_y J_z | e_+ \rangle$ . Further information on  $H_{\text{SO}}$ ,  $H_{\text{R}}$ , and the Rashba coefficient  $\alpha$  can be found in Appendix A.6. This formal analogy of  $H_{\text{DR}}$  and  $H_{\text{R}}$ , Eqs. (2.6) and (2.8), immediately implies that Ge/Si nanowires provide a promising platform for novel quantum effects based on Rashba-type SOI [7, 8, 11–17, 24, 31, 32]. A particular advantage of the DRSOI, as compared to conventional Rashba SOI, is its unusually large strength. While the Rashba term for holes arises in third order of multiband perturbation theory and thus scales with  $1/(\text{band gap})^2$  [30], the DRSOI is a first-order effect and therefore much stronger. Explicit values for Ge are  $U = 0.15 R$ ,  $S = 0.36/R$ , and  $\alpha \approx -0.4 \text{ nm}^2 e$ , so that, in typical nanowires with  $R = 5\text{--}10 \text{ nm}$ ,  $H_{\text{DR}}$  dominates  $H_{\text{R}}$  by one to two orders of magnitude (Appendix A.6). Moreover, sizable RSOI would require unusually small confinement, since  $H_{\text{R}} \propto R^{-1}$ . In stark contrast, for DRSOI we find  $H_{\text{DR}} \propto R$ , which allows one to realize the desired coupling strengths in larger wires as well. The upscaling, however, is limited by the associated decrease of level splitting ( $\propto R^{-2}$ ) and of the term  $C k_z \tau_y \sigma_x$  ( $\propto R^{-1}$ ) in Eq. (2.3).

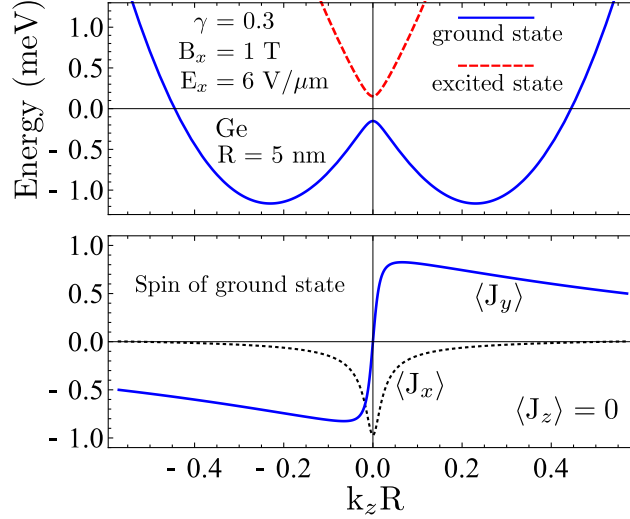


Figure 2.6. Top: Hole spectrum of Fig. 2.5 (top) in the presence of  $B_x = 1$  T. The magnetic field opens a gap of 0.30 meV at  $k_z = 0$ , corresponding to a  $g$  factor above 5. Bottom: Plot of the ground state spin,  $\langle J_x \rangle$  and  $\langle J_y \rangle$ , where  $\langle J_z \rangle = 0$  throughout. At energies within the gap, the Ge/Si nanowire features helical hole states with  $E_{\text{SO}} > 1.0$  meV,  $|k_z| \simeq 90 \mu\text{m}^{-1}$ , and  $|\langle J_y \rangle| \geq 1/2$ .

## 2.7 Magnetic Field Effects

The Kramers degeneracy can be lifted by an external magnetic field  $\mathbf{B}$ , which couples to the holes in two ways, first, via the orbital motion, through the substitution  $\hbar\mathbf{k} \rightarrow -i\hbar\nabla + e\mathbf{A}(\mathbf{r})$ , with  $\mathbf{A}(\mathbf{r})$  as the vector potential, and second, via the Zeeman coupling  $H_{\mathbf{B}}^Z = 2\kappa\mu_B\mathbf{B} \cdot \mathbf{J}$ , where  $\kappa$  is a material parameter. For  $\mathbf{B}$  along  $z$  ( $x$ ), parallel (perpendicular) to the wire, the 1D Hamiltonian is of the form

$$H_{B,z} = \mu_B B_z (Z_1\sigma_z + Z_2\tau_z\sigma_z + Z_3k_z\tau_x\sigma_y), \quad (2.9)$$

$$H_{B,x} = \mu_B B_x (X_1\sigma_x + X_2\tau_z\sigma_x + X_3k_z\tau_y), \quad (2.10)$$

where the real-valued constants  $Z_i$  ( $X_i$ ) are listed in Eq. (A.24) of Appendix A.7. The results agree with recent experiments, where the  $g$  factors in Ge/Si-nanowire-based QDs (multihole regime) were found to vary dramatically with both the orientation of  $\mathbf{B}$  and also the QD confinement [27, 28]. In the absence of electric fields, the ground state  $g$  factor  $g_{\parallel}(k_z)$  for  $B_z$  along the wire turns out to be small for  $k_z = 0$ ,  $|g_{\parallel}(0)| \simeq 0.1$ , and increases as  $|k_z|$  increases. In contrast, the  $g$  factor  $g_{\perp}(k_z)$  for a perpendicular field  $B_x$  is large at  $k_z = 0$ ,  $|g_{\perp}(0)| \simeq 6$ , and decreases as  $|k_z|$  increases, until  $g_{\perp}(k_z)$  eventually changes sign at  $|k_z| \approx 0.5/R$ . We note that these results for the ground state cannot be directly compared to experimental results in the multihole regime, as the  $g$  factors in the excited state already show a clearly different dependence on  $k_z$ . In the presence of an electric field  $E_x$ , the effective  $g_{\parallel}$  and  $g_{\perp}$  at  $k_z = 0$  may, to some extent, be tuned by the strength of  $E_x$ .

Detailed analysis of the low-energy Hamiltonian yields the result that the combination of magnetic and electric fields allows for optimal tuning of the energy spectrum. For instance,  $B_x = 1$  T opens a gap of 0.30 meV at  $k_z = 0$  in Fig. 2.5 (top), keeping the spin properties for  $k_z \neq 0$  unaffected. This corresponds to  $|g_{\perp}(0)| \simeq 5.2$  and is illustrated in Fig. 2.6. With the Fermi level within the induced gap, the spectrum of Fig. 2.6 presents a promising basis for applications using helical hole states. Remarkably, an all-perpendicular setup with, e.g.,  $B_x$  along  $x$  and  $E_y$  along  $y$ ,  $H_{\text{DR},y} = -eE_y U\tau_y$ , leads to an asymmetric spectrum where only states with one particular direction of motion may be occupied, which moreover provide a well-polarized spin along the magnetic field axis. As before, this does not require standard RSOI.

## 2.8 Discussion

The low-energy properties found in this work make Ge/Si core/shell nanowires promising candidates for applications. The dipole-induced formation of helical modes proves useful for several reasons. First, the strength and orientation of externally applied electric fields are well controllable via gates. Second, the DRSOI scales linearly in  $R$ , instead of  $R^{-1}$ , and thicker wires remain operational. Third, the system is sensitive to magnetic fields, and undesired degeneracies at  $k_z = 0$  may easily be lifted, with  $|g_{\perp}(0)| \gtrsim 5$ . Finally, helical modes with large  $E_{\text{SO}}$  and wave numbers  $k_F$  are achievable using moderate electric fields of order  $\text{V}/\mu\text{m}$ . In Fig. 2.6, with the Fermi level inside the gap opened by the magnetic field, these are  $E_{\text{SO}} > 1.0 \text{ meV}$  and  $k_F \simeq 90 \mu\text{m}^{-1}$ , with  $|\langle J_y \rangle| \geq 1/2$ , and optimization via both the gate voltage and the Si shell is possible. For  $R = 10 \text{ nm}$  and thin shells, due to the quasidegeneracy at  $\gamma \rightarrow 0$ , even small electric fields of  $\sim 0.1 \text{ V}/\mu\text{m}$  are sufficient to form helical states with  $E_{\text{SO}} \gtrsim 0.3 \text{ meV}$ . We note that a strong SOI, tuned via electric fields, was recently reported for Ge/Si nanowires based on magnetotransport measurements [41].

The nanowire spectrum can be changed from the quasidegenerate to an electronlike regime, depending on the shell thickness. This moreover holds for QD spectra, so that, given the strong response to electric and magnetic fields, Ge/Si wires also seem attractive for applications in quantum information processing, particularly via electric-dipole-induced spin resonance [7, 8, 42]. Finally, when combined with a superconductor [10], the DRSOI in these wires provides a useful platform for Majorana fermions [11–16].

## Acknowledgments

We thank C. Marcus, Y. Hu, and F. Kuemmeth for helpful discussions and acknowledge support from the Swiss NF, NCCRs Nanoscience and QSIT, DARPA, and the NSF under Grant No. DMR-0840965 (M.T.).



# References

- [1] M. E. Reimer, M. P. van Kouwen, M. Barkelid, M. Hocevar, M. H. M. van Weert, R. E. Algra, E. P. A. M. Bakkers, M. T. Björk, H. Schmid, H. Riel, L. P. Kouwenhoven, and V. Zwiller, *J. Nanophoton.* **5**, 053502 (2011).
- [2] J. Xiang, W. Lu, Y. Hu, Y. Wu, H. Yan, and C. M. Lieber, *Nature (London)* **441**, 489 (2006).
- [3] H. Yan, H. S. Choe, S.W. Nam, Y. Hu, S. Das, J. F. Klemic, J. C. Ellenbogen, and C. M. Lieber, *Nature (London)* **470**, 240 (2011).
- [4] Y. Hu, H. O. H. Churchill, D. J. Reilly, J. Xiang, C. M. Lieber, and C. M. Marcus, *Nat. Nanotechnol.* **2**, 622 (2007).
- [5] W. Lu, J. Xiang, B. P. Timko, Y. Wu, and C. M. Lieber, *Proc. Natl. Acad. Sci. USA* **102**, 10046 (2005).
- [6] C. Fasth, A. Fuhrer, L. Samuelson, V. N. Golovach, and D. Loss, *Phys. Rev. Lett.* **98**, 266801 (2007).
- [7] M. D. Schroer, K. D. Petersson, M. Jung, and J. R. Petta, *Phys. Rev. Lett.* **107**, 176811 (2011).
- [8] S. Nadj-Perge, S. M. Frolov, E. P. A. M. Bakkers, and L. P. Kouwenhoven, *Nature (London)* **468**, 1084 (2010).
- [9] Y.-J. Doh, J. A. van Dam, A. L. Roest, E. P. A. M. Bakkers, L. P. Kouwenhoven, and S. De Franceschi, *Science* **309**, 272 (2005).
- [10] J. Xiang, A. Vidan, M. Tinkham, R. M. Westervelt, and C. M. Lieber, *Nat. Nanotechnol.* **1**, 208 (2006).
- [11] R. M. Lutchyn, J. D. Sau, and S. Das Sarma, *Phys. Rev. Lett.* **105**, 077001 (2010).
- [12] J. D. Sau, S. Tewari, R. M. Lutchyn, T. D. Stanescu, and S. Das Sarma, *Phys. Rev. B* **82**, 214509 (2010).
- [13] Y. Oreg, G. Refael, and F. von Oppen, *Phys. Rev. Lett.* **105**, 177002 (2010).
- [14] J. Alicea, Y. Oreg, G. Refael, F. von Oppen, and M. P. A. Fisher, *Nat. Phys.* **7**, 412 (2011).
- [15] L. Mao, M. Gong, E. Dumitrescu, S. Tewari, and C. Zhang, *Phys. Rev. Lett.* **108**, 177001 (2012).
- [16] S. Gangadharaiah, B. Braunecker, P. Simon, and D. Loss, *Phys. Rev. Lett.* **107**, 036801 (2011).
- [17] C. H. L. Quay, T. L. Hughes, J. A. Sulpizio, L. N. Pfeiffer, K. W. Baldwin, K. W. West, D. Goldhaber-Gordon, and R. de Picciotto, *Nat. Phys.* **6**, 336 (2010).
- [18] D. V. Bulaev and D. Loss, *Phys. Rev. Lett.* **95**, 076805 (2005).
- [19] D. Heiss, S. Schaeck, H. Huebl, M. Bichler, G. Abstreiter, J. J. Finley, D. V. Bulaev, and D. Loss, *Phys. Rev. B* **76**, 241306(R) (2007).
- [20] M. Trif, P. Simon, and D. Loss, *Phys. Rev. Lett* **103**, 106601 (2009).

- [21] J. Fischer, W. A. Coish, D. V. Bulaev, and D. Loss, Phys. Rev. B **78**, 155329 (2008).
- [22] J. Fischer and D. Loss, Phys. Rev. Lett. **105**, 266603 (2010).
- [23] D. Brunner, B. D. Gerardot, P. A. Dalgarno, G. Wüst, K. Karrai, N. G. Stoltz, P. M. Petroff, and R. J. Warburton, Science **325**, 70 (2009).
- [24] P. Streda and P. Seba, Phys. Rev. Lett. **90**, 256601 (2003).
- [25] D. Loss and D. P. DiVincenzo, Phys. Rev. A **57**, 120 (1998).
- [26] G. Katsaros, V. N. Golovach, P. Spathis, N. Ares, M. Stoffel, F. Fournel, O. G. Schmidt, L. I. Glazman, and S. De Franceschi, Phys. Rev. Lett. **107**, 246601 (2011).
- [27] S. Roddaro, A. Fuhrer, C. Fasth, L. Samuelson, J. Xiang, and C. M. Lieber, arXiv:0706.2883.
- [28] S. Roddaro, A. Fuhrer, P. Brusheim, C. Fasth, H. Q. Xu, L. Samuelson, J. Xiang, and C. M. Lieber, Phys. Rev. Lett. **101**, 186802 (2008).
- [29] J.-S. Park, B. Ryu, C.-Y. Moon, and K. J. Chang, Nano Lett. **10**, 116 (2010).
- [30] R. Winkler, *Spin-Orbit Coupling Effects in Two-Dimensional Electron and Hole Systems* (Springer, Berlin, 2003).
- [31] B. Braunecker, G. I. Japaridze, J. Klinovaja, and D. Loss, Phys. Rev. B **82**, 045127 (2010).
- [32] J. Klinovaja, M. J. Schmidt, B. Braunecker, and D. Loss, Phys. Rev. Lett. **106**, 156809 (2011).
- [33] J. M. Luttinger, Phys. Rev. **102**, 1030 (1956).
- [34] Equation (2.1) is valid for  $[k_i, k_j] = 0$  only. Magnetic field effects are included via the form derived in Ref. [33].
- [35] P. Lawaetz, Phys. Rev. B **4**, 3460 (1971).
- [36] P. C. Sercel and K. J. Vahala, Phys. Rev. B **42**, 3690 (1990).
- [37] D. Csontos, P. Brusheim, U. Zülicke, and H. Q. Xu, Phys. Rev. B **79**, 155323 (2009).
- [38] Phases in the off-diagonals depend on the actual representation of the spin operators and eigenstates. The details are summarized in Appendixes A.1 and A.2.
- [39] G. L. Bir and G. E. Pikus, *Symmetry and Strain-Induced Effects in Semiconductors* (Wiley, New York, 1974).
- [40] S. Dhara, H. S. Solanki, V. Singh, A. Narayanan, P. Chaudhari, M. Gokhale, A. Bhattacharya, and M. M. Deshmukh, Phys. Rev. B **79**, 121311(R) (2009).
- [41] X.-J. Hao, T. Tu, G. Cao, C. Zhou, H.-O. Li, G.-C. Guo, W. Y. Fung, Z. Ji, G.-P. Guo, and W. Lu, Nano Lett. **10**, 2956 (2010).
- [42] V. N. Golovach, M. Borhani, and D. Loss, Phys. Rev. B **74**, 165319 (2006).
- [43] C.-Y. Wen, M. C. Reuter, J. Bruley, J. Tersoff, S. Kodambaka, E. A. Stach, and F. M. Ross, Science **326**, 1247 (2009).



## Chapter 3

# Tunable $g$ Factor and Phonon-Mediated Hole Spin Relaxation in Ge/Si Nanowire Quantum Dots

**Adapted from:**

Franziska Maier, Christoph Kloeffel, and Daniel Loss,  
Phys. Rev. B **87**, 161305(R) (2013).

We theoretically consider  $g$  factor and spin lifetimes of holes in a longitudinal Ge/Si core/shell nanowire quantum dot that is exposed to external magnetic and electric fields. For the ground states, we find a large anisotropy of the  $g$  factor which is highly tunable by applying electric fields. This tunability depends strongly on the direction of the electric field with respect to the magnetic field. We calculate the single-phonon hole spin relaxation times  $T_1$  for zero and small electric fields and propose an optimal setup in which very large  $T_1$  of the order of tens of milliseconds can be reached. Increasing the relative shell thickness or the longitudinal confinement length prolongs  $T_1$  further. In the absence of electric fields, the dephasing vanishes and the decoherence time  $T_2$  is determined by  $T_2 = 2T_1$ .

### 3.1 Introduction

Semiconducting nanowires (NWs) allow to create nanoscale systems defined precisely regarding composition, geometry, and electronic properties and hence are subject to great experimental efforts. Furthermore, they offer new ways for implementing spin-based quantum computation [1]. Both III-V compounds and group-IV materials are considered and operated in the conduction band (CB, electrons) [2–9] and in the valence band (VB, holes) [10–22] regime. A particularly favored material is InAs, where single-electron quantum dots (QDs) [3] and electrically controlled spin rotations [5, 6, 8] have been implemented. Recently, qubits have also been implemented in InSb NW QDs [7, 9, 22], a system for which extremely large electron  $g$  factors have been found [4, 7]. However, the strong hyperfine interaction in InAs and InSb is considered the dominant source for the short coherence times observed [5, 9]. The latter may therefore be substantially prolonged in group-IV NWs that can be grown nuclear-spin-free. In this context, Ge and Si have emerged as promising materials for nanoscale systems such as lateral QDs [23–26], self-assembled QDs [27–29], cylindrical core/shell NWs [10–20], and ultrathin, triangular NWs [21].

For applications in spintronics and quantum information processing, it can be advantageous to consider holes instead of electrons. Due to the  $p$ -wave symmetry of the Bloch states, holes experience a strong spin-orbit interaction (SOI) on the atomic level leading to an effective spin  $J = 3/2$  behavior. Hence, spin and momentum are coupled strongly, which allows efficient control of the hole spin by electrical means. Furthermore, hole spin lifetimes are prolonged in the presence of confinement [30–35].

In Ge/Si core/shell NWs, the large VB offset leads to an accumulation of holes in the core [11, 36]. They form a one-dimensional (1D) hole gas with an unusually large, tunable Rashba-type SOI, referred to as direct Rashba SOI (DRSOI) [37]. This DRSOI makes Ge/Si core/shell NWs attractive candidates for quantum information processing via electric-dipole-induced spin resonance [38], and we mention that signatures of a tunable Rashba SOI were already deduced from magnetotransport experiments [17]. Experiments on gate defined QDs in this system revealed an anisotropy and confinement dependence of the  $g$  factor [15, 16]. Recently, singlet-triplet relaxation times in the range of several hundred microseconds were measured [20].

In this work, we consider holes forming qubits in the energetically lowest states of longitudinal QDs in Ge/Si core/shell NWs. We find the effective  $g$  factor  $g_{\text{eff}}$  of this subsystem, which turns out to be strongly anisotropic and tunable by choosing the direction and magnitude of applied electric fields. For small electric fields, we perturbatively derive an effective subspace Hamiltonian and the according hole-spin-phonon coupling and calculate the hole spin relaxation rate  $T_1^{-1}$ . At small Zeeman splittings  $\hbar\omega$  we observe an  $\omega^{7/2}$  proportionality of  $T_1^{-1}$ , which contrasts the  $\omega^5$  behavior found for electrons in QDs [39–44]. The magnitude of  $T_1^{-1}$  depends strongly on the direction of the magnetic field with respect to the wire. For zero electric field, aligning the magnetic field perpendicular to the wire results in very long  $T_1$  of the order of tens of milliseconds. Directing the magnetic field along the wire results in a much shorter  $T_1$ . For both configurations, the dephasing is zero, hence the decoherence time is given by  $T_2 = 2T_1$ . Applying small electric fields can enhance the relaxation rate by several orders of magnitude. This effect depends strongly on the direction of the electric field with respect to the magnetic field. Long  $T_1$  in the presence of electric fields are obtained when electric and magnetic fields are perpendicular to each other and perpendicular to the wire. Moreover, we find that  $T_1$  can be prolonged further by increasing the relative shell thickness and the longitudinal QD confinement. Thus, we predict an optimal field geometry for spin qubits in Ge/Si NWs that can be tested experimentally.

## 3.2 Theoretical Model

### 3.2.1 Effective 1D Hamiltonian for Holes in Ge/Si Nanowires

Low-energetic hole states in a cylindrical Ge/Si core/shell NW are well described by an effective 1D Hamiltonian [37]

$$H_w = H_0 + H' \quad (3.1)$$

that can be split into a leading-order term  $H_0$  and a perturbation  $H'$ ,

$$H_0 = H_{\text{LK}_d} + H_{\text{strain}} + H_{B,Z}, \quad (3.2)$$

$$H' = H_{\text{LK}_{od}} + H_{\text{R}} + H_{\text{DR}} + H_{B,\text{orb}}. \quad (3.3)$$

Using the notation introduced in Ref. [37] and defining the  $z$  axis as the NW axis (see Fig. 3.1), the diagonal terms of the Luttinger-Kohn (LK) Hamiltonian and the strain-induced energy splitting read

$$H_{\text{LK}_d} + H_{\text{strain}} = A_+(k_z, \gamma) + A_-(k_z, \gamma)\tau_z. \quad (3.4)$$

Here and below,  $\tau_i$  and  $\sigma_i$  are the Pauli matrices for band index ( $\{g, e\}$ ) and spin block ( $\{+, -\}$ ) of the basis states  $g_{\pm}(x, y)$  and  $e_{\pm}(x, y)$  that provide the transverse motion. In Eq. (3.4), we defined  $A_{\pm}(k_z, \gamma) = \hbar^2 k_z^2 (m_g^{-1} \pm m_e^{-1})/4 \pm \Delta/2$ , with  $m_g \simeq m/(\gamma_1 + 2\gamma_s)$  and  $m_e = m/(\gamma_1 + \gamma_s)$  as the effective masses along  $z$ . Here  $\gamma_1$  and  $\gamma_s$  are the Luttinger parameters in spherical approximation and  $m$  denotes the bare electron mass. For Ge,  $\gamma_1 = 13.35$  and  $\gamma_s = 5.11$  [45].  $\Delta = \Delta_{\text{LK}} + \Delta_{\text{strain}}(\gamma)$  is the level splitting between the  $g_{\pm}$  and  $e_{\pm}$  states,  $\gamma = (R_s - R)/R$  is the relative shell thickness, and  $R$  ( $R_s$ ) is the core (shell) radius. The Zeeman coupling  $H_{B,Z}$  with splitting  $\hbar\omega_{B,Z}$  in the lowest-energy subspace ( $g$  band) is determined by the magnetic field  $\mathbf{B} = (B_x, 0, B_z) \equiv |\mathbf{B}|(\sin\theta, 0, \cos\theta)$  (Fig. 3.1), where we set  $B_y = 0$  due to cylindrical symmetry. The main contributions to  $H'$  are

$$H_{\text{LK}_{od}} = Ck_z\tau_y\sigma_x, \quad (3.5)$$

$$H_{\text{DR}} = eU(E_x\tau_x\sigma_z - E_y\tau_y), \quad (3.6)$$

where  $H_{\text{LK}_{od}}$  features the off-diagonal couplings with coupling constant  $C = 7.26 \hbar^2/(mR)$  provided by the LK Hamiltonian as a consequence of the strong atomic-level SOI.  $H_{\text{DR}}$  is the DRSOI that results from direct, dipolar coupling to an electric field  $\mathbf{E} = (E_x, E_y, 0)$ , where  $U = 0.15 R$ . We note that  $\hbar k_z = -i\hbar\partial_z$  in Eqs. (3.4) and (3.5) is the momentum operator along the wire. In the absence of longitudinal confinement, the wave functions along  $z$  are of type  $e^{ik_z z}$  with  $k_z$  as the wave number.  $H_{\text{R}}$  is the conventional Rashba SOI, and, although fully taken into account in the present analysis, turns out to be negligible for the typical parameters and electric fields considered here. Finally,  $H_{B,\text{orb}}$  denotes the orbital coupling to the magnetic field. Details on all elements of  $H_0$  and  $H'$  are provided in Ref. [37] and in Appendix B.1.

### 3.2.2 Effective 1D Hamiltonian for Hole-Phonon Interaction

We proceed with the derivation of an effective 1D Hamiltonian  $H_{\text{h-ph}}$  for the coupling between low-energetic holes and acoustic phonons. There are three different types of acoustic phonon modes in cylindrical NWs: torsional, longitudinal, and flexural [46]. We find four different modes  $\lambda$  with dispersion relation  $\omega_{\lambda}(q)$ , where  $q$  is the phonon wave number along the wire and the exact form of  $\omega_{\lambda}$  depends strongly on the shell thickness. For the torsional and longitudinal modes ( $\lambda = T, L$ ),  $\omega_{\lambda}$  depends linearly on  $q$ , whereas for the two flexural modes ( $\lambda = F_{\pm 1}$ ) this dependence is quadratic. The detailed derivation is provided in Chapter 5; here we directly apply the displacement field  $\mathbf{u}(\mathbf{r}, t) = \sum_{\lambda, q} [\mathbf{u}_{\lambda}(q, \mathbf{r}, t)b_{q, \lambda}(t) + \text{H.c.}]$  obtained

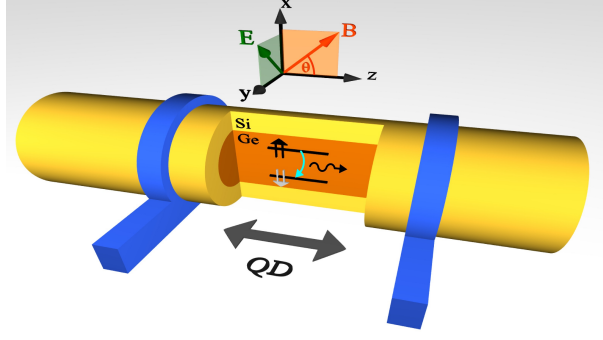


Figure 3.1. Sketch of a Ge/Si core/shell NW aligned with the  $z$  axis of the coordinate system. Electric gates (blue) induce confinement along the  $z$  axis and define a QD. The electric field  $\mathbf{E}$  lies perpendicular to the wire in the  $x$ - $y$  plane and the magnetic field  $\mathbf{B}$  lies in the  $x$ - $z$  plane. *The figure was provided by Franziska Maier.*

for a finite shell following Refs. [46–48]. The introduced  $b_{q,\lambda}(t) = e^{-i\omega_\lambda(q)t}b_{q,\lambda}$  are the time-dependent phonon annihilation operators. To derive  $H_{\text{h-ph}}$ , we insert the associated strain tensor components  $\epsilon_{ij}(\mathbf{r}, t)$  into the Bir-Pikus Hamiltonian [49]

$$H_{\text{BP}} = b \left[ \sum_i \epsilon_{ii} J_i^2 + 2(\epsilon_{xy} \{J_x, J_y\} + \text{c.p.}) \right], \quad (3.7)$$

where we omitted the global shift in energy and used the spherical approximation. The  $J_i$  with  $i = x, y, z$  are the effective spin-3/2 operators of the VB electrons and the anticommutator is defined as  $\{A, B\} = (AB + BA)/2$ . For Ge, the deformation potential  $b$  takes the value  $b \simeq -2.5$  eV [49]. We finally obtain

$$H_{\text{h-ph}} = \sum_\lambda H_\lambda = H_{\text{T}} + H_{\text{L}} + H_{F_{+1}} + H_{F_{-1}} \quad (3.8)$$

by integrating out the transverse part of the matrix elements, i.e., by projecting the Hamiltonian onto the subspace spanned by  $g_\pm$  and  $e_\pm$ . The components of  $H_{\text{h-ph}}$  are given explicitly in Appendix B.2.

### 3.2.3 Harmonic Confinement and Quantum Dot Hamiltonian

Longitudinal confinement is realized by electric gating (see Fig. 3.1), which is modeled by adding a harmonic confinement potential in the  $z$  direction,

$$H_{qd} = H_w + V_c(z), \quad (3.9)$$

where  $V_c(z) = \frac{1}{2}\alpha_c z^2$ .  $H_{qd}$  describes the QD well if the longitudinal confinement length is much larger than  $R$ . The basis states of  $H_{qd}$  are products of type  $g_\pm \psi_n^g$  and  $e_\pm \psi_n^e$ , where the  $\psi_n^{g/e}(z)$  are eigenfunctions of the harmonic oscillator  $\hbar^2 k_z^2 / (2m_{g/e}) + V_c(z)$  and  $n \in \{0, 1, \dots\}$  is the harmonic oscillator quantum number. The confinement energies  $\hbar\omega_{g/e}$  relate to  $\alpha_c$  via  $\alpha_c = m_{g/e}\omega_{g/e}^2$  and the harmonic oscillator confinement lengths read  $l_{g/e} = \sqrt{\hbar/(m_{g/e}\omega_{g/e})}$ .

## 3.3 Large Anisotropy and Electrical Tunability of Hole-Spin $g$ Factor

From  $H_{qd}$  we extract the effective  $g$  factor  $g_{\text{eff}}$  of the lowest-energy subsystem by performing an exact, numerical diagonalization which gives the Zeeman splitting  $\Delta E_{Z,\text{num}}$  (defined as positive) and

$$g_{\text{eff}} = \frac{\Delta E_{Z,\text{num}}}{\mu_B |\mathbf{B}|}, \quad (3.10)$$

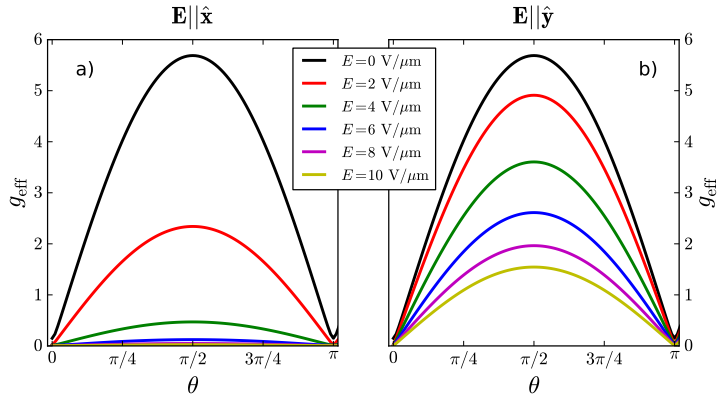


Figure 3.2. Effective  $g$  factor  $g_{\text{eff}}$  as a function of the angle  $\theta$  defined by  $\mathbf{B} = |\mathbf{B}|(\sin \theta, 0, \cos \theta)$  for  $\mathbf{E} \parallel \hat{x}$  (a) and  $\mathbf{E} \parallel \hat{y}$  (b). We vary  $|\mathbf{E}|$  from 0 to 10  $\text{V}/\mu\text{m}$ . For  $|\mathbf{E}| = 0$ , we find  $g_{\text{eff}}(0) \approx 0.14$  and  $g_{\text{eff}}(\pi/2) \approx 5.7$ . It is clearly visible that  $g_{\text{eff}}$  is affected much stronger by changes in  $|\mathbf{E}|$  for  $\mathbf{E} \parallel \hat{x}$  than for  $\mathbf{E} \parallel \hat{y}$ . Even though the curves in panel a seem to overlap for  $|\mathbf{E}| \geq 6 \text{ V}/\mu\text{m}$ ,  $g_{\text{eff}}(\pi/2)$  still decreases for growing fields and  $g_{\text{eff}}$  remains anisotropic. We choose  $R = 10 \text{ nm}$  and  $R_s = 13 \text{ nm}$  for the NW and a QD confinement length of  $l_g \approx 80 \text{ nm}$ . The figure was provided by Franziska Maier.

where  $\mu_B$  is the Bohr magneton. In Fig. 3.2, we plot  $g_{\text{eff}}$  as a function of the angle  $\theta$ , for both  $\mathbf{E} \parallel \hat{x}$  and  $\mathbf{E} \parallel \hat{y}$  (unit vectors along the  $x, y, z$  axes are denoted here by  $\hat{x}, \hat{y}, \hat{z}$ ). In both cases,  $g_{\text{eff}}$  is highly anisotropic and tunable over a wide range of values by adjusting the magnitude of  $\mathbf{E}$ . The tunability is caused by two mechanisms which occur in the system for large  $|\mathbf{E}|$ ; the admixture of the  $e_{\pm}$  states to the effective lowest-energy subsystem increases while the spin-orbit length  $l_{\text{SOI}}$  decreases. For very small  $l_{\text{SOI}}$  ( $l_{\text{SOI}} \ll l_g$ ), the hole spin flips many times while moving through the QD and the resulting  $g_{\text{eff}}$  starts to average out. The tunability is much stronger for  $\mathbf{E} \parallel \hat{x}$  than for  $\mathbf{E} \parallel \hat{y}$ . Note that  $g_{\text{eff}}$  is also tunable by varying  $V_c(z)$ . We find good agreement with the results given in Ref. [20], where  $g_{\text{exp}} \approx 1.02$  was measured for  $\mathbf{B}$  aligned with the NW axis with an accuracy of  $\sim 30^\circ$ . We note, however, that clearly different results for the  $g$  factor can be expected in QDs with very large occupation number, i.e., when the hole-spin qubits are formed in an excited band.

## 3.4 Phonon-Mediated Decay of Hole-Spin Qubits

### 3.4.1 Effective Qubit Hamiltonian and Bloch-Redfield Theory

In the following, we are interested in the dynamics of the lowest-lying, Zeeman split states which we decouple perturbatively from the higher-energy states. This is done by two consecutive Schrieffer-Wolff transformations (SWTs) to account for the two different energy scales  $\Delta$  and  $\hbar\omega_g$ . The general form of the SWT is  $\tilde{H} = e^{-S} H e^S$ , where to lowest order  $S \approx S_1$ . We first remove the coupling between the  $g_{\pm}$  and  $e_{\pm}$  states in the effective 1D picture using  $S_1^g$ . The hole-phonon coupling then transforms according to  $H_{\text{h-ph}} - [S_1^g, H_{\text{h-ph}}]$  and we refer to its projection on  $g_{\pm}$  as  $H_{\text{h-ph}}^g$ . In the second step, we add harmonic confinement as introduced above and decouple the two lowest, Zeeman split states  $|0\rangle \equiv \{|\uparrow\rangle, |\downarrow\rangle\}$  by another SWT using  $S_1^{(0)}$ . A necessary condition for this approach is that the energy splittings obey  $\Delta \gg \hbar\omega_g \gg \hbar\omega_{B,Z}$ , and the magnitude of  $\mathbf{E}$  is restricted by  $2C|\mathbf{E}|eU/(l_g\Delta) \ll \hbar\omega_g$ . The latter condition is fulfilled for  $|\mathbf{E}| \ll 1 \text{ V}/\mu\text{m}$ . We obtain an effective Zeeman term  $H_{Z,\text{eff}} = \mu_B \mathbf{B}_{\text{eff}} \cdot \boldsymbol{\sigma}'$  with Zeeman splitting  $\Delta E_{Z,\text{eff}} = 2\mu_B |\mathbf{B}_{\text{eff}}|$ , where  $\boldsymbol{\sigma}'$  is a vector of Pauli matrices for the hole-spin qubit. The effective hole-spin-phonon coupling is obtained via  $H_{\text{s-ph}} = H_{\text{h-ph}}^g - [S_1^{(0)}, H_{\text{h-ph}}^g]$ , where  $H_{\text{h-ph}}^g$  is now written in the basis given by the confinement. Projecting  $H_{\text{s-ph}}$  on  $|0\rangle$  results in an effective coupling  $H_{\text{s-ph,eff}} = \mu_B \boldsymbol{\delta B} \cdot \boldsymbol{\sigma}'$  with the fluctuating magnetic field  $\boldsymbol{\delta B}(t) = \sum_{\lambda,q} [\mathbf{a}_{\lambda}(q) b_{q,\lambda}(t) + \text{H.c.}]$ . The effective

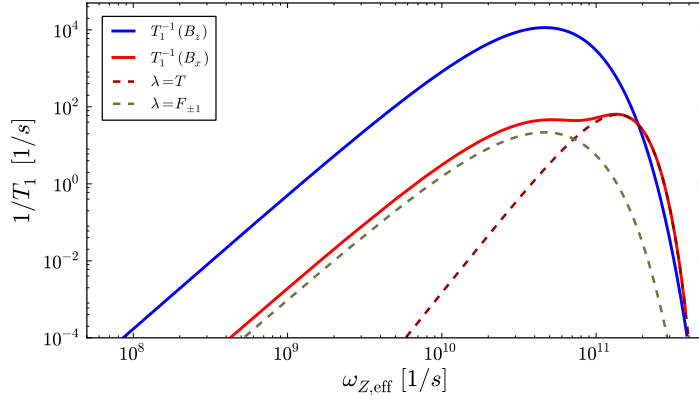


Figure 3.3. Relaxation rate  $T_1^{-1}$  at  $|\mathbf{E}| = 0$  for  $\mathbf{B} \parallel \hat{\mathbf{x}}$  (red, solid) and  $\mathbf{B} \parallel \hat{\mathbf{z}}$  (blue, solid). For  $\mathbf{B} \parallel \hat{\mathbf{x}}$ , we plot the contributing phonon branches  $F_{\pm 1}$  and  $T$  (dashed). We find maximal values  $T_{1,\max}^{-1}(\mathbf{B} \parallel \hat{\mathbf{z}}) \approx 11 \text{ ms}^{-1}$  and  $T_{1,\max}^{-1}(\mathbf{B} \parallel \hat{\mathbf{x}}) \approx 60 \text{ s}^{-1}$ . Note the nonmonotonic behavior of  $T_1^{-1}$  as a function of  $\omega_{Z,\text{eff}}$ . The NW and QD parameters are chosen as in Fig. 3.2. The figure was provided by Franziska Maier.

Hamiltonian for the qubit subspace is then

$$H_{\text{eff}} = H_{Z,\text{eff}} + H_{\text{s-ph,eff}} = \mu_B [\mathbf{B}_{\text{eff}} + \delta\mathbf{B}(t)] \cdot \boldsymbol{\sigma}'. \quad (3.11)$$

The spin relaxation rate in the Born-Markov approximation is given by the Bloch-Redfield approach [40, 50, 51]

$$\frac{1}{T_1} = n_i n_j [\delta_{ij} (\delta_{pq} - n_p n_q) J_{pq}^+(\omega) - (\delta_{ip} - n_i n_p) J_{pj}^+(\omega) - \delta_{ij} \varepsilon_{kpq} n_k J_{pq}^-(\omega) + \varepsilon_{ipq} n_p J_{qj}^-(\omega)], \quad (3.12)$$

where summation over repeated indices is assumed,  $\mathbf{n} = \mathbf{B}_{\text{eff}}/|\mathbf{B}_{\text{eff}}|$  is the unit vector in the direction of the effective magnetic field, and  $\hbar\omega = \hbar\omega_{Z,\text{eff}} = \Delta E_{Z,\text{eff}}$  is the energy splitting of the considered states. Furthermore,  $J_{ij}^+(\omega) = \text{Re}[J_{ij}(\omega) + J_{ij}(-\omega)]$  and  $I_{ij}^-(\omega) = \text{Im}[J_{ij}(\omega) - J_{ij}(-\omega)]$ , with  $J_{ij}(\omega) = (2\mu_B^2/\hbar^2) \int_0^\infty dt e^{-i\omega t} \langle \delta B_i(0) \delta B_j(t) \rangle$  denoting the spectral function.

### 3.4.2 Decay Rates for Various Setup Geometries

In Fig. 3.3, we display  $T_1^{-1}$  for  $|\mathbf{E}| = 0$  and two different directions of  $\mathbf{B}$  with respect to the wire,  $\mathbf{B} \parallel \hat{\mathbf{z}}$  and  $\mathbf{B} \parallel \hat{\mathbf{x}}$ . In the absence of electric fields, the spin-phonon coupling  $H_{\text{s-ph,eff}}$  depends only on the coupling terms of  $H_{B,\text{orb}}$ . For low  $\omega_{Z,\text{eff}}$ , i.e., the long-wavelength regime ( $ql_g \ll 1$ ), both curves are proportional to  $\omega_{Z,\text{eff}}^{7/2}$ . This behavior is valid for low temperatures ( $\hbar\omega_{Z,\text{eff}} \gg k_B T$ ) and will be replaced by  $T_1^{-1} \propto \omega_{Z,\text{eff}}^{5/2} T$  for  $\hbar\omega_{Z,\text{eff}} \ll k_B T$ . The  $\omega_{Z,\text{eff}}^{7/2}$  scaling contrasts the  $\omega_{Z,\text{eff}}^5$  behavior of electrons in QDs [39–44]. For  $\mathbf{B} \parallel \hat{\mathbf{z}}$ , only the  $F_{\pm 1}$  modes contribute significantly to  $T_1^{-1}$ . When  $\mathbf{B} \parallel \hat{\mathbf{x}}$ , the  $F_{\pm 1}$  contributions dominate for low  $\omega_{Z,\text{eff}}$  and, for the chosen QD geometry, are replaced by a dominating contribution from the torsional mode  $T$  at  $|\mathbf{B}| \approx 150 \text{ mT}$  (Fig. 3.3, dashed). This results in a double peak whose relative height can be modified by changing  $l_g$  or  $R$  and  $R_s$ . Most remarkably, for  $\mathbf{B} \parallel \hat{\mathbf{x}}$ ,  $T_1^{-1}$  is several orders of magnitude smaller than for  $\mathbf{B} \parallel \hat{\mathbf{z}}$ . For the chosen QD geometry,  $T_1^{-1}$  reaches maximal values  $T_{1,\max}^{-1}(\mathbf{B} \parallel \hat{\mathbf{x}}) \approx 60 \text{ s}^{-1}$  and  $T_{1,\max}^{-1}(\mathbf{B} \parallel \hat{\mathbf{z}}) \approx 11 \text{ ms}^{-1}$ . These rates are, depending on the direction of  $\mathbf{B}$ , comparable to or much smaller than those for electrons in InAs NW QDs [41].

Considering nonzero electric fields, we plot  $T_1^{-1}$  for  $\mathbf{E} \parallel \hat{\mathbf{x}}$  again for  $\mathbf{B} \parallel \hat{\mathbf{z}}$  and  $\mathbf{B} \parallel \hat{\mathbf{x}}$  (Fig. 3.4). We add the corresponding curves for  $|\mathbf{E}| = 0$  (Fig. 3.4, dotted) to allow for comparison. For both orientations of  $\mathbf{B}$ ,  $T_1^{-1}$  is enhanced significantly for larger  $\omega_{Z,\text{eff}}$ . This is due to phonons of the  $L$  mode coupling  $|\uparrow\rangle$  and  $|\downarrow\rangle$  via a combination of  $H_{\text{LK}_{\text{od}}}$  and  $H_{\text{DR}}$  which dominates  $H_{\text{R}}$ . Due to cylindrical symmetry, applying  $\mathbf{E} \parallel \hat{\mathbf{y}}$  for  $\mathbf{B} \parallel \hat{\mathbf{z}}$  results in the same effect as described for  $\mathbf{E} \parallel \hat{\mathbf{x}}$ . Remarkably, in stark contrast

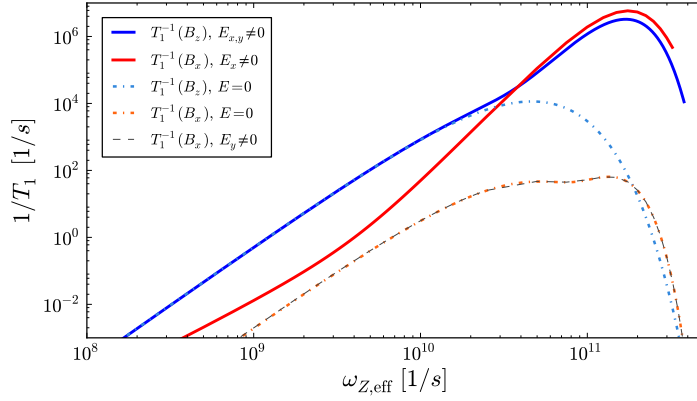


Figure 3.4. Relaxation rates  $T_1^{-1}$  for  $\mathbf{E} \parallel \hat{\mathbf{x}}$  with  $|\mathbf{E}| = 0.1 \text{ V}/\mu\text{m}$  for  $\mathbf{B} \parallel \hat{\mathbf{x}}$  (red, solid) and  $\mathbf{B} \parallel \hat{\mathbf{z}}$  (blue, solid). For comparison we plot  $T_1^{-1}$  at  $|\mathbf{E}| = 0$  (dotted). We find maximal values  $T_{1,\text{max}}^{-1}(\mathbf{B} \parallel \hat{\mathbf{z}}) \approx 3.2 \mu\text{s}^{-1}$  and  $T_{1,\text{max}}^{-1}(\mathbf{B} \parallel \hat{\mathbf{x}}) \approx 5.8 \mu\text{s}^{-1}$ . Rotating the electric field so that  $\mathbf{E} \parallel \hat{\mathbf{y}}$  yields the same curve for  $\mathbf{B} \parallel \hat{\mathbf{z}}$ . Remarkably, for  $\mathbf{B} \parallel \hat{\mathbf{x}}$  almost no difference between the curves at  $\mathbf{E} \parallel \hat{\mathbf{y}}$  (dashed) and  $|\mathbf{E}| = 0$  (dotted) is observed. We use the NW and QD parameters given in the caption of Fig. 3.2. *The figure was provided by Franziska Maier.*

to  $\mathbf{E} \parallel \mathbf{B} \parallel \hat{\mathbf{x}}$ , only minor changes with respect to the curve at  $|\mathbf{E}| = 0$  (Fig. 3.4, dotted) are observed when  $\mathbf{E} \parallel \hat{\mathbf{y}}$  and  $\mathbf{B} \parallel \hat{\mathbf{x}}$  (Fig. 3.4, dashed). In the latter case, the dominant contributions of  $H_{\text{s-ph,eff}}$  are already present in  $H_{\text{s-ph,eff}}$  for  $|\mathbf{E}| = 0$ .

In both cases,  $|\mathbf{E}| = 0$  and  $|\mathbf{E}| \neq 0$ , increasing the relative shell thickness  $\gamma$  shifts the  $T_1^{-1}$  curves to slightly larger  $\omega_{\text{Z,eff}}$  and lowers the peak height; e.g., increasing  $\gamma$  from 0.3 to 0.7 reduces  $T_1^{-1}$  by a factor  $\sim 3$ . However, decreasing (increasing)  $R$  and  $R_s$  while keeping  $\gamma$  constant has no substantial effect on  $T_1^{-1}$  aside from slight shifts to the right (left) on the  $\omega_{\text{Z,eff}}$  axis. Additionally, for  $|\mathbf{E}| = 0$  and for  $\mathbf{E} \parallel \hat{\mathbf{y}}$  and  $\mathbf{B} \parallel \hat{\mathbf{x}}$ , enhancing the confinement length  $l_g$  lowers  $T_{1,\text{max}}^{-1}$  since the short-wavelength regime is reached for smaller  $\omega_{\text{Z,eff}}$ . This effect is quite large; for instance, raising  $l_g$  from 60 to 100 nm reduces  $T_{1,\text{max}}^{-1}$  by factors between 10 and 100. However, for  $\mathbf{E} \parallel \hat{\mathbf{x}}$  and  $\mathbf{B} \parallel \hat{\mathbf{z}}$  or  $\mathbf{B} \parallel \hat{\mathbf{x}}$ , increasing  $l_g$  results in larger  $T_{1,\text{max}}^{-1}$ . From the analysis we conclude that there exist optimal configurations of  $\mathbf{B}$  and  $\mathbf{E}$  in order to obtain long  $T_1$  in this type of NW QD.  $\mathbf{B}$  should be applied perpendicular to the NW and the optional  $\mathbf{E}$  should lie perpendicular to both  $\mathbf{B}$  and the NW. For vanishing  $\mathbf{B}$ , as pointed out in Ref. [20], two-phonon processes [32] might become relevant.

In the Bloch-Redfield framework, the decoherence time  $T_2$  is given by  $T_2^{-1} = (2T_1)^{-1} + T_\varphi^{-1}$ , where  $T_\varphi$  denotes the dephasing time [40, 51]. For  $|\mathbf{E}| = 0$ , we find  $T_2 = 2T_1$  because the corresponding spectral function is superohmic and gives  $T_\varphi^{-1} = 0$ . For  $|\mathbf{E}| \neq 0$ , the SOI results in a nonzero dephasing term  $T_\varphi^{-1} \neq 0$  and hence  $T_2 < 2T_1$ .

### 3.5 Conclusions

In conclusion, we have examined the effective Zeeman splitting and the spin dynamics for holes of lowest energy in a Ge/Si core/shell NW QD. We reported a highly anisotropic effective  $g$  factor that is strongly tunable by applying electric fields. We calculated relaxation rates and found particular configurations of electric and magnetic fields which correspond to very long spin relaxation times. Furthermore, we pointed out that the relative shell thickness and the QD confinement length influence the spin relaxation time.

### Acknowledgments

We thank Peter Stano for helpful discussions. This work has been supported by SNF, NCCR Nano, NCCR QSIT, DARPA, and IARPA.





# References

- [1] D. Loss and D. P. DiVincenzo, Phys. Rev. A **57**, 120 (1998).
- [2] Y.-J. Doh, J. A. van Dam, A. L. Roest, E. P. A. M. Bakkers, L. P. Kouwenhoven, and S. De Franceschi, Science **309**, 272 (2005).
- [3] C. Fasth, A. Fuhrer, L. Samuelson, V. N. Golovach, and D. Loss, Phys. Rev. Lett. **98**, 266801 (2007).
- [4] H. A. Nilsson, P. Caroff, C. Thelander, M. Larsson, J. B. Wagner, L.-E. Wernersson, L. Samuelson, and H. Q. Xu, Nano Lett. **9**, 3151 (2009).
- [5] S. Nadj-Perge, S. M. Frolov, E. P. A. M. Bakkers, and L. P. Kouwenhoven, Nature (London) **468**, 1084 (2010).
- [6] M. D. Schroer, K. D. Petersson, M. Jung, and J. R. Petta, Phys. Rev. Lett. **107**, 176811 (2011).
- [7] S. Nadj-Perge, V. S. Pribiag, J. W. G. van den Berg, K. Zuo, S. R. Plissard, E. P. A. M. Bakkers, S. M. Frolov, and L. P. Kouwenhoven, Phys. Rev. Lett. **108**, 166801 (2012).
- [8] K. D. Petersson, L. W. McFaul, M. D. Schroer, M. Jung, J. M. Taylor, A. A. Houck, and J. R. Petta, Nature (London) **490**, 380 (2012).
- [9] J. W. G. van den Berg, S. Nadj-Perge, V. S. Pribiag, S. R. Plissard, E. P. A. M. Bakkers, S. M. Frolov, and L. P. Kouwenhoven, Phys. Rev. Lett. **110**, 066806 (2013).
- [10] L. J. Lauhon, M. S. Gudiksen, D. Wang, and C. M. Lieber, Nature (London) **420**, 57 (2002).
- [11] W. Lu, J. Xiang, B. P. Timko, Y. Wu, and C. M. Lieber, Proc. Natl. Acad. Sci. USA **102**, 10046 (2005).
- [12] J. Xiang, W. Lu, Y. Hu, Y. Wu, H. Yan, and C. M. Lieber, Nature (London) **441**, 489 (2006).
- [13] J. Xiang, A. Vidan, M. Tinkham, R. M. Westervelt, and C. M. Lieber, Nat. Nanotechnol. **1**, 208 (2006).
- [14] Y. Hu, H. O. H. Churchill, D. J. Reilly, J. Xiang, C. M. Lieber, and C. M. Marcus, Nat. Nanotechnol. **2**, 622 (2007).
- [15] S. Roddaro, A. Fuhrer, C. Fasth, L. Samuelson, J. Xiang, and C. M. Lieber, arXiv:0706.2883.
- [16] S. Roddaro, A. Fuhrer, P. Brusheim, C. Fasth, H. Q. Xu, L. Samuelson, J. Xiang, and C. M. Lieber, Phys. Rev. Lett. **101**, 186802 (2008).
- [17] X.-J. Hao, T. Tu, G. Cao, C. Zhou, H.-O. Li, G.-C. Guo, W. Y. Fung, Z. Ji, G.-P. Guo, and W. Lu, Nano Lett. **10**, 2956 (2010).
- [18] H. Yan, H. S. Choe, S. Nam, Y. Hu, S. Das, J. F. Klemic, J. C. Ellenbogen, and C. M. Lieber, Nature (London) **470**, 240 (2011).
- [19] J. Nah, D. C. Dillen, K. M. Varahramyan, S. K. Banerjee, and E. Tutuc, Nano Lett. **12**, 108 (2012).

- [20] Y. Hu, F. Kuemmeth, C. M. Lieber, and C. M. Marcus, *Nat. Nanotechnol.* **7**, 47 (2012).
- [21] J. J. Zhang, G. Katsaros, F. Montalenti, D. Scopece, R. O. Rezaev, C. Mickel, B. Rellinghaus, L. Miglio, S. De Franceschi, A. Rastelli, and O. G. Schmidt, *Phys. Rev. Lett.* **109**, 085502 (2012).
- [22] V. S. Pribiag, S. Nadj-Perge, S. M. Frolov, J. W. G. van den Berg, I. van Weperen, S. R. Plissard, E. P. A. M. Bakkers, and L. P. Kouwenhoven, *Nat. Nanotechnol.* **8**, 170 (2013).
- [23] C. B. Simmons, J. R. Prance, B. J. Van Bael, T. S. Koh, Z. Shi, D. E. Savage, M. G. Lagally, R. Joynt, M. Friesen, S. N. Coppersmith, and M. A. Eriksson, *Phys. Rev. Lett.* **106**, 156804 (2011).
- [24] J. R. Prance, Z. Shi, C. B. Simmons, D. E. Savage, M. G. Lagally, L. R. Schreiber, L. M. K. Vandersypen, M. Friesen, R. Joynt, S. N. Coppersmith, and M. A. Eriksson, *Phys. Rev. Lett.* **108**, 046808 (2012).
- [25] B. M. Maune, M. G. Borselli, B. Huang, T. D. Ladd, P. W. Deelman, K. S. Holabird, A. A. Kiselev, I. Alvarado-Rodriguez, R. S. Ross, A. E. Schmitz, M. Sokolich, C. A. Watson, M. F. Gyure, and A. T. Hunter, *Nature (London)* **481**, 344 (2012).
- [26] Z. Shi, C. B. Simmons, D. R. Ward, J. R. Prance, R. T. Mohr, T. S. Koh, J. K. Gamble, X. Wu, D. E. Savage, M. G. Lagally, M. Friesen, S. N. Coppersmith, and M. A. Eriksson, *Phys. Rev. B* **88**, 075416 (2013).
- [27] K. L. Wang, D. Cha, J. Liu, and C. Chen, *Proc. IEEE* **95**, 1866 (2007).
- [28] G. Katsaros, P. Spathis, M. Stoffel, F. Fournel, M. Mongillo, V. Bouchiat, F. Lefloch, A. Rastelli, O. G. Schmidt, and S. De Franceschi, *Nat. Nanotechnol.* **5**, 458 (2010).
- [29] G. Katsaros, V. N. Golovach, P. Spathis, N. Ares, M. Stoffel, F. Fournel, O. G. Schmidt, L. I. Glazman, and S. De Franceschi, *Phys. Rev. Lett.* **107**, 246601 (2011).
- [30] D. V. Bulaev and D. Loss, *Phys. Rev. Lett.* **95**, 076805 (2005).
- [31] D. Heiss, S. Schaeck, H. Huebl, M. Bichler, G. Abstreiter, J. J. Finley, D. V. Bulaev, and D. Loss, *Phys. Rev. B* **76**, 241306(R) (2007).
- [32] M. Trif, P. Simon, and D. Loss, *Phys. Rev. Lett.* **103**, 106601 (2009).
- [33] J. Fischer, W. A. Coish, D. V. Bulaev, and D. Loss, *Phys. Rev. B* **78**, 155329 (2008).
- [34] J. Fischer and D. Loss, *Phys. Rev. Lett.* **105**, 266603 (2010).
- [35] D. Brunner, B. D. Gerardot, P. A. Dalgarno, G. Wüst, K. Karrai, N. G. Stoltz, P. M. Petroff, and R. J. Warburton, *Science* **325**, 70 (2009).
- [36] J.-S. Park, B. Ryu, C.-Y. Moon, and K. J. Chang, *Nano Lett.* **10**, 116 (2010).
- [37] C. Kloeffel, M. Trif, and D. Loss, *Phys. Rev. B* **84**, 195314 (2011).  
See Chapter 2
- [38] V. N. Golovach, M. Borhani, and D. Loss, *Phys. Rev. B* **74**, 165319 (2006).
- [39] A. V. Khaetskii and Y. V. Nazarov, *Phys. Rev. B* **64**, 125316 (2001).
- [40] V. N. Golovach, A. V. Khaetskii, and D. Loss, *Phys. Rev. Lett.* **93**, 016601 (2004).
- [41] M. Trif, V. N. Golovach, and D. Loss, *Phys. Rev. B* **77**, 045434 (2008).

- [42] M. Kroutvar, Y. Ducommun, D. Heiss, M. Bichler, D. Schuh, G. Abstreiter, and J. J. Finley, *Nature* (London) **432**, 81 (2004).
- [43] S. Amasha, K. MacLean, I. P. Radu, D. M. Zumbühl, M. A. Kastner, M. P. Hanson, and A. C. Gossard, *Phys. Rev. Lett.* **100**, 046803 (2008).
- [44] J. Dreiser, M. Atatüre, C. Galland, T. Müller, A. Badolato, and A. Imamoglu, *Phys. Rev. B* **77**, 075317 (2008).
- [45] P. Lawaetz, *Phys. Rev. B* **4**, 3460 (1971).
- [46] A. N. Cleland, *Foundations of Nanomechanics: From Solid-State Theory to Device Applications* (Springer, Berlin, 2003).
- [47] N. Nishiguchi, *Phys. Rev. B* **50**, 10970 (1994).
- [48] M. A. Stroscio and M. Dutta, *Phonons in Nanostructures* (Cambridge Univ. Press, Cambridge, 2001).
- [49] G. L. Bir and G. E. Pikus, *Symmetry and Strain-Induced Effects in Semiconductors* (Wiley, New York, 1974).
- [50] C. P. Slichter, *Principles of Magnetic Resonance* (Springer, Berlin, 1980).
- [51] M. Borhani, V. N. Golovach, and D. Loss, *Phys. Rev. B* **73**, 155311 (2006).



## Chapter 4

# Circuit QED with Hole-Spin Qubits in Ge/Si Nanowire Quantum Dots

### Adapted from:

Christoph Kloeffel, Mircea Trif, Peter Stano, and Daniel Loss,  
Phys. Rev. B **88**, 241405(R) (2013).

We propose a setup for universal and electrically controlled quantum information processing with hole spins in Ge/Si core/shell nanowire quantum dots (NW QDs). Single-qubit gates can be driven through electric-dipole-induced spin resonance, with spin-flip times shorter than 100 ps. Long-distance qubit-qubit coupling can be mediated by the cavity electric field of a superconducting transmission line resonator, where we show that operation times below 20 ns seem feasible for the entangling  $\sqrt{i}$ SWAP gate. The absence of Dresselhaus spin-orbit interaction (SOI) and the presence of an unusually strong Rashba-type SOI enable precise control over the transverse qubit coupling via an externally applied, perpendicular electric field. The latter serves as an on-off switch for quantum gates and also provides control over the  $g$  factor, so single- and two-qubit gates can be operated independently. Remarkably, we find that idle qubits are insensitive to charge noise and phonons, and we discuss strategies for enhancing noise-limited gate fidelities.

## 4.1 Introduction

In the past decade, the idea of processing quantum information with spins in quantum dots (QDs) [1] was followed by remarkable progress [2]. While the workhorse systems are highly advanced, such as self-assembled (In)GaAs QDs [3–10] and negatively charged, lateral GaAs QDs [11–17], an emerging theme is the search for systems that allow further optimization. In particular, Ge and Si have attracted attention because they can be grown nuclear-spin-free, which eliminates a major source of decoherence [18–20]. Promising examples based on Ge/Si are core/shell nanowires (NWs) [21–31], self-assembled QDs [32–34], lateral QDs [35, 36], and ultrathin, triangular NWs [37]. In addition, spin qubits formed in the valence band (VB, holes) were found to feature long lifetimes [4, 31, 38–42]. Finally, new sample geometries such as NW QDs are investigated, and have allowed for electric-dipole-induced spin resonance (EDSR) [43] in InAs [44–46] and InSb [47] with spin-flip times down to several nanoseconds only.

Prime examples for novel qubits are hole spins in Ge/Si NW QDs [25, 26, 31, 42, 48], because they combine all the advantages of group-IV materials, VB states, and strong confinement along two axes. The Si shell provides a large VB offset  $\sim 0.5$  eV [22], induces strain, and removes dangling bonds from the core. Furthermore, the holes feature an unusually strong Rashba-type spin-orbit interaction (SOI), referred to as direct Rashba SOI (DRSOI), that is not suppressed by the band gap [48]. We show here that these properties are highly useful for implementing spin qubits.

In this work, we propose a setup for quantum information processing with holes in Ge/Si core/shell NW QDs. In stark contrast to previous systems [13, 43–47, 49], where the EDSR relies on conventional Dresselhaus and Rashba SOI [50], the dynamics in our setup are governed by the DRSOI whose origin fundamentally differs. We find that EDSR allows flipping of hole spins within less than 100 ps. Two-qubit gates can be realized via circuit quantum electrodynamics (CQED), i.e., with an on-chip cavity [51–53], where we estimate that operation times below 20 ns are feasible for  $\sqrt{i\text{SWAP}}$ . The long-range spin-spin interactions [49, 54–56] enable upscaling. Compared to the original proposal for electron spins in InAs [49], which was recently followed by encouraging results [46], we find several new and striking features. First, because of bulk inversion symmetry, the SOI and the quantum gates can be precisely controlled by perpendicular electric fields. In particular, these fields serve as on-off switches for two-qubit operations performed on any two spins in the cavity. Second, a strong electric-field-dependence of the  $g$  factor allows fine tuning and independent control of all quantum gates. Third, the large DRSOI leads to remarkably short operation times. Finally, we find that noise becomes an issue during quantum operations only, and we discuss how noise-limited gate fidelities can be enhanced. While this chapter summarizes our main results, the supplementary information [57] explains all the derivations and provides the details of the theory.

## 4.2 Setup and Model Hamiltonian

Figure 4.1a depicts the setup we consider. Electric gates (not shown) form a Ge/Si NW QD with harmonic confining potential  $V(z) = \hbar\omega_g z^2 / (2l_g^2)$  along the wire axis  $z$ , where  $\hbar\omega_g$  is the level spacing,  $l_g = \sqrt{\hbar/(m_g\omega_g)}$  is the confinement length, and  $m_g$  is the hole mass along  $z$  in the subband of lowest energy. An electric (magnetic) field  $E_y$  ( $B_y$ ) along  $y$  controls the DRSOI (Zeeman splitting). The electric field  $E_z$  is induced either externally,  $E_z = E_{z,0}^e \cos(\omega_{ac}t)$ , or by the cavity,  $E_z = E_{z,0}^c (a^\dagger + a)$ , where  $\omega_{ac}$  is the angular frequency,  $E_{z,0}^{e,c}$  is the amplitude, and  $a^\dagger$  ( $a$ ) is the creation (annihilation) operator for the quasi-resonant cavity mode [51, 57].

When the Ge/Si NW QD of core (shell) radius  $R$  ( $R_s$ ) is elongated,  $l_g \gg R$ , the low-energetic hole states are well described by the Hamiltonian

$$H = H_{1D} + V(z) - eE_z z. \quad (4.1)$$

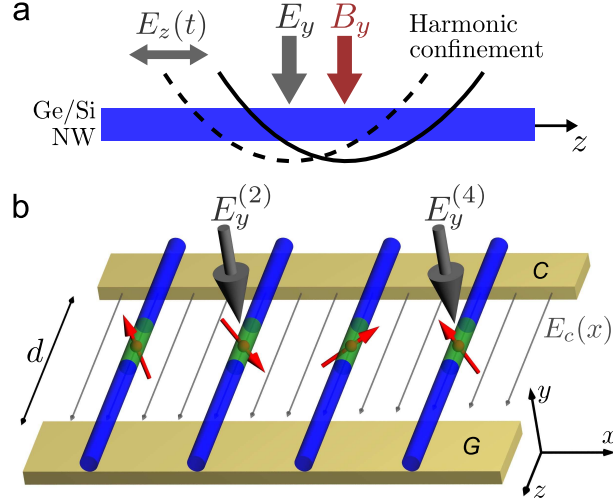


Figure 4.1. Proposed setup. (a) An electric (magnetic) field  $E_y$  ( $B_y$ ) is applied perpendicular to the Ge/Si NW QD. Ac fields  $E_z(t)$  shift the confining potential along the NW axis  $z$ . (b) When placed between the center conductor (C) and the ground plane (G) of a transmission line resonator, the hole-spin qubits (red arrows) can interact via the cavity field  $E_c$ , with the interaction strengths controlled by local electric fields  $E_y^{(i)}$ . In the sketch, a two-qubit gate is performed between qubits 2 and 4. The setup does not require equidistant QDs and is robust against misalignment.

Here  $e$  is the elementary positive charge and  $H_{1D}$  is the effective one-dimensional (1D) Hamiltonian derived in Ref. [48]. For our setup, one finds  $H_{1D} = H_{LK} + H_{BP} + H_B + H_{DR} + H_R$ , with

$$H_{LK} + H_{BP} = A_+ + A_- \tau_z + C k_z \tau_y \sigma_z, \quad (4.2)$$

$$H_B = \mu_B B_y (-X_2 \sigma_y - X_1 \tau_z \sigma_y + L k_z \tau_x \sigma_z), \quad (4.3)$$

$$H_{DR} = -e E_y U \tau_y. \quad (4.4)$$

The Pauli operators  $\tau_i$  and  $\sigma_i$  act on the transverse band index  $\{g, e\}$  and the spin index  $\{+, -\}$ , respectively. Equation (4.2), where  $A_{\pm} = \hbar^2 k_z^2 (m_g^{-1} \pm m_e^{-1})/4 \pm \Delta/2$  and  $\Delta = 0.73 \hbar^2/(mR^2) + \Delta_{BP}(\gamma)$ , combines the Luttinger-Kohn (LK) [58, 59] with the Bir-Pikus (BP) Hamiltonian [60], which describe, respectively, the kinetic energy and the effects of strain. The strain-induced energy  $\Delta_{BP}(\gamma)$  increases with  $\gamma = (R_s - R)/R$ , and we note that  $10 \text{ meV} \lesssim \Delta \lesssim 25 \text{ meV}$  in typical Ge/Si NWs with  $R \sim 5\text{--}10 \text{ nm}$  and  $\gamma \sim 10\%\text{--}50\%$ . Equation (4.3),  $H_B$ , accounts for the orbital effects and the Zeeman coupling due to  $B_y$ . The SOI comprises the DRSOI  $H_{DR}$  induced by  $E_y$ , Eq. (4.4), and the much smaller standard Rashba SOI (RSOI)  $H_R$  due to  $E_y$  and  $E_z$ . For the explicit form of  $H_R$ , see Appendix C. The parameters for Ge are [48]  $C = 7.26 \hbar^2/(mR)$ ,  $U = 0.15R$ ,  $X_1 \equiv (K + M)/2$ ,  $X_2 \equiv (K - M)/2$ ,  $L = 8.04R$ ,  $K = 2.89$ ,  $M = 2.56$ ,  $m_g = 0.043m$ ,  $m_e = 0.054m$ ,  $m$  is the bare electron mass, and  $\hbar k_z = -i\hbar\partial_z$  is the canonical momentum along  $z$ .

### 4.3 Effective Hamiltonian for the Hole-Spin Qubit

Our main result is the derivation of the effective  $2 \times 2$  Hamiltonian for the hole-spin qubit,

$$H_q = \frac{E_Z}{2} \tilde{\sigma}_z + T_q \tilde{\sigma}_x. \quad (4.5)$$

$H_q$  describes the lowest-energy subspace of  $H$ , Eq. (4.1). Its parameters are the Zeeman splitting  $E_Z = |g\mu_B B_y| \equiv \hbar\omega_Z$ , with  $g$  factor  $g$ , and the transverse coupling  $T_q = \bar{\nu} E_z$ . Introducing  $\nu_{e,c} = \bar{\nu} E_{z,0}^{e,c}$ , one obtains  $T_q = \nu_e \cos(\omega_{act})$  for EDSR and  $T_q = \nu_c (a^\dagger + a)$  for the cavity field. The tilde over the  $\tilde{\sigma}_i$

denotes that the Pauli operators act on the two QD states forming the qubit. Both  $E_Z$  and  $\bar{\nu}$  are chosen here as positive. The derivation of  $H_q$  comprises several basis transformations, two of which we expand perturbatively [57]. While the resulting formulas (“model”) for  $E_Z$  and  $\bar{\nu}$  are too lengthy to be displayed here, they can be very well approximated for realistic Ge/Si NW QDs. Performing a linear expansion in  $B_y$  and neglecting  $H_R$  completely, we find (“approximation”)

$$\bar{\nu} \simeq \frac{2E_Z|E_y|e^2UC}{(\hbar\tilde{\omega}_g)^2\tilde{\Delta}}, \quad (4.6)$$

$$g \simeq 2 \left( \tilde{K} - \frac{LC\Delta}{\tilde{l}_g^2\tilde{\Delta}^2} \right) \exp \left[ - \left( \frac{2eUCE_y}{\tilde{l}_g\hbar\tilde{\omega}_g\tilde{\Delta}} \right)^2 \right], \quad (4.7)$$

where

$$\tilde{K} = K - \frac{(K+M)E_y^2}{\left(\frac{\tilde{\Delta}+\Delta}{2eU}\right)^2 + E_y^2}, \quad (4.8)$$

$\tilde{\Delta} = \sqrt{\Delta^2 + (2eUE_y)^2}$  is the effective subband spacing,

$$\hbar\tilde{\omega}_g = \hbar\omega_g \sqrt{1 - \frac{2m_gC^2\Delta^2}{\hbar^2\tilde{\Delta}^3}} \quad (4.9)$$

is the effective level splitting, and  $\tilde{l}_g = l_g\sqrt{\tilde{\omega}_g/\omega_g}$ . Comparing with the exact diagonalization of  $H$  (“numerics”) [57], we find that Eqs. (4.6) and (4.7) provide a quantitatively reliable description of the qubit. Considering the complex character of holes and the nontrivial setup with three control fields, the derived formulas are surprisingly simple and therefore provide insight into the role of various parameters. Next, we demonstrate the usefulness of our results by quantifying the basic characteristics of these qubits, such as operation times and lifetimes, and by identifying the most suitable operation schemes.

## 4.4 Ultrafast Single-Qubit Gates and Tunable $g$ Factors

We consider a Ge/Si NW QD with  $R = 7.5$  nm,  $l_g = 50$  nm, and  $\Delta = 16$  meV based on  $R_s \simeq 10$  nm. At  $E_y = 0$ ,  $g \sim 2K$  and  $\hbar\tilde{\omega}_g = 0.56$  meV  $\equiv \hbar\tilde{\omega}_0$ . When  $2K\mu_B|B_y| \ll \hbar\tilde{\omega}_0$ , a linear expansion in  $B_y$  applies and both  $E_Z \propto |B_y|$  and  $\bar{\nu} \propto |B_y|$ . In Fig. 4.2 (top), we plot  $\bar{\nu}/|B_y|$  as a function of  $E_y$  and find excellent agreement between numerical and perturbative results. The electrical tunability is remarkable. The coefficient  $\bar{\nu}$  goes from the exact zero at  $E_y = 0$  through a peak at  $E_y \simeq 1.8$  V/ $\mu$ m into a decreasing tail. Most striking is the magnitude,  $\bar{\nu}/|B_y| \simeq 10$  nm e/T, which allows for ultrafast single-qubit gates through EDSR. When  $\omega_{ac} = \omega_Z$ , a  $\pi$  rotation on the Bloch sphere requires the spin-flip time  $t_{\text{flip}} = \hbar\pi/\nu_e$  [2]. For  $E_{z,0}^e = 10^3$ – $10^4$  V/m and  $B_y = 0.5$  T, for instance,  $\nu_e \simeq 5$ – $50$   $\mu$ eV and  $t_{\text{flip}} \sim 400$ – $40$  ps, an extremely short operation time.

The decrease of  $\bar{\nu}$  at large  $|E_y|$  is related to the  $g$  factor decay. As shown in Fig. 4.3 (top),  $g$  decreases from  $g \simeq 5.5$  at  $E_y = 0$  toward  $g \sim 0$  when  $E_y$  is increased to several V/ $\mu$ m. This tunability was already observed numerically in Ref. [42], and our model provides an explanation for the rapid decay of  $g$  in this setup. First, as seen in Eqs. (4.7) and (4.8), the main contribution  $\tilde{K}$  changes from  $K$  toward a much smaller value  $(K-M)/2$  when  $E_y$  strongly mixes the subbands  $g$  and  $e$ . In addition, the  $g$  factor averages out to zero when the spin-orbit length becomes much smaller than  $\tilde{l}_g$  [42, 49, 61], leading to the exponential suppression. We note that a similar tunability of  $g$  was recently measured [34] in SiGe nanocrystals.

For the QD under study, the linear expansion applies well for  $|B_y| \lesssim 0.5$  T ( $2K\mu_B|B_y| \lesssim \hbar\tilde{\omega}_0/3$ ).



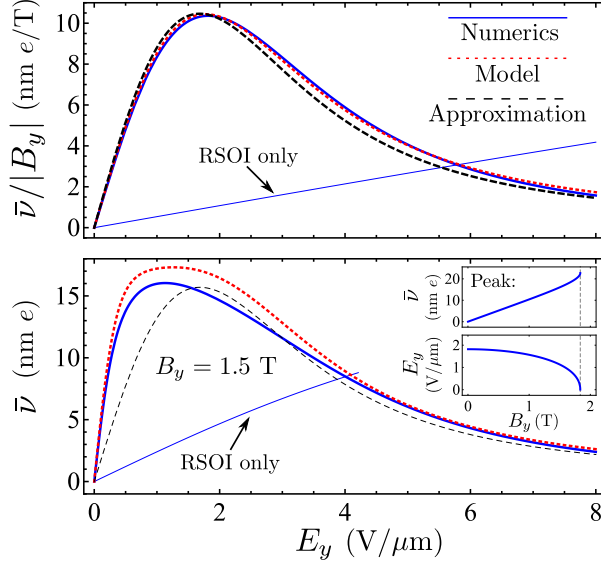


Figure 4.2. Electrical tunability of  $\bar{\nu}$  for the QD in the text. Solid blue (dotted red) curves result from the numerical calculation (effective model) [57]; dashed black lines correspond to Eq. (4.6). The thin blue lines (RSOI only,  $H_{\text{DR}} = 0$ ) illustrate that much stronger  $E_y$  would be required for realizing a given  $\bar{\nu}$  with the conventional RSOI. Top: Result for  $|B_y| \lesssim 0.5$  T, where a linear expansion in  $B_y$  applies. Bottom:  $B_y = 1.5$  T, beyond the linear regime. Inset: Height and position of the peak as a function of  $B_y$ . For  $E_y = 0$ , a level crossing in the numerics occurs at  $B_y \simeq 1.8$  T (vertical dashed line). The achievable operation times scale with  $1/\bar{\nu}$ .

However, it may also be useful to operate the qubit at rather strong  $B_y$ . In Fig. 4.2 (bottom), we plot  $\bar{\nu}$  for the example  $B_y = 1.5$  T. As expected, the perturbative results show deviations from the exact calculation as  $E_Z$  approaches the orbital level spacing. Nevertheless, they remain correct qualitatively. Compared to  $|B_y| \lesssim 0.5$  T, the simulated  $\bar{\nu}$  peaks at smaller  $|E_y|$  and the maximum value,  $\bar{\nu} \simeq 16$  nm  $e$ , is even greater than the one extrapolated from Fig. 4.2 (top). For  $E_{z,0}^e = 10^3\text{--}10^4$  V/m,  $t_{\text{flip}} \sim 100\text{--}10$  ps. As plotted in the inset of Fig. 4.2, the trends found for  $B_y = 1.5$  T are enhanced as  $B_y$  approaches the value at which neighboring levels cross, allowing the realization of  $\bar{\nu} > 20$  nm  $e$ . Figure 4.3 (bottom) shows that the perturbative results for  $E_Z$  are reliable even at high magnetic fields.

## 4.5 Two-Qubit Gates via Circuit QED

Thus far, we have identified three major features: a tunable  $g$  factor, a strong transverse coupling driven by  $E_z$ , and precise electrical control via  $E_y$ . When combined, these features prove ideal for implementing two-qubit gates via CQED. The proposed setup is sketched in Fig. 4.1b. Ge/Si NWs are placed perpendicular to the 1D resonator and host a qubit each inside the cavity. Because the  $i$ th qubit can only couple to the cavity electric field when  $E_y^{(i)} \neq 0$ , the fields  $E_y^{(i)}$  can be used to control qubit-cavity interactions and, hence, two-qubit gates. In addition, the  $E_y^{(i)}$  provide precise control over the detunings  $\Delta_q^{(i)} = E_Z^{(i)} - \hbar\omega_c$ , where  $\hbar\omega_c$  is the energy of the cavity mode. This allows the implementation of fast quantum gates through fine tuning of  $\Delta_q^{(i)}$ . Moreover, as illustrated in Fig. 4.4, all single- and two-qubit gates can be performed independently.

Quantitative information about the cavity field is summarized in Refs. [51, 57]. For the mode of lowest energy, we estimate [57] that  $eE_{z,0}^c/(\hbar\omega_c) \sim 10^{-2}/\mu\text{m}$  is feasible by decreasing the mode volume compared to Refs. [51–53]. From Fig. 4.4, we deduce  $E_Z \simeq 0.35$  meV at maximal  $\bar{\nu}$  for  $B_y = 1.5$  T. With  $E_{z,0}^c = 3$  V/m,  $\nu_c \simeq 50$  neV. Thus, Rabi oscillations in the qubit-cavity system require  $\hbar\pi/\nu_c \sim 40$  ns for a full cycle at resonance. When  $\nu_c^{(i)}/|\Delta_q^{(i)}| < 1$ , the coupling between qubits  $i$  and  $j$  is determined by

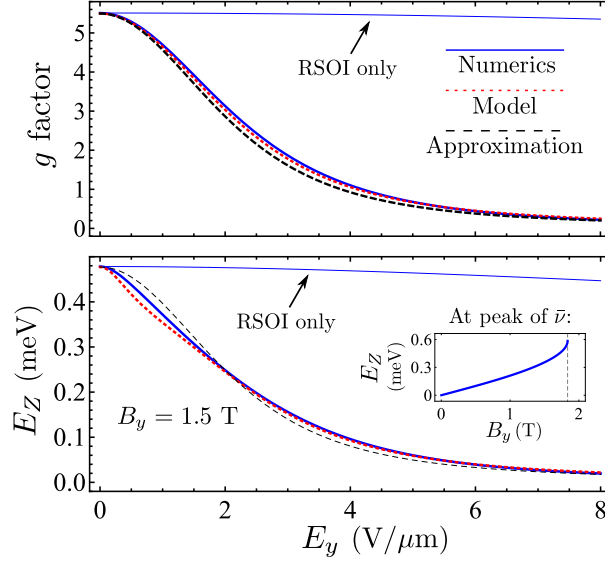


Figure 4.3. The  $g$  factor [ $|B_y| \lesssim 0.5$  T (top)] and Zeeman splitting [ $B_y = 1.5$  T (bottom)] as a function of  $E_y$  for the parameters in the text. Solid blue (dotted red) lines are calculated numerically (perturbatively) [57]; dashed black lines result from Eq. (4.7). The thin blue lines (RSOI only,  $H_{\text{DR}} = 0$ ) confirm that the strong electrical tunability results from the DRSOI, Eq. (4.4). Inset:  $E_Z$  at the  $E_y$  for which  $\bar{\nu}$  is maximal (see inset of Fig. 4.2).

the transverse spin-spin interaction

$$J_{xy}^{(i,j)} = \nu_c^{(i)} \nu_c^{(j)} \left( \frac{1}{\Delta_q^{(i)}} + \frac{1}{\Delta_q^{(j)}} \right), \quad (4.10)$$

which is the basis for the entangling  $\sqrt{i\text{SWAP}}$  gate [49, 51, 54, 57, 62]. For numerical estimates, we set  $\nu_c^{(i)} = \nu_c^{(j)} = \nu_c$ ,  $\Delta_q^{(i)} = \Delta_q^{(j)} = \Delta_q$ , and  $J_{xy}^{(i,j)} = J_{xy} = 2\nu_c^2/\Delta_q$ . Because corrections to  $J_{xy}$  are on the order of  $\nu_c^4/\Delta_q^3$  only, we allow for  $\nu_c/|\Delta_q| \simeq 0.1\text{--}0.5$ , which results in short  $\sqrt{i\text{SWAP}}$  times,  $\hbar\pi/|2J_{xy}| \sim 100\text{--}20$  ns. At larger  $B_y$  (and/or larger  $E_{z,0}$ ), these can be reduced further.

## 4.6 Qubit Lifetimes and Gate Fidelities

In general, qubits that can be manipulated electrically are also sensitive to charge noise [17, 63]. Remarkably, idle qubits in our setup are insulated from the environment; at  $E_y = 0 = E_z$ , all first derivatives of  $E_Z$  and  $T_q$  with respect to  $E_y$  and  $E_z$  vanish, cavity fields are negligible due to off-resonance, and relaxation via phonons is suppressed [42] for the magnetic field  $\mathbf{B}$  along  $y$ . At maximal  $\bar{\nu}$ , we derive [57]

$$1/T_1^{\text{el}} = 2\kappa_z^2 \bar{\nu}^2 R_z E_Z / \hbar^2, \quad (4.11)$$

$$1/T_\varphi^{\text{el}} = \kappa_y^2 (\partial_{E_y} E_Z)^2 R_y k_B T_y / \hbar^2, \quad (4.12)$$

from the Bloch-Redfield theory [64–66] and the spectral functions for Johnson-Nyquist noise [67–69]. Here  $T_1^{\text{el}}$  ( $T_\varphi^{\text{el}}$ ) is the relaxation (dephasing) time due to electrical noise,  $R_\alpha$  ( $T_\alpha$ ) is the resistance (temperature) of the gate that generates  $E_\alpha$  along  $\alpha \in \{y, z\}$ , and the  $\kappa_\alpha$  convert fluctuations in the gate voltages to fluctuations in  $E_\alpha$ . Considering  $E_Z > k_B T_\alpha$ , we find  $T_\varphi^{\text{el}} \gg T_1^{\text{el}}$  for the values from Fig. 4.4, which implies  $T_2^{\text{el}} = 2T_1^{\text{el}} \propto 1/(\kappa_z^2 E_Z^2)$  for the decoherence time. Thus, the setups should be designed such that  $\kappa_z$  is small. Assuming  $R_\alpha = 10^2 \Omega$  and  $\kappa_z = 0.1/\mu\text{m}$ , we obtain  $T_2^{\text{el}} = 1$  ms (30  $\mu\text{s}$ ) for  $B_y = 0.5$  T (1.5 T). If gate fidelities are limited by charge noise, they can be increased by lowering  $E_Z$  or  $\kappa_z$  or even by operation away from maximal  $\bar{\nu}$ . If, instead, the fidelities are limited by phonons, they can be much

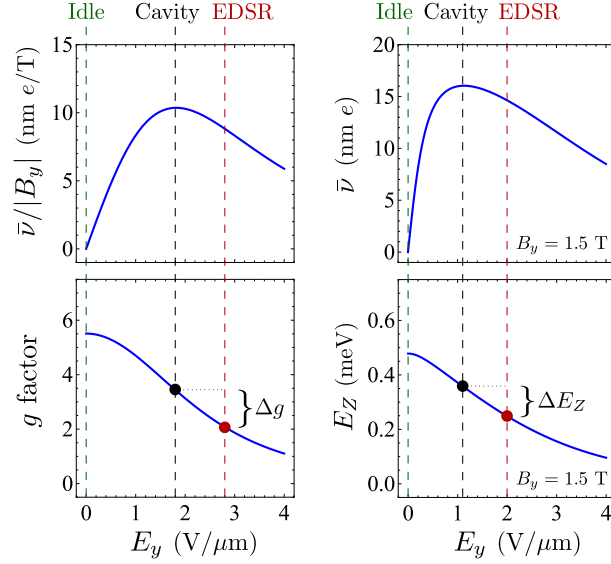


Figure 4.4. Basic operation scheme with the numerical results from Figs. 4.2 and 4.3. When  $E_y = 0$  (idle), the qubit features long lifetimes. Two-qubit operations are envisaged at  $E_y$  with maximal  $\bar{\nu}$  (cavity). Single-qubit gates can be performed independently by applying a different  $E_y$  (EDSR) for which all cavity modes are far off-resonant. The associated change in the  $g$  factor ( $E_Z$ ) is indicated by  $\Delta g$  ( $\Delta E_Z$ ). For  $|B_y| \lesssim 0.5$  T (left),  $\bar{\nu}$  is maximal at  $E_y \simeq 1.8$  V/ $\mu\text{m}$ , where  $g \simeq 3.4$  and  $\partial_{E_y} g \simeq -1.6$   $\mu\text{m}/\text{V}$ . For  $B_y = 1.5$  T (right),  $\bar{\nu}$  peaks at  $E_y \simeq 1.1$  V/ $\mu\text{m}$ , where  $E_Z \simeq 0.35$  meV and  $\partial_{E_y} E_Z \simeq -0.13$  nm  $e$ .

enhanced in the short-wavelength regime at larger  $E_Z$  [42, 49, 65, 70]. Noise that is slow compared to the operation times can be dynamically decoupled [2, 17, 71, 72].

## 4.7 Results for Different Setups

We studied variants in the setup geometry. For  $\mathbf{B}$  along  $x$ ,  $\bar{\nu} = 0$  even at  $E_y \neq 0$ . Although large  $\bar{\nu}$  are possible for  $\mathbf{B}$  along  $z$ , such a setup requires stronger  $\mathbf{B}$  due to the smaller  $g$  factor [31, 42] and exact alignment of all NWs, which is challenging. When the ac fields are perpendicular to the NW,  $\bar{\nu}$  becomes several orders of magnitude weaker because of  $l_q \gg R$ . Hence, the setup we propose in Fig. 4.1 is the most favorable one.

## Acknowledgments

We thank F. Maier, K. D. Petersson, J. R. Petta, R. J. Warburton, J. R. Wootton, and R. Zielke for helpful discussions and acknowledge support from the Swiss NF, NCCRs Nanoscience and QSIT, SiSPIN, DARPA, IARPA (MQCO), S<sup>3</sup>NANO, SCIEX, the NSF under Grant No. DMR-0840965 (M.T.), and QIMABOS-APVV-0808-12 (P.S.).



# References

- [1] D. Loss and D. P. DiVincenzo, *Phys. Rev. A* **57**, 120 (1998).
- [2] C. Kloeffel and D. Loss, *Annu. Rev. Condens. Matter Phys.* **4**, 51 (2013).  
See Chapter 1
- [3] R. J. Warburton, C. Schäfflein, D. Haft, F. Bickel, A. Lorke, K. Karrai, J. M. Garcia, W. Schoenfeld, and P. M. Petroff, *Nature (London)* **405**, 926 (2000).
- [4] B. D. Gerardot, D. Brunner, P. A. Dalgarno, P. Öhberg, S. Seidl, M. Kroner, K. Karrai, N. G. Stoltz, P. M. Petroff, and R. J. Warburton, *Nature (London)* **451**, 441 (2008).
- [5] T. M. Godden, S. J. Boyle, A. J. Ramsay, A. M. Fox, and M. S. Skolnick, *Appl. Phys. Lett.* **97**, 061113 (2010).
- [6] K. Müller, T. Kaldewey, R. Ripszam, J. S. Wildmann, A. Bechtold, M. Bichler, G. Koblmüller, G. Abstreiter, and J. J. Finley, *Sci. Rep.* **3**, 1906 (2013).
- [7] A. N. Vamivakas, C.-Y. Lu, C. Matthiesen, Y. Zhao, S. Fält, A. Badolato, and M. Atatüre, *Nature (London)* **467**, 297 (2010).
- [8] J. Berezovsky, M. H. Mikkelsen, N. G. Stoltz, L. A. Coldren, and D. D. Awschalom, *Science* **320**, 349 (2008).
- [9] D. Press, K. De Greve, P. L. McMahon, T. D. Ladd, B. Friess, C. Schneider, M. Kamp, S. Höfling, A. Forchel, and Y. Yamamoto, *Nat. Photon.* **4**, 367 (2010).
- [10] D. Kim, S. G. Carter, A. Greilich, A. S. Bracker, and D. Gammon, *Nat. Phys.* **7**, 223 (2011).
- [11] J. R. Petta, A. C. Johnson, J. M. Taylor, E. A. Laird, A. Yacoby, M. D. Lukin, C. M. Marcus, M. P. Hanson, and A. C. Gossard, *Science* **309**, 2180 (2005).
- [12] F. H. L. Koppens, C. Buizert, K. J. Tielrooij, I. T. Vink, K. C. Nowack, T. Meunier, L. P. Kouwenhoven, and L. M. K. Vandersypen, *Nature (London)* **442**, 766 (2006).
- [13] K. C. Nowack, F. H. L. Koppens, Yu. V. Nazarov, and L. M. K. Vandersypen, *Science* **318**, 1430 (2007).
- [14] R. Brunner, Y.-S. Shin, T. Obata, M. Pioro-Ladrière, T. Kubo, K. Yoshida, T. Taniyama, Y. Tokura, and S. Tarucha, *Phys. Rev. Lett.* **107**, 146801 (2011).
- [15] K. C. Nowack, M. Shafiei, M. Laforest, G. E. D. K. Prawiroatmodjo, L. R. Schreiber, C. Reichl, W. Wegscheider, and L. M. K. Vandersypen, *Science* **333**, 1269 (2011).
- [16] L. Gaudreau, G. Granger, A. Kam, G. C. Aers, S. A. Studenikin, P. Zawadzki, M. Pioro-Ladrière, Z. R. Wasilewski, and A. S. Sachrajda, *Nat. Phys.* **8**, 54 (2012).
- [17] M. D. Shulman, O. E. Dial, S. P. Harvey, H. Bluhm, V. Umansky, and A. Yacoby, *Science* **336**, 202 (2012).

- [18] A. V. Khaetskii, D. Loss, and L. Glazman, *Phys. Rev. Lett.* **88**, 186802 (2002).
- [19] I. A. Merkulov, A. L. Efros, and M. Rosen, *Phys. Rev. B* **65**, 205309 (2002).
- [20] W. A. Coish and D. Loss, *Phys. Rev. B* **70**, 195340 (2004).
- [21] L. J. Lauhon, M. S. Gudiksen, D. Wang, and C. M. Lieber, *Nature (London)* **420**, 57 (2002).
- [22] W. Lu, J. Xiang, B. P. Timko, Y. Wu, and C. M. Lieber, *Proc. Natl. Acad. Sci. USA* **102**, 10046 (2005).
- [23] J. Xiang, W. Lu, Y. Hu, Y. Wu, H. Yan, and C. M. Lieber, *Nature (London)* **441**, 489 (2006).
- [24] J. Xiang, A. Vidan, M. Tinkham, R. M. Westervelt, and C. M. Lieber, *Nat. Nanotechnol.* **1**, 208 (2006).
- [25] Y. Hu, H. O. H. Churchill, D. J. Reilly, J. Xiang, C. M. Lieber, and C. M. Marcus, *Nat. Nanotechnol.* **2**, 622 (2007).
- [26] S. Roddaro, A. Fuhrer, P. Brusheim, C. Fasth, H. Q. Xu, L. Samuelson, J. Xiang, and C. M. Lieber, *Phys. Rev. Lett.* **101**, 186802 (2008).
- [27] K. M. Varahramyan, D. Ferrer, E. Tutuc, and S. K. Banerjee, *Appl. Phys. Lett.* **95**, 033101 (2009).
- [28] X.-J. Hao, T. Tu, G. Cao, C. Zhou, H.-O. Li, G.-C. Guo, W. Y. Fung, Z. Ji, G.-P. Guo, and W. Lu, *Nano Lett.* **10**, 2956 (2010).
- [29] H. Yan, H. S. Choe, S. Nam, Y. Hu, S. Das, J. F. Klemic, J. C. Ellenbogen, and C. M. Lieber, *Nature (London)* **470**, 240 (2011).
- [30] J. Nah, D. C. Dillen, K. M. Varahramyan, S. K. Banerjee, and E. Tutuc, *Nano Lett.* **12**, 108 (2012).
- [31] Y. Hu, F. Kuemmeth, C. M. Lieber, and C. M. Marcus, *Nat. Nanotechnol.* **7**, 47 (2012).
- [32] K. L. Wang, D. Cha, J. Liu, and C. Chen, *Proc. IEEE* **95**, 1866 (2007).
- [33] G. Katsaros, V. N. Golovach, P. Spathis, N. Ares, M. Stoffel, F. Fournel, O. G. Schmidt, L. I. Glazman, and S. De Franceschi, *Phys. Rev. Lett.* **107**, 246601 (2011).
- [34] N. Ares, V. N. Golovach, G. Katsaros, M. Stoffel, F. Fournel, L. I. Glazman, O. G. Schmidt, and S. De Franceschi, *Phys. Rev. Lett.* **110**, 046602 (2013).
- [35] C. B. Simmons, J. R. Prance, B. J. Van Bael, T. S. Koh, Z. Shi, D. E. Savage, M. G. Lagally, R. Joynt, M. Friesen, S. N. Coppersmith, and M. A. Eriksson, *Phys. Rev. Lett.* **106**, 156804 (2011).
- [36] B. M. Maune, M. G. Borselli, B. Huang, T. D. Ladd, P. W. Deelman, K. S. Holabird, A. A. Kiselev, I. Alvarado-Rodriguez, R. S. Ross, A. E. Schmitz, M. Sokolich, C. A. Watson, M. F. Gyure, and A. T. Hunter, *Nature (London)* **481**, 344 (2012).
- [37] J. J. Zhang, G. Katsaros, F. Montalenti, D. Scopece, R. O. Rezaev, C. Mickel, B. Rellinghaus, L. Miglio, S. De Franceschi, A. Rastelli, and O. G. Schmidt, *Phys. Rev. Lett.* **109**, 085502 (2012).
- [38] D. V. Bulaev and D. Loss, *Phys. Rev. Lett.* **95**, 076805 (2005).
- [39] D. Heiss, S. Schaeck, H. Huebl, M. Bichler, G. Abstreiter, J. J. Finley, D. V. Bulaev, and D. Loss, *Phys. Rev. B* **76**, 241306(R) (2007).
- [40] J. Fischer, W. A. Coish, D. V. Bulaev, and D. Loss, *Phys. Rev. B* **78**, 155329 (2008).

- [41] D. Brunner, B. D. Gerardot, P. A. Dalgarno, G. Wüst, K. Karrai, N. G. Stoltz, P. M. Petroff, and R. J. Warburton, *Science* **325**, 70 (2009).
- [42] F. Maier, C. Kloeffel, and D. Loss, *Phys. Rev. B* **87**, 161305(R) (2013).  
See Chapter 3
- [43] V. N. Golovach, M. Borhani, and D. Loss, *Phys. Rev. B* **74**, 165319 (2006).
- [44] S. Nadj-Perge, S. M. Frolov, E. P. A. M. Bakkers, and L. P. Kouwenhoven, *Nature (London)* **468**, 1084 (2010).
- [45] M. D. Schroer, K. D. Petersson, M. Jung, and J. R. Petta, *Phys. Rev. Lett.* **107**, 176811 (2011).
- [46] K. D. Petersson, L. W. McFaul, M. D. Schroer, M. Jung, J. M. Taylor, A. A. Houck, and J. R. Petta, *Nature (London)* **490**, 380 (2012).
- [47] J. W. G. van den Berg, S. Nadj-Perge, V. S. Pribiag, S. R. Plissard, E. P. A. M. Bakkers, S. M. Frolov, and L. P. Kouwenhoven, *Phys. Rev. Lett.* **110**, 066806 (2013).
- [48] C. Kloeffel, M. Trif, and D. Loss, *Phys. Rev. B* **84**, 195314 (2011).  
See Chapter 2
- [49] M. Trif, V. N. Golovach, and D. Loss, *Phys. Rev. B* **77**, 045434 (2008).
- [50] R. Winkler, *Spin-Orbit Coupling Effects in Two-Dimensional Electron and Hole Systems* (Springer, Berlin, 2003).
- [51] A. Blais, R.-S. Huang, A. Wallraff, S. M. Girvin, and R. J. Schoelkopf, *Phys. Rev. A* **69**, 062320 (2004).
- [52] A. Wallraff, D. I. Schuster, A. Blais, L. Frunzio, R.-S. Huang, J. Majer, S. Kumar, S. M. Girvin, and R. J. Schoelkopf, *Nature (London)* **431**, 162 (2004).
- [53] L. Frunzio, A. Wallraff, D. I. Schuster, J. Majer, and R. J. Schoelkopf, *IEEE Trans. Appl. Supercond.* **15**, 860 (2005).
- [54] A. Imamoglu, D. D. Awschalom, G. Burkard, D. P. DiVincenzo, D. Loss, M. Sherwin, and A. Small, *Phys. Rev. Lett.* **83**, 4204 (1999).
- [55] L. Trifunovic, O. Dial, M. Trif, J. R. Wootton, R. Abebe, A. Yacoby, and D. Loss, *Phys. Rev. X* **2**, 011006 (2012).
- [56] L. Trifunovic, F. L. Pedrocchi, and D. Loss, *Phys. Rev. X* **3**, 041023 (2013).
- [57] See Appendix C for details of the theory.
- [58] J. M. Luttinger and W. Kohn, *Phys. Rev.* **97**, 869 (1955).
- [59] J. M. Luttinger, *Phys. Rev.* **102**, 1030 (1956).
- [60] G. L. Bir and G. E. Pikus, *Symmetry and Strain-Induced Effects in Semiconductors* (Wiley, New York, 1974).
- [61] C. Flindt, A. S. Sorensen, and K. Flensberg, *Phys. Rev. Lett.* **97**, 240501 (2006).
- [62] A. Blais, J. Gambetta, A. Wallraff, D. I. Schuster, S. M. Girvin, M. H. Devoret, and R. J. Schoelkopf, *Phys. Rev. A* **75**, 032329 (2007).

- [63] A. V. Kuhlmann, J. Houel, A. Ludwig, L. Greuter, D. Reuter, A. D. Wieck, M. Poggio, and R. J. Warburton, *Nat. Phys.* **9**, 570 (2013).
- [64] C. P. Slichter, *Principles of Magnetic Resonance* (Springer, Berlin, 1980).
- [65] V. N. Golovach, A. V. Khaetskii, and D. Loss, *Phys. Rev. Lett.* **93**, 016601 (2004).
- [66] M. Borhani, V. N. Golovach, and D. Loss, *Phys. Rev. B* **73**, 155311 (2006).
- [67] J. B. Johnson, *Phys. Rev.* **32**, 97 (1928).
- [68] H. Nyquist, *Phys. Rev.* **32**, 110 (1928).
- [69] A. A. Clerk, M. H. Devoret, S. M. Girvin, F. Marquardt, and R. J. Schoelkopf, *Rev. Mod. Phys.* **82**, 1155 (2010).
- [70] T. Meunier, I. T. Vink, L. H. Willems van Beveren, K-J. Tielrooij, R. Hanson, F. H. L. Koppens, H. P. Tranitz, W. Wegscheider, L. P. Kouwenhoven, and L. M. K. Vandersypen, *Phys. Rev. Lett.* **98**, 126601 (2007).
- [71] L. Viola, S. Lloyd, and E. Knill, *Phys. Rev. Lett.* **83**, 4888 (1999).
- [72] T. van der Sar, Z. H. Wang, M. S. Blok, H. Bernien, T. H. Taminiau, D. M. Toyli, D. A. Lidar, D. D. Awschalom, R. Hanson, and V. V. Dobrovitski, *Nature (London)* **484**, 82 (2012).



# Chapter 5

## Acoustic Phonons and Strain in Core/Shell Nanowires

**Adapted from:**

Christoph Kloeffel, Mircea Trif, and Daniel Loss,  
Phys. Rev. B **90**, 115419 (2014).

We study theoretically the low-energy phonons and the static strain in cylindrical core/shell nanowires (NWs). Assuming pseudomorphic growth, isotropic media, and a force-free wire surface, we derive algebraic expressions for the dispersion relations, the displacement fields, and the stress and strain components from linear elasticity theory. Our results apply to NWs with arbitrary radii and arbitrary elastic constants for both core and shell. The expressions for the static strain are consistent with experiments, simulations, and previous analytical investigations; those for phonons are consistent with known results for homogeneous NWs. Among other things, we show that the dispersion relations of the torsional, longitudinal, and flexural modes change differently with the relative shell thickness, and we identify new terms in the corresponding strain tensors that are absent for uncapped NWs. We illustrate our results via the example of Ge/Si core/shell NWs and demonstrate that shell-induced strain has large effects on the hole spectrum of these systems.

## 5.1 Introduction

In the past years, it has been demonstrated that the performance of nanowires (NWs) can greatly benefit from the presence of a shell. For instance, surface passivation is an option to reduce scattering, and measurements on InAs/InP core/shell NWs have revealed significantly higher mobilities than in uncapped InAs NWs [1]. Furthermore, experiments on various core/shell NWs [2–6] have demonstrated that adding a shell can be very useful for optical applications, a feature that is well-known, e.g., from colloidal quantum dots (QDs) [7, 8]. In Ge/Si core/shell NWs, which recently attracted attention, the shell is beneficial for several reasons. In particular, it provides a large valence band offset at the interface, leading to a strongly confined hole gas inside the Ge core without the need for dopants [9, 10].

Due to lattice mismatch, core/shell heterostructures are usually strained, which can have important consequences on their electrical and optical properties. For instance, strain may affect the lifetimes of spin qubits [11, 12] and has already been used to tune photons from separate QDs into resonance [13, 14]. The reason for such effects lies in the strain dependence of the Hamiltonian of the electronic states [15]. For the core/shell NWs of Refs. [2–5], a strong and strain-based correlation between the shell thickness (or composition) and the wavelength of the emitted photons has already been measured. In addition, the shell-induced strain may lift quasidegeneracies in the spectrum of NWs and NW QDs [16]. Considering these and other possibly relevant consequences, knowledge of the strain distribution in core/shell NWs is crucial. Exact calculations of the lattice displacement, however, typically require numerics [5, 17, 18]. Analytical results are rare and require simplifying assumptions that may or may not be justified, depending on the choice of materials and on the effects that one is interested in. The model of Ref. [18], for instance, assumes purely uniaxial strain along the NW axis. The results of Refs. [19, 20] apply when the core and shell materials are isotropic and have the same elastic properties. To our knowledge, the most general formulas provided so far are those of Ref. [21], assuming isotropic media and requiring only Poisson’s ratio to be the same in core and shell.

A particularly attractive feature of NWs is their potential to host electrically controllable spin qubits [22]. While bare InAs and InSb NWs have been the workhorse systems [23–27], spin qubits may also be implemented in core/shell NWs such as Ge/Si [28–31], for which a large degree of external control has been predicted [32]. As electrons and holes interact with lattice vibrations, understanding of the quantum mechanical behavior of the system requires knowledge of the phonon bath. For instance, it is well-known that phonons can be dominant decay channels for spin qubits [33–38]. The shell of core/shell NWs not only induces static strain, it also affects the phonon modes. While phonons in homogeneous NWs have been discussed in detail in the literature [39, 40], we are not aware of analytical results for NWs with a finite shell.

In this work, we derive algebraic expressions for the static strain and the low-energetic phonon modes in core/shell NWs. Assuming isotropic materials and a force-free wire surface, we allow for arbitrary core and shell radii, independent elastic properties in core and shell, and take all components of the stress and strain tensors into account. Our results for the phonons illustrate that the shell notably affects the phonon-based displacement fields and, among other things, that the dispersion relations of the longitudinal, torsional, and flexural modes change differently with the shell thickness. In particular, new terms arise in the corresponding strain and stress tensors that are absent in homogeneous NWs. We illustrate our results via the example of Ge/Si NWs, given the fact that the coherence of their interfaces has already been demonstrated experimentally [41, 42]. The derived formulas for the static strain can be considered a further extension of those listed in Ref. [21] and are consistent with experiments [2–5, 18, 41, 42] and numerical simulations [3, 5, 17, 18]. We calculate the effects of the static strain on the low-energy hole spectrum of Ge/Si NWs, complementing the analysis of Ref. [16].

The chapter is organized as follows. In Sec. 5.2 we introduce the notation and recall relevant relations from linear elasticity theory. The results for the static strain are derived in Sec. 5.3, where we also

investigate the effects of strain on the spectrum of Ge/Si NWs. Having summarized the low-energetic phonon modes in homogeneous NWs in Sec. 5.4, we extend these results to the case of core/shell NWs in Sec. 5.5, followed by concluding remarks in Sec. 5.6. Appendix D contains useful relations and further details of the calculations. In particular, providing also a comparison to the case of bulk material, we discuss the displacement operator and the normalization condition for phonons in core/shell and core/multishell NWs, as quantization is mandatory for quantum mechanical analyses.

## 5.2 Linear Elasticity Theory

In this section we recall relevant relations from linear elasticity theory and introduce the notation used throughout this chapter. The information summarized here is carefully explained in Refs. [39, 40], and we refer to these for further details.

In a bulk semiconductor without additional forces, the atoms form a periodic and very well structured lattice, characterized by the lattice constant  $a$ . The displacement of an atom  $X$  from its original position  $\mathbf{r}_X$  is described by the displacement vector  $\mathbf{u}(\mathbf{r}_X)$ . It may be caused by externally applied forces, or, as in the case of core/shell NWs, by an interface between materials with different lattice constants. In the continuum model, the displacement field  $\mathbf{u}(\mathbf{r})$  is directly related to the strain tensor elements  $\epsilon_{ij}$  via

$$\epsilon_{ij} = \frac{1}{2} \left( \frac{\partial u_i}{\partial x_j} + \frac{\partial u_j}{\partial x_i} \right), \quad (5.1)$$

leading to strain-induced effects on the conduction and valence band states [15]. The position is denoted here by  $\mathbf{r} = \sum_i x_i \mathbf{e}_i$ , where the three orthonormal basis vectors  $\mathbf{e}_i$  are the unit vectors along the orthogonal axes  $i$ . Important quantities besides the strain are the stress tensor elements  $\sigma_{ij}$ . These are of relevance as  $\sigma_{ij} dA$  corresponds to the force along  $\mathbf{e}_i$  experienced by an area  $dA$  normal to  $\mathbf{e}_j$ . We note that  $\epsilon_{ij} = \epsilon_{ji}$  and  $\sigma_{ij} = \sigma_{ji}$ , which implies that the strain and stress tensors are fully described by three diagonal and three off-diagonal elements each.

For semiconductors with diamond (Ge, Si, ...) or zinc blende (GaAs, InAs, ...) structure, the relation between stress and strain is given by

$$\begin{pmatrix} \sigma_{11} \\ \sigma_{22} \\ \sigma_{33} \\ \sigma_{23} \\ \sigma_{13} \\ \sigma_{12} \end{pmatrix} = \begin{pmatrix} c_{11} & c_{12} & c_{12} & 0 & 0 & 0 \\ c_{12} & c_{11} & c_{12} & 0 & 0 & 0 \\ c_{12} & c_{12} & c_{11} & 0 & 0 & 0 \\ 0 & 0 & 0 & c_{44} & 0 & 0 \\ 0 & 0 & 0 & 0 & c_{44} & 0 \\ 0 & 0 & 0 & 0 & 0 & c_{44} \end{pmatrix} \begin{pmatrix} \epsilon_{11} \\ \epsilon_{22} \\ \epsilon_{33} \\ 2\epsilon_{23} \\ 2\epsilon_{13} \\ 2\epsilon_{12} \end{pmatrix}, \quad (5.2)$$

where the  $c_{ij}$  are the elastic stiffness coefficients and  $\{1, 2, 3\}$  are the main crystallographic axes. Calculations with the exact stiffness matrix often require elaborate numerical analyses, and it is therefore common to replace the stress-strain relations by those of an isotropic material. This simplification usually results in good approximations when compared with the precise simulations [39, 40]. The elastic properties of such a material are fully described by the two Lamé parameters  $\lambda$  and  $\mu$ , which are found from Young's modulus  $Y$  (often denoted by  $E$ ) and Poisson's ratio  $\nu$  through

$$\lambda = \frac{Y\nu}{(1+\nu)(1-2\nu)}, \quad (5.3)$$

$$\mu = \frac{Y}{2(1+\nu)}. \quad (5.4)$$

Considering the limit of isotropic media, we thus replace the stiffness coefficients of Eq. (5.2) by  $c_{12} = \lambda$ ,

$c_{44} = \mu$ , and  $c_{11} = 2\mu + \lambda$ . The relations between stress and strain are now the same for arbitrarily rotated coordinate systems. Hence, referring to NWs, we obtain

$$\begin{pmatrix} \sigma_{rr} \\ \sigma_{\phi\phi} \\ \sigma_{zz} \\ \sigma_{\phi z} \\ \sigma_{rz} \\ \sigma_{r\phi} \end{pmatrix} = \begin{pmatrix} 2\mu + \lambda & \lambda & \lambda & 0 & 0 & 0 \\ \lambda & 2\mu + \lambda & \lambda & 0 & 0 & 0 \\ \lambda & \lambda & 2\mu + \lambda & 0 & 0 & 0 \\ 0 & 0 & 0 & \mu & 0 & 0 \\ 0 & 0 & 0 & 0 & \mu & 0 \\ 0 & 0 & 0 & 0 & 0 & \mu \end{pmatrix} \begin{pmatrix} \epsilon_{rr} \\ \epsilon_{\phi\phi} \\ \epsilon_{zz} \\ 2\epsilon_{\phi z} \\ 2\epsilon_{rz} \\ 2\epsilon_{r\phi} \end{pmatrix}, \quad (5.5)$$

where

$$\mathbf{e}_r = \mathbf{e}_x \cos \phi + \mathbf{e}_y \sin \phi, \quad (5.6)$$

$$\mathbf{e}_\phi = -\mathbf{e}_x \sin \phi + \mathbf{e}_y \cos \phi, \quad (5.7)$$

and  $\mathbf{e}_z = \mathbf{e}_x \times \mathbf{e}_y = \mathbf{e}_r \times \mathbf{e}_\phi$  are the orthonormal basis vectors for cylindrical coordinates  $r$ ,  $\phi$ , and  $z$ . The vector  $\mathbf{e}_z$  is oriented along the symmetry axis of the NW, while  $\mathbf{e}_r$  and  $\mathbf{e}_\phi$  point in the radial and azimuthal direction, respectively. From

$$\mathbf{r} = r\mathbf{e}_r + z\mathbf{e}_z = x\mathbf{e}_x + y\mathbf{e}_y + z\mathbf{e}_z \quad (5.8)$$

it is evident that the Cartesian coordinates  $x$  and  $y$  are related to  $r$  and  $\phi$  through  $x = r \cos \phi$  and  $y = r \sin \phi$  (the  $z$  axis is the same in both coordinate systems). We wish to emphasize that we use

$$r = \sqrt{x^2 + y^2} \quad (5.9)$$

throughout this chapter in order to avoid confusion with the density  $\rho$ , and so  $r \neq |\mathbf{r}|$ . Detailed information about the stress and strain tensor elements in Cartesian and cylindrical coordinates is provided in Appendixes D.2.2 and D.2.3. Finally, we note that Eq. (5.5) is independent of the growth direction of the NW because of the isotropic approximation.

### 5.3 Static Strain in Core/Shell Nanowires

An interface between two materials of mismatched lattice constants induces a static strain field. In core/shell NWs, such an interface is present at the core radius  $R_c$ . When the lattice constants in core ( $a_c$ ) and shell ( $a_s$ ) are different, the system will tend to match these for reasons of energy minimization. For instance,  $a_c = 5.66 \text{ \AA}$  and  $a_s = 5.43 \text{ \AA}$  for Ge/Si core/shell NWs [43, 44], and so the shell tends to compress the core lattice, strongly affecting the properties of the confined hole gas [15, 16]. Below, we analyze the strain in core/shell NWs and derive algebraic expressions for both the inner and outer part of the heterostructure. The resulting static strain is found by assuming a coherent interface between the two materials, i.e., pseudomorphic growth. We consider the limit of an infinite wire, which applies well away from the ends of the NW [17] when the length  $L$  is much larger than the shell radius  $R_s$  ( $L \gg R_s$ ). Our approach is similar to those used previously [17–21].

### 5.3.1 Boundary Conditions

When the strain changes slowly on the scale of the lattice spacing, the displacement field leads to the distorted lattice vectors [17]

$$\mathbf{l}_{c,s}(\mathbf{r}, \mathbf{n}) = \sum_i \mathbf{e}_i \sum_j \left( \delta_{ij} + \frac{\partial u_i^{c,s}(\mathbf{r})}{\partial x_j} \right) n_j a_{c,s} \quad (5.10)$$

when viewed from an atom at position  $\mathbf{r} + \mathbf{u}^{c,s}(\mathbf{r})$  in the core ( $c$ ) or shell ( $s$ ), respectively, where  $\mathbf{e}_i$  are the orthonormal basis vectors of the lattice,  $\mathbf{n}$  is a vector with integer components  $n_i$ , and  $\delta_{ij}$  is the Kronecker delta. Pseudomorphic strain requires the components of the distorted lattice vectors in core and shell that are parallel to the interface to match at the core-shell transition. Thus  $\mathbf{t} \cdot \mathbf{l}_c = \mathbf{t} \cdot \mathbf{l}_s$ , where  $\mathbf{t}$  stands for an arbitrary tangent to the core-shell interface. Using cylindrical coordinates, the two orthogonal directions  $\mathbf{e}_\phi$  and  $\mathbf{e}_z$  are the basis vectors for any  $\mathbf{t}$ , which results in the boundary conditions  $\mathbf{e}_\phi \cdot \mathbf{l}_c = \mathbf{e}_\phi \cdot \mathbf{l}_s$  and  $\mathbf{e}_z \cdot \mathbf{l}_c = \mathbf{e}_z \cdot \mathbf{l}_s$  at radius  $R_c$ . Furthermore, the core-shell transition needs to be spatially matched in the radial direction, i.e., there should be no unrealistic gaps or overlaps between the two materials at the interface.

In order to ensure pseudomorphic strain, we start from an initial configuration where the shell is unstrained and the core is highly strained, such that the lattice constant of the core matches the one in the shell [17, 45]. Of course, this initial arrangement is unstable, and so the system will relax into a stable and energetically favored configuration. Considering the continuum limit, the requirements for a coherent interface at  $r \simeq R_c$  can now be summarized in a simple form [46],

$$\tilde{\mathbf{u}}^c(R_c, \phi, z) = \tilde{\mathbf{u}}^s(R_c, \phi, z), \quad (5.11)$$

where the  $\tilde{\mathbf{u}}^{c,s}$ , in contrast to the  $\mathbf{u}^{c,s}$  of Eq. (5.10), denote the displacement from the initially matched configuration. That is,

$$\mathbf{u}^c(\mathbf{r}) = \tilde{\mathbf{u}}^c(a_s \mathbf{r} / a_c) + \frac{a_s - a_c}{a_c} \mathbf{r} \quad (5.12)$$

and  $\mathbf{u}^s(\mathbf{r}) = \tilde{\mathbf{u}}^s(\mathbf{r})$ . As illustrated in Eq. (5.12), the displacement field  $\mathbf{u}^c(\mathbf{r})$  in the core can be described by a sum of two parts. When the lattice constant changes from  $a_c$  to  $a_s$ , the term  $(a_s/a_c - 1)\mathbf{r}$  shifts an atom that is originally located at  $\mathbf{r}$  to its new position  $a_s \mathbf{r} / a_c$ . Additional displacement from this new position is then accounted for by  $\tilde{\mathbf{u}}^c(a_s \mathbf{r} / a_c)$ . Consequently, the strain tensor elements  $\epsilon_{ij}^{c,s}(\mathbf{r})$  in the core and shell read

$$\epsilon_{ij}^{c,s}(\mathbf{r}) = \frac{a_s}{2a_{c,s}} \left[ \frac{\partial \tilde{u}_i^{c,s}(\mathbf{r}')}{\partial x'_j} + \frac{\partial \tilde{u}_j^{c,s}(\mathbf{r}')}{\partial x'_i} \right]_{\mathbf{r}' = a_s \mathbf{r} / a_{c,s}} + \frac{a_s - a_{c,s}}{a_{c,s}} \delta_{ij}, \quad (5.13)$$

where  $\mathbf{r}' = \sum_i x'_i \mathbf{e}_i$ . The resulting strain tensor  $\epsilon^{c,s}(\mathbf{r})$  is linearly related to the stress tensor  $\sigma^{c,s}(\mathbf{r})$  via the Lamé constants [Eq. (5.5)]. As additional boundary conditions, the stress must be continuous at the interface [46] and we assume that the shell surface is free of forces,

$$\sigma^c(R_c, \phi, z) \mathbf{e}_r = \sigma^s(R_c, \phi, z) \mathbf{e}_r, \quad (5.14)$$

$$\sigma^s(R_s, \phi, z) \mathbf{e}_r = 0. \quad (5.15)$$

Next, using the above-mentioned boundary conditions, we derive algebraic expressions for the static strain in core/shell NWs.

### 5.3.2 Analytical Results

From symmetry considerations, the displacement in both core and shell must be of the form

$$\tilde{\mathbf{u}}^p = \tilde{u}_r^p(r)\mathbf{e}_r + \eta_z^p(r)z\mathbf{e}_z, \quad (5.16)$$

where we introduced  $p \in \{c, s\}$  for convenience. For the displacement field to be static, the differential equations

$$\sum_j \frac{\partial \sigma_{ij}^p}{\partial x_j} = 0 \quad (5.17)$$

need to be solved in the absence of body forces [40], and in doing so we find

$$\tilde{u}_r^p = \alpha_p r + \frac{\beta_p}{r} - \frac{\delta_p(\lambda_p + \mu_p)}{2(\lambda_p + 2\mu_p)} r \ln r, \quad (5.18)$$

$$\eta_z^p = \gamma_p + \delta_p \ln r, \quad (5.19)$$

where  $\lambda_{c,s}$  and  $\mu_{c,s}$  are the Lamé parameters in the core and shell, respectively. The coefficients  $\alpha_{c,s}$  to  $\delta_{c,s}$  are to be determined from the boundary conditions. Since the displacement must be finite in the center, we first conclude that  $\beta_c = 0 = \delta_c$ . Second, also  $\delta_s = 0$  because  $\sigma_{rz}^s \propto \delta_s z/r$  must vanish at the surface [Eq. (5.15)], and so the  $\eta_z^{c,s} = \gamma_{c,s}$  are constants. Consequently, one obtains

$$\gamma_s = \epsilon_{zz}^s = \frac{a_e - a_s}{a_s}, \quad (5.20)$$

with  $a_e$  as the resulting (equilibrium) lattice constant in the  $z$  direction. From the boundary conditions listed in Eqs. (5.11), (5.14), and (5.15), we can express all nonzero coefficients

$$\gamma_c = \gamma_s, \quad (5.21)$$

$$\beta_s = (\alpha_c - \alpha_s)R_c^2, \quad (5.22)$$

and  $\alpha_{c,s}$  in terms of  $a_e$  only. The latter can finally be found by minimizing the elastic energy of the system.

Using Eq. (5.13), the above-mentioned results for  $\tilde{\mathbf{u}}^{c,s}$ , and the equations of Appendix D.2.3 for the strain tensor in cylindrical coordinates, one finds

$$\epsilon_{rr}^c = \epsilon_{\phi\phi}^c = \frac{a_s}{a_c} \alpha_c + \epsilon_0, \quad (5.23)$$

$$\epsilon_{zz}^c = \frac{a_s}{a_c} \gamma_c + \epsilon_0 = \frac{a_e - a_c}{a_c} \quad (5.24)$$

in the core, and

$$\epsilon_{rr}^s = \alpha_s - \frac{\beta_s}{r^2}, \quad (5.25)$$

$$\epsilon_{\phi\phi}^s = \alpha_s + \frac{\beta_s}{r^2}, \quad (5.26)$$

$$\epsilon_{zz}^s = \gamma_s = \frac{a_e - a_s}{a_s} \quad (5.27)$$

in the shell, with  $0 = \epsilon_{r\phi}^{c,s} = \epsilon_{rz}^{c,s} = \epsilon_{\phi z}^{c,s}$ . The parameter

$$\epsilon_0 = \frac{a_s - a_c}{a_c} \quad (5.28)$$

introduced in Eqs. (5.23) and (5.24) is the relative mismatch of the lattice constants. Remarkably, Eqs. (5.23) and (5.24) imply that the stress and strain are constant within the core, which is consistent with simulations [5, 17, 18]. Furthermore, we note that  $\epsilon_{rr}^c = \epsilon_{\phi\phi}^c = \epsilon_{xx}^c = \epsilon_{yy}^c$ . Below, we outline the calculation of  $a_e$  and provide our final results.

The elastic energy density in an isotropic solid is [40]

$$F = \frac{1}{2} \sum_{i,j} \sigma_{ij} \epsilon_{ij} = \frac{\lambda}{2} [\text{Tr}(\epsilon)]^2 + \mu \sum_{i,j} \epsilon_{ij}^2, \quad (5.29)$$

where  $\text{Tr}(\epsilon) = \sum_i \epsilon_{ii}$  is the trace of the strain tensor, and

$$U = \int_V d^3\mathbf{r} F(\mathbf{r}) \quad (5.30)$$

is the elastic energy of an object with volume  $V$ . For the static strain discussed in this section, the elastic energy density  $F_c$  in the core is constant and  $F_s$  in the shell depends solely on the coordinate  $r$ . The elastic energy of the NW can therefore be calculated via

$$U = 2\pi L \left( \frac{R_c^2 F_c}{2} + \int_{R_c}^{R_s} dr r F_s(r) \right). \quad (5.31)$$

By imposing the condition  $\partial U / \partial a_e = 0$  in order to find the energetically favored configuration, we obtain algebraic expressions for  $a_e$  and, thus, for all previously discussed quantities. As expected, these are not affected by the length of the wire, since  $U \propto L$  for the regime  $L \gg R_s$  considered here. Moreover, the coefficients  $\alpha_{c,s}$  and  $\gamma_{c,s}$  do not depend on the absolute values of  $R_c$  and  $R_s$ . Instead, they depend on the relative shell thickness

$$\gamma = \frac{R_s - R_c}{R_c}. \quad (5.32)$$

More precisely, it is possible to write the dependence of  $\alpha_{c,s}$  and  $\gamma_{c,s}$  on the radii in terms of

$$\tilde{\gamma} = \gamma^2 + 2\gamma = \frac{R_s^2 - R_c^2}{R_c^2} \quad (5.33)$$

only, which is the ratio between the shell and core area in the cross section. Similarly, the coefficients  $\alpha_{c,s}$ ,  $\beta_s$ , and  $\gamma_{c,s}$  do not depend on the absolute values of the lattice constants  $a_c$  and  $a_s$ , but on the relative lattice mismatch  $\epsilon_0$  [Eq. (5.28)]. We note that  $|\epsilon_0| \ll 1$ , which is important for the linear elasticity theory of this work to hold.

The full results are rather lengthy. Nevertheless, they can be very well approximated through an expansion in the small parameter  $\epsilon_0$ . Neglecting corrections of order  $\epsilon_0^2$  and rewriting the results in a convenient form, we obtain

$$\alpha_s = -\frac{\epsilon_0 \xi_c}{2D_{\text{str}}} [\mu_c(2\mu_s - \lambda_s) + (2\mu_s^2 - \lambda_s \mu_c) \tilde{\gamma}], \quad (5.34)$$

$$\beta_s = -\frac{R_c^2 \epsilon_0 \xi_c \xi_s}{2D_{\text{str}}} [\mu_c + (\mu_c + \mu_s) \tilde{\gamma} + \mu_s \tilde{\gamma}^2], \quad (5.35)$$

$$\gamma_s = -\frac{\epsilon_0 \xi_c}{D_{\text{str}}} [\mu_c(2\mu_s + \lambda_s) + (\lambda_s \mu_c + \mu_s \mu_c + \mu_s^2) \tilde{\gamma}], \quad (5.36)$$

where we defined

$$\xi_p = 2\mu_p + 3\lambda_p. \quad (5.37)$$

The denominator is

$$D_{\text{str}} = \mu_c \xi_c (2\mu_s + \lambda_s) + [\xi_c (\lambda_s \mu_c + \mu_s \mu_c + \mu_s^2) + \xi_s \mu_s (2\mu_c + \lambda_c)] \tilde{\gamma} + \mu_s \xi_s (\lambda_c + \mu_c + \mu_s) \tilde{\gamma}^2. \quad (5.38)$$

Inserting  $\alpha_c = \alpha_s + \beta_s/R_c^2$ ,  $\gamma_c = \gamma_s$ , and the above-listed expressions into Eqs. (5.23) and (5.24), and neglecting again terms of order  $\epsilon_0^2$ , one finds

$$\epsilon_{\perp}^c = \epsilon_{rr}^c = \epsilon_{\phi\phi}^c = \frac{\epsilon_0 \xi_s \mu_s}{2D_{\text{str}}} [(2\mu_c - \lambda_c) \tilde{\gamma} + (2\mu_s - \lambda_c) \tilde{\gamma}^2], \quad (5.39)$$

$$\epsilon_{zz}^c = \frac{\epsilon_0 \xi_s \mu_s}{D_{\text{str}}} [(2\mu_c + \lambda_c) \tilde{\gamma} + (\lambda_c + \mu_c + \mu_s) \tilde{\gamma}^2] \quad (5.40)$$

for the strain in the core.

The expressions derived in this work are more general than those provided previously [18–21] and may be interpreted as a further extension of those in Ref. [21]. Indeed, by writing the Lamé parameters  $\lambda_{c,s}$  and  $\mu_{c,s}$  in terms of Young's modulus  $Y_{c,s}$  and Poisson's ratio  $\nu_{c,s}$  for core and shell [Eqs. (5.3) and (5.4)], we find that our results are exactly identical to those of Ref. [21] for the case  $\nu_c = \nu_s$  assumed therein. From the ratio of Eqs. (5.39) and (5.40),

$$\frac{\epsilon_{\perp}^c}{\epsilon_{zz}^c} = \frac{2\mu_c - \lambda_c + (2\mu_s - \lambda_c) \tilde{\gamma}}{4\mu_c + 2\lambda_c + 2(\lambda_c + \mu_c + \mu_s) \tilde{\gamma}}, \quad (5.41)$$

we find that typically  $|\epsilon_{zz}^c| > |\epsilon_{\perp}^c|$ , in agreement with numerical results [3, 5, 17, 18]. Our formulas also feature the correct limits. For instance, we obtain  $a_e \rightarrow a_c$  for  $\gamma \rightarrow 0$  as expected, and so the strain in the core vanishes for a negligibly thin shell. In the limit of an infinite shell ( $\gamma \rightarrow \infty$ ), our formulas yield  $a_e \rightarrow a_s$ ,  $\epsilon_{zz}^c \rightarrow \epsilon_0$ , and

$$\lim_{\gamma \rightarrow \infty} \epsilon_{\perp}^c = \frac{\epsilon_0 (2\mu_s - \lambda_c)}{2(\lambda_c + \mu_c + \mu_s)} + \mathcal{O}(\epsilon_0^2), \quad (5.42)$$

which corresponds exactly to the previously studied case of a wire embedded in an infinite matrix [47]. When switching to Cartesian coordinates, we obtain  $\epsilon_{xy}^s = -\beta_s \sin(2\phi)/r^2$ , which seems consistent with numerics [17]. As pointed out in Ref. [17], where core/shell NWs with anisotropic materials have been investigated, also other off-diagonal strain tensor components may be nonzero in reality. However, these were found to be very small, particularly in the core.

### 5.3.3 Results for Ge/Si Core/Shell Nanowires

We conclude our discussion of the static stress and strain fields by applying our results to the example of Ge/Si core/shell NWs, demonstrating that the strain can have major effects on the electronic properties of a system. As illustrated in this example, the strain is usually not negligible, and so our formulas derived for both core and shell may prove very useful for a wide range of material combinations.

Ge/Si core/shell NWs have attracted attention because they host strongly confined hole states inside their cores [9]. Thus, we focus here on the static strain in the core and discuss its effects on the holes in more detail. The lattice mismatch for Ge/Si core/shell NWs is  $\epsilon_0 = -0.040$  [43, 44], and the Lamé constants, listed in units of  $10^9$  N/m<sup>2</sup>, are  $\lambda_c = 39.8$ ,  $\mu_c = 55.6$ ,  $\lambda_s = 54.5$ , and  $\mu_s = 67.5$  (see also Appendix D.1) [39, 44]. In Fig. 5.1 (top), the strain tensor elements  $\epsilon_{\perp}^c$  and  $\epsilon_{zz}^c$  of Eqs. (5.39) and (5.40) are plotted as a function of  $\gamma$ . These are negative over the entire range of shell thicknesses, and so the core material is compressed, as expected from  $a_c > a_s$ . The dependence of the strain on  $\gamma$  is consistent with simulations and experiments [18], and we note that  $|\epsilon_{zz}^c| > |\epsilon_{\perp}^c|$  for any  $\gamma$ .

The effects of strain on hole states in the topmost valence band of Ge are described by the Bir-Pikus Hamiltonian [15]. Using the spherical approximation  $d = \sqrt{3}b$ , which applies well to Ge ( $b \simeq -2.5$  eV,



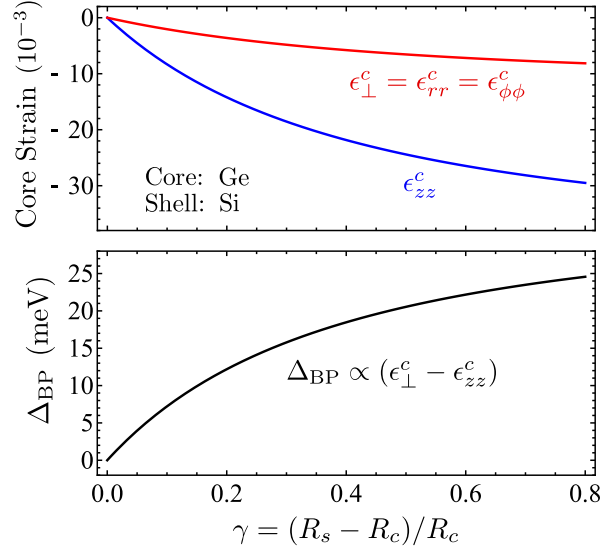


Figure 5.1. Static core strain and its effect on the hole spectrum of Ge/Si core/shell NWs as a function of the relative shell thickness  $\gamma$ . In the top figure, the nonzero components  $\epsilon_{\perp}^c$  and  $\epsilon_{zz}^c$  of Eqs. (5.39) and (5.40) are plotted for the parameters in the text. The resulting splitting  $\Delta_{BP}$  [Eq. (5.47), bottom figure] can be as large as  $\sim 30$  meV and strongly affects the low-energetic hole states, as explained in detail in Chapter 2.

$d \simeq -5.0$  eV [15]), and neglecting global shifts in energy, the Bir-Pikus Hamiltonian for holes reads

$$H_{BP} = b \left[ \sum_i \epsilon_{ii} J_i^2 + 2(\epsilon_{xy} \{J_x, J_y\} + \text{c.p.}) \right]. \quad (5.43)$$

Here  $b$  and  $d$  are the deformation potentials,  $J_i$  are the components of the effective spin 3/2 along the axes  $i$ , “c.p.” stands for cyclic permutations, and  $\{A, B\} = (AB + BA)/2$ . We note that the axes  $x$ ,  $y$ , and  $z$  need not coincide with the main crystallographic axes due to the spherical approximation. Our results for the static strain in core/shell NWs reveal that the relations  $\epsilon_{xx}^c = \epsilon_{yy}^c = \epsilon_{\perp}^c$  and  $0 = \epsilon_{xy}^c = \epsilon_{xz}^c = \epsilon_{yz}^c$  are fulfilled in the core. Exploiting these properties and the equality  $J_x^2 + J_y^2 = 15/4 - J_z^2$ , the Bir-Pikus Hamiltonian for the core is of the simple form

$$H_{BP}^c = b(\epsilon_{zz}^c - \epsilon_{\perp}^c) J_z^2, \quad (5.44)$$

where global shifts in energy have again been omitted. As discussed in Ref. [16], this Hamiltonian has important effects on the hole spectrum in Ge/Si core/shell NWs, because it determines the splitting  $\Delta$  between the ground states  $|g_{\pm}\rangle$  and the first excited states  $|e_{\pm}\rangle$  at wave number  $k_z = 0$  along the NW. The subscripts “+” and “-” refer to the spin states, and we note that the total angular momentum along the wire is  $F_z = \mp 1/2$  for  $|g_{\pm}\rangle$ , whereas  $F_z = \pm 1/2$  for  $|e_{\pm}\rangle$ . The splitting  $\Delta = \Delta_{LK} + \Delta_{BP}$  comprises a strain-independent term  $\Delta_{LK} \propto R_c^{-2}$ , which arises from the radial confinement and the kinetic energy (Luttinger-Kohn Hamiltonian), and the strain-induced term

$$\Delta_{BP} = \langle e_{\pm} | H_{BP}^c | e_{\pm} \rangle - \langle g_{\pm} | H_{BP}^c | g_{\pm} \rangle. \quad (5.45)$$

Defining

$$\Lambda = \langle e_{\pm} | J_z^2 | e_{\pm} \rangle - \langle g_{\pm} | J_z^2 | g_{\pm} \rangle, \quad (5.46)$$

one finally obtains

$$\Delta_{BP} = b\Lambda(\epsilon_{zz}^c - \epsilon_{\perp}^c). \quad (5.47)$$

The parameter  $\Lambda$  turns out to be independent of  $R_c$ , and using  $|g_{\pm}\rangle$  and  $|e_{\pm}\rangle$  of Ref. [16] we find  $\Lambda = 0.46$  for Ge. That is,  $\Delta_{\text{BP}} = \Delta_{\text{BP}}(\gamma)$  is determined by  $\epsilon_{zz}^c - \epsilon_{\perp}^c$  and depends only on the relative shell thickness.

Figure 5.1 (bottom) shows the dependence of  $\Delta_{\text{BP}}$  on  $\gamma$  for Ge/Si core/shell NWs. Remarkably,  $\Delta_{\text{BP}}$  can be as large as 30 meV and exceeds 10 meV at relatively thin shells ( $\gamma \gtrsim 0.15$ ) already. For comparison, one finds  $\Delta_{\text{LK}} \simeq 3.0\text{--}0.75$  meV for typical core radii  $R_c \simeq 5\text{--}10$  nm. Therefore, the splitting  $\Delta$  is mostly determined by  $\Delta_{\text{BP}}$ , i.e., by the relative shell thickness. The combination of a small  $\Delta_{\text{LK}}$  and  $0 \leq \Delta_{\text{BP}}(\gamma) \lesssim 30$  meV is of great importance not only for the spectrum in the wire, but also for, e.g., the properties of hole-spin qubits in NW QDs [12, 16, 27, 32].

## 5.4 Phonons in Homogeneous Nanowires

In this section, we recall the calculation of lattice vibrations in homogeneous NWs [39, 40, 48, 49] and provide the displacement vectors and the core strain for the phonon modes of lowest energy. The information forms a basis for Sec. 5.5, where the analysis is extended to the case of core/shell NWs.

### 5.4.1 Equation of Motion, Ansatz, and Boundary Conditions

For an isotropic material with density  $\rho$  and Lamé parameters  $\lambda$  and  $\mu$ , the equations of motion

$$\rho \ddot{u}_i = \sum_j \frac{\partial \sigma_{ij}}{\partial x_j} \quad (5.48)$$

can be summarized in the form

$$\rho \ddot{\mathbf{u}} = (\lambda + \mu) \nabla (\nabla \cdot \mathbf{u}) + \mu \nabla^2 \mathbf{u}, \quad (5.49)$$

where

$$\nabla = \mathbf{e}_x \partial_x + \mathbf{e}_y \partial_y + \mathbf{e}_z \partial_z = \mathbf{e}_r \partial_r + \mathbf{e}_{\phi} \frac{1}{r} \partial_{\phi} + \mathbf{e}_z \partial_z \quad (5.50)$$

is the Nabla operator and

$$\nabla^2 = \partial_x^2 + \partial_y^2 + \partial_z^2 = \partial_r^2 + \frac{1}{r} \partial_r + \frac{1}{r^2} \partial_{\phi}^2 + \partial_z^2 \quad (5.51)$$

is the Laplacian. In order to find the eigenmodes for the cylindrical NW, the displacement vector may be written in terms of three scalar functions  $\Phi_{\eta}$ ,  $\eta \in \{0, 1, 2\}$ , via [46, 48, 50]

$$\mathbf{u} = \nabla \Phi_0 + \nabla \times \mathbf{e}_z \Phi_1 + \nabla \times (\nabla \times \mathbf{e}_z \Phi_2). \quad (5.52)$$

Inserting Eq. (5.52) into Eq. (5.49) and exploiting identities such as  $\nabla \cdot (\nabla \times \mathbf{A}) = 0$ , the resulting equation of motion reads

$$0 = \nabla \left( \rho \ddot{\Phi}_0 - (2\mu + \lambda) \nabla^2 \Phi_0 \right) + \nabla \times \mathbf{e}_z \left( \rho \ddot{\Phi}_1 - \mu \nabla^2 \Phi_1 \right) + \nabla \times \left[ \nabla \times \mathbf{e}_z \left( \rho \ddot{\Phi}_2 - \mu \nabla^2 \Phi_2 \right) \right]. \quad (5.53)$$

This equation is therefore satisfied when the scalar functions obey the wave equations

$$\rho \ddot{\Phi}_{\eta} = [\mu + \delta_{\eta,0}(\mu + \lambda)] \nabla^2 \Phi_{\eta}, \quad (5.54)$$

where  $\delta_{\eta,0}$  is a Kronecker delta. While these wave equations are sufficient criteria for the equation of motion to be satisfied, we note that some special solutions of Eq. (5.49) can be found that do not obey Eq. (5.54). An example is provided below for the torsional mode. However, we also illustrate that this

solution can be interpreted as the limit of a more general solution obtained with an ansatz that relies on the above-mentioned wave equations.

Due to the cylindrical symmetry and the translational invariance along the NW axis  $z$  ( $L \gg$  radius), the  $\Phi_\eta$  can be written in the form

$$\Phi_\eta = f_\eta(r) e^{i(q_z z + n\phi - \omega\tau)}, \quad (5.55)$$

where  $q_z$  is the wave number along the wire,  $n$  is an integer,  $\omega$  is the angular frequency, and  $\tau$  is the time. Insertion of Eq. (5.55) into Eq. (5.54) results in the differential equation

$$\left( \partial_r^2 + \frac{1}{r} \partial_r - \frac{n^2}{r^2} - q_z^2 + \frac{\rho\omega^2}{\mu + \delta_{\eta,0}(\mu + \lambda)} \right) f_\eta(r) = 0 \quad (5.56)$$

for the function  $f_\eta(r)$ . With  $J_n$  and  $Y_n$  as Bessel functions of the first and second kind, respectively, and with  $\chi_{\eta,J}$  and  $\chi_{\eta,Y}$  as (dimensionful) complex coefficients, the general solution of this differential equation is

$$f_\eta(r) = \chi_{\eta,J} J_n(\kappa_{\eta,J} r) + \chi_{\eta,Y} Y_n(\kappa_{\eta,Y} r), \quad (5.57)$$

where

$$\kappa_{\eta,J}^2 = \kappa_{\eta,Y}^2 = \frac{\rho\omega^2}{\mu + \delta_{\eta,0}(\mu + \lambda)} - q_z^2. \quad (5.58)$$

We mention that  $\kappa_{\eta,J}$  and  $\kappa_{\eta,Y}$  need not be identical and may be chosen arbitrarily, provided that Eq. (5.58) is satisfied. For homogeneous NWs considered in this section,  $\chi_{\eta,Y} = 0$  because  $Y_n$  diverges in the limit  $r \rightarrow 0$ , and so

$$\Phi_\eta = \chi_{\eta,J} J_n(\kappa_{\eta,J} r) e^{i(q_z z + n\phi - \omega\tau)}. \quad (5.59)$$

For given  $n$  and  $q_z$ , the corresponding eigenfrequencies and coefficients can be determined from the boundary conditions that we discuss below.

In vector notation, with the three components referring to  $\mathbf{e}_r$ ,  $\mathbf{e}_\phi$ , and  $\mathbf{e}_z$ , respectively, Eq. (5.52) reads as

$$\mathbf{u} = \begin{pmatrix} u_r \\ u_\phi \\ u_z \end{pmatrix} = \begin{pmatrix} \partial_r \Phi_0 + \frac{1}{r} \partial_\phi \Phi_1 + \partial_r \partial_z \Phi_2 \\ \frac{1}{r} \partial_\phi \Phi_0 - \partial_r \Phi_1 + \frac{1}{r} \partial_\phi \partial_z \Phi_2 \\ \partial_z \Phi_0 - \left( \partial_r^2 + \frac{1}{r} \partial_r + \frac{1}{r^2} \partial_\phi^2 \right) \Phi_2 \end{pmatrix}. \quad (5.60)$$

From Eq. (5.5) and the equations in Appendix D.2.3, one finds

$$\sigma \mathbf{e}_r = \begin{pmatrix} \sigma_{rr} \\ \sigma_{r\phi} \\ \sigma_{rz} \end{pmatrix} = \begin{pmatrix} (2\mu + \lambda) \partial_r u_r + \lambda \left( \frac{1}{r} u_r + \frac{1}{r} \partial_\phi u_\phi + \partial_z u_z \right) \\ \mu \left( \frac{1}{r} \partial_\phi u_r - \frac{1}{r} u_\phi + \partial_r u_\phi \right) \\ \mu (\partial_z u_r + \partial_r u_z) \end{pmatrix} \quad (5.61)$$

for the stress related to the radial direction. For a homogeneous NW of radius  $R$ , the boundary conditions are

$$\sigma(R, \phi, z) \mathbf{e}_r = 0, \quad (5.62)$$

i.e., the stress tensor elements  $\sigma_{rr}$ ,  $\sigma_{r\phi}$ , and  $\sigma_{rz}$  must vanish at  $r = R$  due to the assumption of a force-free wire surface. Using the ansatz introduced above, these boundary conditions can be written in the form

$$\sum_\eta \chi_{\eta,J} \mathbf{V}_\eta = \sum_\eta \chi_{\eta,J} \begin{pmatrix} V_{\eta,r} \\ V_{\eta,\phi} \\ V_{\eta,z} \end{pmatrix} = 0, \quad (5.63)$$

where  $\mathbf{V}_\eta$  are vectors with components  $V_{\eta,r}$ ,  $V_{\eta,\phi}$ , and  $V_{\eta,z}$ . The boundary conditions can only be met in

a nontrivial fashion (i.e., not all  $\chi_{\eta,J}$  are zero) when the corresponding determinant vanishes,

$$\det[\mathbf{V}_0, \mathbf{V}_1, \mathbf{V}_2] = \det \begin{bmatrix} V_{0,r} & V_{1,r} & V_{2,r} \\ V_{0,\phi} & V_{1,\phi} & V_{2,\phi} \\ V_{0,z} & V_{1,z} & V_{2,z} \end{bmatrix} = 0. \quad (5.64)$$

For given  $n$  and  $q_z$ , the allowed angular frequencies  $\omega$  can be found from this determinantal equation. We note, however, that a root of Eq. (5.64) does not necessarily correspond to a physical solution that describes a phonon mode. The latter can be found for given  $n$ ,  $q_z$ , and  $\omega$  by calculating the coefficients  $\chi_{\eta,J}$  from the set of boundary conditions. One of these coefficients can be chosen arbitrarily and determines the phase and amplitude of the lattice vibration. In a quantum mechanical description, this coefficient is finally obtained from the normalization condition.

There are four types of low-energetic phonon modes in a NW: one torsional ( $t$ ;  $n = 0$ ), one longitudinal ( $l$ ;  $n = 0$ ), and two flexural modes ( $f_{\pm}$ ;  $n = \pm 1$ ). These modes are referred to as gapless, as their angular frequencies  $\omega(q_z)$  and, thus, the phonon energies  $\hbar\omega(q_z)$  converge to zero when  $q_z \rightarrow 0$ . In the following, we summarize the dispersion relation, the displacement field, and the strain tensor elements for each of these modes. We consider the regime of lowest energy, i.e., the regime of small  $q_z$  for which an expansion in  $q_z r$  applies. We note that the investigated phonon modes are acoustic modes, as the atoms of a unit cell move in phase, i.e., in the same direction, in contrast to the out-of-phase movement of optical phonons where the atoms of a unit cell move in opposite directions.

## 5.4.2 Torsional Mode

We start our summary with a special solution. It can easily be verified that the displacement [39]

$$\mathbf{u}_{q_z t} = c_{q_z t} r e^{i(q_z z - \omega_{q_z t} \tau)} \mathbf{e}_{\phi} \quad (5.65)$$

meets the boundary conditions, as  $0 = \sigma_{rr} = \sigma_{r\phi} = \sigma_{rz}$ . The prefactor  $c_{q_z t}$  is a dimensionless complex number and may be chosen arbitrarily. Furthermore, defining angular frequencies as positive, the equation of motion [Eq. (5.49)] is satisfied for

$$\omega_{q_z t} = v_t |q_z| = \sqrt{\frac{\mu}{\rho}} |q_z|. \quad (5.66)$$

Due to the displacement along  $\mathbf{e}_{\phi}$ , this mode is referred to as torsional ( $t$ ), and  $v_t$  is the speed of the corresponding sound wave. From Eq. (5.60), it can be seen that  $\mathbf{u}_{q_z t}$  of Eq. (5.65) is generated via  $0 = \Phi_0 = \Phi_2$  and

$$\Phi_1 = -\frac{c_{q_z t}}{2} r^2 e^{i(q_z z - \omega_{q_z t} \tau)}. \quad (5.67)$$

A special feature of this result compared to the others summarized in this work is that  $\Phi_1$  does not obey the wave equation, Eq. (5.54). Moreover, the presented solution for the torsional mode in homogeneous NWs is exact and does not require an expansion in  $q_z r$ . The only nonzero strain tensor element in cylindrical coordinates is

$$\epsilon_{\phi z} = i \frac{c_{q_z t}}{2} q_z r e^{i(q_z z - \omega_{q_z t} \tau)}, \quad (5.68)$$

and we mention that  $\epsilon_{xz} = -\epsilon_{\phi z} \sin \phi$  and  $\epsilon_{yz} = \epsilon_{\phi z} \cos \phi$  in Cartesian coordinates.

In Sec. 5.5.2, the torsional mode in core/shell NWs is investigated with an ansatz based on Bessel functions, for which Eq. (5.54) is satisfied. It is therefore worth mentioning that the special solution for homogeneous NWs is obtained in the limit of a vanishing shell. We consider  $0 = \Phi_0 = \Phi_2$  and

$$\Phi_1 = \chi_{1,J} J_0(\kappa_{1,J} r) e^{i(q_z z - \omega \tau)} \quad (5.69)$$

as an ansatz, assuming  $\kappa_{1,J} \neq 0$ , i.e.,  $\omega \neq |q_z| \sqrt{\mu/\rho}$ , which may be due to the presence of a shell. The resulting displacement function is

$$\mathbf{u} = \chi_{1,J} \kappa_{1,J} J_1(\kappa_{1,J} r) e^{i(q_z z - \omega \tau)} \mathbf{e}_\phi, \quad (5.70)$$

and we note that  $0 = \sigma_{rr} = \sigma_{rz}$ . The arbitrary coefficient  $\chi_{1,J}$  may be written as  $\chi_{1,J} = 2c_{q_z t} / \kappa_{1,J}^2$ . Considering  $\kappa_{1,J} r$  as a small parameter, expansion yields

$$\mathbf{u} = c_{q_z t} r [1 + \mathcal{O}(\kappa_{1,J}^2 r^2)] e^{i(q_z z - \omega \tau)} \mathbf{e}_\phi \quad (5.71)$$

and

$$\sigma_{r\phi} = -\mu \frac{c_{q_z t}}{4} \kappa_{1,J}^2 r^2 [1 + \mathcal{O}(\kappa_{1,J}^2 r^2)] e^{i(q_z z - \omega \tau)}. \quad (5.72)$$

For  $\omega \rightarrow |q_z| \sqrt{\mu/\rho}$ , i.e.,  $\kappa_{1,J} \rightarrow 0$ , which corresponds to the limit of a vanishing shell, one finds that the boundary condition of a force-free wire surface is fulfilled due to  $\sigma_{r\phi} \rightarrow 0$ . As anticipated, the displacement  $\mathbf{u}$  converges to the solution for homogeneous NWs, Eq. (5.65).

### 5.4.3 Longitudinal Mode

The longitudinal and torsional modes in the NW have no angular dependence,  $n = 0$ . In stark contrast to the torsional mode, however, the longitudinal mode ( $l$ ) does not lead to displacement along  $\mathbf{e}_\phi$ , and so  $u_\phi = 0$ . The boundary condition  $\sigma_{r\phi}(R, \phi, z) = 0$  is therefore fulfilled and one may set  $\chi_{1,J} = 0$  in the ansatz discussed in Sec. 5.4.1. Analogously to Eq. (5.64), the eigenfrequencies  $\omega_{q_z l}$  can be calculated via the determinant of a  $2 \times 2$  matrix that summarizes the remaining boundary conditions. Considering angular frequencies as positive, one finds that the dominant terms of this determinant vanish for [39, 40, 50]

$$\omega_{q_z l} = v_l |q_z| = v_{l,0} |q_z| [1 + \mathcal{O}(q_z^2 R^2)], \quad (5.73)$$

$$v_{l,0} = \sqrt{\frac{Y}{\rho}}, \quad (5.74)$$

where  $v_l$  is the corresponding speed of sound. The properties of the longitudinal and flexural modes can conveniently be written in terms of Young's modulus and Poisson's ratio [see also Eqs. (5.3) and (5.4)]:

$$Y = \frac{\mu(2\mu + 3\lambda)}{\mu + \lambda}, \quad (5.75)$$

$$\nu = \frac{\lambda}{2(\mu + \lambda)}. \quad (5.76)$$

Introducing the dimensionless  $c_{q_z l}$  as an arbitrary complex prefactor, the resulting displacement vector is of the form

$$\mathbf{u}_{q_z l} = c_{q_z l} R \begin{pmatrix} -i\nu q_z r + \mathcal{O}(\delta^3) \\ 0 \\ 1 + \mathcal{O}(\delta^2) \end{pmatrix} e^{i(q_z z - \omega_{q_z l} \tau)}, \quad (5.77)$$

with  $\mathbf{e}_r$ ,  $\mathbf{e}_\phi$ , and  $\mathbf{e}_z$  as the basis vectors. Here and in the remainder of the section,  $\mathcal{O}(\delta^m)$  refers to higher-order terms of type  $q_z^m R^k r^{m-k}$ , where  $k \geq 0$  and  $m \geq k$  are integers. For the strain tensor elements in

cylindrical coordinates, one obtains

$$\epsilon_{rr} = -ic_{q_z l} \nu q_z R [1 + \mathcal{O}(\delta^2)] e^{i(q_z z - \omega_{q_z l} \tau)}, \quad (5.78)$$

$$\epsilon_{\phi\phi} = -ic_{q_z l} \nu q_z R [1 + \mathcal{O}(\delta^2)] e^{i(q_z z - \omega_{q_z l} \tau)}, \quad (5.79)$$

$$\epsilon_{zz} = ic_{q_z l} q_z R [1 + \mathcal{O}(\delta^2)] e^{i(q_z z - \omega_{q_z l} \tau)}, \quad (5.80)$$

and  $0 = \epsilon_{r\phi} = \epsilon_{rz} = \epsilon_{\phi z}$ . We note that the corrections to  $\epsilon_{rr}$  and  $\epsilon_{\phi\phi}$  are not identical. In Cartesian coordinates, one therefore finds nonzero  $\epsilon_{xy}$ , with

$$\epsilon_{xy} = ic_{q_z l} \sin(2\phi) \frac{\nu(1-2\nu^2)}{8(1-\nu)} q_z^3 R r^2 [1 + \mathcal{O}(\delta^2)] e^{i(q_z z - \omega_{q_z l} \tau)}. \quad (5.81)$$

The dominant term for  $\epsilon_{xx}$  and  $\epsilon_{yy}$  is the same as that for  $\epsilon_{rr}$  and  $\epsilon_{\phi\phi}$ , and for completeness we mention that  $0 = \epsilon_{xz} = \epsilon_{yz}$ .

#### 5.4.4 Flexural Modes

The flexural modes, also referred to as bending modes, comprise displacement in all three dimensions. Furthermore, the displacement is angular-dependent due to  $n = \pm 1$ . Considering positive  $\omega$ , we note that a lattice vibration of type  $\exp[i(q_z z + \phi - \omega\tau)]$  cannot be written as a linear combination of those of type  $\exp[i(q_z z - \phi - \omega\tau)]$ , as the waves travel in opposite directions around the NW for fixed  $z$ . Therefore, the flexural modes  $f_+$  and  $f_-$ , which correspond to  $n = +1$  and  $n = -1$ , respectively, are independent. Among the gapless modes, the flexural ones are the most complicated, and neither of the  $\chi_{\eta,J}$  can be set to zero in the ansatz discussed in Sec. 5.4.1. Solving Eq. (5.64) yields the parabolic dispersion relation [39, 40, 50]

$$\omega_{q_z f} = \omega_{q_z f_+} = \omega_{q_z f_-} = \zeta_f q_z^2 = \zeta_{f,0} q_z^2 [1 + \mathcal{O}(\delta^2)], \quad (5.82)$$

$$\zeta_{f,0} = \frac{R}{2} \sqrt{\frac{Y}{\rho}}. \quad (5.83)$$

The displacement vectors for  $f_{\pm}$  can be written as

$$\mathbf{u}_{q_z f_{\pm}} = c_{q_z f_{\pm}} R \begin{pmatrix} \mp i \pm \mathcal{O}(\delta^2) \\ 1 + \mathcal{O}(\delta^2) \\ \mp q_z r \pm \mathcal{O}(\delta^3) \end{pmatrix} e^{i(q_z z \pm \phi - \omega_{q_z f} \tau)}, \quad (5.84)$$

where the components of the vector refer again to the basis  $\{\mathbf{e}_r, \mathbf{e}_{\phi}, \mathbf{e}_z\}$ , and  $c_{q_z f_{\pm}}$  are dimensionless complex prefactors. Introducing the shorthand notation

$$e^{(\pm)} = e^{i(q_z z \pm \phi - \omega_{q_z f} \tau)} \quad (5.85)$$

for convenience, the diagonal strain tensor elements for the flexural modes  $f_{\pm}$  are

$$\epsilon_{rr} = \pm ic_{q_z f_{\pm}} \nu q_z^2 R r [1 + \mathcal{O}(\delta^2)] e^{(\pm)}, \quad (5.86)$$

$$\epsilon_{\phi\phi} = \pm ic_{q_z f_{\pm}} \nu q_z^2 R r [1 + \mathcal{O}(\delta^2)] e^{(\pm)}, \quad (5.87)$$

$$\epsilon_{zz} = \mp ic_{q_z f_{\pm}} q_z^2 R r [1 + \mathcal{O}(\delta^2)] e^{(\pm)}, \quad (5.88)$$

and the off-diagonal ones are

$$\epsilon_{r\phi} = \frac{c_{q_z f_{\pm}}}{48} [q_z^4 R r (R^2 - r^2) (1 - 2\nu) + \mathcal{O}(\delta^6)] e^{(\pm)}, \quad (5.89)$$

$$\epsilon_{rz} = \pm \frac{c_{q_z f_{\pm}}}{8} [q_z^3 R (R^2 - r^2) (3 + 2\nu) + \mathcal{O}(\delta^5)] e^{(\pm)}, \quad (5.90)$$

$$\epsilon_{\phi z} = i \frac{c_{q_z f_{\pm}}}{8} [q_z^3 R (R^2 (3 + 2\nu) - r^2 (1 - 2\nu)) + \mathcal{O}(\delta^5)] e^{(\pm)}. \quad (5.91)$$

From the above equations, it is evident that  $\epsilon_{r\phi}$  and  $\epsilon_{rz}$  vanish at  $r = R$ , consistent with the boundary conditions. The dominant terms of the strain components in Cartesian coordinates may easily be obtained with the relations listed in Appendix D.2.2. We note that calculation of  $\epsilon_{xy}$  requires knowledge of the difference

$$\epsilon_{rr} - \epsilon_{\phi\phi} = \pm i \frac{c_{q_z f_{\pm}}}{24} [W_1 + \mathcal{O}(\delta^6)] e^{(\pm)}, \quad (5.92)$$

where we defined

$$W_1 = q_z^4 R r [2r^2 (1 + \nu) - R^2 (1 - 2\nu)]. \quad (5.93)$$

It is worth mentioning that the listed expressions for displacement and strain do not depend on Young's modulus, whereas the dispersion relation does not depend on Poisson's ratio. The same feature is seen for the longitudinal mode.

### 5.4.5 Normalization

When quantum mechanical effects of lattice vibrations in NWs are investigated, such as, e.g., the phonon-mediated decay of spin qubits in NW QDs [12, 49], the amplitudes of the modes are no longer arbitrary as the phonon field must be quantized [48]. Defining the time-independent displacement operator as

$$\mathbf{u}(\mathbf{r}) = \sum_{q_z, s} (a_{q_z s} \mathbf{u}_{q_z s}(\mathbf{r}, \tau = 0) + \text{H.c.}), \quad (5.94)$$

where  $\mathbf{u}_{q_z s} = \mathbf{u}_{q_z s}(\mathbf{r}, \tau)$  are the displacement functions discussed in this section,  $s \in \{l, t, f_+, f_-\}$  indicates the mode, and ‘‘H.c.’’ stands for the Hermitian conjugate, the normalization condition for the coefficients  $c_{q_z s}$  is [51]

$$\int_0^R dr r \mathbf{u}_{q_z s}^* \cdot \mathbf{u}_{q_z s} = \frac{\hbar}{4\pi L \rho \omega_{q_z s}} \quad (5.95)$$

in the case of homogeneous NWs. The introduced operators  $a_{q_z s}^\dagger$  and  $a_{q_z s}$  are the creation and annihilation operators for the phonons, and we mention that

$$H = \sum_{q_z, s} \hbar \omega_{q_z s} \left( a_{q_z s}^\dagger a_{q_z s} + \frac{1}{2} \right) \quad (5.96)$$

is the phonon Hamiltonian. As in Eq. (5.94), the sum runs over all mode types  $s$  and all wave numbers  $q_z$  within the first Brillouin zone. For details, see Appendix D.4 (wherein  $\mathbf{u}_{q_z s}$  is written as  $c_{q_z s} \mathbf{u}_{q_z s}$  for illustration purposes).

From Eq. (5.95) and the derived expressions for  $\mathbf{u}_{q_z s}$ , we calculate the normalization condition for the coefficients  $c_{q_z s}$  in leading order of  $q_z R$ . For the torsional, longitudinal, and flexural modes, respectively,

one finds

$$|c_{q_z t}|^2 = \frac{\hbar}{\pi L R^4 \rho v_t |q_z|}, \quad (5.97)$$

$$|c_{q_z l}|^2 = \frac{\hbar}{2\pi L R^4 \rho v_{l,0} |q_z|} [1 + \mathcal{O}(\delta^2)], \quad (5.98)$$

$$|c_{q_z f_{\pm}}|^2 = \frac{\hbar}{4\pi L R^4 \rho \zeta_{f,0} q_z^2} [1 + \mathcal{O}(\delta^2)]. \quad (5.99)$$

## 5.5 Phonons in Core/Shell Nanowires

We now extend the analysis of the previous section to the more complicated case of core/shell NWs. Considering the complexity of the system, the resulting formulas are surprisingly simple, and so we believe that our results will prove very helpful in future investigations that involve acoustic phonons in core/shell NWs.

### 5.5.1 Ansatz and Boundary Conditions

We assume pseudomorphic growth and start from a core/shell NW that is statically strained. The static strain in the NW was calculated in Sec. 5.3 and ensures that the surface is free of forces, that the core-shell interface is coherent, and that the stress at the interface is continuous. The dynamical displacement field of the lattice vibrations discussed in this section describes the displacement from this statically strained configuration. As the lattice mismatch  $|\epsilon_0| \ll 1$  is small, the static and dynamical displacement fields can be considered as independent and add linearly in good approximation (analogous for the stress and strain) [39].

The dynamical displacement  $\mathbf{u}^{c,s}$  and the stress tensor  $\sigma^{c,s}$  for core ( $c$ ;  $0 \leq r \leq R_c$ ) and shell ( $s$ ;  $R_c \leq r \leq R_s$ ), respectively, are calculated with the ansatz introduced in Sec. 5.4.1 [46]. Suitable functions  $\Phi_\eta^{c,s}$  are

$$\Phi_\eta^c = \chi_{\eta,J}^c J_n(\kappa_{\eta,J}^c r) e^{i(q_z z + n\phi - \omega\tau)}, \quad (5.100)$$

$$\Phi_\eta^s = [\chi_{\eta,J}^s J_n(\kappa_{\eta,J}^s r) + \chi_{\eta,Y}^s Y_n(\kappa_{\eta,Y}^s r)] e^{i(q_z z + n\phi - \omega\tau)}, \quad (5.101)$$

where

$$(\kappa_{\eta,J}^c)^2 = \frac{\rho_c \omega^2}{\mu_c + \delta_{\eta,0}(\mu_c + \lambda_c)} - q_z^2, \quad (5.102)$$

$$(\kappa_{\eta,J}^s)^2 = (\kappa_{\eta,Y}^s)^2 = \frac{\rho_s \omega^2}{\mu_s + \delta_{\eta,0}(\mu_s + \lambda_s)} - q_z^2. \quad (5.103)$$

The boundary conditions are the same as for the static strain and can be summarized as

$$\mathbf{u}^c(R_c, \phi, z) = \mathbf{u}^s(R_c, \phi, z), \quad (5.104)$$

$$\sigma^c(R_c, \phi, z) \mathbf{e}_r = \sigma^s(R_c, \phi, z) \mathbf{e}_r, \quad (5.105)$$

$$\sigma^s(R_s, \phi, z) \mathbf{e}_r = 0. \quad (5.106)$$

For a given mode type and wave number  $q_z$ , these boundary conditions determine the eigenfrequency and the set of coefficients  $\{\chi_{\eta,J}^{c,s}, \chi_{\eta,Y}^s\}$ . As in the case of homogeneous NWs, one of the coefficients may be chosen arbitrarily and quantifies the amplitude and phase of the lattice vibration. Analogous to Eq. (5.64), the eigenfrequency can be calculated by solving a determinantal equation that comprises the boundary conditions (see also Fig. 5.2).



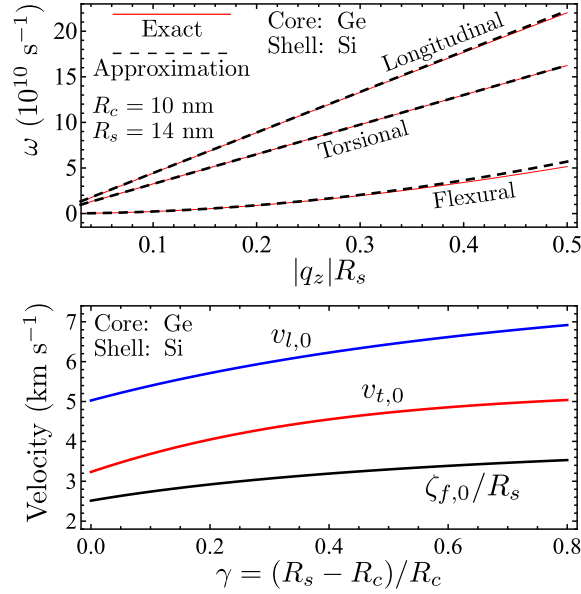


Figure 5.2. Dispersion relation of gapless phonon modes in Ge/Si core/shell NWs. Top: The thin red lines are numerically calculated roots of the determinant that comprises the nine boundary conditions described in Sec. 5.5.1. For the parameters in Appendix D.1 and an assumed core (shell) radius of  $R_c = 10$  nm ( $R_s = 14$  nm), phonons with gapped spectra were found at  $\omega > 5 \times 10^{11} \text{s}^{-1}$ , i.e.,  $\hbar\omega > 0.3$  meV. The dashed black lines correspond to  $\omega = v_{t,0}|q_z|$ ,  $\omega = v_{l,0}|q_z|$ , and  $\omega = \zeta_{f,0}q_z^2$ , respectively, and agree well with the exact result even at relatively large  $q_z$ . Bottom: The mode velocities  $v_{t,0}$  [torsional, Eq. (5.110)],  $v_{l,0}$  [longitudinal, Eq. (5.116)], and  $\zeta_{f,0}/R_s$  [flexural, Eq. (5.138)] are plotted as a function of the relative shell thickness  $\gamma$ .

In order to derive algebraic expressions, we consider again the regime of lowest energy (small  $q_z$ ) for which an expansion in  $q_z r$  applies. In this section, higher-order contributions denoted by  $\mathcal{O}(\delta^m)$  refer to corrections of type  $q_z^m R_s^j R_c^k r^l$ , where  $j$ ,  $k$ ,  $l$ , and  $m = j + k + l$  are integers. We note that  $l < 0$  is allowed in the shell due to the Bessel functions of the second kind. While we list the dominant terms of the displacement field for both the core and the shell, the phonon-based strain tensor is provided in detail for the core only. This is typically sufficient, as qubit states, for instance, are usually confined therein.

## 5.5.2 Torsional Mode

As expected from symmetry considerations, it turns out that the main features of the gapless phonon modes remain unchanged when the NW is surrounded by a shell. For instance, the torsional mode has no angular dependence ( $n = 0$ ) and involves displacement along  $e_\phi$  only. Thus, one obtains  $0 = \chi_{0,J}^{c,s} = \chi_{2,J}^{c,s} = \chi_{0,Y}^s = \chi_{2,Y}^s$ , and the eigenfrequency  $\omega_{q_z t}$  can be calculated via the determinant of a  $3 \times 3$  matrix that contains the three remaining boundary conditions. We find

$$\omega_{q_z t} = v_t |q_z| = v_{t,0} |q_z| [1 + \mathcal{O}(\delta^2)], \quad (5.107)$$

$$v_{t,0} = \sqrt{\frac{\mu_c R_c^4 + \mu_s (R_s^4 - R_c^4)}{\rho_c R_c^4 + \rho_s (R_s^4 - R_c^4)}}, \quad (5.108)$$

and note that  $v_{t,0}$ , in fact, is a function of the relative shell thickness. Defining

$$\hat{\gamma} = \tilde{\gamma}^2 + 2\tilde{\gamma} = \frac{R_s^4 - R_c^4}{R_c^4} \quad (5.109)$$

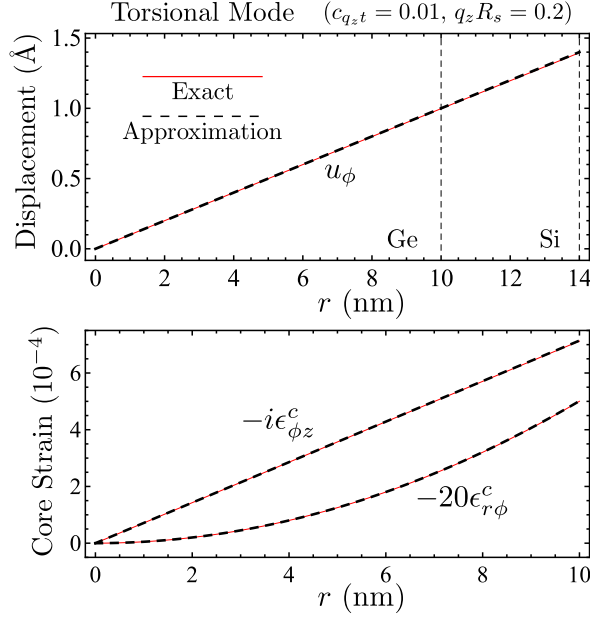


Figure 5.3. Radial dependence of the displacement field (top) and core strain (bottom) in cylindrical coordinates due to the torsional phonon mode in a Ge/Si NW with core radius  $R_c = 10$  nm and shell radius  $R_s = 14$  nm. Thin red lines correspond to the exact, numerical solution of the ansatz described in Sec. 5.5.1, while dashed black lines are calculated with the algebraic expressions listed in Sec. 5.5.2. Besides the parameters for Ge and Si in the text (see also Appendix D.1), we use  $c_{q_z t} = 0.01$  and  $q_z = 0.2/R_s$ . The global phase factor  $\exp[i(q_z z - \omega_{q_z t} \tau)]$  is set to 1. Excellent agreement between the exact and approximate solutions is found even when  $q_z$  is relatively large. We note that  $0 = u_r = u_z$  and  $0 = \epsilon_{rr}^c = \epsilon_{\phi\phi}^c = \epsilon_{zz}^c = \epsilon_{rz}^c$ .

analogously to Eqs. (5.32) and (5.33), the mode velocity  $v_{t,0}$  has the remarkably simple form

$$v_{t,0} = \sqrt{\frac{\mu_c + \mu_s \hat{\gamma}}{\rho_c + \rho_s \hat{\gamma}}}. \quad (5.110)$$

The displacement field is

$$\mathbf{u}_{q_z t}^c = c_{q_z t} r [1 + \mathcal{O}(\delta^2)] e^{i(q_z z - \omega_{q_z t} \tau)} \mathbf{e}_\phi, \quad (5.111)$$

$$\mathbf{u}_{q_z t}^s = c_{q_z t} r [1 + \mathcal{O}(\delta^2)] e^{i(q_z z - \omega_{q_z t} \tau)} \mathbf{e}_\phi, \quad (5.112)$$

i.e., the dominant term for core and shell is the same. The strain tensor elements for the core are

$$\epsilon_{r\phi}^c = \frac{c_{q_z t}}{8} \left[ q_z^2 r^2 \left( 1 - v_{t,0}^2 \frac{\rho_c}{\mu_c} \right) + \mathcal{O}(\delta^4) \right] e^{i(q_z z - \omega_{q_z t} \tau)}, \quad (5.113)$$

$$\epsilon_{\phi z}^c = i \frac{c_{q_z t}}{2} [q_z r + \mathcal{O}(\delta^3)] e^{i(q_z z - \omega_{q_z t} \tau)}, \quad (5.114)$$

and  $0 = \epsilon_{rr}^c = \epsilon_{\phi\phi}^c = \epsilon_{zz}^c = \epsilon_{rz}^c$ . We emphasize that  $\epsilon_{r\phi}^c$  is nonzero, in stark contrast to  $\epsilon_{r\phi}$  in homogeneous NWs. The strain components in Cartesian coordinates, among which only  $\epsilon_{zz}^c$  is zero, can be calculated with the above-mentioned  $\epsilon_{r\phi}^c$  and  $\epsilon_{\phi z}^c$  and the relations in Appendix D.2.2.

In Fig. 5.2 (top), we illustrate that the derived formula for the velocity  $v_{t,0}$  is consistent with exact, numerical solutions of the underlying model (Sec. 5.5.1). This also holds for the dispersion relation of the longitudinal and flexural modes that we investigate next. The dependence of the different phonon velocities on the relative shell thickness of a Ge/Si core/shell NW is shown in Fig. 5.2 (bottom). A comparison between exact results and the above-listed expressions for the displacement and strain caused by torsional lattice vibrations is provided in Fig. 5.3.

### 5.5.3 Longitudinal Mode

In the ansatz for the longitudinal mode, we set  $n = 0$  and  $0 = \chi_{1,J}^{c,s} = \chi_{1,Y}^s$ . From the boundary conditions, we obtain

$$\omega_{q_z l} = v_l |q_z| = v_{l,0} |q_z| [1 + \mathcal{O}(\delta^2)], \quad (5.115)$$

$$v_{l,0} = \sqrt{\frac{Y_c G_0 + Y_s G_1 \tilde{\gamma}^2 + Y_c G_2 \tilde{\gamma}}{(G_0 + G_1 \tilde{\gamma})(\rho_c + \rho_s \tilde{\gamma})}}, \quad (5.116)$$

where we introduced

$$G_0 = 2Y_c(1 - \nu_s^2), \quad (5.117)$$

$$G_1 = Y_c(1 + \nu_s) + Y_s(1 - \nu_c - 2\nu_c^2), \quad (5.118)$$

$$G_2 = Y_c(1 + \nu_s) + Y_s(3 - \nu_c - 4\nu_c\nu_s) \quad (5.119)$$

for convenience. The resulting displacement field  $\mathbf{u}_{q_z l}$  is

$$\mathbf{u}_{q_z l}^c = c_{q_z l} R_s \begin{pmatrix} -i \frac{\nu_c G_0 + G_3 \tilde{\gamma}}{G_0 + G_1 \tilde{\gamma}} q_z r + \mathcal{O}(\delta^3) \\ 0 \\ 1 + \mathcal{O}(\delta^2) \end{pmatrix} e^{i(q_z z - \omega_{q_z l} \tau)} \quad (5.120)$$

within the core and

$$\mathbf{u}_{q_z l}^s = c_{q_z l} R_s \begin{pmatrix} -i \left[ \frac{(G_4 + \nu_s G_1 \tilde{\gamma}) q_z r}{G_0 + G_1 \tilde{\gamma}} + \frac{G_5 q_z R_s^2}{(G_0 + G_1 \tilde{\gamma}) r} \right] + \mathcal{O}(\delta^3) \\ 0 \\ 1 + \mathcal{O}(\delta^2) \end{pmatrix} e^{i(q_z z - \omega_{q_z l} \tau)} \quad (5.121)$$

within the shell, where

$$G_3 = Y_c(1 + \nu_s)\nu_c + Y_s(1 - \nu_c - 2\nu_c^2)\nu_s, \quad (5.122)$$

$$G_4 = Y_c(1 + \nu_s)(\nu_c + \nu_s - 2\nu_c\nu_s), \quad (5.123)$$

$$G_5 = Y_c(1 + \nu_s)(\nu_c - \nu_s). \quad (5.124)$$

An example based on Ge/Si NWs for the displacement and the strain discussed below is shown in Fig. 5.4, where we also provide a comparison with the exact solution.

The diagonal strain tensor elements for the core are similar to those for homogeneous NWs,

$$\epsilon_{rr}^c = -i c_{q_z l} \frac{\nu_c G_0 + G_3 \tilde{\gamma}}{G_0 + G_1 \tilde{\gamma}} q_z R_s [1 + \mathcal{O}(\delta^2)] e^{i(q_z z - \omega_{q_z l} \tau)}, \quad (5.125)$$

$$\epsilon_{\phi\phi}^c = -i c_{q_z l} \frac{\nu_c G_0 + G_3 \tilde{\gamma}}{G_0 + G_1 \tilde{\gamma}} q_z R_s [1 + \mathcal{O}(\delta^2)] e^{i(q_z z - \omega_{q_z l} \tau)}, \quad (5.126)$$

$$\epsilon_{zz}^c = i c_{q_z l} q_z R_s [1 + \mathcal{O}(\delta^2)] e^{i(q_z z - \omega_{q_z l} \tau)}. \quad (5.127)$$

Furthermore, we note that  $0 = \epsilon_{r\phi}^c = \epsilon_{\phi z}^c$  as the longitudinal mode is independent of  $\phi$  and does not provide displacement along  $\mathbf{e}_\phi$ . In stark contrast to homogeneous NWs, however, we find nonzero  $\epsilon_{rz}^c$ ,

$$\epsilon_{rz}^c = c_{q_z l} (1 + \nu_c) \frac{Y_c(G_0 \rho_s - G_6 \rho_c) \tilde{\gamma} + (Y_c G_7 \rho_s - Y_s G_1 \rho_c) \tilde{\gamma}^2}{2Y_c(G_0 + G_1 \tilde{\gamma})(\rho_c + \rho_s \tilde{\gamma})} q_z^2 R_s r [1 + \mathcal{O}(\delta^2)] e^{i(q_z z - \omega_{q_z l} \tau)}, \quad (5.128)$$

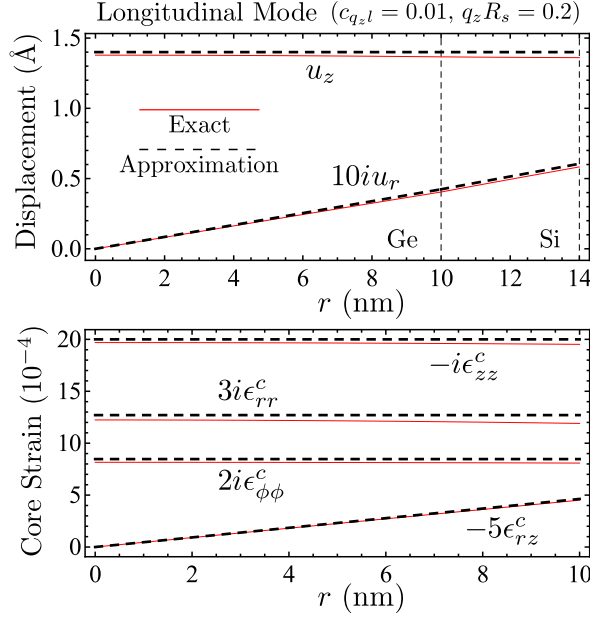


Figure 5.4. Comparison between exact results and derived formulas for the longitudinal phonon mode, analogous to Fig. 5.3. Good agreement is found for all components at  $q_z = 0.2/R_s$  assumed here, and the quality of the approximation increases with decreasing  $|q_z|$ . The longitudinal mode features  $u_\phi = 0$  and  $0 = \epsilon_{r\phi}^c = \epsilon_{\phi z}^c$ . For details, see Sec. 5.5.3.

with

$$G_6 = 2Y_s(1 - \nu_c\nu_s), \quad (5.129)$$

$$G_7 = Y_c(1 + \nu_s) + Y_s(1 - \nu_c - 2\nu_c\nu_s). \quad (5.130)$$

The dominant term for  $\epsilon_{rr}^c$  and  $\epsilon_{\phi\phi}^c$  is identical to that for  $\epsilon_{xx}^c$  and  $\epsilon_{yy}^c$ , and the off-diagonal strain components in Cartesian coordinates may be calculated via  $\epsilon_{xz}^c = \epsilon_{rz}^c \cos \phi$ ,  $\epsilon_{yz}^c = \epsilon_{rz}^c \sin \phi$ , and  $\epsilon_{xy}^c = (\epsilon_{rr}^c - \epsilon_{\phi\phi}^c) \sin \phi \cos \phi$ . The resulting formula for  $\epsilon_{xy}^c$  involves higher-order corrections to  $\epsilon_{rr}^c$  and  $\epsilon_{\phi\phi}^c$  and is too lengthy to be displayed here in its entirety. Nevertheless, we provide an approximation that applies to the case of a very thin shell ( $\tilde{\gamma} \ll 1$ ),

$$\epsilon_{xy}^c \simeq ic_{q_z l} \sin(2\phi) \left[ \frac{\nu_c(1 - 2\nu_c^2)}{8(1 - \nu_c)} + \frac{\tilde{\gamma}(1 + \nu_c)}{16(1 - \nu_c)} \left( \frac{G_8}{G_0} - \frac{\rho'}{\rho_c} \right) \right] q_z^3 R_s r^2 [1 + \mathcal{O}(\delta^2)] e^{i(q_z z - \omega_{q_z l} \tau)}. \quad (5.131)$$

In the opposite limit of a very thick shell, we find

$$\lim_{\tilde{\gamma} \rightarrow \infty} \epsilon_{xy}^c = ic_{q_z l} \sin(2\phi) \frac{1}{16G_1} \left( \frac{Y_s(1 + \nu_c)\rho_c}{Y_c(1 - \nu_c)\rho_s} G_9 - G_{10} \right) q_z^3 R_s r^2 [1 + \mathcal{O}(\delta^2)] e^{i(q_z z - \omega_{q_z l} \tau)}. \quad (5.132)$$

In Eq. (5.131),

$$G_8 = 2Y_s \left[ 1 + \nu_s + \nu_c(1 - 3\nu_s) + 2\nu_c^2(2\nu_c - 1)(3\nu_s + 1) - 8\nu_c^4 \right] \quad (5.133)$$

and

$$\rho' = \rho_s(1 + 2\nu_c - 4\nu_c^2), \quad (5.134)$$

while

$$G_9 = Y_c(1 + 2\nu_c - 4\nu_c^2)(1 + \nu_s) + Y_s(1 - \nu_c - 2\nu_c^2)(1 + 2\nu_s - 4\nu_c\nu_s), \quad (5.135)$$

$$G_{10} = Y_c(1 + 2\nu_c)(1 + \nu_s) + Y_s(1 + \nu_c)(1 - 4\nu_c\nu_s) \quad (5.136)$$

in Eq. (5.132).

### 5.5.4 Flexural Modes

The calculation for the flexural modes in core/shell NWs is most complicated as neither of the coefficients  $\chi_{\eta,J}^{c,s}$  and  $\chi_{\eta,Y}^s$  is zero. Furthermore, the flexural modes have an angular dependence due to  $n = \pm 1$ . Despite this complexity, the resulting formulas are relatively simple and can be written in a compact form. By solving the determinantal equation that comprises the nine boundary conditions, we find the dispersion relation

$$\omega_{q_z f} = \omega_{q_z f_+} = \omega_{q_z f_-} = \zeta_f q_z^2 = \zeta_{f,0} q_z^2 [1 + \mathcal{O}(\delta^2)], \quad (5.137)$$

$$\zeta_{f,0} = \frac{R_s}{2} \sqrt{\frac{Y_c K_0 + Y_s K_1 \hat{\gamma}^2 + Y_c K_2 \hat{\gamma}}{(1 + \tilde{\gamma})(K_0 + K_1 \hat{\gamma})(\rho_c + \rho_s \tilde{\gamma})}}, \quad (5.138)$$

where

$$K_0 = 4Y_c(1 - \nu_s^2), \quad (5.139)$$

$$K_1 = Y_c(1 + \nu_s) + Y_s(3 - \nu_c - 4\nu_c^2), \quad (5.140)$$

$$K_2 = Y_c(1 + \nu_s) + Y_s(7 - \nu_c - 8\nu_c \nu_s), \quad (5.141)$$

and  $\hat{\gamma} = \tilde{\gamma}^2 + 2\tilde{\gamma}$  has been introduced in Eq. (5.109). We note that  $R_s/\sqrt{1 + \tilde{\gamma}} = R_s/(1 + \gamma) = R_c$  in the expression for  $\zeta_{f,0}$  may be substituted by the core radius. Remarkably, the dominant terms of the displacement field in both core and shell turn out to be equivalent to those for a homogeneous NW. Referring again to the basis vectors  $\mathbf{e}_r$ ,  $\mathbf{e}_\phi$ , and  $\mathbf{e}_z$ , we obtain

$$\mathbf{u}_{q_z f_\pm}^c = c_{q_z f_\pm} R_s \begin{pmatrix} \mp i \pm \mathcal{O}(\delta^2) \\ 1 + \mathcal{O}(\delta^2) \\ \mp q_z r \pm \mathcal{O}(\delta^3) \end{pmatrix} e^{(\pm)} \quad (5.142)$$

for the core, and the formally identical result

$$\mathbf{u}_{q_z f_\pm}^s = c_{q_z f_\pm} R_s \begin{pmatrix} \mp i \pm \mathcal{O}(\delta^2) \\ 1 + \mathcal{O}(\delta^2) \\ \mp q_z r \pm \mathcal{O}(\delta^3) \end{pmatrix} e^{(\pm)} \quad (5.143)$$

for the shell. The shorthand notation  $e^{(\pm)}$  for the phase factor has been introduced in Eq. (5.85).

With the definitions

$$K_3 = Y_c(1 + \nu_s)\nu_c + Y_s(1 + \nu_c)(\nu_s + 2\nu_c - 4\nu_c \nu_s), \quad (5.144)$$

$$K_4 = Y_c(1 + \nu_s)\nu_c + Y_s(3 - \nu_c - 4\nu_c^2)\nu_s, \quad (5.145)$$

the diagonal core strain components due to the flexural modes  $f_\pm$  are

$$\epsilon_{rr}^c = \pm i c_{q_z f_\pm} \frac{\nu_c K_0 + K_3 \hat{\gamma}}{K_0 + K_1 \hat{\gamma}} q_z^2 R_s r [1 + \mathcal{O}(\delta^2)] e^{(\pm)}, \quad (5.146)$$

$$\epsilon_{\phi\phi}^c = \pm i c_{q_z f_\pm} \frac{\nu_c K_0 + K_4 \hat{\gamma}}{K_0 + K_1 \hat{\gamma}} q_z^2 R_s r [1 + \mathcal{O}(\delta^2)] e^{(\pm)}, \quad (5.147)$$

$$\epsilon_{zz}^c = \mp i c_{q_z f_\pm} q_z^2 R_s r [1 + \mathcal{O}(\delta^2)] e^{(\pm)}. \quad (5.148)$$

Thus, in contrast to the case of homogeneous NWs, the leading-order terms for  $\epsilon_{rr}^c$  and  $\epsilon_{\phi\phi}^c$  differ when

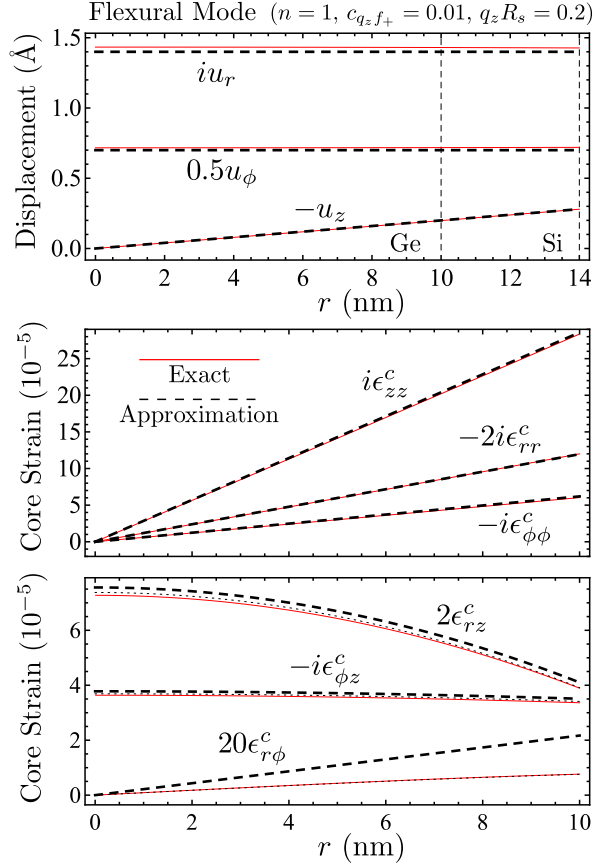


Figure 5.5. Comparison between exact and approximate solutions for a flexural phonon mode ( $n = 1$ ), analogous to Figs. 5.3 and 5.4. Assuming again  $q_z = 0.2/R_s$ , the top and middle figures exhibit very good agreement for the displacement and the diagonal strain components, respectively. In the bottom figure,  $\epsilon_{rz}^c$  and  $\epsilon_{\phi z}^c$  are well approximated by Eqs. (5.157) and (5.158) (dashed black lines,  $\tilde{\gamma} \rightarrow \infty$ ). Equations (5.151) and (5.152) (not plotted,  $\tilde{\gamma} \ll 1$ ) yield a slightly worse but still good approximation. We note that the quantitative agreement can be improved by taking  $\tilde{\gamma} \sim 1$  of the studied NW fully into account in the terms of order  $c_{q_z f_{\pm}} \mathcal{O}(\delta^3)$  (thin dotted lines for  $\epsilon_{rz}^c$  and  $\epsilon_{\phi z}^c$ , expressions too lengthy for text). For  $\epsilon_{r\phi}^c$ , the observed deviation between Eq. (5.150) (dashed black line) and the exact result decreases rapidly with decreasing  $|q_z|$ , as expected. We illustrate that corrections of order  $c_{q_z f_{\pm}} \mathcal{O}(\delta^4)$  become important in the considered example by taking them into account (thin dotted line for  $\epsilon_{r\phi}^c$ , expressions too long for text). For details, see Sec. 5.5.4.

Poisson's ratios  $\nu_c$  and  $\nu_s$  are different,

$$\epsilon_{rr}^c - \epsilon_{\phi\phi}^c = \pm i c_{q_z f_{\pm}} \left[ \frac{2Y_s(1+\nu_c)(\nu_c - \nu_s)\tilde{\gamma}}{K_0 + K_1\tilde{\gamma}} q_z^2 R_s r + \mathcal{O}(\delta^4) \right] e^{(\pm)}. \quad (5.149)$$

Similarly, the off-diagonal strain tensor element

$$\epsilon_{r\phi}^c = c_{q_z f_{\pm}} \left[ \frac{Y_s(1+\nu_c)(\nu_s - \nu_c)\tilde{\gamma}}{K_0 + K_1\tilde{\gamma}} q_z^2 R_s r + \mathcal{O}(\delta^4) \right] e^{(\pm)} \quad (5.150)$$

exhibits a new term that vanishes in homogeneous NWs or when  $\nu_c = \nu_s$ . The expressions for  $\epsilon_{rz}^c$  and  $\epsilon_{\phi z}^c$  are rather lengthy and therefore cannot be provided here completely. When  $\tilde{\gamma} \ll 1$ , they are well approximated by

$$\epsilon_{rz}^c \simeq \pm c_{q_z f_{\pm}} q_z R_s \left[ q_z^2 \frac{(R_s^2 - r^2)\nu'}{8} + \tilde{\gamma} q_z^2 \frac{R_s^2 K_5 + r^2 K_6}{2K_0} + \mathcal{O}(\delta^4) \right] e^{(\pm)}, \quad (5.151)$$

$$\epsilon_{\phi z}^c \simeq i c_{q_z f_{\pm}} q_z R_s \left[ q_z^2 \frac{R_s^2 \nu' - r^2(1 - 2\nu_c)}{8} + \tilde{\gamma} q_z^2 \frac{R_s^2 K_5 + r^2 K_7}{2K_0} + \mathcal{O}(\delta^4) \right] e^{(\pm)}, \quad (5.152)$$

where

$$K_5 = Y_s(1 + \nu_c)(3 - \nu_s + 4\nu_c^2 - 6\nu_c\nu_s) - Y_c(3 + 2\nu_c)(1 - \nu_s^2), \quad (5.153)$$

$$K_6 = 2Y_s(1 + 3\nu_c + 2\nu_c^2)(\nu_s - \nu_c), \quad (5.154)$$

$$K_7 = 2Y_s(3 + \nu_c - 2\nu_c^2)(\nu_s - \nu_c), \quad (5.155)$$

$$\nu' = 3 + 2\nu_c. \quad (5.156)$$

In the opposite regime, i.e.,  $\tilde{\gamma} \gg 1$ , the results for  $\epsilon_{rz}^c$  and  $\epsilon_{\phi z}^c$  converge to

$$\lim_{\gamma \rightarrow \infty} \epsilon_{rz}^c = \pm c_{q_z f_{\pm}} \left[ q_z^3 R_s \left( \frac{R_s^2 K_8}{8K_9} - \frac{r^2 K_{10}}{8K_1} \right) + \mathcal{O}(\delta^5) \right] e^{(\pm)}, \quad (5.157)$$

$$\lim_{\gamma \rightarrow \infty} \epsilon_{\phi z}^c = i c_{q_z f_{\pm}} \left[ q_z^3 R_s \left( \frac{R_s^2 K_8}{8K_9} - \frac{r^2 K_{11}}{8K_1} \right) + \mathcal{O}(\delta^5) \right] e^{(\pm)}, \quad (5.158)$$

where we defined

$$K_8 = 2Y_s(1 + \nu_c)(3 + 2\nu_s), \quad (5.159)$$

$$K_9 = Y_c(1 + \nu_s) + Y_s(1 + \nu_c), \quad (5.160)$$

and

$$K_{10} = Y_c(3 + 2\nu_c)(1 + \nu_s) + Y_s(1 + \nu_c)(9 - 2\nu_c - 4\nu_s - 8\nu_c\nu_s), \quad (5.161)$$

$$K_{11} = Y_c(1 - 2\nu_c)(1 + \nu_s) + Y_s(1 + \nu_c)(3 + 2\nu_c - 12\nu_s + 8\nu_c\nu_s). \quad (5.162)$$

The strain tensor elements in Cartesian coordinates may again be calculated with the relations listed in Appendix D.2.2. The radial dependence of the displacement field and the core strain of a flexural lattice vibration is plotted in Fig. 5.5, confirming that our formulas are consistent with exact solutions.

As mentioned before, the new terms in Eqs. (5.149) and (5.150) vanish when  $R_s \rightarrow R_c$  or  $\nu_s \rightarrow \nu_c$ . Therefore, the higher-order contributions of order  $c_{q_z f_{\pm}} \mathcal{O}(\delta^4)$  may become important for the calculation of  $\epsilon_{r\phi}^c$  and  $\epsilon_{xy}^c$ , particularly when  $q_z R_s$  is rather large and  $\gamma$  and  $\nu_s - \nu_c$  are small [see also Fig. 5.5 (bottom)]. The expressions for these higher-order corrections in core/shell NWs are too lengthy to be displayed here. However, if needed, they can be approximated via the formulas that we provide in Eqs. (5.89) and (5.92) for homogeneous NWs.

### 5.5.5 Normalization

The normalization condition of Eq. (5.95) applies only to the special case of homogeneous NWs with cylindrical symmetry. In the more general case of cylindrically symmetric core/shell and core/multishell NWs, the normalization condition reads

$$\int_0^{R_{\text{tot}}} dr r \rho(r) \mathbf{u}_{q_z s}^* \cdot \mathbf{u}_{q_z s} = \frac{\hbar}{4\pi L \omega_{q_z s}}, \quad (5.163)$$

where  $\rho(r)$  is the radially dependent density,  $s \in \{l, t, f_+, f_-\}$  is the mode type, and  $R_{\text{tot}}$  is the total radius of the NW, i.e., the radius of the outermost shell. Considering core/shell NWs, we therefore obtain

the normalization conditions

$$|c_{q_z t}|^2 = \frac{\hbar(1 + \hat{\gamma})}{\pi L R_s^4 (\rho_c + \rho_s \hat{\gamma}) v_{t,0} |q_z|} [1 + \mathcal{O}(\delta^2)], \quad (5.164)$$

$$|c_{q_z l}|^2 = \frac{\hbar(1 + \tilde{\gamma})}{2\pi L R_s^4 (\rho_c + \rho_s \tilde{\gamma}) v_{l,0} |q_z|} [1 + \mathcal{O}(\delta^2)], \quad (5.165)$$

$$|c_{q_z f_{\pm}}|^2 = \frac{\hbar(1 + \tilde{\gamma})}{4\pi L R_s^4 (\rho_c + \rho_s \tilde{\gamma}) \zeta_{f,0} q_z^2} [1 + \mathcal{O}(\delta^2)] \quad (5.166)$$

for the coefficients of the phonons investigated in this section. Details about the derivation of Eq. (5.163) are provided in Appendixes D.3 and D.4.

### 5.5.6 Limits of Vanishing and Infinite Shell

Our results for phonons in core/shell NWs are fully consistent with those in Sec. 5.4 for homogeneous NWs. For instance, when  $R_s \rightarrow R_c$ , i.e.,  $\gamma \rightarrow 0$ , the expressions for the mode velocities and for the displacement and strain in the core converge exactly to those for a homogeneous wire made of the core material. Analogously, it can easily be verified that the dispersion relations and the shell displacement (also the shell strain, not shown) match those of a bare wire made of the shell material in the limit  $\gamma \rightarrow \infty$ .

## 5.6 Conclusions

In conclusion, we have derived a comprehensive list of algebraic expressions that describe the static strain and the low-energy phonons in core/shell NWs. We take all stress and strain tensor elements into account, allow for arbitrary core and shell radii, and consider the elastic properties of the involved materials as independent. While the common approximation  $\nu_c = \nu_s$  for Poisson's ratio in core and shell is often justified, we find that possibly important terms are ignored with this assumption [see, e.g., Eq. (5.150)].

We have investigated the resulting strain field for both the static and dynamical lattice displacement in great detail. Among other things, knowledge of the strain tensor elements is important for analyzing electron and hole spectra [15, 43] and for studies that involve electron- and hole-phonon interactions [48, 52, 53]. As seen in the example of Ge/Si NWs (Sec. 5.3.3), the shell-induced strain can affect the carrier spectrum substantially [16]. Furthermore, we have shown that the presence of a shell leads to additional, phonon-based strain components within the core that are absent in homogeneous NWs. Although the elements of the stress tensor are not listed in this work explicitly, they can directly be obtained via the stress-strain relations in Eqs. (5.2) and (5.5).

Given pseudomorphic growth, the dominant source of error in our model is certainly the assumption of isotropic materials ( $c_{11} = c_{12} + 2c_{44}$ ). Taking anisotropies exactly into account, however, is usually not possible without extensive numerical simulations [5, 17, 18] and, moreover, leads only to quantitative rather than qualitative corrections in most applications (see also Sec. 5.3.2). We are therefore convinced that the results of our work will be very useful for future studies based on core/shell NWs.

## Acknowledgments

We thank P. Stano, S. Hoffman, and A. A. Zyuzin for helpful discussions and acknowledge support from the Swiss NF, NCCRs Nanoscience and QSIT, SiSPIN, DARPA, IARPA (MQCO), S<sup>3</sup>NANO, and the NSF under Grant No. DMR-0840965 (M.T.).



# References

- [1] J. W. W. van Tilburg, R. E. Algra, W. G. G. Immink, M. Verheijen, E. P. A. M. Bakkers, and L. P. Kouwenhoven, *Semicond. Sci. Technol.* **25**, 024011 (2010).
- [2] N. Sköld, L. S. Karlsson, M. W. Larsson, M.-E. Pistol, W. Seifert, J. Trägårdh, and L. Samuelson, *Nano Lett.* **5**, 1943 (2005).
- [3] L. Rigutti, G. Jacopin, L. Largeau, E. Galopin, A. De Luna Bugallo, F. H. Julien, J.-C. Harmand, F. Glas, and M. Tchernycheva, *Phys. Rev. B* **83**, 155320 (2011).
- [4] J. Treu, M. Bormann, H. Schmeiduch, M. Döblinger, S. Morkötter, S. Matich, P. Wiecha, K. Saller, B. Mayer, M. Bichler, M.-C. Amann, J. J. Finley, G. Abstreiter, and G. Koblmüller, *Nano Lett.* **13**, 6070 (2013).
- [5] M. Hocevar, L. T. T. Giang, R. Songmuang, M. den Hertog, L. Besombes, J. Bleuse, Y.-M. Niquet, and N. T. Pelekanos, *Appl. Phys. Lett.* **102**, 191103 (2013).
- [6] B. Mayer, D. Rudolph, J. Schnell, S. Morkötter, J. Winnerl, J. Treu, K. Müller, G. Bracher, G. Abstreiter, G. Koblmüller, and J. J. Finley, *Nat. Commun.* **4**, 2931 (2013).
- [7] B. Mahler, P. Spinicelli, S. Buil, X. Quelin, J.-P. Hermier, and B. Dubertret, *Nat. Mater.* **7**, 659 (2008).
- [8] O. Chen, J. Zhao, V. P. Chauhan, J. Cui, C. Wong, D. K. Harris, H. Wei, H.-S. Han, D. Fukumura, R. K. Jain, and M. G. Bawendi, *Nat. Mater.* **12**, 445 (2013).
- [9] W. Lu, J. Xiang, B. P. Timko, Y. Wu, and C. M. Lieber, *Proc. Natl. Acad. Sci. USA* **102**, 10046 (2005).
- [10] J.-S. Park, B. Ryu, C.-Y. Moon, and K. J. Chang, *Nano Lett.* **10**, 116 (2010).
- [11] F. Maier and D. Loss, *Phys. Rev. B* **85**, 195323 (2012).
- [12] F. Maier, C. Kloeffel, and D. Loss, *Phys. Rev. B* **87**, 161305(R) (2013).  
See Chapter 3
- [13] E. B. Flagg, A. Muller, S. V. Polyakov, A. Ling, A. Migdall, and G. S. Solomon, *Phys. Rev. Lett.* **104**, 137401 (2010).
- [14] C. E. Kuklewicz, R. N. E. Malein, P. M. Petroff, and B. D. Gerardot, *Nano Lett.* **12**, 3761 (2012).
- [15] G. L. Bir and G. E. Pikus, *Symmetry and Strain-Induced Effects in Semiconductors* (Wiley, New York, 1974).
- [16] C. Kloeffel, M. Trif, and D. Loss, *Phys. Rev. B* **84**, 195314 (2011).  
See Chapter 2
- [17] J. Grönqvist, N. Sondergaard, F. Boxberg, T. Guhr, S. Aberg, and H. Q. Xu, *J. Appl. Phys.* **106**, 053508 (2009).

- [18] K. Hestroffer, R. Mata, D. Camacho, C. Leclere, G. Tourbot, Y. M. Niquet, A. Cros, C. Bougerol, H. Renevier, and B. Daudin, *Nanotechnology* **21**, 415702 (2010).
- [19] Y. Liang, W. D. Nix, P. B. Griffin, and J. D. Plummer, *J. Appl. Phys.* **97**, 043519 (2005).
- [20] V. Schmidt, P. C. McIntyre, and U. Gösele, *Phys. Rev. B* **77**, 235302 (2008).
- [21] J. Menéndez, R. Singh, and J. Drucker, *Ann. Phys. (Berlin)* **523**, 145 (2011).
- [22] D. Loss and D. P. DiVincenzo, *Phys. Rev. A* **57**, 120 (1998).
- [23] C. Fasth, A. Fuhrer, L. Samuelson, V. N. Golovach, and D. Loss, *Phys. Rev. Lett.* **98**, 266801 (2007).
- [24] S. Nadj-Perge, S. M. Frolov, E. P. A. M. Bakkers, and L. P. Kouwenhoven, *Nature (London)* **468**, 1084 (2010).
- [25] M. D. Schroer, K. D. Petersson, M. Jung, and J. R. Petta, *Phys. Rev. Lett.* **107**, 176811 (2011).
- [26] J. W. G. van den Berg, S. Nadj-Perge, V. S. Pribiag, S. R. Plissard, E. P. A. M. Bakkers, S. M. Frolov, and L. P. Kouwenhoven, *Phys. Rev. Lett.* **110**, 066806 (2013).
- [27] C. Kloeffel and D. Loss, *Annu. Rev. Condens. Matter Phys.* **4**, 51 (2013).  
See Chapter 1
- [28] Y. Hu, H. O. H. Churchill, D. J. Reilly, J. Xiang, C. M. Lieber, and C. M. Marcus, *Nat. Nanotechnol.* **2**, 622 (2007).
- [29] S. Roddaro, A. Fuhrer, P. Brusheim, C. Fasth, H. Q. Xu, L. Samuelson, J. Xiang, and C. M. Lieber, *Phys. Rev. Lett.* **101**, 186802 (2008).
- [30] Y. Hu, F. Kuemmeth, C. M. Lieber, and C. M. Marcus, *Nat. Nanotechnol.* **7**, 47 (2012).
- [31] A. P. Higginbotham, T. W. Larsen, J. Yao, H. Yan, C. M. Lieber, C. M. Marcus, and F. Kuemmeth, *Nano Lett.* **14**, 3582 (2014).
- [32] C. Kloeffel, M. Trif, P. Stano, and D. Loss, *Phys. Rev. B* **88**, 241405(R) (2013).  
See Chapter 4
- [33] A. V. Khaetskii and Y. V. Nazarov, *Phys. Rev. B* **64**, 125316 (2001).
- [34] V. N. Golovach, A. V. Khaetskii, and D. Loss, *Phys. Rev. Lett.* **93**, 016601 (2004).
- [35] M. Kroutvar, Y. Ducommun, D. Heiss, M. Bichler, D. Schuh, G. Abstreiter, and J. J. Finley, *Nature (London)* **432**, 81 (2004).
- [36] R. Hanson, L. P. Kouwenhoven, J. R. Petta, S. Tarucha, and L. M. K. Vandersypen, *Rev. Mod. Phys.* **79**, 1217 (2007).
- [37] M. O. Hachiya, G. Burkard, and J. C. Egues, *Phys. Rev. B* **89**, 115427 (2014).
- [38] V. Kornich, C. Kloeffel, and D. Loss, *Phys. Rev. B* **89**, 085410 (2014).  
See Chapter 6
- [39] A. N. Cleland, *Foundations of Nanomechanics: From Solid-State Theory to Device Applications* (Springer, Berlin, 2003).
- [40] L. D. Landau and E. M. Lifshitz, *Theory of Elasticity*, 2nd ed. (Pergamon, New York, 1970).
- [41] D. C. Dillen, K. M. Varahramyan, C. M. Corbet, and E. Tutuc, *Phys. Rev. B* **86**, 045311 (2012).

- [42] D. C. Dillen, K. Kim, E.-S. Liu, and E. Tutuc, *Nat. Nanotechnol.* **9**, 116 (2014).
- [43] R. Winkler, *Spin-Orbit Coupling Effects in Two-Dimensional Electron and Hole Systems* (Springer, Berlin, 2003).
- [44] S. Adachi, *Properties of Group-IV, III-V and II-VI Semiconductors* (Wiley, Chichester, 2005).
- [45] M. Povolotskyi and A. Di Carlo, *J. Appl. Phys.* **100**, 063514 (2006).
- [46] N. Nishiguchi, *Phys. Rev. B* **50**, 10970 (1994).
- [47] M. Yang, J. C. Sturm, and J. Prevost, *Phys. Rev. B* **56**, 1973 (1997).
- [48] M. A. Stroscio and M. Dutta, *Phonons in Nanostructures* (Cambridge Univ. Press, Cambridge, 2001).
- [49] M. Trif, V. N. Golovach, and D. Loss, *Phys. Rev. B* **77**, 045434 (2008).
- [50] Y. M. Sirenko, M. A. Stroscio, and K. W. Kim, *Phys. Rev. E* **54**, 1816 (1996).
- [51] M. A. Stroscio, K. W. Kim, S. Yu, and A. Ballato, *J. Appl. Phys.* **76**, 4670 (1994).
- [52] P. Y. Yu and M. Cardona, *Fundamentals of Semiconductors: Physics and Materials Properties*, 4th ed. (Springer, Berlin, 2010).
- [53] U. Rössler, *Solid State Theory: An Introduction*, 2nd ed. (Springer, Berlin, 2009).



## **PART III**

# **Lifetimes of Singlet-Triplet Qubits in Lateral Double Quantum Dots With and Without Detuning**

(Theory)



## Chapter 6

# Phonon-Mediated Decay of Singlet-Triplet Qubits in Double Quantum Dots

### Adapted from:

Viktoriia Kornich, Christoph Kloeffel, and Daniel Loss,  
Phys. Rev. B **89**, 085410 (2014).

We study theoretically the phonon-induced relaxation ( $T_1$ ) and decoherence times ( $T_2$ ) of singlet-triplet qubits in lateral GaAs double quantum dots (DQDs). When the DQD is biased, Pauli exclusion enables strong dephasing via two-phonon processes. This mechanism requires neither hyperfine nor spin-orbit interaction and yields  $T_2 \ll T_1$ , in contrast to previous calculations of phonon-limited lifetimes. When the DQD is unbiased, we find  $T_2 \simeq 2T_1$  and much longer lifetimes than in the biased DQD. For typical setups, the decoherence and relaxation rates due to one-phonon processes are proportional to the temperature  $T$ , whereas the rates due to two-phonon processes reveal a transition from  $T^2$  to higher powers as  $T$  is decreased. Remarkably, both  $T_1$  and  $T_2$  exhibit a maximum when the external magnetic field is applied along a certain axis within the plane of the two-dimensional electron gas. We compare our results with recent experiments and analyze the dependence of  $T_1$  and  $T_2$  on system properties such as the detuning, the spin-orbit parameters, the hyperfine coupling, and the orientation of the DQD and the applied magnetic field with respect to the main crystallographic axes.

## 6.1 Introduction

The spin states of quantum dots (QDs) are promising platforms for quantum computation [1, 2]. In particular, remarkable progress has been made with  $S$ - $T_0$  qubits in lateral GaAs double quantum dots (DQDs) [3–7], where a qubit is based on the spin singlet ( $S$ ) and triplet ( $T_0$ ) state of two electrons in the DQD. In this encoding scheme, rotations around the  $z$  axis of the Bloch sphere can be performed on a subnanosecond timescale [4] through the exchange interaction, and rotations around the  $x$  axis are enabled by magnetic field gradients across the QDs [5].

The lifetimes of  $S$ - $T_0$  qubits have been studied with great efforts. When the qubit state precesses around the  $x$  axis, dephasing mainly results from Overhauser field fluctuations, leading to short dephasing times  $T_2^* \sim 10$  ns [4, 8–12]. This low-frequency noise can be dynamically decoupled with echo pulses [4, 13–15], and long decoherence times  $T_2 > 200$   $\mu$ s have already been measured [14]. In contrast to  $x$  rotations, precessions around the  $z$  axis dephase predominantly due to charge noise [16, 17]. Rather surprisingly, however, recent Hahn echo experiments by Dial *et al.* [16] revealed a relatively short  $T_2 \simeq 0.1$ – $1$   $\mu$ s and a power-law dependence of  $T_2$  on the temperature  $T$ . The origin of the observed decoherence is so far unknown, although the dependence on  $T$  suggests that lattice vibrations (phonons) may play an important role.

In this work, we calculate the phonon-induced lifetimes of a  $S$ - $T_0$  qubit in a lateral GaAs DQD. Taking into account the spin-orbit interaction (SOI) and the hyperfine coupling, we show that one- and two-phonon processes can become the dominant decay channels in these systems and may lead to qubit lifetimes on the order of microseconds only. While the decoherence and relaxation rates due to one-phonon processes scale with  $T$  for the parameter range considered here, the rates due to two-phonon processes scale with  $T^2$  at rather high temperatures and obey power laws with higher powers of  $T$  as the temperature decreases. Among other things, the qubit lifetimes depend strongly on the applied magnetic field, the interdot distance, and the detuning between the QDs. Based on the developed theory, we discuss how the lifetimes can be significantly prolonged.

The chapter is organized as follows. In Sec. 6.2, we present the Hamiltonian and the basis states of our model. In the main part, Sec. 6.3, we discuss the calculation of the lifetimes in a biased DQD and investigate the results in detail. In particular, we show that two-phonon processes lead to short dephasing times and identify the magnetic field direction at which the lifetimes peak. The results for unbiased DQDs are discussed in Sec. 6.4, followed by our conclusions in Sec. 6.5. Details and further information are appended (Appendix E).

## 6.2 System, Hamiltonian, and Basis States

We consider a lateral GaAs DQD within the two-dimensional electron gas (2DEG) of an AlGaAs/GaAs heterostructure that is grown along the [001] direction, referred to as the  $z$  axis. Confinement in the  $x$ - $y$ -plane is generated by electric gates on the sample surface, and the magnetic field  $\mathbf{B}$  is applied in plane to avoid orbital effects. When the DQD is occupied by two electrons, the Hamiltonian of the system reads

$$H = \sum_{j=1,2} \left( H_0^{(j)} + H_Z^{(j)} + H_{\text{SOI}}^{(j)} + H_{\text{hyp}}^{(j)} + H_{\text{el-ph}}^{(j)} \right) + H_C + H_{\text{ph}}, \quad (6.1)$$

where the index  $j$  labels the electrons,  $H_0$  comprises the kinetic and potential energy of an electron in the DQD potential,  $H_Z$  is the Zeeman coupling,  $H_{\text{SOI}}$  is the SOI,  $H_{\text{hyp}}$  is the hyperfine coupling to the nuclear spins,  $H_{\text{el-ph}}$  is the electron-phonon coupling,  $H_C$  is the Coulomb repulsion, and  $H_{\text{ph}}$  describes the phonon bath.



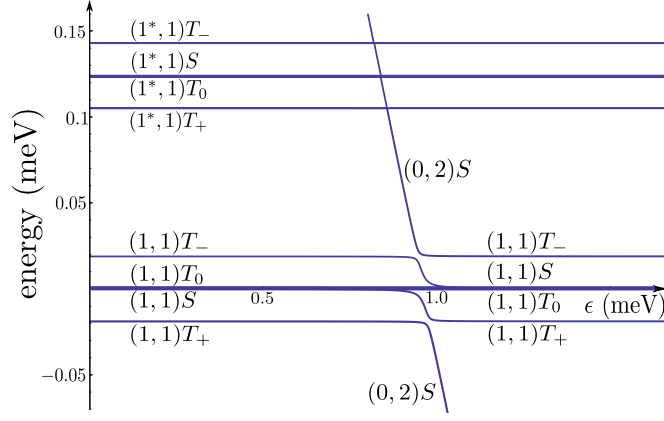


Figure 6.1. The energy spectrum of the DQD calculated for the parameters described in the text. The  $S$ - $T_0$  qubit is formed by the eigenstates of type  $|(1, 1)S\rangle$  and  $|(1, 1)T_0\rangle$ . The figure was provided by Viktoriia Kornich.

The electron-phonon interaction has the form

$$H_{\text{el-ph}} = \sum_{\mathbf{q}, s} W_s(\mathbf{q}) a_{\mathbf{q}s} e^{i\mathbf{q}\cdot\mathbf{r}} + \text{H.c.}, \quad (6.2)$$

where  $\mathbf{r}$  is the position of the electron,  $\mathbf{q}$  is a phonon wave vector within the first Brillouin zone,  $s \in \{l, t_1, t_2\}$  stands for the longitudinal ( $l$ ) and the two transverse ( $t_1, t_2$ ) phonon modes, and “H.c.” is the Hermitian conjugate. The coefficient  $W_s(\mathbf{q})$  depends strongly on  $\mathbf{q}$  and  $s$ , and is determined by material properties such as the relative permittivity  $\epsilon_r$ , the density  $\rho$ , the speed  $v_l$  ( $v_t$ ) of a longitudinal (transverse) sound wave, and the constants  $\Xi$  and  $h_{14}$  for the deformation potential and piezoelectric coupling, respectively. The annihilation operator for a phonon of wave vector  $\mathbf{q}$  and mode  $s$  is denoted by  $a_{\mathbf{q}s}$ . The Hamiltonian

$$H_{\text{SOI}} = \alpha (p_{x'} \sigma_{y'} - p_{y'} \sigma_{x'}) + \beta (p_{y'} \sigma_{y'} - p_{x'} \sigma_{x'}) \quad (6.3)$$

contains both Rashba and Dresselhaus SOI. Here  $p_{x'}$  and  $p_{y'}$  are the momentum operators for the  $x'$  and  $y'$  axes, respectively. The latter coincide with the crystallographic axes  $[100]$  and  $[010]$ , respectively, and  $\sigma_{x'}$  and  $\sigma_{y'}$  are the corresponding Pauli operators for the electron spin. We take into account the coupling to states of higher energy by performing a Schrieffer-Wolff transformation that removes  $H_{\text{SOI}}$  in lowest order [18–24]. The resulting Hamiltonian  $\tilde{H}$  is equivalent to  $H$ , except that  $H_{\text{SOI}}$  is replaced by

$$\tilde{H}_{\text{SOI}} \simeq g\mu_B (\mathbf{r}_{\text{SOI}} \times \mathbf{B}) \cdot \boldsymbol{\sigma}, \quad (6.4)$$

where  $g$  is the in-plane  $g$  factor,  $\boldsymbol{\sigma}$  is the vector of Pauli matrices, and

$$\mathbf{r}_{\text{SOI}} = \left( \frac{y'}{l_R} + \frac{x'}{l_D} \right) \mathbf{e}_{[100]} - \left( \frac{x'}{l_R} + \frac{y'}{l_D} \right) \mathbf{e}_{[010]}. \quad (6.5)$$

Here  $x'$  and  $y'$  are the coordinates of the electron along the main crystallographic axes, whose orientation is provided by the unit vectors  $\mathbf{e}_{[100]}$  and  $\mathbf{e}_{[010]}$ , respectively. The spin-orbit lengths are defined as  $l_R = \hbar/(m_{\text{eff}}\alpha)$  and  $l_D = \hbar/(m_{\text{eff}}\beta)$ , where  $m_{\text{eff}}$  is the effective electron mass in GaAs and  $\alpha$  ( $\beta$ ) is the Rashba (Dresselhaus) coefficient. For our analysis, the most relevant effect of the nuclear spins is the generation of an effective magnetic field gradient between the QDs, which is accounted for by  $H_{\text{hyp}}$ . We note that this magnetic field gradient may also result from a nearby positioned micromagnet [25–27]. For details of  $H$  and  $\tilde{H}$ , see Appendix E.2.

The  $S$ - $T_0$  qubit in this work is formed by the basis states  $|(1,1)S\rangle$  and  $|(1,1)T_0\rangle$ , where the notation  $(m,n)$  means that  $m$  ( $n$ ) electrons occupy the left (right) QD. In first approximation, these states read

$$|(1,1)S\rangle = |\Psi_+\rangle |S\rangle, \quad (6.6)$$

$$|(1,1)T_0\rangle = |\Psi_-\rangle |T_0\rangle, \quad (6.7)$$

with

$$|\Psi_\pm\rangle = \frac{|\Phi_L^{(1)}\Phi_R^{(2)}\rangle \pm |\Phi_R^{(1)}\Phi_L^{(2)}\rangle}{\sqrt{2}}, \quad (6.8)$$

where the  $\Phi_{L,R}(\mathbf{r})$  are orthonormalized single-electron wave functions for the left and right QD, respectively (see also Appendix E.1) [28, 29]. The spin singlet is

$$|S\rangle = \frac{|\uparrow\downarrow\rangle - |\downarrow\uparrow\rangle}{\sqrt{2}}, \quad (6.9)$$

whereas

$$|T_0\rangle = \frac{|\uparrow\downarrow\rangle + |\downarrow\uparrow\rangle}{\sqrt{2}}, \quad (6.10)$$

with the quantization axis of the spins along  $\mathbf{B}$ . Analogously, one can define the states  $|(1,1)T_+\rangle = |\Psi_-\rangle |\uparrow\uparrow\rangle$  and  $|(1,1)T_-\rangle = |\Psi_-\rangle |\downarrow\downarrow\rangle$ , which are energetically split from the qubit by  $\pm g\mu_B|\mathbf{B}|$ . For our analysis of the phonon-induced lifetimes, a simple projection of  $\tilde{H}$  onto this 4D subspace of lowest energy is not sufficient, because

$$\sum_j \left( \langle \Psi_+ | H_{\text{el-ph}}^{(j)} | \Psi_+ \rangle - \langle \Psi_- | H_{\text{el-ph}}^{(j)} | \Psi_- \rangle \right) = 0. \quad (6.11)$$

That is, corrections from higher states must be taken into account in order to obtain finite lifetimes [23, 30]. The spectrum that results from the states considered in our model is plotted in Fig. 6.1. Depending on the detuning  $\epsilon$  between the QDs, the lifetimes of the qubit are determined by admixtures from  $|(2,0)S\rangle$ ,  $|(0,2)S\rangle$ , or states with excited orbital parts.

## 6.3 Regime of Large Detuning

### 6.3.1 Effective Hamiltonian and Bloch-Redfield Theory

We first consider the case of a large, positive detuning  $\epsilon$  at which the energy gap between  $|(0,2)S\rangle$  and the qubit states is smaller than the orbital level spacing  $\hbar\omega_0$ . In this regime, contributions from states with excited orbital parts are negligible, and projection of  $\tilde{H}$  onto the basis states  $|(1,1)T_0\rangle$ ,  $|(1,1)S\rangle$ ,  $|(1,1)T_+\rangle$ ,  $|(1,1)T_-\rangle$ ,  $|(0,2)S\rangle$ , and  $|(2,0)S\rangle$  yields

$$\tilde{H} = \begin{pmatrix} P_T & \frac{\delta b_B}{2} & 0 & 0 & 0 & 0 \\ \frac{\delta b_B}{2} & V_+ - V_- + P_T & \frac{\Omega}{\sqrt{2}} & -\frac{\Omega}{\sqrt{2}} & -\sqrt{2}t + P_S^\dagger & -\sqrt{2}t + P_S \\ 0 & \frac{\Omega}{\sqrt{2}} & E_Z + P_T & 0 & 0 & 0 \\ 0 & -\frac{\Omega}{\sqrt{2}} & 0 & -E_Z + P_T & 0 & 0 \\ 0 & -\sqrt{2}t + P_S & 0 & 0 & -\epsilon + U - V_- + P_{SR} & 0 \\ 0 & -\sqrt{2}t + P_S^\dagger & 0 & 0 & 0 & \epsilon + U - V_- + P_{SL} \end{pmatrix} + H_{\text{ph}}. \quad (6.12)$$

Here  $P_T$ ,  $P_S$ ,  $P_S^\dagger$ ,  $P_{SL}$ , and  $P_{SR}$  are the matrix elements of the electron-phonon interaction,  $t$  is the tunnel coupling,  $U$  is the on-site repulsion,  $V_\pm = \langle \Psi_\pm | H_C | \Psi_\pm \rangle$ ,  $E_Z = g\mu_B|\mathbf{B}|$ ,

$$\Omega = g\mu_B (\langle \Phi_L | (\mathbf{r}_{\text{SOI}} \times \mathbf{B})_z | \Phi_L \rangle - \langle \Phi_R | (\mathbf{r}_{\text{SOI}} \times \mathbf{B})_z | \Phi_R \rangle), \quad (6.13)$$

and  $\delta b_B = 2\langle(1,1)S|H_{\text{hyp}}|(1,1)T_0\rangle$  (see also Appendix E.2.5). We note that the energy in Eq. (6.12) was globally shifted by  $\langle(1,1)T_0|(H_0^{(1)} + H_0^{(2)} + H_C)|(1,1)T_0\rangle$ . Furthermore, we mention that the state  $|(2,0)S\rangle$  is very well decoupled when  $\epsilon$  is large and positive. In Eq. (6.12),  $|(2,0)S\rangle$  is mainly included for illustration purposes, allowing also for large and negative  $\epsilon$  and for an estimate of the exchange energy at  $\epsilon \simeq 0$ .

In order to decouple the qubit subspace  $\{|(1,1)S\rangle, |(1,1)T_0\rangle\}$ , we first apply a unitary transformation to  $\tilde{H}$  that diagonalizes  $\tilde{H} - \sum_j H_{\text{el-ph}}^{(j)}$  exactly. Then we perform a third-order Schrieffer-Wolff transformation that provides corrections up to the third power in the electron-phonon coupling, which is sufficient for the analysis of one- and two-phonon processes. The resulting effective Hamiltonian can be written as  $H_q + H_{q\text{-ph}}(\tau) + H_{\text{ph}}$  in the interaction representation, where the time is denoted by  $\tau$  to avoid confusion with the tunnel coupling. Introducing the effective magnetic fields  $\mathbf{B}_{\text{eff}}$  and  $\delta\mathbf{B}(\tau)$  and defining  $\boldsymbol{\sigma}'$  as the vector of Pauli matrices for the  $S$ - $T_0$  qubit,

$$H_q = \frac{1}{2}g\mu_B\mathbf{B}_{\text{eff}} \cdot \boldsymbol{\sigma}' \quad (6.14)$$

describes the qubit and

$$H_{q\text{-ph}}(\tau) = \frac{1}{2}g\mu_B\delta\mathbf{B}(\tau) \cdot \boldsymbol{\sigma}' \quad (6.15)$$

describes the interaction between the qubit and the phonons. The time dependence results from

$$H_{q\text{-ph}}(\tau) = e^{iH_{\text{ph}}\tau/\hbar}H_{q\text{-ph}}e^{-iH_{\text{ph}}\tau/\hbar}. \quad (6.16)$$

For convenience, we define the basis of  $\boldsymbol{\sigma}'$  such that  $B_{\text{eff},x} = 0 = B_{\text{eff},y}$ . Following Refs. [20, 31], the decoherence time ( $T_2$ ), the relaxation time ( $T_1$ ), and the dephasing contribution ( $T_\varphi$ ) to  $T_2$  of the qubit can then be calculated via the Bloch-Redfield theory (see also Appendix E.5), which yields

$$\frac{1}{T_2} = \frac{1}{2T_1} + \frac{1}{T_\varphi}, \quad (6.17)$$

$$\frac{1}{T_1} = J_{xx}^+(\omega_Z) + J_{yy}^+(\omega_Z), \quad (6.18)$$

$$\frac{1}{T_\varphi} = J_{zz}^+(0), \quad (6.19)$$

where  $\hbar\omega_Z = J_{\text{tot}} = |g\mu_B\mathbf{B}_{\text{eff}}|$  and

$$J_{ii}^+(\omega) = \frac{g^2\mu_B^2}{2\hbar^2} \int_{-\infty}^{\infty} \cos(\omega\tau)\langle\delta B_i(0)\delta B_i(\tau)\rangle d\tau. \quad (6.20)$$

The correlator  $\langle\delta B_i(0)\delta B_i(\tau)\rangle$  is evaluated for a phonon bath in thermal equilibrium and depends strongly on the temperature  $T$ .

### 6.3.2 Input Parameters

The material properties of GaAs are  $g = -0.4$ ,  $m_{\text{eff}} = 6.1 \times 10^{-32}$  kg,  $\epsilon_r \simeq 13$ ,  $\rho = 5.32$  g/cm<sup>3</sup>,  $v_l \simeq 5.1 \times 10^3$  m/s and  $v_t \simeq 3.0 \times 10^3$  m/s (see also Appendix E.2.6.1) [32–34],  $h_{14} \simeq -0.16$  As/m<sup>2</sup> [33–35], and  $\Xi \approx -8$  eV [36, 37]. In agreement with  $\omega_0/(2\pi) = 30$  GHz [16], we set  $l_c = \sqrt{\hbar/(m_{\text{eff}}\omega_0)} \simeq 96$  nm, which is the confinement length of the QDs due to harmonic confining potential in the  $x$ - $y$  plane. For all basis states, the orbital part along the  $z$  axis is described by a Fang-Howard wave function [38] of width  $3a_z = 6$  nm (see Appendix E.1). Unless stated otherwise, we set  $l_R = 2$   $\mu\text{m}$  and  $l_D = 1$   $\mu\text{m}$  [39–41], where  $l_D$  is consistent with the assumed  $a_z$  (see also Appendix E.9) [41]. We note, however, that adapting  $a_z$  to  $l_D$  is not required, because changing the width of the 2DEG by several nanometers

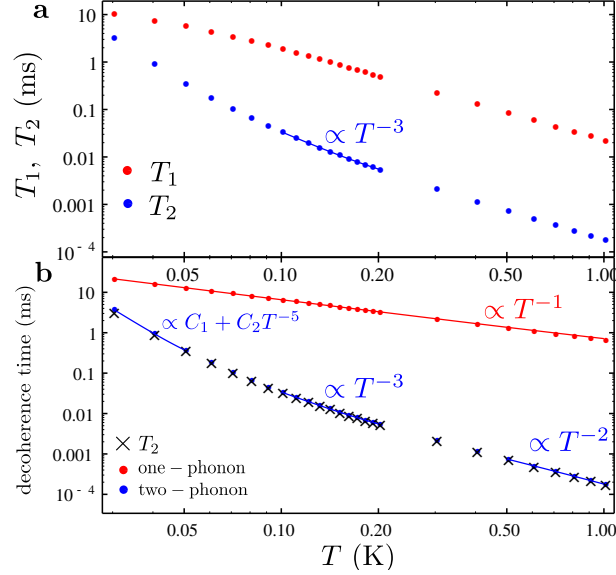


Figure 6.2. (a) Temperature dependence of the decoherence time ( $T_2$ , blue) and relaxation time ( $T_1$ , red) for the parameters in the text. The solid line corresponds to a power-law fit to  $T_2$  for  $0.1 \text{ K} \leq T \leq 0.2 \text{ K}$ , which yields  $T_2 \propto T^{-3}$  and good agreement with recent experiments [16]. We note that  $T_2 \ll T_1$ . (b) The decoherence time due to one-phonon ( $1/\Gamma_2^{1\text{P}}$ ) and two-phonon processes ( $1/\Gamma_2^{2\text{P}}$ ) and the full decoherence time  $T_2 = 1/\Gamma_2 = 1/(\Gamma_2^{1\text{P}} + \Gamma_2^{2\text{P}})$  as a function of temperature. We note that  $1/\Gamma_2^{2\text{P}}$  changes its behaviour from  $\propto C_1 + C_2 T^{-5}$  to  $\propto T^{-2}$ , where  $C_1$  and  $C_2$  are constants, whereas  $1/\Gamma_2^{1\text{P}} \propto T^{-1}$  for the range of  $T$  considered here. *The figure was provided by Viktoriia Kornich.*

turns out not to affect our results. All calculations are done for  $|\mathbf{B}| = 0.7 \text{ T}$  [6, 12],  $\delta b_B = -0.14 \mu\text{eV}$ , in good agreement with, e.g., Refs. [12, 16], and an interdot distance of  $2a = 400 \text{ nm}$ . For Figs. 6.1 to 6.5 (large  $\epsilon$ ), we use  $U = 1 \text{ meV}$ ,  $t = 7.25 \mu\text{eV}$ , and  $V_+ = 40 \mu\text{eV}$  [29]. We choose here  $V_- = 39.78 \mu\text{eV}$  such that the resulting energy splitting  $J_{\text{tot}}(\epsilon)$  between the qubit states is mostly determined by the hyperfine coupling at  $\epsilon \rightarrow 0$ , as commonly realized experimentally [4, 16]. The detuning  $\epsilon$  is then set such that  $0 < U - V_{\pm} - \epsilon < \hbar\omega_0$  and  $J_{\text{tot}} = 1.43 \mu\text{eV}$ , and we note that this splitting is within the range studied in Ref. [16].

### 6.3.3 Temperature Dependence

Figures 6.1 to 6.3 consider  $\mathbf{B}$  applied along the  $x$  axis that connects the two QDs, assuming that the  $x$  axis coincides with the crystallographic [110] direction. The geometry  $x \parallel [110]$  is realized in most experiments [13, 15, 17], particularly because GaAs cleaves nicely along [110]. In stark contrast to previous theoretical studies of phonon-limited lifetimes, where  $T_2 = 2T_1$  [20, 42–45], Fig. 6.2a reveals  $T_2 \ll T_1$  at  $30 \text{ mK} \leq T \leq 1 \text{ K}$  considered here, which implies  $T_\varphi \ll T_1$ . In the discussion below we therefore focus on the details of the temperature dependence of  $\Gamma_2 = 1/T_2$ . We note, however, that the contributions to  $\Gamma_2$  and  $\Gamma_1 = 1/T_1$  from one-phonon processes scale similarly with  $T$ , and analogously for two-phonon processes. Defining  $\Gamma_2^{1\text{P}}$  ( $\Gamma_2^{2\text{P}}$ ) as the decoherence rate due to one-phonon (two-phonon) processes, Fig. 6.2b illustrates  $\Gamma_2^{2\text{P}} \gg \Gamma_2^{1\text{P}}$ , and so  $\Gamma_2 = \Gamma_2^{1\text{P}} + \Gamma_2^{2\text{P}} \simeq \Gamma_2^{2\text{P}}$ . In the considered range of temperatures, we find  $\Gamma_2^{1\text{P}} \propto T$ . This behavior results from the fact that  $\hbar\omega_Z/(k_B T) < 1$  for our parameters, where  $k_B$  is the Boltzmann constant. Therefore, the dominant terms in the formula for  $\Gamma_2^{1\text{P}}$  are proportional to Bose-Einstein distributions defined as

$$n_B(\omega) = \frac{1}{e^{\hbar\omega/(k_B T)} - 1} \quad (6.21)$$

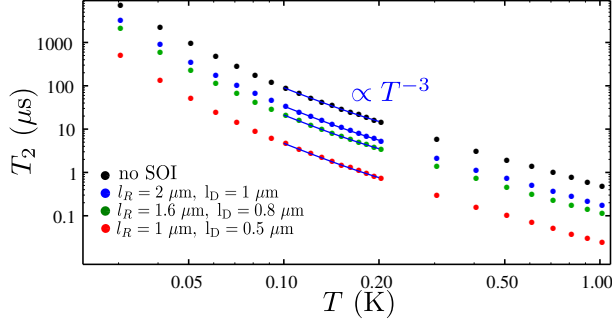


Figure 6.3. Dependence of the decoherence time  $T_2$  on the temperature for the parameters in the text and different spin-orbit lengths. Keeping the splitting  $J_{\text{tot}}$  between the qubit states constant, the values chosen for the detuning  $\epsilon$  are 0.896 meV (black), 0.912 meV (blue), 0.918 meV (green), and 0.933 meV (red), increasing with increasing SOI. Within the range  $T = 100\text{--}200$  mK,  $T_2 \propto T^{-3}$  in all cases. We note that the best quantitative agreement with the experiment [16] is obtained for the strongest SOI (red), where  $l_R = 1 \mu\text{m}$  and  $l_D = 0.5 \mu\text{m}$ . *The figure was provided by Viktoriia Kornich.*

and may all be expanded according to  $n_B(\omega) \simeq k_B T / (\hbar\omega)$ , keeping in mind that the  $n_B(\omega)$  contributing to  $\Gamma_2^{1\text{p}}$  are evaluated at  $\omega = \omega_Z$  because of energy conservation. The time  $1/\Gamma_2^{2\text{p}}$  due to two-phonon processes smoothly changes its behaviour from  $C_1 + C_2 T^{-5}$  at  $T \sim 40$  mK to  $T^{-2}$  with increasing temperature, where  $C_n$  are constants. This transition is explained by the fact that, in the continuum limit, the rate corresponds to an integral over the phonon wave vector  $\mathbf{q}$ , where the convergence of this integral is guaranteed by the combination of the Bose-Einstein distribution and the Gaussian suppression that results from averaging over the electron wave functions. More precisely, the decay rate is obtained by integrating over the wave vectors of the two involved phonons. Due to conservation of the total energy, however, considering only one wave vector  $\mathbf{q}$  is sufficient for this qualitative discussion. For  $\Gamma_2^{2\text{p}}$ , we find that the dominating terms decay with  $\mathbf{q}$  due to factors of type

$$f_s(\mathbf{q}) = e^{-(q_x^2 + q_y^2)l_c^2} n_B(\omega_{\mathbf{q}s}) [n_B(\omega_{\mathbf{q}s}) + 1], \quad (6.22)$$

where  $q_x$  and  $q_y$  are the projections of  $\mathbf{q}$  onto the  $x$  and  $y$  axes, respectively, and  $\hbar\omega_{\mathbf{q}s} = \hbar v_s |\mathbf{q}|$  is the phonon energy. Whether the Bose-Einstein part or the Gaussian part from  $f_s(\mathbf{q})$  provides the convergence of the integral depends on  $l_c$ ,  $v_s \in \{v_l, v_t\}$ , and mainly  $T$ , as the latter can be changed significantly. When the Gaussian part  $\exp[-(q_x^2 + q_y^2)l_c^2]$  cuts the integral,  $\Gamma_2^{2\text{p}} \propto T^2$  due to the expansion  $n_B(n_B + 1) \simeq (k_B T)^2 / (\hbar\omega_{\mathbf{q}s})^2$  that applies in this case. When  $n_B(n_B + 1)$  affects the convergence of the integral, terms with higher powers of  $T$  occur. The resulting temperature dependence is rather complex, but is usually well described by  $1/\Gamma_2^{2\text{p}} = C_m + C_n T^{-\nu}$  with  $\nu \geq 2$  for different ranges of  $T$  [see Fig. 6.2b]. The temperature ranges for the different regimes are determined by the details of the setup and the sample. For the parameters considered here, a power-law approximation  $T_2 \propto T^\eta$  for  $T = 100\text{--}200$  mK yields  $\eta \simeq -3$  mainly because of the dephasing due to two-phonon processes (see Figs. 6.2 and 6.3), which agrees well with the experimental data of Ref. [16].

Figure 6.3 shows the resulting temperature dependence of  $T_2$  for different spin-orbit lengths. Remarkably, the calculation yields short  $T_2$  even when SOI is completely absent. Keeping  $J_{\text{tot}} = 1.43 \mu\text{eV}$  fixed by adapting the value of  $\epsilon$ , one finds that  $T_2$  decreases further with increasing SOI. As seen in Eq. (6.12),  $\tilde{H}_{\text{SOI}}$  couples  $|(1, 1)S\rangle$  to the triplet states  $|(1, 1)T_+\rangle$  and  $|(1, 1)T_-\rangle$ . An important consequence of the resulting admixtures is that greater detunings are required in order to realize a desired  $J_{\text{tot}}$ . In Fig. 6.3, for instance,  $\epsilon$  increases from 0.896 meV (no SOI) to 0.933 meV ( $l_R = 1 \mu\text{m}$ ,  $l_D = 0.5 \mu\text{m}$ ). As explained below, increasing  $\epsilon$  decreases the lifetimes because it enhances the effects of  $|(0, 2)S\rangle$  through reduction of the energy gap (see also Fig. 6.1).

### 6.3.4 Origin of Strong Dephasing

The results discussed thus far have revealed two special features of the phonon-mediated lifetimes of  $S$ - $T_0$  qubits in biased DQDs. First,  $T_2 \ll T_1$ , as seen in Fig. 6.2a. Second, the strong decay does not require SOI, as seen in Fig. 6.3. These features have not been observed in previous calculations for, e.g., spin qubits formed by single-electron [20, 39] or single-hole [42, 43] or two-electron [23] states in GaAs QDs, hole-spin qubits in Ge/Si nanowire QDs [44], or electron-spin qubits in graphene QDs [45]. Therefore, we discuss the dominant decay mechanism for  $S$ - $T_0$  qubits in DQDs in further detail and provide an intuitive explanation for our results.

Assuming again a large, positive detuning  $\epsilon$ , with  $0 < U - V_{\pm} - \epsilon < \hbar\omega_0$ , and setting  $\Omega = 0$  (no SOI), the states  $|(1, 1)T_+\rangle$ ,  $|(1, 1)T_-\rangle$ , and  $|(0, 2)S\rangle$  of Eq. (6.12) are practically decoupled from the qubit. The relevant dynamics are then very well described by

$$\tilde{H} = \begin{pmatrix} 0 & \frac{\delta b_B}{2} & 0 \\ \frac{\delta b_B}{2} & V_+ - V_- & -\sqrt{2}t + P_S^\dagger \\ 0 & -\sqrt{2}t + P_S & -\epsilon + U - V_- + \tilde{P} \end{pmatrix} + H_{\text{ph}}, \quad (6.23)$$

with  $|(1, 1)T_0\rangle$ ,  $|(1, 1)S\rangle$ , and  $|(0, 2)S\rangle$  as the basis states and

$$\tilde{P} = P_{SR} - P_T. \quad (6.24)$$

In the absence of SOI, the hyperfine interaction ( $\delta b_B$ ) is the only mechanism that couples the spin states and enables relaxation of the  $S$ - $T_0$  qubit. We note that even when  $\Omega$  is nonzero, the relaxation times  $T_1$  are largely determined by the hyperfine coupling instead of the SOI for the parameters considered in this work. At sufficiently large temperatures, where  $T_2 \ll T_1$ ,  $\delta b_B$  is negligible in the calculation of  $T_2$ , leading to pure dephasing  $T_2 = T_\varphi$ . In addition, the matrix element  $P_S$  turns out to be negligible for our parameters. Following Appendix E.7, we finally obtain

$$\frac{1}{T_2} = \frac{1}{T_\varphi} = \frac{2t^4}{\hbar^2(\Delta'_S)^6} \int_{-\infty}^{\infty} \langle \tilde{P}^2(0)\tilde{P}^2(\tau) \rangle d\tau \quad (6.25)$$

from this simple model, where

$$\Delta'_S = \sqrt{(U - V_+ - \epsilon)^2 + 8t^2} \quad (6.26)$$

corresponds to the energy difference between the eigenstates of type  $|(1, 1)S\rangle$  and  $|(0, 2)S\rangle$  (using  $\delta_B = 0$ ). We note that terms of type  $a_{\mathbf{q}s}^\dagger a_{\mathbf{q}s}$  and  $a_{\mathbf{q}s} a_{\mathbf{q}s}^\dagger$  must be removed from  $\tilde{P}^2$  in Eq. (6.25), as the Bloch-Redfield theory requires  $\langle \delta \mathbf{B}(\tau) \rangle$  to vanish (see also Appendix E.7) [46]. In Fig. 6.4, we compare  $T_2$  from Eq. (6.25) with  $T_2$  derived from Eq. (6.12) for  $\Omega = 0$  (see also Fig. 6.3), and find excellent agreement at  $T \gtrsim 50$  mK where relaxation is negligible.

The above analysis provides further insight and gives explanations for the results observed in this work. First, Eq. (6.25) illustrates that dephasing requires two-phonon processes and cannot be achieved with a single phonon only. As dephasing leaves the energy of the electrons and the phonon bath unchanged, the single phonon would have to fulfill  $\omega_{\mathbf{q}s} = 0 = |\mathbf{q}|$ . However, phonons with infinite wavelengths do not affect the lifetimes, which can be explained both via  $e^{i\mathbf{q}\cdot\mathbf{r}} \rightarrow 1$  [see Eq. (6.2)] and via the vanishing density of states at  $\omega_{\mathbf{q}s} \rightarrow 0$  for acoustic phonons in bulk. Thus,  $\Gamma_2^{1\text{P}} = \Gamma_1^{1\text{P}}/2$  in all our calculations, where  $\Gamma_1^{1\text{P}}$  is the relaxation rate due to one-phonon processes. Second, as discussed above, we find that the hyperfine interaction in combination with electron-phonon coupling presents an important source of relaxation in this system [24]. Third, the strong dephasing at large detuning  $\epsilon$  results from two-phonon processes between states of type  $|(1, 1)S\rangle$  and  $|(0, 2)S\rangle$ . This mechanism is very effective because the spin state remains unchanged. Therefore, the dephasing requires neither SOI nor hyperfine coupling, and we note

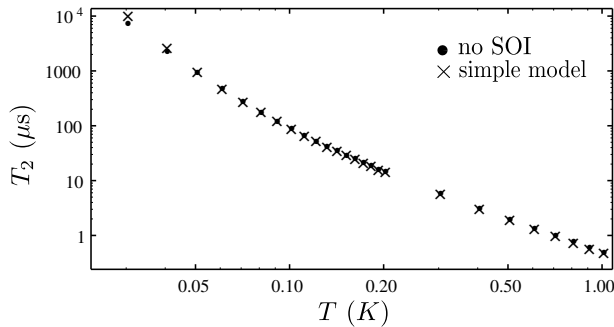


Figure 6.4. Decoherence time  $T_2$  as a function of temperature from two different models. The dotted line is also shown in Fig. 6.3 and was calculated via Eq. (6.12), using the parameters in the text with  $\Omega = 0$  (no SOI) and  $\epsilon = 0.896$  meV. The crosses result from Eq. (6.25), using exactly the same parameters. We note that the associated  $J_{\text{tot}}$  differ only slightly. The remarkable agreement demonstrates that the simple model of Sec. 6.3.4 accounts for the dominant decay mechanism. At  $T \lesssim 50$  mK, the curves start to deviate because relaxation is no longer negligible. When the hyperfine coupling in Eq. (6.23) is not omitted, excellent agreement is obtained also at low temperatures. *The figure was provided by Viktoriia Kornich.*

that Eq. (6.25) reveals a strong dependence of  $T_\varphi$  on the tunnel coupling  $t$  and the splitting  $\Delta'_S$ . Hence, the short  $T_\varphi$  in the biased DQD can be interpreted as a consequence of the Pauli exclusion principle. When the energy of the right QD is lowered ( $\epsilon > 0$ ), the singlet state of lowest energy changes from  $|(1,1)S\rangle$  toward  $|(0,2)S\rangle$  since the symmetric orbital part of the wave function allows double-occupancy of the orbital ground state in the right QD. The triplet states, however, remain in the (1,1) charge configuration. While this feature allows tuning of the exchange energy and readout via spin-to-charge conversion on the one hand [4], it enables strong dephasing via electron-phonon coupling on the other hand: effectively, phonons lead to small fluctuations in  $\epsilon$ ; due to Pauli exclusion, these result in fluctuations of the exchange energy and, thus, in dephasing [47]. This mechanism is highly efficient in biased DQDs, but strongly suppressed in unbiased ones, as we show in Sec. 6.4 and Appendix E.8.

We note that the discussed dephasing mechanism that does not require SOI or hyperfine coupling corresponds to a two-phonon Raman process and has been studied before for impurity atoms [48–51], particularly in the presence of singlet states [49–51]. The same mechanism is used in Ref. [47] to analyze the dephasing of singlet-triplet qubits in unbiased DQDs. We note that the conclusions of Ref. [47] and our work substantially differ from each other. While Ref. [47] finds dominant dephasing times due to this Raman process, we find that this process for dephasing is negligible in the unbiased regime for realistic DQD parameter values (see also Appendix E.8).

### 6.3.5 Angular Dependence

We also calculate the dependence of  $T_1$  and  $T_2$  on the angle between  $\mathbf{B}$  and the  $x$  axis, assuming that  $x \parallel [110]$ . The results for  $T = 100$  mK and  $J_{\text{tot}} = 1.43$   $\mu\text{eV}$  are plotted in Fig. 6.5. Remarkably, the phonon-induced lifetimes of the qubit are maximal when  $\mathbf{B} \perp x$  and minimal when  $\mathbf{B} \parallel x$ . The difference between minimum and maximum increases strongly with the SOI, and for  $l_R = 1$   $\mu\text{m}$  and  $l_D = 0.5$   $\mu\text{m}$  we already expect improvements by almost two orders of magnitude. These features can be understood via the matrix elements of the effective SOI [22–24],

$$\Omega = F_{\text{SOI}}(a, l_c) E_Z \frac{l_D \cos(\theta_B - \theta) + l_R \cos(\theta_B + \theta)}{l_D l_R}, \quad (6.27)$$

where  $\theta_B$  ( $\theta$ ) is the angle between  $\mathbf{B}$  (the  $x$  axis) and the crystallographic axis [110], and  $F_{\text{SOI}}(a, l_c)$  is a function of  $a$  and  $l_c$ . From this result, we conclude that there always exists an optimal orientation for the in-plane magnetic field for which the effective SOI is suppressed and, thus, for which the phonon-mediated decay of the qubit state is minimal (comparing the lifetimes at fixed  $J_{\text{tot}}$ ). Remarkably, one

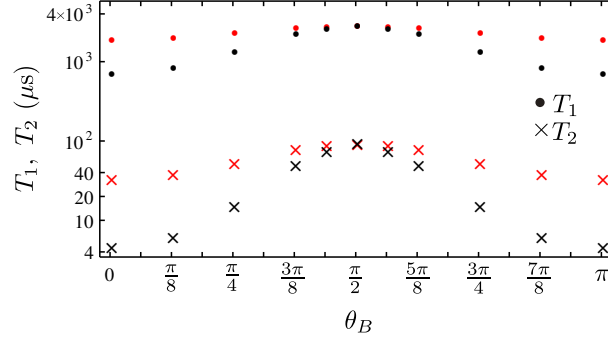


Figure 6.5. Dependence of the relaxation ( $T_1$ ) and decoherence time ( $T_2$ ) on the angle  $\theta_B$  between the in-plane magnetic field  $\mathbf{B}$  and the  $x$  axis that connects the QDs. When  $\mathbf{B} \perp x$  ( $\theta_B = \pi/2$ ), both  $T_1$  and  $T_2$  exhibit a maximum. Red (black) corresponds to the spin-orbit lengths  $l_R = 2 \mu\text{m}$  and  $l_D = 1 \mu\text{m}$  ( $l_R = 1 \mu\text{m}$  and  $l_D = 0.5 \mu\text{m}$ ). For the stronger SOI, the lifetimes increase by almost two orders of magnitude. For details, see text. *The figure was provided by Viktoriia Kornich.*

finds for  $x \parallel [110]$  ( $\theta = 0$ ) that this suppression always occurs when  $\mathbf{B} \perp x$  ( $\theta_B = \pi/2$ ), independent of  $l_R$  and  $l_D$ . In the case where  $\Omega = 0$ , the finite  $T_2$  in our model results from admixtures with  $|(0, 2)S\rangle$ , as explained in Sec. 6.3.4. Due to the hyperfine interaction, these admixtures also lead to finite  $T_1$ . We wish to emphasize, however, that suppression of the effective SOI only results in a substantial prolongation of the lifetimes when the spin-orbit lengths are rather short, as the dominant decay mechanism in biased DQDs is very effective even at  $\Omega = 0$ .

## 6.4 Regime of Small Detuning

All previous results were calculated for a large detuning  $\epsilon \sim U - V_{\pm}$ . Now we consider an unbiased DQD, i.e., the region of very small  $\epsilon$ . The dominant decay mechanism in the biased DQD is strongly suppressed at  $\epsilon \simeq 0$ , where the basis states  $|(2, 0)S\rangle$  and  $|(0, 2)S\rangle$  are both split from  $|(1, 1)S\rangle$  by a large energy  $U - V_+$ . Adapting the simple model behind Eq. (6.25) to an unbiased DQD yields

$$\frac{8t^4}{\hbar^2(U - V_+)^6} \int_{-\infty}^{\infty} \langle \tilde{P}^2(0) \tilde{P}^2(\tau) \rangle d\tau \quad (6.28)$$

as the associated dephasing time (see Appendix E.8 for details). Comparing the prefactor with that of Eq. (6.25) results in a remarkable suppression factor below  $10^{-4}$  for the parameters in this work. As explained in Appendix E.8, this suppression factor may also be estimated via  $(\Delta'_S)^4 / (U - V_+)^4$  for fixed  $J_{\text{tot}}$ , where  $\Delta'_S$  is the splitting between the eigenstates of type  $|(1, 1)S\rangle$  and  $|(0, 2)S\rangle$  at large  $\epsilon$  and  $U - V_+$  is the above-mentioned splitting at  $\epsilon \simeq 0$ .

Consequently, the lifetimes  $T_1$  and  $T_2$  in the unbiased DQD are no longer limited by  $|(2, 0)S\rangle$  or  $|(0, 2)S\rangle$ , but by states with an excited orbital part (see Fig. 6.1). We therefore extend the subspace by the basis states  $|(1^*, 1)S\rangle$ ,  $|(1^*, 1)T_0\rangle$ ,  $|(1^*, 1)T_+\rangle$ , and  $|(1^*, 1)T_-\rangle$ , and proceed analogously to the case of large detuning (see Appendixes E.1 and E.3 for details). The asterisk denotes that the electron is in the first excited state, leading to an energy gap of  $\hbar\omega_0$  compared to the states without asterisk. Setting  $\mathbf{B} \parallel x \parallel [110]$ , the orbital excitation is taken along the  $x$  axis, because states with the excitation along  $y$  turn out to have negligible effects on the qubit lifetimes. From symmetry considerations, states with the excited electron in the right QD should only provide quantitative corrections of the lifetimes by factors on the order of 2 and are therefore neglected in this analysis. The resulting temperature dependence of  $T_2$ ,  $1/\Gamma_2^{1\text{p}}$ , and  $1/\Gamma_2^{2\text{p}}$  is shown in Fig. 6.6. The plotted example illustrates that two-phonon processes affect  $T_2$  only at rather high temperatures when  $\epsilon$  is small, leading to  $T_2 \propto T^{-1}$  for a wide range of  $T$  due to single-phonon processes. In stark contrast to the biased DQD, we find  $T_2 \simeq 2T_1$ . Remarkably,



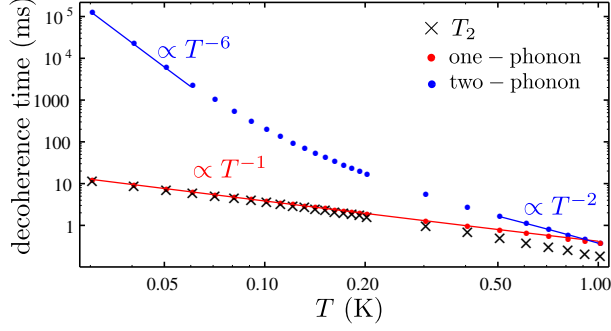


Figure 6.6. Temperature dependence of the decoherence time ( $T_2$ ) and its one-phonon ( $1/\Gamma_2^{1P}$ ) and two-phonon ( $1/\Gamma_2^{2P}$ ) parts for the detuning  $\epsilon \simeq 0$ , where excited states are taken into account. For this plot,  $U = 1$  meV,  $V_+ = 50$   $\mu$ eV,  $V_- = 49.5$   $\mu$ eV,  $t = 24$   $\mu$ eV,  $J_{\text{tot}} = 1.41$   $\mu$ eV, and the other parameters as described in the text. We note that  $T_2 \simeq 2T_1$ . The figure was provided by Viktoriia Kornich.

the absolute value of  $T_2$  is of the order of milliseconds, which exceeds the  $T_2$  at large  $\epsilon$  by 2–3 orders of magnitude. For  $\mathbf{B} \perp x$ ,  $x \parallel [110]$ , and typical sample temperatures  $T \sim 0.1$  K, we find that the lifetimes can be enhanced even further.

## 6.5 Conclusions and Outlook

In conclusion, we showed that one- and two-phonon processes can be major sources of relaxation and decoherence for  $S$ - $T_0$  qubits in DQDs. Our theory provides a possible explanation for the experimental data of Ref. [16], and we predict that the phonon-induced lifetimes are prolonged by orders of magnitude at small detunings and, when the SOI is strong, at certain orientations of the magnetic field. Our results may also allow substantial prolongation of the relaxation time recently measured in resonant exchange qubits [52].

While the model developed in this work applies to a wide range of host materials, the resulting lifetimes depend on the input parameters and, thus, on the setup and the heterostructure. By separately neglecting the deformation potential coupling ( $\Xi = 0$ ) and the piezoelectric coupling ( $h_{14} = 0$ ), we find that the qubit lifetimes of Figs. 6.2 to 6.6 for GaAs DQDs are limited by the piezoelectric electron-phonon interaction, the latter providing much greater decay rates than the deformation potential coupling. Consequently, the phonon-limited lifetimes of singlet-triplet qubits may be long in group-IV materials such as Ge or Si [53–55], where the piezoelectric effect is absent due to bulk inversion symmetry.

Essentially, there are two different schemes for manipulating singlet-triplet qubits in DQDs electrically. The first and commonly realized approach is based on biased DQDs and uses the detuning to control the exchange energy [4]. Alternatively, the exchange energy can be controlled by tuning the tunnel barrier [1] rather than the detuning. Our results suggest that the second approach is advantageous, as it applies to unbiased DQDs for which the phonon-mediated decay of the qubit state is strongly suppressed. In addition, one finds  $dJ_{\text{tot}}/d\epsilon \propto \epsilon$  at very small detunings  $\epsilon$  [28], which implies that not only  $dJ_{\text{tot}}/d\epsilon \simeq 0$  but also  $\langle dJ_{\text{tot}}/d\epsilon \rangle \simeq 0$  at  $\epsilon \simeq 0$ , where  $\langle \dots \rangle$  now stands for the average over some random fluctuations of  $\epsilon$ . Therefore, singlet-triplet qubits in unbiased DQDs are also protected against electrical noise. The latter, for instance, turned out to be a major obstacle for the implementation of high-fidelity controlled-phase gates between  $S$ - $T_0$  qubits [6]. Keeping in mind that two-qubit gates for singlet-triplet qubits may also be realized with unbiased DQDs [7], we conclude that operation at  $\epsilon \simeq 0$  with a tunable tunnel barrier is a promising alternative to the commonly realized schemes that require nonzero detuning. As single-qubit gates for  $S$ - $T_0$  qubits correspond to two-qubit gates for single-electron spin qubits, the regime  $\epsilon \simeq 0$  is also beneficial for many other encoding schemes.

## **Acknowledgments**

We thank P. Stano, F. L. Pedrocchi, M. Trif, J. R. Wootton, R. Zielke, H. Bluhm, and A. Yacoby for helpful discussions and acknowledge support from the Swiss NF, NCCR QSIT, S<sup>3</sup>NANO, and IARPA.

# References

- [1] D. Loss and D. P. DiVincenzo, *Phys. Rev. A* **57**, 120 (1998).
- [2] C. Kloeffel and D. Loss, *Annu. Rev. Condens. Matter Phys.* **4**, 51 (2013).  
See Chapter 1
- [3] J. Levy, *Phys. Rev. Lett.* **89**, 147902 (2002).
- [4] J. R. Petta, A. C. Johnson, J. M. Taylor, E. A. Laird, A. Yacoby, M. D. Lukin, C. M. Marcus, M. P. Hanson, and A. C. Gossard, *Science* **309**, 2180 (2005).
- [5] S. Foletti, H. Bluhm, D. Mahalu, V. Umansky, and A. Yacoby, *Nat. Phys.* **5**, 903 (2009).
- [6] M. D. Shulman, O. E. Dial, S. P. Harvey, H. Bluhm, V. Umansky, A. Yacoby, *Science* **336**, 202 (2012).
- [7] J. Klinovaja, D. Stepanenko, B. I. Halperin, and D. Loss, *Phys. Rev. B* **86**, 085423 (2012).
- [8] A. V. Khaetskii, D. Loss, and L. Glazman, *Phys. Rev. Lett.* **88**, 186802 (2002).
- [9] I. A. Merkulov, A. L. Efros, and M. Rosen, *Phys. Rev. B* **65**, 205309 (2002).
- [10] W. A. Coish and D. Loss, *Phys. Rev. B* **70**, 195340 (2004).
- [11] A. C. Johnson, J. R. Petta, J. M. Taylor, A. Yacoby, M. D. Lukin, C. M. Marcus, M. P. Hanson, and A. C. Gossard, *Nature (London)* **435**, 925 (2005).
- [12] H. Bluhm, S. Foletti, D. Mahalu, V. Umansky, and A. Yacoby, *Phys. Rev. Lett.* **105**, 216803 (2010).
- [13] C. Barthel, J. Medford, C. M. Marcus, M. P. Hanson, and A. C. Gossard, *Phys. Rev. Lett.* **105**, 266808 (2010).
- [14] H. Bluhm, S. Foletti, I. Neder, M. Rudner, D. Mahalu, V. Umansky, and A. Yacoby, *Nat. Phys.* **7**, 109 (2011).
- [15] J. Medford, L. Cywinski, C. Barthel, C. M. Marcus, M. P. Hanson, and A. C. Gossard, *Phys. Rev. Lett.* **108**, 086802 (2012).
- [16] O. E. Dial, M. D. Shulman, S. P. Harvey, H. Bluhm, V. Umansky, and A. Yacoby, *Phys. Rev. Lett.* **110**, 146804 (2013).
- [17] A. P. Higginbotham, F. Kuemmeth, M. P. Hanson, A. C. Gossard, and C. M. Marcus, *Phys. Rev. Lett.* **112**, 026801 (2014).
- [18] A. V. Khaetskii and Y. V. Nazarov, *Phys. Rev. B* **61**, 12639 (2000).
- [19] I. L. Aleiner and V. I. Fal'ko, *Phys. Rev. Lett.* **87**, 256801 (2001).
- [20] V. N. Golovach, A. V. Khaetskii, and D. Loss, *Phys. Rev. Lett.* **93**, 016601 (2004).
- [21] P. Stano and J. Fabian, *Phys. Rev. B* **72**, 155410 (2005).

- [22] P. Stano and J. Fabian, Phys. Rev. Lett. **96**, 186602 (2006).
- [23] V. N. Golovach, A. V. Khaetskii, and D. Loss, Phys. Rev. B **77**, 045328 (2008).
- [24] M. Raith, P. Stano, F. Baruffa, and J. Fabian, Phys. Rev. Lett. **108**, 246602 (2012).
- [25] E. A. Laird, C. Barthel, E. I. Rashba, C. M. Marcus, M. P. Hanson, and A. C. Gossard, Phys. Rev. Lett. **99**, 246601 (2007).
- [26] M. Pioro-Ladrière, T. Obata, Y. Tokura, Y.-S. Shin, T. Kubo, K. Yoshida, T. Taniyama, and S. Tarucha, Nat. Phys. **4**, 776 (2008).
- [27] R. Brunner, Y.-S. Shin, T. Obata, M. Pioro-Ladrière, T. Kubo, K. Yoshida, T. Taniyama, Y. Tokura, and S. Tarucha, Phys. Rev. Lett. **107**, 146801 (2011).
- [28] G. Burkard, D. Loss, and D. P. DiVincenzo, Phys. Rev. B **59**, 2070 (1999).
- [29] D. Stepanenko, M. Rudner, B. I. Halperin, and D. Loss, Phys. Rev. B **85**, 075416 (2012).
- [30] T. Meunier, I. T. Vink, L. H. Willems van Beveren, K.-J. Tielrooij, R. Hanson, F. H. L. Koppens, H. P. Tranitz, W. Wegscheider, L. P. Kouwenhoven, and L. M. K. Vandersypen, Phys. Rev. Lett. **98**, 126601 (2007).
- [31] M. Borhani, V. N. Golovach, and D. Loss, Phys. Rev. B **73**, 155311 (2006).
- [32] A. N. Cleland, *Foundations of Nanomechanics: From Solid-State Theory to Device Applications* (Springer, Berlin, 2003).
- [33] S. Adachi, *Properties of Group-IV, III-V and II-VI Semiconductors* (Wiley, Chichester, 2005).
- [34] <http://www.ioffe.ru/SVA/NSM/Semicond/GaAs>.
- [35] K. Hübner, Phys. Status Solidi B **57**, 627 (1973).
- [36] S. Adachi, *GaAs and Related Materials: Bulk Semiconducting and Superlattice Properties* (World Scientific, Singapore, 1994).
- [37] C. G. Van de Walle, Phys. Rev. B **39**, 1871 (1989).
- [38] F. F. Fang and W. E. Howard, Phys. Rev. Lett. **16**, 797 (1966).
- [39] A. V. Khaetskii and Y. V. Nazarov, Phys. Rev. B **64**, 125316 (2001).
- [40] R. Hanson, L. P. Kouwenhoven, J. R. Petta, S. Tarucha, and L. M. K. Vandersypen, Rev. Mod. Phys. **79**, 1217 (2007).
- [41] R. Winkler, *Spin-Orbit Coupling Effects in Two-Dimensional Electron and Hole Systems* (Springer, Berlin, 2003).
- [42] D. V. Bulaev and D. Loss, Phys. Rev. Lett. **95**, 076805 (2005).
- [43] M. Trif, P. Simon, and D. Loss, Phys. Rev. Lett. **103**, 106601 (2009).
- [44] F. Maier, C. Kloeffel, and D. Loss, Phys. Rev. B **87**, 161305(R) (2013).  
See Chapter 3
- [45] M. O. Hachiya, G. Burkard, and J. C. Egues, Phys. Rev. B **89**, 115427 (2014).
- [46] C. P. Slichter, *Principles of Magnetic Resonance* (Springer, Berlin, 1980).

- [47] K. Roszak and P. Machnikowski, Phys. Rev. B **80**, 195315 (2009).
- [48] D. E. McCumber and M. D. Sturge, J. Appl. Phys. **34**, 1682 (1963).
- [49] W. M. Yen, W. C. Scott, and A. L. Schawlow, Phys. Rev. **136**, A271 (1964).
- [50] S. B. Altner, G. Zumofen, U. P. Wild, and M. Mitsunaga, Phys. Rev. B **54**, 17493 (1996).
- [51] R. S. Meltzer, in *Spectroscopic Properties of Rare Earths in Optical Materials*, edited by G. Liu and B. Jacquier (Springer, Berlin, 2005), Chap. 4, pp. 191–265.
- [52] J. Medford, J. Beil, J. M. Taylor, E. I. Rashba, H. Lu, A. C. Gossard, and C. M. Marcus, Phys. Rev. Lett. **111**, 050501 (2013).
- [53] B. M. Maune, M. G. Borselli, B. Huang, T. D. Ladd, P. W. Deelman, K. S. Holabird, A. A. Kiselev, I. Alvarado-Rodriguez, R. S. Ross, A. E. Schmitz, M. Sokolich, C. A. Watson, M. F. Gyure, and A. T. Hunter, Nature (London) **481**, 344 (2012).
- [54] J. R. Prance, Z. Shi, C. B. Simmons, D. E. Savage, M. G. Lagally, L. R. Schreiber, L. M. K. Vandersypen, M. Friesen, R. Joynt, S. N. Coppersmith, and M. A. Eriksson, Phys. Rev. Lett. **108**, 046808 (2012).
- [55] F. A. Zwanenburg, A. S. Dzurak, A. Morello, M. Y. Simmons, L. C. L. Hollenberg, G. Klimeck, S. Rogge, S. N. Coppersmith, and M. A. Eriksson, Rev. Mod. Phys. **85**, 961 (2013).



## **PART IV**

# **Optical and Electrical Control of the Nuclear Spin Polarization and the Photoluminescence of a Self-Assembled Quantum Dot**

(Experiment & Theory)





## Chapter 7

# Controlling the Interaction of Electron and Nuclear Spins in a Tunnel-Coupled Quantum Dot

**Adapted from:**

Christoph Kloeffer, Paul A. Dalgarno, Bernhard Urbaszek, Brian D. Gerardot, Daniel Brunner, Pierre M. Petroff, Daniel Loss, and Richard J. Warburton, *Phys. Rev. Lett.* **106**, 046802 (2011).

We present a technique for manipulating the nuclear spins and the emission polarization from a single optically active quantum dot. When the quantum dot is tunnel coupled to a Fermi sea, we have discovered a natural cycle in which an electron spin is repeatedly created with resonant optical excitation. The spontaneous emission polarization and the nuclear spin polarization exhibit a bistability. For a  $\sigma^+$  pump, the emission switches from  $\sigma^+$  to  $\sigma^-$  at a particular detuning of the laser. Simultaneously, the nuclear spin polarization switches from positive to negative. Away from the bistability, the nuclear spin polarization can be changed continuously from negative to positive, allowing precise control via the laser wavelength.

## 7.1 Introduction

Semiconductor quantum dots are very attractive for applications as qubits [1] and sources of quantum light [2–4]. Versatile materials are the III-V semiconductors, notably GaAs which has established itself as the workhorse material. A significant property is that all the Ga, As, and In isotopes have large nuclear spins. In a typical quantum dot there is an intermediate number of atoms, too large to use each nuclear spin as a resource yet too small for efficient cancellation in the total spin, and noise in the nuclear spins limits the electron spin coherence to just  $\sim 10$  ns through the hyperfine interaction [5–7]. An emerging theme is that the nuclear spin noise may be reduced by narrowing the distribution [8–11] and that the nuclear spin ensemble may represent as much opportunity as trouble. Currently, schemes exist to tune both the optical transition energy [12] and the selection rules [13] of a quantum dot in situ, but presently, the possibilities of using nuclear spins beneficially are limited.

We present here a new control over the electron-nuclear-spin interaction on driving an optical transition resonantly. Dynamic nuclear polarization at the single quantum dot level is established [14–18]. The crucial advance here is to operate in the tunneling regime [17, 18] where we discover a natural cycle. There are two interrelated features. First, spontaneous emission following resonant excitation either preserves the circular polarization of the source or inverts it. For instance, with a  $\sigma^+$  pump, we can switch from predominantly  $\sigma^+$  to  $\sigma^-$  emission either with a small change in pump wavelength or device bias allowing the polarization of a single photon source to be controlled in situ. Secondly, the resonant excitation creates a large nuclear spin polarization which changes sign abruptly at the bistability, a new feature compared to the bistabilities following nonresonant optical excitation [14, 19]. At smaller laser wavelengths, the nuclear spin polarization changes monotonically from a large negative value to a large positive value. This bidirectional tuning is demonstrated here at low magnetic fields (0.5 T), and complements the optical dragging effect at high magnetic fields [12]. Control of the nuclear spins via the optical wavelength is a powerful route to narrowing the distribution [12] and to tuning the quantum dot exciton over tens of  $\mu\text{eV}$ .

## 7.2 Setup

Our experiments use a field effect device in which InGaAs self-assembled quantum dots are in tunnel contact with an  $n^+$  GaAs Fermi sea via a 25 nm thick GaAs tunnel barrier [20]. A voltage is applied to a Schottky contact on the sample surface, 150 nm above the quantum dot layer, at 4.2 K. Photoluminescence (PL) is excited either nonresonantly at 830 nm wavelength, or resonantly using 13 kW/cm<sup>2</sup> from a tunable narrowband cw laser. The PL is dispersed with a monochromator and detected with a CCD array detector, a system with resolution 50  $\mu\text{eV}$ . The polarization of excitation and collection are independently controlled. A small magnetic field,  $B_z = +0.5$  T, is applied along the growth  $z$  direction.

## 7.3 Natural Cycle in the Hybridization Region

Excited nonresonantly, the PL from a single quantum dot shows a clear charging step from the neutral exciton,  $X^0$ , to the negatively charged trion,  $X^{1-}$ . The energies of the initial states  $|X^0\rangle$  and  $|X^{1-}\rangle$ , and their corresponding final states,  $|0\rangle$  (vacuum) and  $|e\rangle$  (single electron), as a function of gate voltage are shown in Fig. 7.1. In the final states (no hole present), the ground state charges from  $|0\rangle$  to  $|e\rangle$  at a more positive voltage than the change in the initial states from  $|X^0\rangle$  to  $|X^{1-}\rangle$  [20], a consequence of the different electron-hole and electron-electron Coulomb energies. A “hybridization region” is created, a voltage region in which both excitons are tunnel coupled to the Fermi sea,  $X^0$  in the initial state,  $X^{1-}$  in the final state [20]. We show here that this region is ideal for controlling the electron-nuclear-spin interaction.

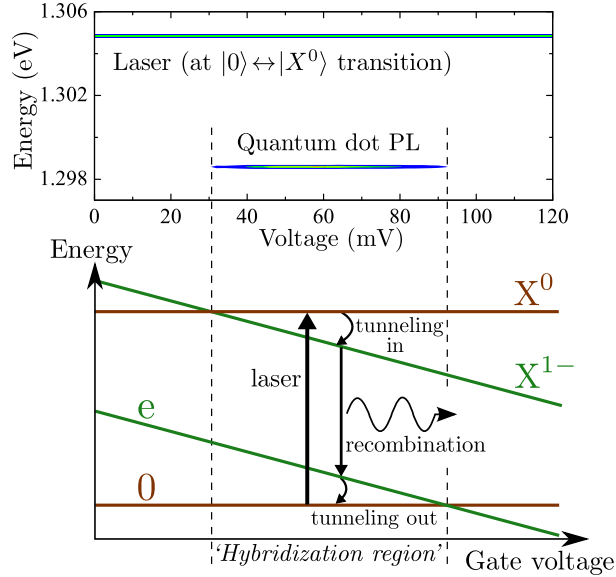


Figure 7.1. Top: Photoluminescence (PL) at 4.2 K from a single quantum dot versus bias driven with excitation at the  $X^0$  energy.  $X^{1-}$  PL appears in a narrow range of voltage, the hybridization regime. Bottom: Energy dependence versus bias for the quantum dot vacuum state  $|0\rangle$  and the single electron state  $|e\rangle$ , showing a crossing where the ground state changes.  $X^0$  and  $X^{1-}$  cross at lower bias on account of the hole. Within the hybridization region, automatic cycling takes place when a laser is tuned to the  $|0\rangle \leftrightarrow |X^0\rangle$  transition. An electron tunneling from the Fermi sea turns the  $|X^0\rangle$  into  $|X^{1-}\rangle$ ; recombination leaves the system in state  $|e\rangle$ ; tunneling out returns the dot to  $|0\rangle$ .

Figure 7.1 shows the result of pumping the  $|0\rangle \leftrightarrow |X^0\rangle$  transition of a single quantum dot. Over a small region of voltage,  $X^{1-}$  PL is observed, redshifted by 6 meV with respect to the laser. A comparison with the nonresonantly excited PL demonstrates that this region corresponds to the low bias edge of the  $X^{1-}$  plateau, i.e., the hybridization region, and that the resonantly excited PL has the  $X^0$  energy. In terms of the level diagram in Fig. 7.1, the dot is initially in the vacuum state  $|0\rangle$ . The laser then creates an  $X^0$ , which, although neutral, is unstable with respect to tunneling. Electron tunneling into the dot (time scale  $\sim 50$  ps, considerably shorter than the radiative lifetime of  $\sim 1$  ns) creates an  $X^{1-}$  which then recombines. After spontaneous emission, the dot is in the  $|e\rangle$  state. Now that the hole has disappeared, this state is also unstable with respect to tunneling: electron tunneling out of the dot (time scale  $\sim 10$  ps) returns the dot to  $|0\rangle$  whereupon the process can be repeated. This cycle offers a number of attractive features. First, the  $X^0$  spin is determined by the polarization of the laser through the optical selection rules. Second, the cycle round-trip time is small, just  $\sim 1$  ns, limited only by spontaneous emission. Third, the redshift of the PL with respect to the excitation makes it easy to distinguish spontaneous emission from scattered laser light even though one of the transitions is driven resonantly. The PL is useful in its own right as an antibunched source. It also provides an in situ monitor of the nuclear spin polarization through the Overhauser shift. Finally, the process can be described quantitatively with no ad hoc assumptions.

## 7.4 Control of Emission Polarization and Overhauser Field

The main experiment consists of monitoring the  $X^{1-}$  PL as a function of laser detuning with respect to the  $X^0$  transition for a constant pump polarization, e.g.,  $\sigma^+$ . A PL spectrum is recorded for both  $\sigma^+$  and  $\sigma^-$  polarizations. These counts-energy spectra are fitted to Lorentzians [21], yielding both the signal energy  $E(\sigma^\pm)$  (center of Lorentzian) and the signal intensity  $S(\sigma^\pm)$  (area under Lorentzian). Figure 7.2 shows both  $S(\sigma^+)$  and  $S(\sigma^-)$  for a  $\sigma^+$  pump, and the associated polarization degree

$$P = \frac{S(\sigma^+) - S(\sigma^-)}{S(\sigma^+) + S(\sigma^-)}. \quad (7.1)$$

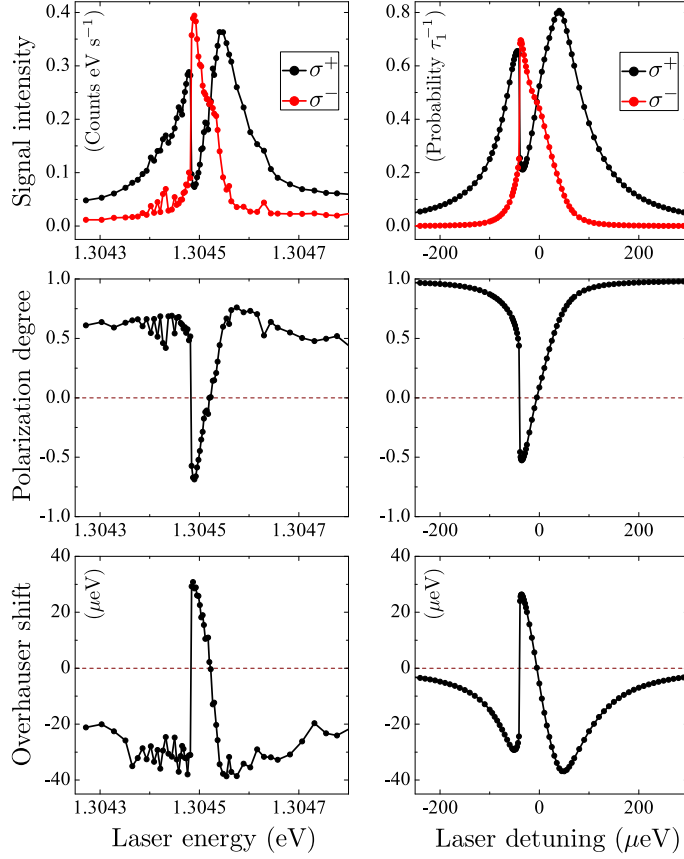


Figure 7.2. Left (right) panels: Experimentally measured (calculated) signal intensity, polarization degree, and Overhauser shift versus laser energy (laser detuning) for a  $\sigma^+$  pump and an external field of +0.5 T at fixed bias in the center of the hybridization region. In the experiment, the laser is tuned close to the  $|0\rangle \leftrightarrow |X^0\rangle$  transition and the dot (at 4.2 K) is the same as in Fig. 7.1.

At large negative and positive detunings, the PL has largely  $\sigma^+$  character with  $P$  up to  $0.76 \pm 0.05$ . This is the intuitive result from the selection rules. Absorption of a  $\sigma^+$  photon with spin angular momentum  $+\hbar$  along  $z$  creates an  $|\uparrow\downarrow\rangle$  exciton consisting of a heavy hole  $\uparrow$  with spin  $z$  projection  $+\frac{3}{2}\hbar$  and an electron  $\downarrow$  with  $-\frac{1}{2}\hbar$ . An electron tunnels in to form the  $X^{1-}$  exciton  $|\uparrow\downarrow\uparrow\rangle$ . Hole spin relaxation is slow compared to recombination [22, 23] such that recombination  $|\uparrow\downarrow\uparrow\rangle \rightarrow |\uparrow\rangle$  creates a  $\sigma^+$  photon. The counterintuitive result in Fig. 7.2 is that close to the center of the resonance, the PL has an inverted polarization degree, with  $P \sim -0.7$ . Strikingly,  $P$  changes abruptly at a particular detuning.

An indicator that the nuclear spins are involved is provided by the Overhauser shift

$$\Delta_n = E(\sigma^+) - E(\sigma^-) - g_X \mu_B B_z. \quad (7.2)$$

$\Delta_n$  is interpreted as an energy shift of the unpaired electron spin in the  $X^{1-}$  final state arising from the nuclear spin polarization along  $z$ . Its determination requires a knowledge of the exciton  $g$  factor, and we measure  $g_X = 1.55 \pm 0.10$  as described in Appendix F. Close to the center of the resonance we now find that  $\Delta_n$  switches sign exactly at the point where  $P$  switches sign. The Overhauser shift is related to the average nuclear spin  $z$  projection  $\langle I_z \rangle$  (in units of  $\hbar$ ) through  $\Delta_n \simeq -A \langle I_z \rangle$  [21]. Taking the coupling constant  $A \approx 90 \mu\text{eV}$ , an averaged value for  $\text{In}_{0.5}\text{Ga}_{0.5}\text{As}$  [24], we find that  $\langle I_z \rangle \approx +0.36 \leftrightarrow -0.36$ . Full polarization corresponds to  $\langle I_z \rangle = \pm 2.25$ , where  $I = 2.25$  is the average nuclear spin quantum number in the dot.

The abrupt jump in  $P$  corresponds to a bistability. With  $\sigma^+$  excitation, in state I (II) the dot emits  $\sigma^+$  ( $\sigma^-$ ) photons and the nuclear spins point up (down). The bistability is demonstrated clearly in

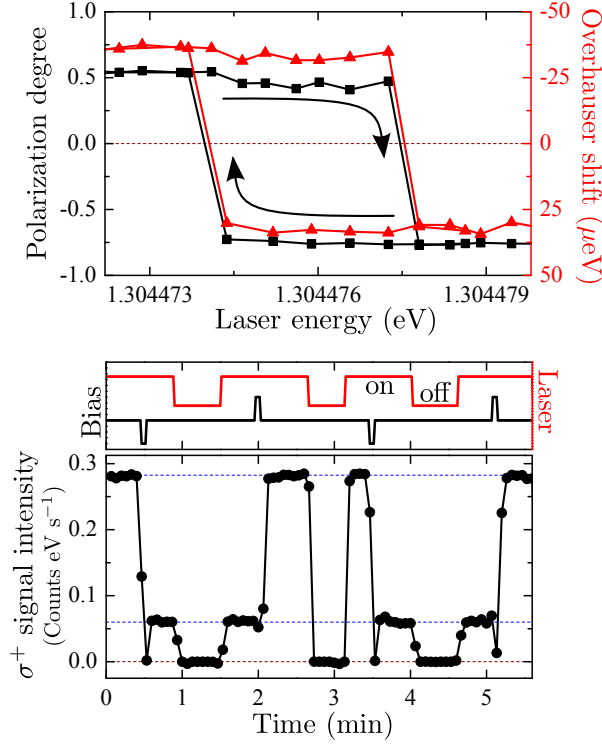


Figure 7.3. Top: Bistability between state I ( $\sigma^+$  PL, nuclear spins up) and state II ( $\sigma^-$  PL, nuclear spins down). The polarization degree  $P$  and Overhauser shift  $\Delta_n$  were measured as the laser was tuned. The laser was blocked for 30 s between each point. Bottom: Demonstration of switching with gate voltage pulses (40 mV, 5 s duration) by measuring the  $\sigma^+$  PL; strong PL signifying state I, weak PL signifying state II. In between voltage pulses, the laser was turned off. Both curves were recorded at +0.5 T, 4.2 K, using a  $\sigma^+$  pump and the same dot as in Figs. 7.1 and 7.2.

the hysteresis curve of Fig. 7.3 (top). In this case, the laser energy was tuned in fine steps (less than  $0.5 \mu\text{eV}$ ), blocking the laser path for about 30 s between each data point during which time the state of the system was always preserved. At more positive laser detunings, the polarization degree  $P$  and the nuclear spin polarization are continuous monotonic functions of detuning, changing from large negative to large positive values. Correspondingly,  $\Delta_n$  goes smoothly from +30 to  $-35 \mu\text{eV}$ . The total electron Zeeman splitting,  $g_e^{\text{eff}} \mu_B B_z = g_e \mu_B B_z + A \langle I_z \rangle$ , changes sign at the bistability, followed by continuous tuning from  $-45$  to  $+20 \mu\text{eV}$  (tuning of effective electron  $g$  factor  $g_e^{\text{eff}}$  from  $-1.6$  to  $+0.7$ ).

To switch from state I to state II, it is more convenient to change the gate voltage than the laser wavelength. We have achieved this by exploiting the Stark effect of the exciton energy. Figure 7.3 (bottom) demonstrates controlled switching between state I and II by applying voltage pulses to the gate, monitoring the state of the system via the  $\sigma^+$  PL. The system is initially in state I. It is forced into state II with a negative voltage pulse, equivalent to moving the laser energy up and back down again. This results in a lower  $\sigma^+$  PL, the signature of state II. Analogously, we can switch the system back into state I with a positive voltage pulse. In between these voltage pulses, the laser is turned off. When it is turned back on again  $\sim 30$  s later, the system always adopts its original state, demonstrating a slow I-II relaxation rate ( $< 0.1 \text{ s}^{-1}$ ).

## 7.5 Quantitative Model

We present a quantitative model to describe these results. The two crucial ingredients are first, a coherent coupling between  $|\uparrow\downarrow\rangle$  and  $|\downarrow\uparrow\rangle$ , the so-called fine structure which arises from the anisotropic part of the electron-hole exchange, and second, a hyperfine coupling between the nuclear spins and the unpaired electron spin. A full description of the model is given in Appendix F.

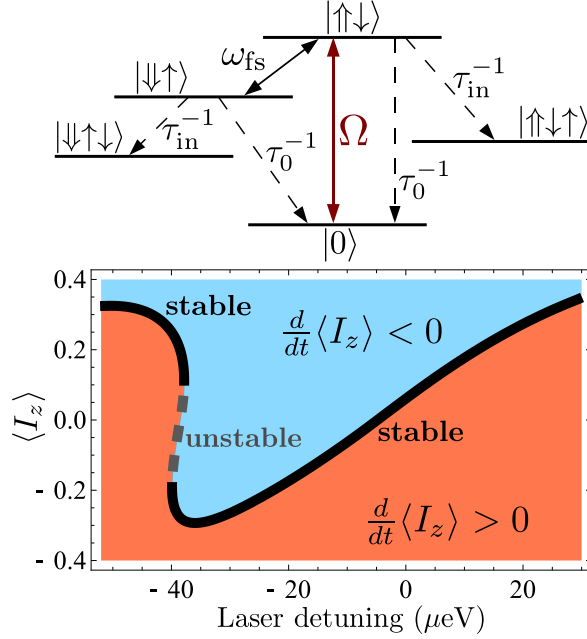


Figure 7.4. Top: The five quantum states in the simulation showing an optical coupling (Rabi energy  $\hbar\Omega$ ) and a coherent coupling (energy  $\hbar\omega_{fs}$ ) between the two neutral exciton states. Decay processes are drawn with dashed lines. Bottom: The calculated nuclear spin dynamics as a function of laser detuning for a  $\sigma^+$  pump, +0.5 T external field, and the parameters described in the text. The solid (dashed) line shows the stable (unstable) solution of  $\frac{d}{dt}\langle I_z \rangle = 0$ .

First, we calculate the effect of the laser field on the dynamics of a five-level system, consisting of the vacuum state  $|0\rangle$ , the two  $X^0$  exciton states  $|\uparrow\downarrow\rangle$  and  $|\downarrow\uparrow\rangle$ , and the two  $X^{1-}$  states  $|\uparrow\uparrow\downarrow\rangle$  and  $|\downarrow\downarrow\uparrow\rangle$ . The laser is  $\sigma^+$  polarized and drives the  $|0\rangle \leftrightarrow |\uparrow\downarrow\rangle$  but not the  $|0\rangle \leftrightarrow |\downarrow\uparrow\rangle$  transition on account of the selection rules. The optical Rabi energy is  $\hbar\Omega$ , the detuning  $\hbar\delta = \hbar\omega - \hbar\omega_0$ , where  $\omega$  is the angular frequency of the laser and  $\hbar\omega_0$  is the eigenenergy of  $|\uparrow\downarrow\rangle$  and  $|\downarrow\uparrow\rangle$  in the absence of magnetic field, fine structure, and nuclear spins. Coupling between  $|\uparrow\downarrow\rangle$  and  $|\downarrow\uparrow\rangle$  is characterized by the fine structure  $\hbar\omega_{fs}$ . Decay processes are sketched in the level diagram, Fig. 7.4 (top). The neutral excitons can decay by spontaneous emission to  $|0\rangle$  at rate  $\tau_0^{-1}$ ; or they can become trion states via tunneling at rate  $\tau_{in}^{-1}$ . Starting with the entire population in the ground state, we use the master equation for the density matrix to determine the occupation probabilities  $p_{|\uparrow\uparrow\downarrow\rangle}$  and  $p_{|\downarrow\downarrow\uparrow\rangle}$  of the trion states after time  $\tau_1$ , the spontaneous recombination lifetime of  $X^{1-}$ , resulting in the rates of creating an  $\uparrow, \downarrow$  electron via optical recombination.

After trion recombination, the free electron interacts with the  $N$  quantum dot nuclei through the contact hyperfine interaction before it tunnels out at rate  $\tau_{out}^{-1}$ . The spin flip-flop probability  $p_{ff}$  is

$$p_{ff} = \frac{2\gamma\tau_{out}^2}{(4\gamma + \xi)\tau_{out}^2 + \hbar^2}, \quad (7.3)$$

where  $\gamma = \frac{A^2}{4N}(I - |\langle I_z \rangle|)$  and  $\xi = (g_e\mu_B B_z + A\langle I_z \rangle)^2$ , with  $g_e$  as the electron  $g$  factor [21]. The combination of electron creation rate and flip-flop probability results in a dynamic equation for the nuclear spin polarization.  $\langle I_z \rangle$  is driven up depending on  $p_{|\uparrow\uparrow\downarrow\rangle}$ , down depending on  $p_{|\downarrow\downarrow\uparrow\rangle}$ , and decays in the absence of driving with rate  $\Gamma_{leak}$ ,

$$\frac{d}{dt}\langle I_z \rangle \simeq \frac{p_{ff}}{N\tau_1} [p_{|\uparrow\uparrow\downarrow\rangle} - p_{|\downarrow\downarrow\uparrow\rangle}]_{t=\tau_1} - \Gamma_{leak}\langle I_z \rangle. \quad (7.4)$$

We solve this equation numerically to find stable values of  $\langle I_z \rangle$  as a function of laser detuning  $\hbar\delta$ . At each solution one can also calculate the Overhauser shift  $\Delta_n$  and the polarization degree  $P$  in the quantum dot emission [21].

Parameters are set by in situ characterization and by comparison with previous experiments, making small tweaks to fit the experimental data in Fig. 7.2. We use the following values [21]:  $\hbar\Omega = 23 \mu\text{eV}$ ,  $\hbar\omega_{\text{fs}} = 40 \mu\text{eV}$ ,  $\tau_0 = 0.75 \text{ ns}$ ,  $\tau_1 = 0.95 \text{ ns}$ ,  $\tau_{\text{in}} = 35 \text{ ps}$ ,  $\tau_{\text{out}} = 5 \text{ ps}$ ,  $N = 8.5 \times 10^4$ ,  $\Gamma_{\text{leak}} = 0.1 \text{ s}^{-1}$ , and  $g_e = -0.5$ . Figure 7.4 (bottom) contains a plot of  $\frac{d}{dt}\langle I_z \rangle$ , showing that the solution for  $\langle I_z \rangle$  changes from positive to negative with a region of bistability. The calculated  $P$  and  $\Delta_n$  are plotted in the right panels to Fig. 7.2. Close to the optical resonance, there is an excellent agreement with the experimental results.

The theory offers an explanation for the counterintuitive inversion of the PL polarization. When the  $\sigma^+$  polarized laser comes into resonance with the forbidden  $|0\rangle \leftrightarrow |\downarrow\uparrow\rangle$  transition, a combination of the allowed  $|0\rangle \leftrightarrow |\uparrow\downarrow\rangle$  transition and the  $|\uparrow\downarrow\rangle \leftrightarrow |\downarrow\uparrow\rangle$  coupling causes the population to build up in the  $|\downarrow\uparrow\rangle$  state, leading to electron spin  $\downarrow$  creation following tunneling in and recombination. When the laser is then tuned further, the allowed  $|0\rangle \leftrightarrow |\uparrow\downarrow\rangle$  transition takes over and the cycle results in the creation of electron spin  $\uparrow$ . The creation of a particular electron spin leads to nuclear spin polarization which alters the energies of the  $|\downarrow\uparrow\rangle$ ,  $|\uparrow\downarrow\rangle$  states via the Overhauser field. This feedback results in a bistability close to the forbidden transition and continuous tuning thereafter.

## 7.6 Outlook

We have explored some of the parameter space theoretically. For parameters close to the ones used in this experiment, a region of bistability exists when  $\Gamma_{\text{leak}}$  is small enough. A bistability is definitely possible even at zero magnetic field, provided that  $\Gamma_{\text{leak}} \lesssim 1 \text{ s}^{-1}$  and that the tunneling times are increased relative to those in this experiment. The inversion in polarization can be enhanced to at least  $P = +0.85 \leftrightarrow -0.85$ , again by increasing the tunneling times and also by optimizing the  $\omega_{\text{fs}} : \Omega$  ratio. Furthermore, at detunings larger than those at the bistability, these parameters allow continuous control of the  $|\uparrow\rangle$ ,  $|\downarrow\rangle$  eigenenergies from  $\mp 40$  to  $\pm 50 \mu\text{eV}$ , and, following Refs. [21, 25], a reduction in the variance of the nuclear spin distribution by factors  $\sim 5$ . All these features are attractive for spin qubits and single photon emitters.

## Acknowledgments

We thank Bill Coish for helpful discussions and acknowledge funding from Swiss NSF, DARPA QuEST, EPSRC, The Royal Society (BDG), and ANR QUAMOS (BU).





# References

- [1] D. Loss and D. P. DiVincenzo, *Phys. Rev. A* **57**, 120 (1998).
- [2] P. Michler, A. Kiraz, C. Becher, W. V. Schoenfeld, P. M. Petroff, L. Zhang, E. Hu, and A. Imamoglu, *Science* **290**, 2282 (2000).
- [3] N. Akopian, N. H. Lindner, E. Poem, Y. Berlatzky, J. Avron, D. Gershoni, B. D. Gerardot, and P. M. Petroff, *Phys. Rev. Lett.* **96**, 130501 (2006).
- [4] C. L. Salter, R. M. Stevenson, I. Farrer, C. A. Nicoll, D. A. Ritchie, and A. J. Shields, *Nature (London)* **465**, 594 (2010).
- [5] A. V. Khaetskii, D. Loss, and L. Glazman, *Phys. Rev. Lett.* **88**, 186802 (2002).
- [6] M. H. Mikkelsen, J. Berezovsky, N. G. Stoltz, L. A. Coldren, and D. D. Awschalom, *Nat. Phys.* **3**, 770 (2007).
- [7] X. Xu, B. Sun, P. R. Berman, D. G. Steel, A. S. Bracker, D. Gammon, and L. J. Sham, *Nat. Phys.* **4**, 692 (2008).
- [8] W. A. Coish and D. Loss, *Phys. Rev. B* **70**, 195340 (2004).
- [9] A. Greilich, D. R. Yakovlev, A. Shabaev, A. L. Efros, I. A. Yugova, R. Oulton, V. Stavarache, D. Reuter, A. Wieck, and M. Bayer, *Science* **313**, 341 (2006).
- [10] X. Xu, W. Yao, B. Sun, D. G. Steel, A. S. Bracker, D. Gammon, and L. J. Sham, *Nature (London)* **459**, 1105 (2009).
- [11] H. Bluhm, S. Foletti, D. Mahalu, V. Umansky, and A. Yacoby, *Phys. Rev. Lett.* **105**, 216803 (2010).
- [12] C. Latta, A. Högele, Y. Zhao, A. N. Vamivakas, P. Maletinsky, M. Kroner, J. Dreiser, I. Carusotto, A. Badolato, D. Schuh, W. Wegscheider, M. Atatüre, and A. Imamoglu, *Nat. Phys.* **5**, 758 (2009).
- [13] T. Belhadj, C.-M. Simon, T. Amand, P. Renucci, B. Chatel, O. Krebs, A. Lemaitre, P. Voisin, X. Marie, and B. Urbaszek, *Phys. Rev. Lett.* **103**, 086601 (2009).
- [14] A. I. Tartakovskii, T. Wright, A. Russell, V. I. Fal'ko, A. B. Van'kov, J. Skiba-Szymanska, I. Drouzas, R. S. Kolodka, M. S. Skolnick, P. W. Fry, A. Tahraoui, H.-Y. Liu, and M. Hopkinson, *Phys. Rev. Lett.* **98**, 026806 (2007).
- [15] P. Maletinsky, A. Badolato, and A. Imamoglu, *Phys. Rev. Lett.* **99**, 056804 (2007).
- [16] M. N. Makhonin, A. I. Tartakovskii, A. Ebbens, M. S. Skolnick, A. Russell, V. I. Fal'ko, and M. Hopkinson, *Appl. Phys. Lett.* **93**, 073113 (2008).
- [17] E. A. Chekhovich, M. N. Makhonin, K. V. Kavokin, A. B. Krysa, M. S. Skolnick, and A. I. Tartakovskii, *Phys. Rev. Lett.* **104**, 066804 (2010).
- [18] F. Klotz, V. Jovanov, J. Kierig, E. C. Clark, M. Bichler, G. Abstreiter, M. S. Brandt, J. J. Finley, H. Schwager, and G. Giedke, *Phys. Rev. B* **82**, 121307(R) (2010).

- [19] P.-F. Braun, B. Urbaszek, T. Amand, X. Marie, O. Krebs, B. Eble, A. Lemaitre, and P. Voisin, *Phys. Rev. B* **74**, 245306 (2006)
- [20] P. A. Dalgarno, M. Ediger, B. D. Gerardot, J. M. Smith, S. Seidl, M. Kroner, K. Karrai, P. M. Petroff, A. O. Govorov, and R. J. Warburton, *Phys. Rev. Lett.* **100**, 176801 (2008).
- [21] See Appendix F for the details of the theory.
- [22] D. Heiss, S. Schaeck, H. Huebl, M. Bichler, G. Abstreiter, J. J. Finley, D. V. Bulaev, and D. Loss, *Phys. Rev. B* **76**, 241306(R) (2007).
- [23] B. D. Gerardot, D. Brunner, P. A. Dalgarno, P. Öhberg, S. Seidl, M. Kroner, K. Karrai, N. G. Stoltz, P. M. Petroff, and R. J. Warburton, *Nature (London)* **451**, 441 (2008).
- [24] W. A. Coish and J. Baugh, *Phys. Status Solidi B* **246**, 2203 (2009).
- [25] I. T. Vink, K. C. Nowack, F. H. L. Koppens, J. Danon, Y. V. Nazarov, and L. M. K. Vandersypen, *Nat. Phys.* **5**, 764 (2009).

# **APPENDIX**

## **Supplementary Information to Chapters 2–7**



# Appendix A

## Supplementary Information to Chapter 2 “Strong Spin-Orbit Interaction and Helical Hole States in Ge/Si Nanowires”

**Adapted from:**

Christoph Kloeffel, Mircea Trif, and Daniel Loss,  
Phys. Rev. B **84**, 195314 (2011).

## A.1 Representation of Spin Matrices

All results presented in Chapter 2 are based on the following representation of the spin-3/2 matrices:

$$J_x = \begin{pmatrix} 0 & \frac{\sqrt{3}}{2} & 0 & 0 \\ \frac{\sqrt{3}}{2} & 0 & 1 & 0 \\ 0 & 1 & 0 & \frac{\sqrt{3}}{2} \\ 0 & 0 & \frac{\sqrt{3}}{2} & 0 \end{pmatrix}, \quad (\text{A.1})$$

$$J_y = \begin{pmatrix} 0 & -i\frac{\sqrt{3}}{2} & 0 & 0 \\ i\frac{\sqrt{3}}{2} & 0 & -i & 0 \\ 0 & i & 0 & -i\frac{\sqrt{3}}{2} \\ 0 & 0 & i\frac{\sqrt{3}}{2} & 0 \end{pmatrix}, \quad (\text{A.2})$$

$$J_z = \begin{pmatrix} \frac{3}{2} & 0 & 0 & 0 \\ 0 & \frac{1}{2} & 0 & 0 \\ 0 & 0 & -\frac{1}{2} & 0 \\ 0 & 0 & 0 & -\frac{3}{2} \end{pmatrix}. \quad (\text{A.3})$$

The Pauli operators  $\tau_i$  (referring to  $\{g, e\}$ ) and  $\sigma_i$  (acting on  $\{+, -\}$ ) are defined as

$$\tau_x = \begin{pmatrix} 0 & 1 \\ 1 & 0 \end{pmatrix}, \quad \tau_y = \begin{pmatrix} 0 & -i \\ i & 0 \end{pmatrix}, \quad \tau_z = \begin{pmatrix} 1 & 0 \\ 0 & -1 \end{pmatrix}, \quad (\text{A.4})$$

and analogously for  $\sigma_i$ .

## A.2 Basis States for the Effective 1D Hamiltonian

In this appendix we outline the calculation of the basis states  $\{g_+, g_-, e_+, e_-\}$ . For  $k_z = 0$ , each of the  $4 \times 4$  blocks for given quantum number  $F_z$  and energy  $E$  reduces to two  $2 \times 2$  blocks, labeled by  $\pm$  according to the sign of the contained spin state  $|\pm 3/2\rangle$ . In the absence of confinement, using an ansatz analogous to those in Refs. [1, 2], the eigenstates to be considered are

$$\psi_{\text{hh},\pm}^{F_z} = J_{F_z \mp 3/2}(k_{\text{hh}}r) e^{i(F_z \mp 3/2)\phi} |\pm 3/2\rangle - \sqrt{3} J_{F_z \pm 1/2}(k_{\text{hh}}r) e^{i(F_z \pm 1/2)\phi} |\mp 1/2\rangle, \quad (\text{A.5})$$

$$\psi_{\text{lh},\pm}^{F_z} = \sqrt{3} J_{F_z \mp 3/2}(k_{\text{lh}}r) e^{i(F_z \mp 3/2)\phi} |\pm 3/2\rangle + J_{F_z \pm 1/2}(k_{\text{lh}}r) e^{i(F_z \pm 1/2)\phi} |\mp 1/2\rangle, \quad (\text{A.6})$$

where the  $J_n(x)$  are Bessel functions of the first kind, and

$$k_{\text{hh},\text{lh}} \equiv \frac{1}{\hbar} \sqrt{\frac{2mE}{\gamma_1 \mp 2\gamma_s}}. \quad (\text{A.7})$$

When confinement is present, the eigenstates read

$$\Phi_{\pm}^{F_z}(r, \phi) = a_{\pm}^{F_z} \psi_{\text{hh},\pm}^{F_z}(r, \phi) + b_{\pm}^{F_z} \psi_{\text{lh},\pm}^{F_z}(r, \phi), \quad (\text{A.8})$$

where the coefficients  $a_{\pm}^{F_z}, b_{\pm}^{F_z}$  and the energies  $E$  are to be found from the boundary condition  $\Phi_{\pm}^{F_z}(R, \phi) = 0$ , resulting in the determinant equations

$$0 = J_{F_z \mp 3/2}(k_{\text{hh}}R) J_{F_z \pm 1/2}(k_{\text{lh}}R) + 3 J_{F_z \pm 1/2}(k_{\text{hh}}R) J_{F_z \mp 3/2}(k_{\text{lh}}R). \quad (\text{A.9})$$

By solving the above equations, we find that for  $\pm$  the lowest eigenenergy corresponds to  $F_z = \mp 1/2$ , and the second lowest one to  $F_z = \pm 1/2$ . The associated eigenstates  $g_{\pm} \equiv \Phi_{\pm}^{\mp 1/2}$  and  $e_{\pm} \equiv \Phi_{\pm}^{\pm 1/2}$  for the

transverse motion are found by calculating the coefficients  $a_{\pm}^{\mp 1/2}$ ,  $b_{\pm}^{\mp 1/2}$ ,  $a_{\pm}^{\pm 1/2}$ , and  $b_{\pm}^{\pm 1/2}$ , respectively, and serve as the basis states in the effective 1D Hamiltonian. Normalization requires

$$\langle g_{\pm} | g_{\pm} \rangle = \int_0^R dr r \int_0^{2\pi} d\phi |g_{\pm}|^2 = 1, \quad (\text{A.10})$$

and analogously for  $e_{\pm}$ . It turns out that the excited states are purely heavy-hole-like,  $b_{\pm}^{\pm 1/2} = 0$ , and we choose the complex phases such that all coefficients are real, with  $a_{\pm}^{\mp 1/2} < 0$ ,  $b_{\pm}^{\mp 1/2} > 0$ , and  $a_{\pm}^{\pm 1/2} > 0$ .

### A.3 Bir-Pikus Hamiltonian

Referring to holes, the Bir-Pikus Hamiltonian reads

$$H_{\text{BP}} = - \left( a + \frac{5}{4}b \right) \sum_i \epsilon_{ii} + b \sum_i \epsilon_{ii} J_i^2 + \frac{2d}{\sqrt{3}} \left( \epsilon_{xy} \{J_x, J_y\} + \text{c.p.} \right), \quad (\text{A.11})$$

where  $a$ ,  $b$ , and  $d$  are the deformation potentials,  $\epsilon_{ij} = \epsilon_{ji}$  are the strain tensor elements,  $\{A, B\} \equiv (AB + BA)/2$ , and ‘‘c.p.’’ stands for cyclic permutations [3]. The axes  $x, y, z$  refer here to the main crystallographic axes. For Ge, the deformation potentials are  $b \simeq -2.5$  eV and  $d \simeq -5.0$  eV [3], so that the spherical approximation  $d = \sqrt{3}b$  applies. The hydrostatic deformation potential  $a$  accounts for the constant energy shift of the VB in the presence of hydrostatic strain, and therefore does not contribute to  $\Delta_{\text{BP}}(\gamma)$ , i.e., the rescaling of the energy gap  $\Delta_{\text{LK}}$ .

### A.4 Quantum Dot Spectrum

When the quantum dot length  $L$  is much larger than the core radius  $R$  (Fig. 2.1), the spectrum can be well approximated using the effective Hamiltonian for extended states. In the absence of external fields,  $F_z$  remains a good quantum number and the Hamiltonian

$$H_{\text{LK}}^{\text{eff}} = \begin{pmatrix} \frac{\hbar^2 k_z^2}{2m_g} & -iCk_z & 0 & 0 \\ iCk_z & \frac{\hbar^2 k_z^2}{2m_e} + \Delta_{\text{LK}} + \Delta_{\text{BP}}(\gamma) & 0 & 0 \\ 0 & 0 & \frac{\hbar^2 k_z^2}{2m_g} & -iCk_z \\ 0 & 0 & iCk_z & \frac{\hbar^2 k_z^2}{2m_e} + \Delta_{\text{LK}} + \Delta_{\text{BP}}(\gamma) \end{pmatrix}, \quad (\text{A.12})$$

here explicitly written out in the basis  $\{g_+, e_-, g_-, e_+\}$  for illustration purposes, is  $2 \times 2$  block diagonal with degenerate eigenstates. The subspace  $\{g_+, e_-\}$  corresponds to  $F_z = -1/2$ , while  $\{g_-, e_+\}$  corresponds to  $F_z = +1/2$ . Aiming at the quantum dot spectrum, we introduce two complex functions  $g_n(z)$  and  $e_n(z)$ , for which we require

$$\begin{pmatrix} \frac{\hbar^2 k_z^2}{2m_g} & -iCk_z \\ iCk_z & \frac{\hbar^2 k_z^2}{2m_e} + \Delta_{\text{LK}} + \Delta_{\text{BP}}(\gamma) \end{pmatrix} \begin{pmatrix} g_n(z) \\ e_n(z) \end{pmatrix} = E_n \begin{pmatrix} g_n(z) \\ e_n(z) \end{pmatrix}. \quad (\text{A.13})$$

The associated set of coupled differential equations reads

$$0 = -\frac{\hbar^2}{2m_g} g_n''(z) - C e_n'(z) - E_n g_n(z), \quad (\text{A.14})$$

$$0 = -\frac{\hbar^2}{2m_e} e_n''(z) + C g_n'(z) + [\Delta_{\text{LK}} + \Delta_{\text{BP}}(\gamma) - E_n] e_n(z), \quad (\text{A.15})$$

and in addition we demand  $g_n(0) = e_n(0) = g_n(L) = e_n(L) = 0$  due to hard wall confinement at  $z = 0$  and  $z = L$ . When the differential equations have been solved, these boundary conditions finally lead to a determinant equation for the eigenenergies  $E_n$ , which can be analyzed numerically. The results are plotted in Fig. 2.3.

## A.5 Spin-Orbit Energy in InAs Nanowires

For electrons in an electric field  $E_x$  along  $x$ , the Hamiltonian for Rashba SOI is of the form

$$H_{\text{SO}}^{\text{el}} = \alpha E_x (k_z \tilde{\sigma}_y - k_y \tilde{\sigma}_z), \quad (\text{A.16})$$

where  $\alpha$  is the Rashba coefficient in the conduction band ( $\Gamma_6^c$ ) and  $\tilde{\sigma}_i$  are the Pauli matrices for spin 1/2 [4]. In the following, we use the notation  $\alpha_x \equiv \alpha E_x$  for illustration purposes. Assuming a nanowire in which the electron moves freely along the  $z$  direction with effective mass  $m^*$ , the Hamiltonian of the system becomes

$$H^{\text{el}} = \frac{\hbar^2 k_z^2}{2m^*} + \alpha_x k_z \tilde{\sigma}_y, \quad (\text{A.17})$$

with eigenspectrum

$$\begin{aligned} E_{\pm} &= \frac{\hbar^2}{2m^*} \left( k_z \pm \frac{m^* |\alpha_x|}{\hbar^2} \right)^2 - \frac{m^* \alpha_x^2}{2\hbar^2} \\ &= \frac{\hbar^2}{2m^*} (k_z \pm l_{\text{SO}}^{-1})^2 - E_{\text{SO}}. \end{aligned} \quad (\text{A.18})$$

The spin-orbit length is defined as  $l_{\text{SO}} = \hbar^2 / (m^* |\alpha_x|)$ , and the SO energy, the energy difference between the band minima and the degeneracy at  $k_z = 0$ , is  $E_{\text{SO}} = m^* \alpha_x^2 / (2\hbar^2)$ , so that

$$E_{\text{SO}} = \frac{\hbar^2}{2m^*} l_{\text{SO}}^{-2}. \quad (\text{A.19})$$

We can use Eq. (A.19) to calculate the spin-orbit energy for InAs wires, where  $l_{\text{SO}}$  has recently been measured [5, 6]. Using  $l_{\text{SO}} \simeq 127$  nm and  $m^* \simeq m_{\text{bulk}}^* = 0.023 m$  [5], the SO energy in InAs is  $E_{\text{SO}} \simeq 100$   $\mu\text{eV}$ . Further experiments confirmed that  $l_{\text{SO}}$  typically varies between 100 and 200 nm in InAs nanowires [6], and in the latter case  $E_{\text{SO}} \simeq 40$   $\mu\text{eV}$  only.

## A.6 Standard Rashba SOI and Rashba Coefficient

Both Ge and Si are inversion symmetric, and thus coupling of Dresselhaus type is absent. However, this does not exclude the conventional Rashba term (RSOI) [Eq. (2.7) in Chapter 2]. Here we briefly outline its derivation; details are described in Ref. [4]. As in Sec. 2.6, we assume a constant electric field  $E_x$  along the  $x$  axis, which, referring to holes, results in the dipole term  $H_{\text{ed}} = -eE_x x$  as a perturbation added to the potential energy. Accordingly,  $H_{\text{ed}}$  is added to the multiband Hamiltonian (envelope function approximation), where it appears only on the diagonal, while off-diagonal parts provide the  $\mathbf{k} \cdot \mathbf{p}$  coupling. Finally, a Schrieffer-Wolff transformation of the multiband Hamiltonian, with focus on the valence band  $\Gamma_8^v$ , yields the Rashba term

$$H_{\text{SO}} = \alpha E_x (k_y J_z - k_z J_y), \quad (\text{A.20})$$

$$\alpha \simeq -\frac{eP^2}{3E_0^2} \quad (\text{A.21})$$



in third order of perturbation theory, where  $\alpha$  is the Rashba coefficient and additional, negligible terms have been omitted. In Eq. (A.21),  $E_0$  is the band gap (direct,  $k = 0$ ) between conduction ( $\Gamma_6^c$ ) and valence ( $\Gamma_8^v$ ) band, and  $P$  is the corresponding momentum matrix element between the  $s$ -like  $\Gamma_6^c$  and the  $p$ -like  $\Gamma_8^v, \Gamma_7^v$  states [4]. For Ge, explicit values are  $E_0 = 0.90$  eV and  $P = 9.7$  eVÅ [7], which yields  $\alpha \approx -0.4$  nm<sup>2</sup>e.

We can project Eq. (A.20) onto the low-energy subspace  $\{g_+, g_-, e_+, e_-\}$  by calculating the 16 matrix elements. The effective Hamiltonian for RSOI takes on the form

$$H_R = H_{\text{SO}}^{\text{eff}} = \alpha E_x S \tau_x \sigma_z + \alpha E_x k_z \dots, \quad (\text{A.22})$$

where  $S = \langle g_+ | k_y J_z | e_+ \rangle$ . This Hamiltonian has two effects: first, it features a constant coupling between the  $g$  and  $e$  states, and second, it provides a term which is linear in  $k_z$  and mixes the spin blocks. The latter is absent at  $k_z = 0$ , so that only the constant term  $\alpha E_x S \tau_x \sigma_z$  contributes for small  $k_z$ ; this is of the same form as the direct Rashba SOI  $H_{\text{DR}} = e E_x U \tau_x \sigma_z$  (DRSOI) resulting from dipolar coupling. [We note that it is not directly obvious that the second term in Eq. (A.22) can be omitted at nonzero  $k_z$  as well. The negligibility is seen from a suitable unitary transformation of the final 1D Hamiltonian that contains  $H_{\text{LK}}^{\text{eff}} + H_{\text{DR}} + H_R$  and the effects of additional (magnetic) fields, if present.] Finally, we note that

$$\frac{e E_x U}{\alpha E_x S} \simeq -1.1 \frac{R^2}{\text{nm}^2} \quad (\text{A.23})$$

for Ge, so that the DRSOI dominates RSOI by one to two orders of magnitude in typical Ge/Si nanowires of 5–10 nm core radius.

## A.7 Coupling to Magnetic Fields

In Eqs. (2.9) and (2.10) of Chapter 2, we show the effect of external magnetic fields on the low-energy sector for fields applied along ( $z$ ) and perpendicular ( $x$ ) to the nanowire, respectively. Below, the explicit values for  $Z_i$  and  $X_i$  are listed,

$$\begin{aligned} Z_1 &= 0.75, & X_1 &= 2.72, \\ Z_2 &= -0.81, & X_2 &= 0.17, \\ Z_3 &= 2.38 R, & X_3 &= 8.04 R, \end{aligned} \quad (\text{A.24})$$

using the parameters  $\gamma_1 = 13.35$ ,  $\gamma_s = 5.11$ , and  $\kappa = 3.41$  for Ge [8].



# References

- [1] P. C. Sercel and K. J. Vahala, Phys. Rev. B **42**, 3690 (1990).
- [2] D. Csontos, P. Brusheim, U. Zülicke, and H. Q. Xu, Phys. Rev. B **79**, 155323 (2009).
- [3] G. L. Bir and G. E. Pikus, *Symmetry and Strain-Induced Effects in Semiconductors* (Wiley, New York, 1974).
- [4] R. Winkler, *Spin-Orbit Coupling Effects in Two-Dimensional Electron and Hole Systems* (Springer, Berlin, 2003).
- [5] C. Fasth, A. Fuhrer, L. Samuelson, V. N. Golovach, and D. Loss, Phys. Rev. Lett. **98**, 266801 (2007).
- [6] S. Dhara, H. S. Solanki, V. Singh, A. Narayanan, P. Chaudhari, M. Gokhale, A. Bhattacharya, and M. M. Deshmukh, Phys. Rev. B **79**, 121311(R) (2009).
- [7] S. Richard, F. Aniel, and G. Fishman, Phys. Rev. B **70**, 235204 (2004).
- [8] P. Lawaetz, Phys. Rev. B **4**, 3460 (1971).



## **Appendix B**

# **Supplementary Information to Chapter 3 “Tunable $g$ Factor and Phonon-Mediated Hole Spin Relaxation in Ge/Si Nanowire Quantum Dots”**

**Adapted from:**

Franziska Maier, Christoph Kloeffel, and Daniel Loss,  
Phys. Rev. B **87**, 161305(R) (2013).

## B.1 Effective 1D Hamiltonian for Holes

In this appendix, we display the effective 1D Hamiltonians used in Eqs. (3.2) and (3.3) of Chapter 3. The derivation of these terms is discussed in Chapter 2. We use the basis  $\{g_+, g_-, e_+, e_-\}$  and refer to, e.g., Appendix C.1.1 for the exact form of the basis states  $g_\pm(x, y)$  and  $e_\pm(x, y)$ .

The diagonal elements of the Luttinger-Kohn (LK) Hamiltonian and the strain-induced splitting are combined in

$$H_{\text{LK,d}} + H_{\text{strain}} = \begin{pmatrix} \frac{\hbar^2 k_z^2}{2m_g} & 0 & 0 & 0 \\ 0 & \frac{\hbar^2 k_z^2}{2m_g} & 0 & 0 \\ 0 & 0 & \frac{\hbar^2 k_z^2}{2m_e} + \Delta & 0 \\ 0 & 0 & 0 & \frac{\hbar^2 k_z^2}{2m_e} + \Delta \end{pmatrix}, \quad (\text{B.1})$$

where  $\hbar k_z = -i\hbar\partial_z$  is the momentum operator for the wire axis  $z$ , and  $m_g \simeq m/(\gamma_1 + 2\gamma_s)$  and  $m_e = m/(\gamma_1 + \gamma_s)$  are the corresponding effective masses. Here  $\gamma_1$  and  $\gamma_s$  are the Luttinger parameters in spherical approximation and  $m$  denotes the bare electron mass.  $\Delta = \Delta_{\text{LK}} + \Delta_{\text{strain}}(\gamma)$  quantifies the level splitting between  $g_\pm$  and  $e_\pm$ ,  $\gamma = (R_s - R)/R$  is the relative shell thickness, and  $R$  ( $R_s$ ) is the core (shell) radius. One finds  $\Delta_{\text{LK}} = 0.73 \hbar^2/(mR^2)$ , and the strain-dependent energy splitting can take values  $\Delta_{\text{strain}}(\gamma) \simeq 0\text{--}30$  meV (see also Sec. 5.3.3, wherein  $\Delta_{\text{strain}} = \Delta_{\text{BP}}$ ). The magnetic field  $\mathbf{B} = (B_x, 0, B_z) = |\mathbf{B}|(\sin\theta, 0, \cos\theta)$  interacts via the effective Zeeman coupling

$$H_{B,Z} = \mu_B \begin{pmatrix} B_z G & B_x K & 0 & 0 \\ B_x K & -B_z G & 0 & 0 \\ 0 & 0 & B_z F & B_x M \\ 0 & 0 & B_x M & -B_z F \end{pmatrix}, \quad (\text{B.2})$$

where we set  $B_y = 0$  due to cylindrical symmetry. The Bohr magneton is  $\mu_B$  and the parameters take the numerical values  $G = -0.06$ ,  $K = 2.89$ ,  $M = 2.56$ , and  $F = 1.56$ . The LK Hamiltonian provides also off-diagonal coupling terms, and we find

$$H_{\text{LK,od}} = \begin{pmatrix} 0 & 0 & 0 & -iCk_z \\ 0 & 0 & -iCk_z & 0 \\ 0 & iCk_z & 0 & 0 \\ iCk_z & 0 & 0 & 0 \end{pmatrix} \quad (\text{B.3})$$

with coupling constant  $C = 7.26 \hbar^2/(mR)$ . In order to describe interactions with the electric field  $\mathbf{E} = (E_x, E_y, 0) = |\mathbf{E}|(\cos\varphi_{\text{el}}, \sin\varphi_{\text{el}}, 0)$ , we introduce the shorthand notation  $\tilde{E} = |\mathbf{E}|e^{i\varphi_{\text{el}}}$ . With this definition, the effective conventional Rashba SOI reads

$$H_{\text{R}} = \alpha \begin{pmatrix} 0 & -i\tilde{E}k_z T & \tilde{E}S & 0 \\ i\tilde{E}^*k_z T & 0 & 0 & -\tilde{E}^*S \\ \tilde{E}^*S & 0 & 0 & -\frac{3}{4}i\tilde{E}^*k_z \\ 0 & -\tilde{E}S & \frac{3}{4}i\tilde{E}k_z & 0 \end{pmatrix}, \quad (\text{B.4})$$

where  $T = 0.98$ ,  $S = 0.36/R$ , and  $\alpha = -0.4 \text{ nm}^2 e$ . The asterisk denotes complex conjugation. Although fully taken into account,  $H_{\text{R}}$  turns out to be negligible for the typical parameters and electric fields

considered here [see also Eq. (B.6)]. The direct, dipolar coupling to  $\mathbf{E}$  is given by

$$H_{\text{DR}} = eU \begin{pmatrix} 0 & 0 & \tilde{E} & 0 \\ 0 & 0 & 0 & -\tilde{E}^* \\ \tilde{E}^* & 0 & 0 & 0 \\ 0 & -\tilde{E} & 0 & 0 \end{pmatrix}, \quad (\text{B.5})$$

where  $U = 0.15R$  scales linearly in the core radius  $R$ . We note that the parameters  $S$  and  $U$  in  $H_{\text{R}}$  and  $H_{\text{DR}}$  are related by

$$\frac{eU}{\alpha S} \simeq -1.1 \frac{R^2}{\text{nm}^2}, \quad (\text{B.6})$$

so  $H_{\text{DR}}$  dominates  $H_{\text{R}}$  by one to two orders of magnitude for  $R = 5\text{--}10$  nm. Lastly, effects of the magnetic field due to the orbital motion along  $z$  are described by

$$H_{B,\text{orb}} = i\mu_B \begin{pmatrix} 0 & 0 & -B_x L k_z & -B_z D k_z \\ 0 & 0 & B_z D k_z & -B_x L k_z \\ B_x L k_z & -B_z D k_z & 0 & 0 \\ B_z D k_z & B_x L k_z & 0 & 0 \end{pmatrix} \quad (\text{B.7})$$

with  $L = 8.04R$  and  $D = 2.38R$ .

## B.2 Effective 1D Hamiltonian for Hole-Phonon Interaction

Inserting our results for acoustic phonons (see Chapter 5) into the spherical Bir-Pikus Hamiltonian [Eq. (3.7) of Chapter 3], we derive the effective 1D hole-phonon coupling for each mode type  $\lambda$ . Again, this is done by projecting the corresponding terms onto the low-energy subspace spanned by  $g_{\pm}(x, y)$  and  $e_{\pm}(x, y)$ , i.e., by integrating out the degrees of freedom for the transverse motion. To improve readability, we introduce here the modified phonon annihilation operators  $\tilde{b}_{\lambda} = e^{iqz} b_{q,\lambda}(t) = e^{iqz} e^{-i\omega_{\lambda}(q)t} b_{q,\lambda}$  as a shorthand notation.

Referring again to the basis  $\{g_+, g_-, e_+, e_-\}$ , the torsional phonon mode  $T$  couples through

$$H_T = \sum_q a_1 \begin{pmatrix} 0 & 0 & 0 & \tilde{b}_T - \tilde{b}_T^{\dagger} \\ 0 & 0 & -\tilde{b}_T + \tilde{b}_T^{\dagger} & 0 \\ 0 & \tilde{b}_T - \tilde{b}_T^{\dagger} & 0 & 0 \\ -\tilde{b}_T + \tilde{b}_T^{\dagger} & 0 & 0 & 0 \end{pmatrix}, \quad (\text{B.8})$$

and the longitudinal mode  $L$  yields

$$H_L = \sum_q \begin{pmatrix} a_2(\tilde{b}_L + \tilde{b}_L^{\dagger}) & 0 & 0 & ia_3(\tilde{b}_L - \tilde{b}_L^{\dagger}) \\ 0 & a_2(\tilde{b}_L + \tilde{b}_L^{\dagger}) & ia_3(\tilde{b}_L - \tilde{b}_L^{\dagger}) & 0 \\ 0 & ia_3(\tilde{b}_L - \tilde{b}_L^{\dagger}) & a_4(\tilde{b}_L + \tilde{b}_L^{\dagger}) & 0 \\ ia_3(\tilde{b}_L - \tilde{b}_L^{\dagger}) & 0 & 0 & a_4(\tilde{b}_L + \tilde{b}_L^{\dagger}) \end{pmatrix}. \quad (\text{B.9})$$

For the two flexural modes  $F_{\pm 1}$ , we find

$$H_{F_{\pm 1}} = \sum_q ia_5 \begin{pmatrix} 0 & 0 & \tilde{b}_{F_{\pm 1}}^{\dagger} & 0 \\ 0 & 0 & 0 & \tilde{b}_{F_{\pm 1}} \\ -\tilde{b}_{F_{\pm 1}} & 0 & 0 & 0 \\ 0 & -\tilde{b}_{F_{\pm 1}}^{\dagger} & 0 & 0 \end{pmatrix} \quad (\text{B.10})$$

and

$$H_{F-1} = \sum_q i a_5 \begin{pmatrix} 0 & 0 & -\tilde{b}_{F-1} & 0 \\ 0 & 0 & 0 & -\tilde{b}_{F-1}^\dagger \\ \tilde{b}_{F-1}^\dagger & 0 & 0 & 0 \\ 0 & \tilde{b}_{F-1} & 0 & 0 \end{pmatrix}, \quad (\text{B.11})$$

respectively. The prefactors  $a_i$  with  $i = 1, 2, 3, 4, 5$  are real and  $q$ -dependent. The total effective hole-phonon coupling  $H_{\text{h-ph}}$  is finally given by

$$H_{\text{h-ph}} = \sum_\lambda H_\lambda = H_{\text{T}} + H_{\text{L}} + H_{F+1} + H_{F-1}. \quad (\text{B.12})$$



## **Appendix C**

# **Supplementary Information to Chapter 4 “Circuit QED with Hole-Spin Qubits in Ge/Si Nanowire Quantum Dots”**

**Adapted from:**

Christoph Kloeffel, Mircea Trif, Peter Stano, and Daniel Loss,  
Phys. Rev. B **88**, 241405(R) (2013).

## C.1 Effective 1D Hamiltonian

### C.1.1 Basis States

The low-energy hole states in a Ge/Si core/shell nanowire (NW) are well described by the effective 1D Hamiltonian derived in Ref. [1]. Using the notation introduced therein, with the NW axis referred to as the  $z$  axis, the four basis states that comprise the spin and the transverse subband degrees of freedom read

$$\begin{aligned} |g_+\rangle &= \left( a_g J_2(k_{\text{hh}}^g r) + \sqrt{3} b_g J_2(k_{\text{hh}}^g r) \right) e^{-2i\phi} |3/2\rangle \\ &\quad + \left( b_g J_0(k_{\text{hh}}^g r) - \sqrt{3} a_g J_0(k_{\text{hh}}^g r) \right) |-1/2\rangle, \end{aligned} \quad (\text{C.1})$$

$$\begin{aligned} |g_-\rangle &= \left( a_g J_2(k_{\text{hh}}^g r) + \sqrt{3} b_g J_2(k_{\text{hh}}^g r) \right) e^{2i\phi} |-3/2\rangle \\ &\quad + \left( b_g J_0(k_{\text{hh}}^g r) - \sqrt{3} a_g J_0(k_{\text{hh}}^g r) \right) |1/2\rangle, \end{aligned} \quad (\text{C.2})$$

$$|e_+\rangle = -a_e J_1(k_{\text{hh}}^e r) \left( e^{-i\phi} |3/2\rangle + \sqrt{3} e^{i\phi} |-1/2\rangle \right), \quad (\text{C.3})$$

$$|e_-\rangle = a_e J_1(k_{\text{hh}}^e r) \left( e^{i\phi} |-3/2\rangle + \sqrt{3} e^{-i\phi} |1/2\rangle \right), \quad (\text{C.4})$$

where the  $J_i(\kappa)$  with integer  $i$  are Bessel functions of the first kind. The polar coordinates  $r$  and  $\phi$  in the cross section are related to the Cartesian coordinates by  $x = r \cos \phi$  and  $y = r \sin \phi$  (origin on the symmetry axis of the NW). The  $|m_z\rangle$ ,  $m_z \in \{\pm 3/2, \pm 1/2\}$ , correspond to the effective electron spin states in the topmost valence band (VB) and fulfill  $J_z |m_z\rangle = m_z |m_z\rangle$ , where  $J_z$  is the operator for the  $z$ -projection of this effective spin 3/2. The wave numbers  $k_{\text{hh}}^g$ ,  $k_{\text{hh}}^g$ ,  $k_{\text{hh}}^e$  and the coefficients  $a_g$ ,  $b_g$ ,  $a_e$  are determined by the Luttinger parameters of Ge and result from the hard-wall boundary conditions at the Ge/Si interface and the normalization. We choose all coefficients as real, with  $a_g < 0$ ,  $b_g > 0$ , and  $a_e > 0$ . For further details, see Ref. [1].

### C.1.2 Effective 1D Hamiltonian

In the setup studied in Chapter 4, we consider a magnetic field  $B_y$  along the  $y$  axis and electric fields  $E_y$  and  $E_z$  along the  $y$  and  $z$  axes, respectively. For the externally controlled electric-dipole-induced spin resonance (EDSR), we assume  $E_z = E_z(t) = E_{z,0}^e \cos(\omega_{\text{ac}} t)$  with amplitude  $E_{z,0}^e$  and angular frequency  $\omega_{\text{ac}}$ . The quantized field of the cavity is described by  $E_z = E_{z,0}^c (a^\dagger + a)$ , see also Appendix C.5, where  $E_{z,0}^c$  is the amplitude and  $a^\dagger$  ( $a$ ) is the bosonic creation (annihilation) operator for the cavity mode that is near or at resonance with the qubit. The different contributions to the Hamiltonian

$$H = H_{\text{LK}} + H_{\text{BP}} + H_B + H_{\text{DR}} + H_{\text{R},y} + H_{\text{R},z} - eE_z z + V(z) \quad (\text{C.5})$$

for this setup take the following  $4 \times 4$  representation when written out explicitly in the basis  $\Sigma_{1\text{D}} = \{g_+, g_-, e_+, e_-\}$ . First,

$$H_{\text{LK}} + H_{\text{BP}} = \begin{pmatrix} \frac{\hbar^2 k_z^2}{2m_g} & 0 & 0 & -iCk_z \\ 0 & \frac{\hbar^2 k_z^2}{2m_g} & -iCk_z & 0 \\ 0 & iCk_z & \frac{\hbar^2 k_z^2}{2m_e} + \Delta & 0 \\ iCk_z & 0 & 0 & \frac{\hbar^2 k_z^2}{2m_e} + \Delta \end{pmatrix} \quad (\text{C.6})$$

combines the Luttinger-Kohn (LK) and the Bir-Pikus (BP) Hamiltonian, where the latter changes the energy gap  $\Delta = \Delta_{\text{LK}} + \Delta_{\text{BP}}(\gamma)$  through the static strain that is caused by the Si shell of relative

Table C.1. Constants in the 1D model for holes in Ge/Si nanowires. The values were calculated as explained in Ref. [1] and in the text;  $\alpha$  was obtained following Ref. [2], and underlying Luttinger parameters for Ge were taken from Ref. [3].  $R$  denotes the core radius,  $m$  is the bare electron mass, and  $e$  is the elementary positive charge.

Constant	Value	Constant	Value
$C$	$7.26 \hbar^2/(mR)$	$\Delta_{\text{LK}}$	$0.73 \hbar^2/(mR^2)$
$m_g$	$0.043 m$	$m_e$	$0.054 m$
$K$	$2.89$	$L$	$8.04 R$
$M$	$2.56$	$U$	$0.15 R$
$S$	$0.36/R$	$T$	$0.98$
$\alpha$	$-0.4 \text{ nm}^2 e$		

thickness  $\gamma$ . The latter is defined as  $\gamma = (R_s - R)/R$ , where  $R$  ( $R_s$ ) is the core (shell) radius. Second,

$$H_B = \mu_B B_y \begin{pmatrix} 0 & iK & Lk_z & 0 \\ -iK & 0 & 0 & -Lk_z \\ Lk_z & 0 & 0 & -iM \\ 0 & -Lk_z & iM & 0 \end{pmatrix} \quad (\text{C.7})$$

describes the orbital and Zeeman-type coupling due to  $B_y$ . Third,

$$H_{\text{DR}} = eE_y U \begin{pmatrix} 0 & 0 & i & 0 \\ 0 & 0 & 0 & i \\ -i & 0 & 0 & 0 \\ 0 & -i & 0 & 0 \end{pmatrix} \quad (\text{C.8})$$

is the direct Rashba spin-orbit interaction (DRSOI) induced by  $E_y$ , and the conventional Rashba spin-orbit interaction (RSOI) reads

$$H_{\text{R},y} = \alpha E_y \begin{pmatrix} 0 & Tk_z & iS & 0 \\ Tk_z & 0 & 0 & iS \\ -iS & 0 & 0 & -\frac{3}{4}k_z \\ 0 & -iS & -\frac{3}{4}k_z & 0 \end{pmatrix}. \quad (\text{C.9})$$

Finally, one finds

$$H_{\text{R},z} = 2\alpha E_z S \begin{pmatrix} 0 & 0 & 0 & 1 \\ 0 & 0 & 1 & 0 \\ 0 & 1 & 0 & 0 \\ 1 & 0 & 0 & 0 \end{pmatrix} \quad (\text{C.10})$$

for the RSOI due to  $E_z$ . In Chapter 4, we write  $H_{\text{R}} = H_{\text{R},y} + H_{\text{R},z}$  for brevity. The longitudinal confinement  $V(z)$  and the linear shift  $-eE_z z$  do not affect the states  $|g_{\pm}\rangle$ ,  $|e_{\pm}\rangle$ , and therefore come with the identity matrix in this basis. We note that  $H_{\text{DR}}$  is obtained by projecting the direct coupling to the hole charge,  $-eE_y y$ , onto the low-energy subspace, whereas  $H_{\text{R},y}$  and  $H_{\text{R},z}$  result from  $\alpha E_y (k_z J_x - k_x J_z)$  and  $\alpha E_z (k_x J_y - k_y J_x)$ , respectively. Here,  $e$  is the elementary positive charge,  $\alpha$  is a material-dependent constant  $\propto (\text{band gap})^{-2}$  [2], and  $\hbar k_i$  ( $\hbar J_i$ ) is the operator for the momentum (spin) along the  $i$  axis. Further information on the different contributions can be found in Ref. [1], and the values of all relevant constants are summarized in Table C.1.

## C.2 Quantum Dot: Perturbative Analysis

### C.2.1 Hamiltonian

In the presence of harmonic confinement

$$V(z) = \frac{m_g \omega_g^2 z^2}{2} = \frac{\hbar \omega_g z^2}{2l_g^2}, \quad (\text{C.11})$$

where the confinement length

$$l_g = \sqrt{\frac{\hbar}{m_g \omega_g}} \quad (\text{C.12})$$

is defined by the effective mass  $m_g$  and the associated level spacing  $\hbar \omega_g$ , we now derive an effective  $2 \times 2$  Hamiltonian

$$H_q = \frac{E_Z}{2} \tilde{\sigma}_z + T_q \tilde{\sigma}_x \quad (\text{C.13})$$

for qubits that are formed by the two hole states of lowest energy in the quantum dot (QD). Here, the  $\tilde{\sigma}_i$  are spin-1/2 Pauli operators, and the tilde denotes that they act on the two QD states that form the qubit, in contrast to the  $\sigma_i$  that act on the spin index  $\{+, -\}$ . The parameters in  $H_q$  are the Zeeman splitting  $E_Z$  and the transverse coupling  $T_q \propto E_z$  that is induced by the electric field along the NW. Writing  $T_q = \bar{\nu} E_z$ , one has  $T_q = \nu_e \cos(\omega_{ac} t)$  for externally driven EDSR, and  $T_q = \nu_c (a^\dagger + a)$  for the cavity field. The coupling strengths  $\nu_{e,c} = \bar{\nu} E_{z,0}^{e,c}$  are proportional to the amplitudes  $E_{z,0}^{e,c}$ , and we calculate the proportionality factor  $\bar{\nu}$  below. Without loss of generality,  $E_Z$  and  $\bar{\nu}$  will always be defined as positive. Because typical Ge/Si NWs are rather thin,  $R \sim 5\text{--}10$  nm, we consider elongated QDs with  $l_g \gg R$ . This implies that the hole states are very well described by  $H$ , Eq. (C.5), where the effective 1D Hamiltonian is supplemented with the confinement  $V(z)$ . We now derive an analytical expression for  $H_q$  perturbatively.

From numerical results, Appendix C.3, we find that  $H_{R,z}$  and the difference between  $m_g$  and  $m_e$  may be neglected to a very good accuracy. Within the perturbative analysis, we therefore omit  $H_{R,z}$  and set  $m_g = m_e \equiv m_g$  for simplicity. The part of  $H$ , Eq. (C.5), that comes with the identity matrix in the basis  $\Sigma_{1D}$  then reads

$$H^{\text{id}} = \frac{\hbar^2 k_z^2}{2m_g} - eE_z z + V(z). \quad (\text{C.14})$$

With the definition

$$U' \equiv U + \alpha S/e, \quad (\text{C.15})$$

the remaining terms of  $H$  may be written as  $H_{1D}^a + H_{1D}^b + H_B$ , where

$$H_{1D}^a = \begin{pmatrix} 0 & 0 & ieE_y U' & 0 \\ 0 & 0 & 0 & ieE_y U' \\ -ieE_y U' & 0 & \Delta & 0 \\ 0 & -ieE_y U' & 0 & \Delta \end{pmatrix} \quad (\text{C.16})$$

and

$$H_{1D}^b = k_z \begin{pmatrix} 0 & \alpha E_y T & 0 & -iC \\ \alpha E_y T & 0 & -iC & 0 \\ 0 & iC & 0 & -\frac{3}{4} \alpha E_y \\ iC & 0 & -\frac{3}{4} \alpha E_y & 0 \end{pmatrix}. \quad (\text{C.17})$$

### C.2.2 Step 1

For Ge/Si NWs with typically  $R \sim 5\text{--}10$  nm and  $\gamma \sim 10\%\text{--}50\%$ , one finds  $10 \text{ meV} \lesssim \Delta \lesssim 25 \text{ meV}$ . Although this energy scale is rather large, we want to derive an effective model that also applies for rather strong electric fields for which  $|eE_y U'| \sim \Delta$ . Therefore, we first perform a unitary transformation

$$\begin{aligned} H' &= U_1^\dagger H U_1 \\ &= H^{\text{id}} + H'_{1\text{D}}{}^a + U_1^\dagger (H'_{1\text{D}}{}^b + H_B) U_1, \end{aligned} \quad (\text{C.18})$$

where the transformation matrix

$$U_1 = \begin{pmatrix} \cos \theta & 0 & i \sin \theta & 0 \\ 0 & \cos \theta & 0 & i \sin \theta \\ i \sin \theta & 0 & \cos \theta & 0 \\ 0 & i \sin \theta & 0 & \cos \theta \end{pmatrix} \quad (\text{C.19})$$

brings  $H'_{1\text{D}}{}^a$  into the diagonal form

$$H'_{1\text{D}}{}^a = U_1^\dagger H'_{1\text{D}}{}^a U_1 = \begin{pmatrix} 0 & 0 & 0 & 0 \\ 0 & 0 & 0 & 0 \\ 0 & 0 & \Delta' & 0 \\ 0 & 0 & 0 & \Delta' \end{pmatrix}. \quad (\text{C.20})$$

Above, we neglect global shifts in energy and use

$$\cos \theta \equiv \frac{\Delta + \Delta'}{\sqrt{(\Delta + \Delta')^2 + (2eE_y U')^2}}, \quad (\text{C.21})$$

$$\sin \theta \equiv \frac{2eE_y U'}{\sqrt{(\Delta + \Delta')^2 + (2eE_y U')^2}}, \quad (\text{C.22})$$

$$\Delta' \equiv \sqrt{\Delta^2 + (2eE_y U')^2}. \quad (\text{C.23})$$

We note that  $U_1$  and  $H'_{1\text{D}}{}^a$  in Eqs. (C.19) and (C.20) are represented in the basis  $\Sigma_{1\text{D}}$  introduced before. That is, we keep the basis states fixed and rearrange the matrix elements according to  $U_1$ . Although  $H' \neq H$  in general,  $H$  can, of course, be represented in exactly the same quasi-diagonal form as  $H'$ , as the inverse transformation  $H = U_1 H' U_1^\dagger$  may be performed by changing the basis states while keeping the matrix elements the same. In the proposed setup, knowledge of the eigenstates that form the qubit is not required (see Appendix C.2.8). Therefore, we proceed analogously with the remaining unitary transformations, i.e., we keep the basis states fixed and work with the formally equivalent, rotated versions of the Hamiltonian. If needed, the basis states of the unrotated system may be calculated either numerically (see Appendix C.3) or via inverse transformations as mentioned above.

### C.2.3 Step 2

The second unitary transformation corresponds to a Schrieffer-Wolff (SW) transformation that perturbatively decouples  $|g_\pm\rangle$  from  $|e_\pm\rangle$  to second order, where  $\Delta'$  in  $H'_{1\text{D}}{}^a$  provides the large energy. When the SW transformation is formally denoted by  $U_2$ , we find

$$H_g = P_g U_2^\dagger H' U_2 P_g = H_g^0 + H_g^r \quad (\text{C.24})$$

for the projection ( $P_g$ ) onto the subspace  $\Sigma_g = \{g_+, g_-\}$  of the bands of lowest-energy, where

$$H_g^0 = \begin{pmatrix} \frac{\hbar^2 k_z^2}{2m'_g} + V(z) & C'k_z + iE_{Z,g}^0/2 \\ C'k_z - iE_{Z,g}^0/2 & \frac{\hbar^2 k_z^2}{2m'_g} + V(z) \end{pmatrix} \quad (\text{C.25})$$

contains the dominant contributions and  $H_g^r$  contains the rest. In Eq. (C.25), the shorthand notation

$$E_{Z,g}^0 \equiv 2\mu_B B_y (K \cos^2 \theta - M \sin^2 \theta) \quad (\text{C.26})$$

stands for the Zeeman splitting at  $k_z = 0$ , and

$$m'_g = \left( \frac{1}{m_g} - \frac{2\tilde{C}^2}{\hbar^2 \Delta'} \right)^{-1} \quad (\text{C.27})$$

is the corrected effective mass, where

$$\tilde{C} \equiv C \cos(2\theta) - \alpha E_y \frac{3 + 4T}{8} \sin(2\theta). \quad (\text{C.28})$$

Due to the large coupling constants  $C$  and  $U$ , the expression

$$C' \equiv C \sin(2\theta) + \alpha E_y \left( T \cos^2 \theta - \frac{3}{4} \sin^2 \theta \right) \quad (\text{C.29})$$

in Eq. (C.25) becomes large even at moderate  $E_y$ , so that  $C'k_z$  is no longer a small perturbation when the applied field exceeds a certain threshold value. In typical Ge/Si NW QDs, one finds  $|C'|/l_g \sim \hbar\omega_g$  for  $|E_y| \sim 1 \text{ V}/\mu\text{m}$ , and we therefore treat this coupling as part of the leading-order Hamiltonian.

### C.2.4 Step 3

Next, we introduce a suitable basis for the QD states. For this, we consider the Hamiltonian

$$H'_g = U_3^\dagger H_g U_3 = H_g'^0 + H_g'^r, \quad (\text{C.30})$$

where

$$U_3 = \frac{1}{\sqrt{2}} \begin{pmatrix} 1 & -1 \\ 1 & 1 \end{pmatrix} \quad (\text{C.31})$$

was chosen such that  $H_g'^0 = U_3^\dagger H_g^0 U_3$  reads

$$H_g'^0 = \frac{\hbar^2 k_z^2}{2m'_g} + V(z) + \begin{pmatrix} C'k_z & iE_{Z,g}^0/2 \\ -iE_{Z,g}^0/2 & -C'k_z \end{pmatrix}. \quad (\text{C.32})$$

We note that

$$\frac{\hbar^2 k_z^2}{2m'_g} \pm C'k_z = \frac{\hbar^2}{2m'_g} \left( k_z \pm \frac{C'm'_g}{\hbar^2} \right)^2 - \frac{C'^2 m'_g}{2\hbar^2}, \quad (\text{C.33})$$

and from the diagonal elements of Eq. (C.32) we identify

$$|n_\pm\rangle \equiv |g_\pm\rangle \otimes e^{\mp iC'm'_g z/\hbar^2} |\varphi_n\rangle \quad (\text{C.34})$$

as a well-suited set of basis states for  $H'_g$ . The  $|\varphi_n\rangle$ , with quantum number  $n \in \{0, 1, \dots\}$ , correspond to the solutions  $\varphi_n(z)$  of the 1D harmonic oscillator

$$\left(\frac{\hbar^2 k_z^2}{2m'_g} + V(z)\right) \varphi_n(z) = \hbar\omega'_g \left(n + \frac{1}{2}\right) \varphi_n(z), \quad (\text{C.35})$$

where  $k_z = -i\partial_z$  in coordinate space. The effective level spacing reads

$$\hbar\omega'_g = \sqrt{\frac{m_g}{m'_g}} \hbar\omega_g \quad (\text{C.36})$$

and, consequently, one may define the corrected confinement length  $l'_g$  as

$$l'_g = \sqrt{\frac{\hbar}{m'_g \omega'_g}} = l_g \left(\frac{m_g}{m'_g}\right)^{1/4}. \quad (\text{C.37})$$

We mention in passing that  $H_g^r$  and  $H_g^{rr}$  contain a term  $\propto B_y^2 k_z^2$  that gives rise to additional rescaling of the effective mass. Taking this term into account, the corrected effective mass reads

$$m''_g = \left(\frac{1}{m_g} - \frac{2\tilde{C}^2 + 2(\mu_B L B_y)^2}{\hbar^2 \Delta'}\right)^{-1}, \quad (\text{C.38})$$

which implies that the level spacing depends on both  $E_y$  and  $B_y$ . However, the above correction due to  $B_y$  turns out to be very small, and we therefore treat this term as part of  $H_g^{rr}$ .

Using

$$\left(\frac{\hbar^2 k_z^2}{2m'_g} + V(z) \pm C' k_z\right) |n_{\pm}\rangle = E_n |n_{\pm}\rangle, \quad (\text{C.39})$$

with

$$E_n = \hbar\omega'_g \left(n + \frac{1}{2}\right) - \frac{C'^2 m'_g}{2\hbar^2}, \quad (\text{C.40})$$

we represent  $H'_g$  by a  $2N$ -dimensional matrix with basis

$$\Sigma_N = \{0_+, 0_-, \dots, (N-1)_+, (N-1)_-\}. \quad (\text{C.41})$$

The projection onto this basis is denoted by  $P_N^{\text{QD}}$ , and the projected versions of  $H'_g$ ,  $H_g^0$ , and  $H_g^{rr}$  are referred to as

$$H_N = P_N^{\text{QD}} H'_g P_N^{\text{QD}}, \quad (\text{C.42})$$

$$H_N^0 = P_N^{\text{QD}} H_g^0 P_N^{\text{QD}}, \quad (\text{C.43})$$

$$H_N^r = P_N^{\text{QD}} H_g^{rr} P_N^{\text{QD}}. \quad (\text{C.44})$$

We note that  $H_N = H'_g$  in the limit  $N \rightarrow \infty$  (analogously for  $H_N^0$  and  $H_N^r$ ). As discussed below, we find that  $N = 3$  is usually sufficient for a quantitatively reliable estimate of  $H_q$ , Eq. (C.13).

### C.2.5 Step 4

A fourth unitary transformation is required to derive a leading-order Hamiltonian  $H_N^{\prime\alpha}$  that is diagonal and includes the Zeeman splitting. This Hamiltonian is calculated via

$$H_N^{\prime\alpha} = \text{Diagonal}[U_4^\dagger H_N^0 U_4], \quad (\text{C.45})$$

where  $\text{Diagonal}[A]$  stands for the diagonal part of matrix  $A$ . The transformation matrix  $U_4$  corresponds to a Kronecker product

$$U_4 = \mathbb{1}_N \otimes U_y \quad (\text{C.46})$$

of an  $N$ -dimensional unit matrix  $\mathbb{1}_N$  for the states  $|\varphi_n\rangle$  and

$$U_y = \frac{1}{\sqrt{2}} \begin{pmatrix} 1 & 1 \\ -i & i \end{pmatrix} \quad (\text{C.47})$$

for  $|g_\pm\rangle$ . Based on Eq. (C.32),  $U_y$  was chosen to fulfill

$$\frac{E_{Z,g}^0}{2} U_y^\dagger \begin{pmatrix} 0 & i \\ -i & 0 \end{pmatrix} U_y = \frac{E_{Z,g}^0}{2} \begin{pmatrix} 1 & 0 \\ 0 & -1 \end{pmatrix}. \quad (\text{C.48})$$

We note, however, that the resulting Zeeman splitting between states  $|n_+\rangle$  and  $|n_-\rangle$  in  $H_N^a$  is not simply  $E_{Z,g}^0$  and changes with  $n$ . In contrast, the orbital level spacing is always  $\hbar\omega'_g$ . The remaining terms of the Hamiltonian are summarized in

$$H_N^b = U_4^\dagger H_N U_4 - H_N^a. \quad (\text{C.49})$$

## C.2.6 Step 5

We perturbatively decouple the two lowest QD states  $|0_\pm\rangle$  from higher states via a second-order SW transformation. The large energy is now provided by the level spacing  $\hbar\omega'_g$  in  $H_N^a$ , and  $H_N^b$  corresponds to the perturbation. The resulting projection ( $P_q^0$ ) onto the qubit subspace  $\Sigma_q = \{0_+, 0_-\}$  reads

$$H'_q = P_q^0 U_5^\dagger (H_N^a + H_N^b) U_5 P_q^0, \quad (\text{C.50})$$

where the SW transformation is denoted by  $U_5$ . Neglecting global shifts in energy, the result can be written in terms of Pauli matrices,

$$H'_q = c_x \sigma'_x + c_y \sigma'_y + c_z \sigma'_z. \quad (\text{C.51})$$

For the setup under study and with the standard representation in the basis  $\Sigma_q$ ,

$$\sigma'_x = \begin{pmatrix} 0 & 1 \\ 1 & 0 \end{pmatrix}, \quad \sigma'_y = \begin{pmatrix} 0 & -i \\ i & 0 \end{pmatrix}, \quad \sigma'_z = \begin{pmatrix} 1 & 0 \\ 0 & -1 \end{pmatrix}, \quad (\text{C.52})$$

we find  $c_x = 0$  and  $c_y \propto E_z$  for arbitrarily large  $N$ . That is,  $c_z$  provides the Zeeman splitting between the qubit states, whereas  $c_y$  corresponds to the transverse coupling driven by  $E_z$ . In fact, within the second-order perturbation theory,  $c_y$  is fully determined by the coupling between states  $|0_\pm\rangle$  and  $|1_\pm\rangle$ , so that the result for  $c_y$  does not change for  $N > 2$ . This is different for  $c_z$ . The reason, in particular, is that  $H'_g$  features terms of type  $\sigma_{x,y}$  that couple the two spin blocks ( $\sigma_i$ : Pauli operators acting on the spin index  $\{+, -\}$  [1]). Because of

$$|\langle n_\pm | \sigma_{x,y} | m_\mp \rangle| \neq \delta_{mn}, \quad (\text{C.53})$$

these also generate nonzero matrix elements between  $|0_\pm\rangle$  and  $|n_\mp\rangle$  with large  $n$ . However, as  $H'_g$  contains terms up to the second power in  $k_z$  only, the dominant contributions to  $c_z$  are provided within the subspace of states  $|0_\pm\rangle$ ,  $|1_\pm\rangle$ , and  $|2_\pm\rangle$ . Remarkably, we find from Taylor expansions that linear terms in  $B_y$  are due to the first four states  $|0_\pm\rangle$  and  $|1_\pm\rangle$  only. Hence, the calculated  $g$  factor  $g \equiv 2c_z/(\mu_B B_y)$  remains unchanged for  $N > 2$  (as for  $c_y$ ), provided that  $B_y$  is weak enough for the linear expansion of  $c_z$



to apply. In the main text, we use  $N = 3$  for all plots presenting the effective model. The quantitative corrections from  $N > 3$  to the Zeeman splitting are only expected in the regime where both  $E_y$  and  $B_y$  are large.

The full formulas for  $c_y$  and  $c_z$  are too lengthy to be displayed here. However, as mentioned above, we can perform a linear expansion in  $B_y$  when the Zeeman splitting is small compared to the orbital level spacing. The results are shown in Eqs. (C.123) and (C.124) of Appendix C.7, and we note that the corrections for both  $c_y$  and  $c_z$  are of order  $B_y^3$ . By keeping only the dominant terms, these formulas can be simplified even further. In particular, we find that DRSOI  $\gg$  RSOI in typical Ge/Si NW QDs, and conventional RSOI may therefore be neglected. The simplified results without RSOI are summarized in Eqs. (C.127) and (C.128).

### C.2.7 Step 6

From  $H'_q$ , Eq. (C.51), the final form of the effective  $2 \times 2$  Hamiltonian  $H_q$ , Eq. (C.13), is obtained through a unitary transformation

$$H''_q = U_6^\dagger H'_q U_6 = \frac{E_Z}{2} \sigma'_z + T_q \sigma'_x, \quad (\text{C.54})$$

where  $E_Z$  is the Zeeman splitting and  $T_q = \bar{\nu} E_z$  is the transverse coupling due to the electric field  $E_z$ . We recall that  $T_q = \nu_e \cos(\omega_{\text{ac}} t)$  for EDSR and  $T_q = \nu_c (a^\dagger + a)$  for operations based on the cavity field, with  $\nu_{e,c} = \bar{\nu} E_{z,0}^{e,c}$  as the coupling strengths. When  $U_6$  is chosen such that  $E_Z$  and  $\bar{\nu}$  are both positive, one identifies

$$E_Z = |2c_z|, \quad (\text{C.55})$$

$$\bar{\nu} = \frac{|c_y(E_{z,0})|}{E_{z,0}}, \quad (\text{C.56})$$

where  $E_{z,0}$  stands for an arbitrary electric field amplitude and  $c_y = c_y(E_z)$  is the transverse coupling coefficient derived in this appendix. Because the ac fields along the NW are small in the studied setup, corrections of type  $E_z^2$  in  $c_z$  [see, e.g., Eq. (C.124)] are neglected in Eq. (C.55), and, thus, the Zeeman splitting  $E_Z$  is independent of  $\cos(\omega_{\text{ac}} t)$  and  $(a^\dagger + a)$ , respectively.

We note that  $H_q$  is obtained from the formally equivalent  $H''_q$  when the Pauli operators  $\sigma'_i$  are replaced by  $\tilde{\sigma}_i$ , i.e., when the basis states  $|0_\pm\rangle$  in  $\Sigma_q$  are replaced by the corresponding eigenstates of  $H$  that form the qubit.

### C.2.8 Remarks

The unitary transformations presented here illustrate that the true basis states of the qubit will differ from  $|0_\pm\rangle$ , Eq. (C.34). The eigenstates may be calculated either by an inverse transformation or numerically, see Appendix C.3. However, we emphasize that knowledge of the qubit states is not required for the implementation of quantum gates proposed here. EDSR only requires knowledge about the Zeeman splitting and the presence of an electric-field-induced transverse coupling. Moreover, long-range qubit-qubit interactions mediated by the cavity field are independent of the basis states of the individual qubits (see also Appendix C.5).

## C.3 Quantum Dot: Numerical Analysis

### C.3.1 Basis States

The Zeeman energy  $E_Z$  and the coupling parameter  $\bar{\nu}$  in QDs with  $l_g \gg R$ , for which  $H$  of Eq. (C.5) applies, can also be calculated numerically. For this, we represent  $H = H(E_z)$  by a matrix with  $4N'$

basis states. The basis of the matrix reads  $\Sigma_{N'} = \{\Sigma_{N'}^g, \Sigma_{N'}^e\}$ , where

$$\Sigma_{N'}^{g,e} = \{0_+^{g,e}, 0_-^{g,e}, \dots, (N'-1)_+^{g,e}, (N'-1)_-^{g,e}\}, \quad (\text{C.57})$$

and we denote the projector for  $\Sigma_{N'}$  by  $P_{N'}$ . The basis states are defined as

$$|n_\pm^g\rangle = |g_\pm\rangle \otimes |\varphi_n^g\rangle, \quad (\text{C.58})$$

$$|n_\pm^e\rangle = |e_\pm\rangle \otimes |\varphi_n^e\rangle. \quad (\text{C.59})$$

Here, analogous to Appendix C.2, the  $|\varphi_n^{g,e}\rangle$  are the eigenstates of the 1D harmonic oscillator

$$\left(\frac{\hbar^2 k_z^2}{2m_{g,e}} + V(z)\right) |\varphi_n^{g,e}\rangle = \hbar\omega_{g,e} \left(n + \frac{1}{2}\right) |\varphi_n^{g,e}\rangle, \quad (\text{C.60})$$

where  $n$  is the quantum number and  $\omega_e = \omega_g \sqrt{m_g/m_e}$ . When an electric field  $E_z$  with amplitude  $E_{z,0}$  is applied along the NW, two approaches are suitable for the numerical calculation of  $E_Z$  and  $\bar{\nu}$  in  $H_q$ , Eq. (C.13). Provided that  $N'$  is chosen large enough, both approaches make use of an exact diagonalization in the degrees of freedom of the longitudinal coordinate  $z$ . However, they differ in the range of allowed  $E_{z,0}$  and in the computation time. Both algorithms are outlined below.

### C.3.2 Algorithm 1

The first approach requires calculation of all  $4N'$  eigenstates. As explained in more detail in the next paragraph, it applies for any strength of  $E_z$  and can therefore be regarded as generally valid. At first, we calculate all the eigenstates  $|m\rangle$  and corresponding eigenenergies  $E_m$  of  $P_{N'}H(0)P_{N'}$ . Based on this eigensystem, where  $m \in \{0, 1, \dots, 4N'-1\}$  and  $E_0 \leq E_1 \leq \dots \leq E_{4N'-1}$ , we generate a transformation matrix  $U_0$  that diagonalizes the Hamiltonian according to

$$\text{diag}(E_0, E_1, \dots, E_{4N'-1}) = U_0^\dagger P_{N'} H(0) P_{N'} U_0. \quad (\text{C.61})$$

The transverse coupling  $\nu \equiv \bar{\nu} E_{z,0}$  is then calculated via

$$\nu = |\langle 1 | U_0^\dagger P_{N'} H(E_{z,0}) P_{N'} U_0 | 0 \rangle|, \quad (\text{C.62})$$

and the Zeeman energy  $E_Z$  is obtained through

$$E_Z = |\langle 1 | U_0^\dagger P_{N'} H(E_{z,0}) P_{N'} U_0 | 1 \rangle - \langle 0 | U_0^\dagger P_{N'} H(E_{z,0}) P_{N'} U_0 | 0 \rangle|. \quad (\text{C.63})$$

We note that, for realistic  $E_{z,0}$ , the latter is very well approximated by  $E_1 - E_0$ , which is the Zeeman splitting between the qubit states in the absence of  $E_z$ .

When  $E_{z,0}$  is large, the two eigenstates of  $H(E_{z,0})$  with lowest energy cannot be expressed in terms of  $|0\rangle$  and  $|1\rangle$  only. In systems driven through EDSR, however, where  $E_z$  is an ac field that is in (quasi-)resonance with the Zeeman splitting  $E_1 - E_0$ , the dynamics are determined by the coupling strength induced between  $|0\rangle$  and  $|1\rangle$ , Eq. (C.62). Therefore, this algorithm applies for any strength of  $E_z$  when  $N'$  is large enough for the diagonalization in the degrees of freedom of the coordinate  $z$  to be accurate.

### C.3.3 Algorithm 2

The second approach applies for small  $E_{z,0}$  only and allows for reduced computation times when  $N'$  is chosen very large, because only four instead of  $4N'$  eigenstates need to be calculated and a transformation matrix  $U_0$  is not required. Analogously to the first method, we calculate the eigenenergies  $E_m$  of

$P_{N'}H(0)P_{N'}$  and the two eigenstates  $|0\rangle$  and  $|1\rangle$  of lowest energy. In addition, we compute the eigenenergies  $E'_m$  and the eigenstates  $|0'\rangle$  and  $|1'\rangle$  of  $P_{N'}H(E_{z,0})P_{N'}$ . When  $E_{z,0}$  is small, such that  $|0'\rangle \approx |0\rangle$ ,  $|1'\rangle \approx |1\rangle$ , and

$$|\langle 0|0'\rangle|^2 + |\langle 1|0'\rangle|^2 \simeq 1, \quad (\text{C.64})$$

$$|\langle 0|1'\rangle|^2 + |\langle 1|1'\rangle|^2 \simeq 1, \quad (\text{C.65})$$

one finds

$$\nu = \frac{E'_1 - E'_0}{2} |\langle 1|1'\rangle \langle 1'|0\rangle - \langle 1|0'\rangle \langle 0'|0\rangle|, \quad (\text{C.66})$$

$$E_Z = (E'_1 - E'_0) \left( |\langle 0|0'\rangle|^2 + |\langle 1|1'\rangle|^2 - 1 \right). \quad (\text{C.67})$$

### C.3.4 Remarks

The plots in Chapter 4 were generated with the first, more general method, using  $N' = 10$ . The latter was chosen because, on the one hand,  $N' = 10$  is large enough so that notable changes in the results are not observed as  $N'$  is increased, and, on the other hand, it is small enough to enable fast evaluation, as  $40 \times 40$  matrices can be diagonalized quickly. For the Ge/Si NW QD considered in Chapter 4, we find that plots from approaches 1 and 2 are basically indistinguishable at  $E_{z,0} \lesssim 2 \times 10^3$  V/m, i.e., for  $eE_{z,0}l_g/(\sqrt{2}\hbar\omega_g) \lesssim 0.1$  [see also Eq. (C.71)]. At  $E_{z,0} > 2 \times 10^3$  V/m, the  $\nu$  from method 2 become smaller than those from method 1. This deviation is expected, because the assumptions of approach 2 are no longer well fulfilled when  $E_{z,0}$  is large.

## C.4 Parameter Range and Validity of Results

### C.4.1 Effective 1D Hamiltonian

In the presence of a Si shell, we estimate that the effective 1D Hamiltonian

$$H_{1D} = H_{LK} + H_{BP} + H_B + H_{DR} + H_{R,y} + H_{R,z} \quad (\text{C.68})$$

is valid for  $2 \text{ nm} \lesssim R \lesssim 12 \text{ nm}$ . At  $R \lesssim 2 \text{ nm}$ , the holes notably leak into the Si shell, despite the large VB offset  $\sim 0.5 \text{ eV}$  [4] at the interface. Furthermore, the LK Hamiltonian loses validity when the cross section consists of very few atoms only [5, 6]. When both  $R$  and  $\gamma$  are large, a simple projection of the BP Hamiltonian onto the low-energy subspace is no longer reliable as the strain-induced coupling to higher bands may exceed the energy separation  $\propto R^{-2}$  [1].

In general,  $H_{1D}$  is valid as long as the low-energy  $4 \times 4$  subspace is well isolated from these higher bands. This criterion puts restrictions on the strength of  $E_y$  in our model, and the limits for  $E_y$  depend on the energy difference to the next excited band ( $|F_z| = 3/2$ ). Because the total angular momentum  $F_z$  along the Ge/Si NW is conserved in the spherical approximation, which applies well for both the LK and the BP Hamiltonian of the system, the hole spectrum can be calculated exactly in the absence of external fields, as outlined in Ref. [1]. Based on these exact spectra, we estimate that the  $4 \times 4$  subspace can be considered well isolated when

$$|E_y| \lesssim 5 \frac{\text{kV nm}^3}{\mu\text{m} R^3}. \quad (\text{C.69})$$

This criterion holds for any shell thickness, and higher transverse subbands should be included when  $|E_y|$  is much larger than the boundary value. The proportionality to  $R^{-3}$  is consistent with  $U \propto R$  and the  $R^{-2}$ -type decrease of the level spacings. For  $R = 7.5 \text{ nm}$  discussed in Chapter 4, Eq. (C.69) yields  $|E_y| \lesssim 12 \text{ V}/\mu\text{m}$ .

### C.4.2 Qubit Hamiltonian

Our numerical and analytical results for  $H_q$  describing the qubit are based on the Hamiltonian  $H$ , Eq. (C.5). The latter is valid when both  $l_g \gg R$  and  $H_{1D}$  apply.

The perturbative approach from Appendix C.2 furthermore assumes that  $m'_g$  in Eq. (C.27) is positive and finite, which corresponds to

$$\frac{2m_g \tilde{C}^2}{\hbar^2 \Delta'} \ll 1. \quad (\text{C.70})$$

In addition, the two SW transformations require that the block-off-diagonal terms are small enough for the perturbative decoupling to be possible. From careful analysis of all matrices, we deduce a list of inequalities that have to be fulfilled. It turns out, however, that all these criteria are usually very well met when Eq. (C.70) holds and when  $B_y$  is chosen such that the Zeeman splitting does not exceed the orbital level spacing. We note that the left-hand side of Eq. (C.70) roughly scales with  $R^{-2}$ . Based on all criteria, we find that the perturbative approach applies when  $5 \text{ nm} \lesssim R \lesssim 12 \text{ nm}$  for typical Ge/Si NW QDs, and the agreement between numerics (Appendix C.3) and the derived formulas improves as  $R$  increases. For small core radii  $R \lesssim 5 \text{ nm}$ , the Hamiltonian  $H_q$  should, e.g., be calculated numerically as described in Appendix C.3. The condition for the electric field amplitude  $E_{z,0}$  along the NW reads

$$E_{z,0} \ll \frac{\sqrt{2} \hbar \omega'_g}{l'_g e}. \quad (\text{C.71})$$

This inequality has a simple physical meaning. For the perturbation theory to be applicable, the shift of the minimum of  $V(z)$  due to  $E_{z,0}$  should not exceed the confinement length  $l'_g$ . With  $m'_g \sim m_g$  and the value from Table C.1, one obtains  $E_{z,0} \ll 2.5 \text{ V nm}^2/l_g^3$ . For  $l_g = 50 \text{ nm}$  discussed in Chapter 4, this implies  $E_{z,0} \ll 2 \times 10^4 \text{ V/m}$ .

The numerical results from Appendix C.3 hold whenever  $H$  applies, provided that  $N'$  is large enough. Furthermore, they can provide detailed information about the basis states of the qubit, if required.

### C.4.3 Remarks

In conclusion, although the parameter range is limited due to the complexity of the system, our theories are very well suited for commonly used Ge/Si NWs and NW QDs [4, 7–16]. All electric fields considered in Chapter 4 are far below the boundary values listed here.

## C.5 Cavity-Based Interactions

### C.5.1 Electric Cavity Field

We consider a 1D superconducting transmission line resonator [17, 18] of length  $L_c$  along the  $x$  axis. The center conductor ranges from  $x = 0$  to  $x = L_c$ , and the distance between the ground planes and the center conductor is denoted by  $d$ . When  $c$  ( $l$ ) stands for the capacitance (inductance) per unit length of the resonator, the electric field  $E_c(x)$  within the cavity reads

$$E_c(x) = \frac{1}{d} \sum_{p=1}^{\infty} \sqrt{\frac{\hbar \omega_p}{c L_c}} \cos\left(\frac{p\pi x}{L_c}\right) (a_p^\dagger + a_p), \quad (\text{C.72})$$

where

$$\hbar \omega_p = \frac{\hbar p \pi}{L_c \sqrt{lc}} \quad (\text{C.73})$$

are the energies of the photon modes  $p \in \{1, 2, \dots\}$  inside the cavity. Details of the derivation can be found in Ref. [17]. In Eq. (C.72), the operators  $a_p^\dagger$  and  $a_p$  are the creation and annihilation operators,

respectively, for the modes  $p$ , and obey the commutation relations  $[a_p, a_{p'}^\dagger] = a_p a_{p'}^\dagger - a_{p'}^\dagger a_p = \delta_{pp'}$  and  $[a_p, a_{p'}] = 0 = [a_p^\dagger, a_{p'}^\dagger]$ . With these ladder operators, the cavity photon Hamiltonian is

$$H_\gamma = \sum_{p=1}^{\infty} \hbar\omega_p \left( a_p^\dagger a_p + \frac{1}{2} \right). \quad (\text{C.74})$$

In the hybrid system with Ge/Si NW QDs inside the cavity, we assume that the qubits are quasi-resonant with one particular photon mode  $p = \tilde{p}$  (typically  $\tilde{p} = 1, 2$ ), so that all other modes can be neglected. With the notation  $a \equiv a_{\tilde{p}}$ ,  $a^\dagger \equiv a_{\tilde{p}}^\dagger$ , and  $\omega_c \equiv \omega_{\tilde{p}}$ , the cavity electric field that is relevant for the qubit dynamics reduces to

$$E_c(x) = \frac{1}{d} \sqrt{\frac{\hbar\omega_c}{cL_c}} \cos\left(\frac{\tilde{p}\pi x}{L_c}\right) (a^\dagger + a), \quad (\text{C.75})$$

and the relevant part of  $H_\gamma$  reads

$$H_\gamma = \hbar\omega_c a^\dagger a. \quad (\text{C.76})$$

When a NW QD is located near an antinode of  $E_c(x)$ , with the cavity field oriented along the symmetry axis of the NW ( $z$  axis), the cavity-induced electric field inside the dot is

$$E_z = E_{z,0}^c (a^\dagger + a), \quad (\text{C.77})$$

where the effective strength  $E_{z,0}^c$  corresponds to

$$E_{z,0}^c = \frac{1}{\epsilon_r d} \sqrt{\frac{\hbar\omega_c}{cL_c}}. \quad (\text{C.78})$$

Because the hole states in Ge/Si NWs are located in the Ge core, the electric field  $E_z$  inside the NW QD is reduced compared to  $E_c$  by the relative permittivity  $\epsilon_r \simeq 16$  of Ge.

From a rough estimate, we obtain  $1/\sqrt{\epsilon_r} \simeq c_0/n_{\text{eff}}$  and  $E_{z,0}^c \propto \hbar\omega_c/\sqrt{\tilde{p}hd}$ , where  $c_0$  is the speed of light in vacuum,  $n_{\text{eff}}$  is the effective refractive index within the cavity, and  $h$  is the height of the superconductor. This relation allows us to estimate experimentally feasible values of  $E_{z,0}^c$ . Based on the numbers provided in Refs. [17–19], we consider  $\hbar\omega_c = 25 \mu\text{eV}$ ,  $d = 5 \mu\text{m}$ ,  $h = 0.2 \mu\text{m}$ ,  $\tilde{p} = 2$ , and  $\epsilon_r E_{z,0}^c = 0.2 \text{ V/m}$  as reference values. When  $hd = 1 \mu\text{m}^2$  is reduced to  $hd = 10^{-2} \mu\text{m}^2$ , which seems feasible, one obtains  $E_{z,0}^c = 0.7 \text{ V/m}$  for  $\tilde{p} = 1$  and  $\hbar\omega_c = 0.1 \text{ meV}$ . In Chapter 4, we therefore set  $E_{z,0}^c = 3 \text{ V/m}$  for the example of  $\hbar\omega_c \simeq 0.35 \text{ meV}$ . Higher values for  $E_{z,0}^c$  can easily be realized for qubits with larger Zeeman energies, but may also be possible for fixed frequencies when the fabrication can be further optimized (reducing the cavity mode volume).

Finally, we note that magnetic fields  $|B_y| > 0.2 \text{ T}$  imply that the superconducting transmission line resonators are fabricated from suitable materials, as  $B_y$  exceeds the critical magnetic field of commonly used Nb resonators [18–20]. One possible material is NbTiN, which remains superconducting at magnetic fields of several Tesla [21, 22].

## C.5.2 Qubit-Cavity Coupling

The coupled system of cavity field and qubit is described by  $H_{c-q} = H_q + H_\gamma$ ,

$$H_{c-q} = \frac{E_z}{2} \tilde{\sigma}_z + \nu_c \tilde{\sigma}_x (a^\dagger + a) + \hbar\omega_c a^\dagger a, \quad (\text{C.79})$$

where we recall the notation  $\nu_c = \bar{\nu} E_{z,0}^c$ . Introducing

$$\tilde{\sigma}_{\pm} = \tilde{\sigma}_x \pm i\tilde{\sigma}_y \quad (\text{C.80})$$

as the raising and lowering operator, respectively, of the qubit, one obtains

$$H_{c-q} = \frac{E_Z}{2} \tilde{\sigma}_z + \frac{\nu_c}{2} (\tilde{\sigma}_+ + \tilde{\sigma}_-) (a^\dagger + a) + \hbar\omega_c a^\dagger a. \quad (\text{C.81})$$

When the detuning

$$\Delta_q \equiv E_Z - \hbar\omega_c \quad (\text{C.82})$$

between the qubit and the cavity is small, i.e.,  $|\Delta_q| \ll E_Z$  and  $|\Delta_q| \ll \hbar\omega_c$ , one can adopt the rotating wave approximation [23] and get the Jaynes-Cummings Hamiltonian

$$H_{c-q} = \frac{E_Z}{2} \tilde{\sigma}_z + \frac{\nu_c}{2} (\tilde{\sigma}_+ a + \tilde{\sigma}_- a^\dagger) + \hbar\omega_c a^\dagger a. \quad (\text{C.83})$$

If, for instance, the qubit is prepared in the excited state,  $H_{c-q}$  implies that the excitation is coherently swapped between the qubit and the cavity. At resonance and at low temperatures ( $k_B T \ll \hbar\omega_c$ ;  $k_B$  is the Boltzmann constant,  $T$  the temperature), for which the occupation number of the cavity mode approaches zero, the resulting Rabi oscillation has a full-cycle duration on the order of  $\pi\hbar/\nu_c$ .

### C.5.3 Qubit-Qubit Coupling

Long-distance two-qubit gates can be implemented by operating two qubits near resonance with the cavity field. With the index in superscript parentheses labeling qubits, the corresponding Hamiltonian reads

$$H_{c-2q} = \sum_{i=1}^2 \left[ \frac{E_Z^{(i)}}{2} \tilde{\sigma}_z^{(i)} + \frac{\nu_c^{(i)}}{2} (\tilde{\sigma}_+^{(i)} a + \tilde{\sigma}_-^{(i)} a^\dagger) \right] + \hbar\omega_c a^\dagger a. \quad (\text{C.84})$$

Analogous to the single-qubit case, this Hamiltonian applies for  $|\Delta_q^{(i)}| \ll E_Z^{(i)}$  and  $|\Delta_q^{(i)}| \ll \hbar\omega_c$ , where  $\Delta_q^{(i)} = E_Z^{(i)} - \hbar\omega_c$ . If furthermore  $\nu_c^{(i)} \ll |\Delta_q^{(i)}|$ , it is possible to remove the qubit-cavity interaction

$$H_{c-2q}^{\text{int}} = \sum_{i=1}^2 \frac{\nu_c^{(i)}}{2} (\tilde{\sigma}_+^{(i)} a + \tilde{\sigma}_-^{(i)} a^\dagger) \quad (\text{C.85})$$

perturbatively via a Schrieffer-Wolff transformation [17, 23–25]. For this, we define

$$\tilde{H}_{c-2q} = e^T H_{c-2q} e^{-T}, \quad (\text{C.86})$$

where  $H_{c-2q} = H_{c-2q}^0 + H_{c-2q}^{\text{int}}$  and  $T = T_1 + \mathcal{O}(\nu_c^3/\Delta_q^3)$  with

$$T_1 = \sum_{i=1}^2 \frac{\nu_c^{(i)}}{2\Delta_q^{(i)}} (\tilde{\sigma}_+^{(i)} a - \tilde{\sigma}_-^{(i)} a^\dagger). \quad (\text{C.87})$$

Exploiting  $[T_1, H_{c-2q}^0] = -H_{c-2q}^{\text{int}}$ , expansion of Eq. (C.86) yields

$$\begin{aligned}\tilde{H}_{c-2q} &= H_{c-2q}^0 + \frac{1}{2} [T_1, H_{c-2q}^{\text{int}}] + \mathcal{O}\left(\frac{\nu_c^4}{\Delta_q^3}\right) \\ &= H_{c-2q}^0 + \sum_{i=1}^2 \frac{(\nu_c^{(i)})^2}{2\Delta_q^{(i)}} \left(1 + \tilde{\sigma}_z^{(i)} + 2\tilde{\sigma}_z^{(i)} a^\dagger a\right) \\ &\quad + \frac{J_{xy}}{8} \left(\tilde{\sigma}_+^{(1)}\tilde{\sigma}_-^{(2)} + \tilde{\sigma}_-^{(1)}\tilde{\sigma}_+^{(2)}\right) + \mathcal{O}\left(\frac{\nu_c^4}{\Delta_q^3}\right),\end{aligned}\tag{C.88}$$

where we defined

$$J_{xy} = J_{xy}^{(1,2)} = \nu_c^{(1)}\nu_c^{(2)} \left(\frac{1}{\Delta_q^{(1)}} + \frac{1}{\Delta_q^{(2)}}\right).\tag{C.89}$$

The subscript of  $J_{xy}$  indicates that the qubit-qubit interaction in  $\tilde{H}_{c-2q}$  is equivalent to a transverse spin-spin coupling,

$$\tilde{\sigma}_+^{(1)}\tilde{\sigma}_-^{(2)} + \tilde{\sigma}_-^{(1)}\tilde{\sigma}_+^{(2)} = 2\left(\tilde{\sigma}_x^{(1)}\tilde{\sigma}_x^{(2)} + \tilde{\sigma}_y^{(1)}\tilde{\sigma}_y^{(2)}\right).\tag{C.90}$$

Finally, when the photon number operator in Eq. (C.88) is replaced by the average occupation number, i.e.,  $a^\dagger a \rightarrow \langle a^\dagger a \rangle \equiv \bar{n}$ , and when global shifts in energy are neglected,  $\tilde{H}_{c-2q}$  results in the effective two-qubit Hamiltonian

$$H_{q-q} = \sum_{i=1}^2 \frac{\bar{E}_Z^{(i)}}{2} \tilde{\sigma}_z^{(i)} + \frac{J_{xy}}{8} \left(\tilde{\sigma}_+^{(1)}\tilde{\sigma}_-^{(2)} + \tilde{\sigma}_-^{(1)}\tilde{\sigma}_+^{(2)}\right),\tag{C.91}$$

where

$$\bar{E}_Z^{(i)} = E_Z^{(i)} + (1 + 2\bar{n}) \frac{(\nu_c^{(i)})^2}{\Delta_q^{(i)}}.\tag{C.92}$$

The cavity-induced correction to the Zeeman splitting that is independent of (proportional to)  $\bar{n}$  corresponds to the Lamb shift (ac Stark shift) [17, 23].

### C.5.4 Two-Qubit Gates

The Hamiltonian  $H_{q-q}$ , Eq. (C.91), enables the implementation of entangling two-qubit gates ( $i$ SWAP,  $\sqrt{i}$ SWAP) and, thus, in combination with single-qubit operations, allows for universal quantum computing [17, 23–26]. For illustration purposes, we discuss below the special case  $\bar{E}_Z^{(1)} = \bar{E}_Z^{(2)} \equiv \bar{E}_Z$  in more detail. In the basis  $\Sigma_{q-q} = \{11, 10, 01, 00\}$  with  $|ab\rangle = |a^{(1)}\rangle \otimes |b^{(2)}\rangle$ , where the qubit states  $|0\rangle$  (ground) and  $|1\rangle$  (excited) are eigenstates of  $\tilde{\sigma}_z$  with eigenvalues  $\mp 1$ , the matrix representation of  $H_{q-q}$  is of the simple form

$$H_{q-q} = \begin{pmatrix} \bar{E}_Z & 0 & 0 & 0 \\ 0 & 0 & J_{xy}/2 & 0 \\ 0 & J_{xy}/2 & 0 & 0 \\ 0 & 0 & 0 & -\bar{E}_Z \end{pmatrix}.\tag{C.93}$$

The eigenstates and eigenenergies are  $|11\rangle$ ,  $(|10\rangle \pm |01\rangle)/\sqrt{2}$ ,  $|00\rangle$ , and  $\bar{E}_Z, \pm J_{xy}/2, -\bar{E}_Z$ , respectively. Provided that  $H_{q-q}$  is constant within the time interval  $0 \leq t' \leq t$ , one finds from the Schrödinger equation that the time evolution  $|\psi(t)\rangle = U_{xy}(t) |\psi(0)\rangle$  for an arbitrary state  $|\psi(0)\rangle$  is described by the operator

$$U_{xy}(t) = \begin{pmatrix} e^{-i\bar{E}_Z t/\hbar} & 0 & 0 & 0 \\ 0 & f_{xy}(t) & g_{xy}(t) & 0 \\ 0 & g_{xy}(t) & f_{xy}(t) & 0 \\ 0 & 0 & 0 & e^{i\bar{E}_Z t/\hbar} \end{pmatrix},\tag{C.94}$$

where

$$f_{xy}(t) = \cos\left(\frac{J_{xy}t}{2\hbar}\right), \quad (\text{C.95})$$

$$g_{xy}(t) = -i \sin\left(\frac{J_{xy}t}{2\hbar}\right). \quad (\text{C.96})$$

We note that the relation  $U_{xy}(t_2)U_{xy}(t_1) = U_{xy}(t_1 + t_2)$  may easily be verified. After the time  $t_{i\text{SWAP}} = \pi\hbar/|J_{xy}|$ , the states  $|10\rangle$  and  $|01\rangle$  have been coherently exchanged, which is commonly referred to as an  $i\text{SWAP}$  operation. For  $J_{xy} > 0$ ,

$$U_{xy}(t_{i\text{SWAP}}) = \begin{pmatrix} e^{-i\pi\bar{E}_Z/J_{xy}} & 0 & 0 & 0 \\ 0 & 0 & -i & 0 \\ 0 & -i & 0 & 0 \\ 0 & 0 & 0 & e^{i\pi\bar{E}_Z/J_{xy}} \end{pmatrix}, \quad (\text{C.97})$$

and, for  $J_{xy} < 0$ ,

$$U_{xy}(t_{i\text{SWAP}}) = \begin{pmatrix} e^{i\pi\bar{E}_Z/J_{xy}} & 0 & 0 & 0 \\ 0 & 0 & i & 0 \\ 0 & i & 0 & 0 \\ 0 & 0 & 0 & e^{-i\pi\bar{E}_Z/J_{xy}} \end{pmatrix}. \quad (\text{C.98})$$

An entangling  $\sqrt{i\text{SWAP}}$  gate is obtained when the system evolves for the time  $t_{i\text{SWAP}}/2$ . We note that also  $i\text{SWAP}$  is entangling, in stark contrast to the SWAP operation that we recall below.

For comparison, we consider the Hamiltonian for an isotropic (Heisenberg-type) spin-spin coupling

$$H_{\text{q-q}}^H = \sum_{i=1}^2 \frac{E_Z}{2} \tilde{\sigma}_z^{(i)} + \frac{J_H}{4} \tilde{\sigma}^{(1)} \cdot \tilde{\sigma}^{(2)} - \frac{J_H}{4}, \quad (\text{C.99})$$

where  $\tilde{\sigma} = (\tilde{\sigma}_x, \tilde{\sigma}_y, \tilde{\sigma}_z)$  is the vector of Pauli matrices and the global energy shift  $-J_H/4$  was added for convenience. In matrix form, with basis  $\Sigma_{\text{q-q}}$  as above,  $H_{\text{q-q}}^H$  reads

$$H_{\text{q-q}}^H = \begin{pmatrix} E_Z & 0 & 0 & 0 \\ 0 & -J_H/2 & J_H/2 & 0 \\ 0 & J_H/2 & -J_H/2 & 0 \\ 0 & 0 & 0 & -E_Z \end{pmatrix}. \quad (\text{C.100})$$

The resulting time evolution  $|\psi(t)\rangle = U_H(t)|\psi(0)\rangle$  for an arbitrary state  $|\psi(0)\rangle$  is given by

$$U_H(t) = \begin{pmatrix} e^{-iE_Z t/\hbar} & 0 & 0 & 0 \\ 0 & f_H(t) & g_H(t) & 0 \\ 0 & g_H(t) & f_H(t) & 0 \\ 0 & 0 & 0 & e^{iE_Z t/\hbar} \end{pmatrix}, \quad (\text{C.101})$$

where

$$f_H(t) = \frac{1}{2} \left(1 + e^{iJ_H t/\hbar}\right), \quad (\text{C.102})$$

$$g_H(t) = \frac{1}{2} \left(1 - e^{iJ_H t/\hbar}\right). \quad (\text{C.103})$$



The operation time for a SWAP gate is  $t_{\text{SWAP}} = \pi\hbar/|J_H|$  (usually  $J_H > 0$ ),

$$U_H(t_{\text{SWAP}}) = \begin{pmatrix} e^{-i\pi E_Z/|J_H|} & 0 & 0 & 0 \\ 0 & 0 & 1 & 0 \\ 0 & 1 & 0 & 0 \\ 0 & 0 & 0 & e^{i\pi E_Z/|J_H|} \end{pmatrix}, \quad (\text{C.104})$$

and the entangling  $\sqrt{\text{SWAP}}$  operation [27] is realized after the time  $t_{\text{SWAP}}/2$ . As for  $U_{xy}$ , we note that verification of  $U_H(t_2)U_H(t_1) = U_H(t_1 + t_2)$  is easily possible for  $U_H$ , which implies  $(\sqrt{\text{SWAP}})^2 = \text{SWAP}$  (analogous for  $i\text{SWAP}$ ).

## C.6 Charge Noise

### C.6.1 Perturbation due to Electric Field Fluctuations

The Hamiltonian  $H_q$ , Eq. (C.13), depends on the applied electric fields, and random fluctuations  $\delta E_y(t)$  and  $\delta E_z(t)$  therefore lead to a noisy perturbation

$$\delta H_q^{\text{el}}(t) = \frac{\delta E_Z(t)}{2} \tilde{\sigma}_z + \delta T_q(t) \tilde{\sigma}_x. \quad (\text{C.105})$$

Linear expansion yields

$$\delta E_Z(t) \simeq (\partial_{E_y} E_Z) \delta E_y(t) + (\partial_{E_z} E_Z) \delta E_z(t), \quad (\text{C.106})$$

$$\delta T_q(t) \simeq (\partial_{E_y} T_q) \delta E_y(t) + (\partial_{E_z} T_q) \delta E_z(t), \quad (\text{C.107})$$

where the partial derivatives are evaluated at the electric fields  $E_y$  and  $E_z$  applied to the QD. This implies  $\delta E_Z(t) \simeq 0$  and  $\delta T_q(t) \simeq 0$  for an idle qubit, because all first derivatives vanish at  $E_y = 0 = E_z$ . That is, the proposed setup is highly insensitive to charge noise when the electric fields are switched off during the waiting time between quantum operations. The system, however, becomes sensitive to electrical noise when  $E_y$  is applied in order to induce the DRSOI. Since, as shown in Chapter 4, single-qubit gates are much faster than two-qubit gates, the system performance is limited by the noisy perturbations during two-qubit operations, and below we study the resulting lifetimes in further detail.

### C.6.2 Relaxation and Dephasing at Maximal Transverse Coupling

The long-distance two-qubit gates are much slower than single-qubit gates. During two-qubit operations,  $E_y$  should therefore be chosen such that the coupling parameter  $\bar{\nu}$  is maximal, which implies  $\partial_{E_y} T_q = 0$ . Furthermore,  $\partial_{E_z} E_Z = 0$ , as illustrated, e.g., in Eq. (C.124). When the electric field fluctuations  $\delta E_\alpha(t)$ ,  $\alpha \in \{y, z\}$ , are related to the voltage fluctuations  $\delta V_\alpha(t)$  in the corresponding electric gates by  $\delta E_\alpha(t) = \kappa_\alpha \delta V_\alpha(t)$ , we find

$$\delta E_Z(t) \simeq \kappa_y (\partial_{E_y} E_Z) \delta V_y(t), \quad (\text{C.108})$$

$$\delta T_q(t) \simeq \kappa_z \bar{\nu} \delta V_z(t), \quad (\text{C.109})$$

where the  $\kappa_\alpha$  are device and geometry dependent constants. We recall that  $T_q = \bar{\nu} E_z$  and, thus,  $\partial_{E_z} T_q = \bar{\nu}$ , which is used in Eq. (C.109).

The relaxation ( $T_1^{\text{el}}$ ) and dephasing ( $T_\varphi^{\text{el}}$ ) times of the qubit in the presence of  $\delta H_q^{\text{el}}(t)$  can be calculated

with the Bloch-Redfield theory [28–30]. With  $\omega_Z \equiv E_Z/\hbar$  and  $\text{Re}[\dots]$  as the real part, the rates read

$$\begin{aligned} \frac{1}{T_1^{\text{el}}} &= \frac{4}{\hbar^2} \int_0^\infty \cos(\omega_Z t) \text{Re}[\langle \delta T_q(0) \delta T_q(t) \rangle] dt \\ &= \frac{2}{\hbar^2} \int_{-\infty}^\infty \cos(\omega_Z t) \langle \delta T_q(0) \delta T_q(t) \rangle dt \end{aligned} \quad (\text{C.110})$$

and

$$\begin{aligned} \frac{1}{T_\varphi^{\text{el}}} &= \frac{1}{\hbar^2} \int_0^\infty \text{Re}[\langle \delta E_Z(0) \delta E_Z(t) \rangle] dt \\ &= \frac{1}{2\hbar^2} \int_{-\infty}^\infty \langle \delta E_Z(0) \delta E_Z(t) \rangle dt. \end{aligned} \quad (\text{C.111})$$

The correlation functions obtained from ensemble averages  $\langle \dots \rangle$  fulfill  $\langle \delta T_q(0) \delta T_q(-t) \rangle = \langle \delta T_q(0) \delta T_q(t) \rangle^*$  and  $\langle \delta E_Z(0) \delta E_Z(-t) \rangle = \langle \delta E_Z(0) \delta E_Z(t) \rangle^*$ , where the asterisk denotes complex conjugation, because the correlation functions are invariant under time translation and  $\delta T_q(t)$  and  $\delta E_Z(t)$  are hermitian. We note that the Bloch-Redfield approach requires  $\langle \delta E_Z(t) \rangle = 0 = \langle \delta T_q(t) \rangle$ , which is fulfilled for  $\langle \delta V_\alpha(t) \rangle = 0$  combined with Eqs. (C.108) and (C.109). When we introduce the spectral functions [31]

$$S_{V_\alpha}(\omega) \equiv \int_{-\infty}^\infty e^{i\omega t} \langle \delta V_\alpha(t) \delta V_\alpha(0) \rangle dt = \int_{-\infty}^\infty e^{-i\omega t} \langle \delta V_\alpha(0) \delta V_\alpha(t) \rangle dt, \quad (\text{C.112})$$

i.e., the Fourier transforms of  $\langle \delta V_\alpha(t) \delta V_\alpha(0) \rangle = \langle \delta V_\alpha(0) \delta V_\alpha(-t) \rangle$ , Eqs. (C.110) and (C.111) take the form

$$\frac{1}{T_1^{\text{el}}} = \frac{\kappa_z^2 \bar{\nu}^2}{\hbar^2} [S_{V_z}(\omega_Z) + S_{V_z}(-\omega_Z)], \quad (\text{C.113})$$

$$\frac{1}{T_\varphi^{\text{el}}} = \frac{\kappa_y^2}{2\hbar^2} (\partial_{E_y} E_Z)^2 S_{V_y}(0). \quad (\text{C.114})$$

$S_{V_z}(\omega_Z)$  describes the process in which the gate for  $E_z$  absorbs the energy  $E_Z$  from the qubit, and vice versa for  $S_{V_z}(-\omega_Z)$  [31]. In contrast to the relaxation, dephasing happens without an energy transfer between the gate and the qubit, and it is correspondingly quantified by  $S_{V_y}(0)$ .

A major source of electrical noise is the Johnson-Nyquist noise [32, 33]. Following Refs. [31, 33], we therefore consider the spectral functions

$$S_{V_\alpha}(\omega) = \frac{2R_\alpha \hbar \omega}{1 - e^{-\beta_\alpha \hbar \omega}}, \quad (\text{C.115})$$

where  $\beta_\alpha \equiv 1/(k_B T_\alpha)$  and  $R_\alpha$  ( $T_\alpha$ ) is the effective resistance (temperature) of the gate that generates  $E_\alpha$ . We note in passing that these spectral functions fulfill  $S_{V_\alpha}(\omega) = e^{\beta_\alpha \hbar \omega} S_{V_\alpha}(-\omega)$ , which corresponds to the detailed balance relation for a noise source in thermal equilibrium. Furthermore, the equality  $\langle \delta V_\alpha(0) \delta V_\alpha(-t) \rangle = \langle \delta V_\alpha(0) \delta V_\alpha(t) \rangle^*$  is ensured because  $S_{V_\alpha}(\omega)$  is real. Finally, substitution into Eqs. (C.113) and (C.114) yields

$$\frac{1}{T_1^{\text{el}}} = \frac{2\kappa_z^2 \bar{\nu}^2 R_z E_Z (e^{\beta_z E_Z} + 1)}{\hbar^2 (e^{\beta_z E_Z} - 1)}, \quad (\text{C.116})$$

$$\frac{1}{T_\varphi^{\text{el}}} = \frac{\kappa_y^2}{\hbar^2} (\partial_{E_y} E_Z)^2 R_y k_B T_y. \quad (\text{C.117})$$

The decoherence time  $T_2^{\text{el}}$  obeys the relation  $1/T_2^{\text{el}} = 1/(2T_1^{\text{el}}) + 1/T_\varphi^{\text{el}}$  [29, 30].

### C.6.3 Numerical Estimates

For numerical estimates of the lifetimes discussed above, we set  $T_y = T_z \sim 10$  mK on the order of typical sample temperatures [18, 20]. When  $k_B T_z \ll E_Z$ , which is very well fulfilled for  $E_Z > 3 \mu\text{eV}$  here, the gates can only absorb energy and the relaxation rate becomes independent of the temperature,

$$\frac{1}{T_1^{\text{el}}} = \frac{2\kappa_z^2 \bar{\nu}^2 R_z E_Z}{\hbar^2}. \quad (\text{C.118})$$

From an estimate based on typical gate dimensions (length  $\sim 1$  cm; cross section  $\sim 10^3$  nm<sup>2</sup>) and the residual resistivities of copper and gold ( $\sim 10^{-11}$   $\Omega\text{m}$ ), we choose  $R_y = R_z \sim 10^2$   $\Omega$ . Assuming that the material between the gates and the NW has a permittivity similar to that of Ge,  $\kappa_y$  can be approximated by  $\kappa_y \approx 1/d_y$ , where  $d_y \sim 0.1$   $\mu\text{m}$  is the distance between the electric gates for  $E_y$ . Because the NW QD is usually located above the gates that generate the confinement along the NW axis [20, 34–36], it is likely that the conversion factor for  $\delta E_z(t)$  is smaller than that for  $\delta E_y(t)$ , and we set here  $\kappa_z = 1/\mu\text{m} = \kappa_y/10$ . We emphasize, however, that both  $\kappa_y$  and  $\kappa_z$  depend strongly on the details of the setup.

The derivatives  $\partial_{E_y} E_Z$  and  $\partial_{E_z} T_q = \bar{\nu}$  are extracted from the numerical results summarized in Fig. 4.4 of Chapter 4. At magnetic fields  $|B_y| \lesssim 0.5$  T,  $\bar{\nu}$  is maximal for  $E_y \simeq 1.8$  V/ $\mu\text{m}$ . At this electric field, we calculate  $\bar{\nu} \simeq 10|B_y|$  nm e/T, and find  $g \simeq 3.4$  and  $\partial_{E_y} g \simeq -1.6$   $\mu\text{m}/\text{V}$  for the  $g$  factor. With  $E_Z = |g\mu_B B_y|$ , substitution of all numbers into Eqs. (C.117) and (C.118) yields

$$T_\varphi^{\text{el}} \sim \frac{3.7 \times 10^{-2} \text{ s T}^2}{B_y^2}, \quad (\text{C.119})$$

$$T_1^{\text{el}} \sim \frac{6.3 \times 10^{-7} \text{ s T}^3}{|B_y|^3}, \quad (\text{C.120})$$

which, in terms of the Zeeman energy, is equivalent to

$$T_\varphi^{\text{el}} \sim \frac{1.4 \times 10^3 \text{ s } \mu\text{eV}^2}{E_Z^2}, \quad (\text{C.121})$$

$$T_1^{\text{el}} \sim \frac{4.8 \text{ s } \mu\text{eV}^3}{E_Z^3}. \quad (\text{C.122})$$

We note that  $T_\varphi^{\text{el}} \propto 1/E_Z^2$ , whereas  $T_1^{\text{el}} \propto 1/E_Z^3$ . Because the dephasing due to Johnson-Nyquist noise is strongly suppressed at low temperatures, we find here that  $T_1^{\text{el}} \ll T_\varphi^{\text{el}}$  for all reasonable  $B_y$ , leading to  $T_2^{\text{el}} = 2T_1^{\text{el}}$ .

In the example of a rather strong magnetic field  $B_y = 1.5$  T,  $\bar{\nu}$  peaks at  $E_y \simeq 1.1$  V/ $\mu\text{m}$ . At these fields, we obtain  $\bar{\nu} \simeq 16$  nm e,  $E_Z \simeq 0.35$  meV, and  $\partial_{E_y} E_Z \simeq -0.13$  nm e. The resulting lifetimes are  $T_\varphi^{\text{el}} \sim 19$  ms and  $T_1^{\text{el}} \sim 0.15$   $\mu\text{s}$ , and we mention in passing that these are very similar to the lifetimes extrapolated from Eqs. (C.119) to (C.122) derived for the case of relatively weak  $B_y$ . Again,  $T_2^{\text{el}} = 2T_1^{\text{el}}$ , i.e., the dephasing is negligible compared to the relaxation.

### C.6.4 Remarks

For both strong and weak magnetic fields, we find that the above calculated relaxation times are relatively close to the operation times of cavity-based two-qubit gates. In order to enhance the gate fidelities, relaxation due to Johnson-Nyquist noise should be suppressed by choosing a setup with small  $\kappa_z$ . For instance, when the details of the setup are designed such that  $\kappa_z = 0.1/\mu\text{m}$  instead of  $\kappa_z = 1/\mu\text{m}$  assumed above, the lifetimes  $T_1^{\text{el}}$  and  $T_2^{\text{el}}$  are prolonged by two orders of magnitude because of  $T_1^{\text{el}} \propto 1/\kappa_z^2$ . Further possibilities for increasing noise-limited gate fidelities are discussed in Chapter 4.

We also note that high-frequency cut-offs were not considered in the analysis of the electrical noise.

Consequently, the correlation functions  $\langle \delta T_q(0) \delta T_q(t) \rangle$  and  $\langle \delta E_Z(0) \delta E_Z(t) \rangle$  cannot be calculated explicitly as the spectral functions do not converge at infinite  $\omega$ , and, moreover, one finds  $T_1^{\text{el}} \rightarrow 0$  in the limit  $E_Z \rightarrow \infty$ . Cut-offs in the spectral functions of noisy perturbations can have various origins. When spin qubits relax via the phonon bath, for instance, the lifetimes turn out to be minimal when the corresponding phonon wavelength matches the dot size [23, 29, 37, 38]. This is because the relevant matrix elements vanish after integration over the wave functions when the phonon wavelength is much smaller than the QD. Analogously, one may argue that  $T_1^{\text{el}}$  increases when  $E_Z \gtrsim \hbar\pi c_0 / (2l_g \sqrt{\epsilon_r}) \sim 1$  eV. Since the speed of light is by orders of magnitude greater than the speed of sound in Ge, this wavelength-based cut-off for charge noise occurs at much higher energies than that for phonons [38]. It is likely that other mechanisms in the metal itself lead to an increase of  $T_1^{\text{el}}$  and  $T_2^{\text{el}}$  at  $E_Z < 1$  eV already. However, we assume that high-frequency cut-offs in the spectral functions of the Johnson-Nyquist noise do not set in within the range of Zeeman energies discussed here. If they do occur, the resulting lifetimes will be increased significantly.

Finally, three more features of the proposed setup are worth mentioning in the context of charge noise. First, we note that the confinement length  $l_g$  presents an additional control parameter for the  $g$  factor [see, e.g., Eqs. (C.124) and (C.128)]. Hence, if required, fine tuning of  $l_g^{(i)}$  should allow realizing both  $\partial_{E_y^{(i)}} T_q^{(i)} = 0$  (maximal  $\bar{\nu}^{(i)}$ ) and the desired  $\Delta_q^{(i)}$  for any qubit  $i$  in the cavity. Second, static electric fields from the substrate, if present, will most likely be oriented along the  $y$  axis. Therefore, in order to achieve the desired  $E_y$  (particularly  $E_y = 0$ ), they may easily be compensated with the electric gates. Third, radial fields from the Ge/Si interface, if present, do not break the symmetry of the wire and may result in small corrections to  $\Delta$ ,  $C$ , and  $K$  only. All these properties are useful in an experimental realization.

## C.7 Results from Effective Model

Below, we summarize the coefficients  $c_y$  and  $c_z$  of  $H'_q$ , Eq. (C.51), that result from the perturbative analysis described in Appendix C.2. Although the full results are lengthy and cannot be written out explicitly here, a Taylor expansion in the magnetic field  $B_y$  for  $N \rightarrow \infty$  yields

$$c_y = \mu_B B_y E_z \frac{2eC'}{(\hbar\omega'_g)^2} e^{-\left(\frac{C'}{l'_g \hbar\omega'_g}\right)^2} \left[ (K - (K + M) \sin^2 \theta) - \frac{L\tilde{C}}{l'^2_g \Delta'} \right] + \mathcal{O}(B_y^3) \quad (\text{C.123})$$

and

$$c_z = \mu_B B_y e^{-\left(\frac{C'}{l'_g \hbar\omega'_g}\right)^2} \left[ (K - (K + M) \sin^2 \theta) \left( 1 - \frac{C'^2 e^2 E_z^2}{(\hbar\omega'_g)^4} \right) - \frac{L\tilde{C}}{l'^2_g \Delta'} \right] + \mathcal{O}(B_y^3). \quad (\text{C.124})$$

The correction  $\propto E_z^2$  in  $c_z$  is negligible for the small electric fields  $E_z$  in our setup. In the regime of relatively weak  $B_y$ , where the linear expansion in  $B_y$  applies, the coefficients can therefore be summarized as follows,

$$c_y \simeq E_z \frac{2eC'}{(\hbar\omega'_g)^2} c_z, \quad (\text{C.125})$$

$$c_z \simeq \mu_B B_y e^{-\left(\frac{C'}{l'_g \hbar\omega'_g}\right)^2} \left[ (K - (K + M) \sin^2 \theta) - \frac{L\tilde{C}}{l'^2_g \Delta'} \right]. \quad (\text{C.126})$$

Finally, because the DRSOI is much stronger than the conventional RSOI [1], it turns out that the latter results in small quantitative corrections only and may be omitted. For  $\alpha \rightarrow 0$ , one finds  $\Delta' \rightarrow \tilde{\Delta}$ ,

$C' \rightarrow 2CeE_yU/\tilde{\Delta}$ ,  $\tilde{C} \rightarrow C\Delta/\tilde{\Delta}$ ,  $\omega'_g \rightarrow \tilde{\omega}_g$ ,  $l'_g \rightarrow \tilde{l}_g$ , and the coefficients read

$$c_y \simeq E_z \frac{4e^2UC E_y}{(\hbar\tilde{\omega}_g)^2\tilde{\Delta}} c_z, \quad (\text{C.127})$$

$$c_z \simeq \mu_B B_y e^{-\left(\frac{2eUC E_y}{\tilde{l}_g \hbar \tilde{\omega}_g \tilde{\Delta}}\right)^2} \left( \tilde{K} - \frac{LC\Delta}{\tilde{l}_g^2 \tilde{\Delta}^2} \right), \quad (\text{C.128})$$

where  $\tilde{l}_g = l_g \sqrt{\tilde{\omega}_g/\omega_g}$  and

$$\tilde{K} = K - \frac{(K+M)E_y^2}{\left(\frac{\tilde{\Delta}+\Delta}{2eU}\right)^2 + E_y^2}, \quad (\text{C.129})$$

$$\tilde{\Delta} = \sqrt{\Delta^2 + (2eE_yU)^2}, \quad (\text{C.130})$$

$$\tilde{\omega}_g = \omega_g \sqrt{1 - \frac{2m_g C^2 \Delta^2}{\hbar^2 \tilde{\Delta}^3}}. \quad (\text{C.131})$$



# References

- [1] C. Kloeffel, M. Trif, and D. Loss, Phys. Rev. B **84**, 195314 (2011).  
See Chapter 2
- [2] R. Winkler, *Spin-Orbit Coupling Effects in Two-Dimensional Electron and Hole Systems* (Springer, Berlin, 2003).
- [3] P. Lawaetz, Phys. Rev. B **4**, 3460 (1971).
- [4] W. Lu, J. Xiang, B. P. Timko, Y. Wu, and C. M. Lieber, Proc. Natl. Acad. Sci. USA **102**, 10046 (2005).
- [5] J. M. Luttinger and W. Kohn, Phys. Rev. **97**, 869 (1955).
- [6] J. M. Luttinger, Phys. Rev. **102**, 1030 (1956).
- [7] L. J. Lauhon, M. S. Gudixsen, D. Wang, and C. M. Lieber, Nature (London) **420**, 57 (2002).
- [8] J. Xiang, W. Lu, Y. Hu, Y. Wu, H. Yan, and C. M. Lieber, Nature (London) **441**, 489 (2006).
- [9] J. Xiang, A. Vidan, M. Tinkham, R. M. Westervelt, and C. M. Lieber, Nat. Nanotechnol. **1**, 208 (2006).
- [10] Y. Hu, H. O. H. Churchill, D. J. Reilly, J. Xiang, C. M. Lieber, and C. M. Marcus, Nat. Nanotechnol. **2**, 622 (2007).
- [11] S. Roddaro, A. Fuhrer, P. Brusheim, C. Fasth, H. Q. Xu, L. Samuelson, J. Xiang, and C. M. Lieber, Phys. Rev. Lett. **101**, 186802 (2008).
- [12] K. M. Varahramyan, D. Ferrer, E. Tutuc, and S. K. Banerjee, Appl. Phys. Lett. **95**, 033101 (2009).
- [13] X.-J. Hao, T. Tu, G. Cao, C. Zhou, H.-O. Li, G.-C. Guo, W. Y. Fung, Z. Ji, G.-P. Guo, and W. Lu, Nano Lett. **10**, 2956 (2010).
- [14] H. Yan, H. S. Choe, S. Nam, Y. Hu, S. Das, J. F. Klemic, J. C. Ellenbogen, and C. M. Lieber, Nature (London) **470**, 240 (2011).
- [15] J. Nah, D. C. Dillen, K. M. Varahramyan, S. K. Banerjee, and E. Tutuc, Nano Lett. **12**, 108 (2012).
- [16] Y. Hu, F. Kuemmeth, C. M. Lieber, and C. M. Marcus, Nat. Nanotechnol. **7**, 47 (2012).
- [17] A. Blais, R.-S. Huang, A. Wallraff, S. M. Girvin, and R. J. Schoelkopf, Phys. Rev. A **69**, 062320 (2004).
- [18] A. Wallraff, D. I. Schuster, A. Blais, L. Frunzio, R.-S. Huang, J. Majer, S. Kumar, S. M. Girvin, and R. J. Schoelkopf, Nature (London) **431**, 162 (2004).
- [19] L. Frunzio, A. Wallraff, D. I. Schuster, J. Majer, and R. J. Schoelkopf, IEEE Trans. Appl. Supercond. **15**, 860 (2005).

- [20] K. D. Petersson, L. W. McFaul, M. D. Schroer, M. Jung, J. M. Taylor, A. A. Houck, and J. R. Petta, *Nature (London)* **490**, 380 (2012).
- [21] V. Mourik, K. Zuo, S. M. Frolov, S. R. Plissard, E. P. A. M. Bakkers, and L. P. Kouwenhoven, *Science* **336**, 1003 (2012).
- [22] H. O. H. Churchill, V. Fatemi, K. Grove-Rasmussen, M. T. Deng, P. Caroff, H. Q. Xu, and C. M. Marcus, *Phys. Rev. B* **87**, 241401(R) (2013).
- [23] M. Trif, V. N. Golovach, and D. Loss, *Phys. Rev. B* **77**, 045434 (2008).
- [24] A. Imamoglu, D. D. Awschalom, G. Burkard, D. P. DiVincenzo, D. Loss, M. Sherwin, and A. Small, *Phys. Rev. Lett.* **83**, 4204 (1999).
- [25] A. Blais, J. Gambetta, A. Wallraff, D. I. Schuster, S. M. Girvin, M. H. Devoret, and R. J. Schoelkopf, *Phys. Rev. A* **75**, 032329 (2007).
- [26] A. Barenco, C. H. Bennett, R. Cleve, D. P. DiVincenzo, N. Margolus, P. Shor, T. Sleator, J. A. Smolin, and H. Weinfurter, *Phys. Rev. A* **52**, 3457 (1995).
- [27] D. Loss and D. P. DiVincenzo, *Phys. Rev. A* **57**, 120 (1998).
- [28] C. P. Slichter, *Principles of Magnetic Resonance* (Springer, Berlin, 1980).
- [29] V. N. Golovach, A. V. Khaetskii, and D. Loss, *Phys. Rev. Lett.* **93**, 016601 (2004).
- [30] M. Borhani, V. N. Golovach, and D. Loss, *Phys. Rev. B* **73**, 155311 (2006).
- [31] A. A. Clerk, M. H. Devoret, S. M. Girvin, F. Marquardt, and R. J. Schoelkopf, *Rev. Mod. Phys.* **82**, 1155 (2010).
- [32] J. B. Johnson, *Phys. Rev.* **32**, 97 (1928).
- [33] H. Nyquist, *Phys. Rev.* **32**, 110 (1928).
- [34] C. Fasth, A. Fuhrer, L. Samuelson, V. N. Golovach, and D. Loss, *Phys. Rev. Lett.* **98**, 266801 (2007).
- [35] S. Nadj-Perge, S. M. Frolov, E. P. A. M. Bakkers, and L. P. Kouwenhoven, *Nature (London)* **468**, 1084 (2010).
- [36] M. D. Schroer, K. D. Petersson, M. Jung, and J. R. Petta, *Phys. Rev. Lett.* **107**, 176811 (2011).
- [37] T. Meunier, I. T. Vink, L. H. Willems van Beveren, K-J. Tielrooij, R. Hanson, F. H. L. Koppens, H. P. Tranitz, W. Wegscheider, L. P. Kouwenhoven, and L. M. K. Vandersypen, *Phys. Rev. Lett.* **98**, 126601 (2007).
- [38] F. Maier, C. Kloeffel, and D. Loss, *Phys. Rev. B* **87**, 161305(R) (2013).  
See Chapter 3



## **Appendix D**

# **Supplementary Information to Chapter 5 “Acoustic Phonons and Strain in Core/Shell Nanowires”**

**Adapted from:**

Christoph Kloeffel, Mircea Trif, and Daniel Loss,  
Phys. Rev. B **90**, 115419 (2014).

## D.1 Parameters for Ge/Si Core/Shell Nanowires

In this appendix, we summarize the most important parameters used in the calculations for Ge/Si core/shell nanowires (NWs) in Chapter 5. The lattice constants of the core ( $c$ , Ge) and shell ( $s$ , Si) material are  $a_c = 5.66 \text{ \AA}$  and  $a_s = 5.43 \text{ \AA}$  [1, 2]. The densities are  $\rho_c = 5.32 \text{ g/cm}^3$  and  $\rho_s = 2.33 \text{ g/cm}^3$  [2, 3]. As explained below, the Lamé parameters are approximately  $\lambda_c = 39.8 \times 10^9 \text{ N/m}^2$ ,  $\mu_c = 55.6 \times 10^9 \text{ N/m}^2$ ,  $\lambda_s = 54.5 \times 10^9 \text{ N/m}^2$ , and  $\mu_s = 67.5 \times 10^9 \text{ N/m}^2$ .

The elastic stiffness coefficients, taken from Ref. [3] and listed here in units of  $10^9 \text{ N/m}^2$ , are  $c_{11}^c = 129$ ,  $c_{12}^c = 48$ ,  $c_{44}^c = 67.1$ ,  $c_{11}^s = 165$ ,  $c_{12}^s = 64$ , and  $c_{44}^s = 79.2$ . We note that the numbers agree very well with those provided, e.g., in Ref. [2]. Introducing  $p \in \{c, s\}$  for convenience and following Ref. [4] (Appendix E.2.6.1), we approximate these stiffness coefficients by  $\tilde{c}_{11}^p$ ,  $\tilde{c}_{12}^p$ , and  $\tilde{c}_{44}^p$ , respectively, such that the conditions  $\tilde{c}_{11}^p = \tilde{c}_{12}^p + 2\tilde{c}_{44}^p$  for isotropic media are fulfilled. When the relative deviations of the three coefficients for a material are chosen to be the same, this approximation yields a relative deviation from the original values of 17.1% in Ge and 14.8% in Si. The results are  $\tilde{c}_{12}^c = 39.8$ ,  $\tilde{c}_{44}^c = 55.6$ ,  $\tilde{c}_{12}^s = 54.5$ , and  $\tilde{c}_{44}^s = 67.5$ , leading to the above-mentioned Lamé parameters due to  $\tilde{c}_{12}^p = \lambda_p$  and  $\tilde{c}_{44}^p = \mu_p$ .

## D.2 Coordinate Systems for Stress and Strain

### D.2.1 Cartesian and Cylindrical Coordinates

We mainly consider two different coordinate systems in this work. In the case of Cartesian coordinates  $(x, y, z)$ , a position  $\mathbf{r}$  is described by

$$\mathbf{r} = x\mathbf{e}_x + y\mathbf{e}_y + z\mathbf{e}_z. \quad (\text{D.1})$$

The  $z$  axis coincides with the symmetry axis of the NW, and  $\mathbf{e}_x$ ,  $\mathbf{e}_y$ , and  $\mathbf{e}_z = \mathbf{e}_x \times \mathbf{e}_y$  are the orthonormal basis vectors pointing along the axes indicated by subscripts. In cylindrical coordinates  $(r, \phi, z)$ , we write

$$\mathbf{r} = r\mathbf{e}_r + z\mathbf{e}_z, \quad (\text{D.2})$$

with

$$x = r \cos \phi, \quad (\text{D.3})$$

$$y = r \sin \phi, \quad (\text{D.4})$$

and so the  $z$  axis is the same for both coordinate systems. We use

$$r = \sqrt{x^2 + y^2} \quad (\text{D.5})$$

in this work in order to avoid confusion with the density  $\rho$ . Therefore  $r \neq |\mathbf{r}|$ . The unit vectors

$$\mathbf{e}_r = \mathbf{e}_x \cos \phi + \mathbf{e}_y \sin \phi, \quad (\text{D.6})$$

$$\mathbf{e}_\phi = -\mathbf{e}_x \sin \phi + \mathbf{e}_y \cos \phi \quad (\text{D.7})$$

point in the radial and azimuthal direction, respectively, and we note that  $\{\mathbf{e}_r, \mathbf{e}_\phi, \mathbf{e}_z\}$  forms again a right-handed, orthonormal basis.

## D.2.2 Transformation of Second Rank Tensors

In the following, we recall how the strain and stress tensors transform under a change of basis and summarize the relations between the tensor elements in Cartesian and cylindrical coordinates. The chosen notation is similar to the one in Ref. [3].

We consider two coordinate systems  $\Sigma$  and  $\Sigma'$  with basis vectors  $\mathbf{e}_i$  and  $\mathbf{e}'_i$ , respectively, which are related via

$$\mathbf{e}'_j = \sum_i R_{ij} \mathbf{e}_i. \quad (\text{D.8})$$

Given the two sets of basis vectors, an arbitrary vector  $\mathbf{a}$  can be written as

$$\mathbf{a} = \sum_i a_i \mathbf{e}_i = \sum_i a'_i \mathbf{e}'_i, \quad (\text{D.9})$$

where  $a_i$  ( $a'_i$ ) are the coefficients in  $\Sigma$  ( $\Sigma'$ ). Inserting Eq. (D.8) into Eq. (D.9) yields

$$a_j = \sum_i R_{ji} a'_i. \quad (\text{D.10})$$

These linear relations between the coefficients of  $\mathbf{a}$  can conveniently be written as (considering three dimensions)

$$\begin{pmatrix} a_1 \\ a_2 \\ a_3 \end{pmatrix} = R \begin{pmatrix} a'_1 \\ a'_2 \\ a'_3 \end{pmatrix}, \quad (\text{D.11})$$

where the matrix

$$R = \begin{pmatrix} R_{11} & R_{12} & R_{13} \\ R_{21} & R_{22} & R_{23} \\ R_{31} & R_{32} & R_{33} \end{pmatrix} \quad (\text{D.12})$$

comprises the elements  $R_{ij}$  introduced in Eq. (D.8). Since the basis vectors of  $\Sigma$  and  $\Sigma'$ , respectively, are orthonormal, one finds  $R^T R = \mathbf{1} = R R^T$ , and so the transposed matrix  $R^T$  corresponds to the inverse operation, i.e.,  $R^T = R^{-1}$ . Consequently, the inverse relations between the coefficients  $a_i$  and  $a'_i$  read

$$\begin{pmatrix} a'_1 \\ a'_2 \\ a'_3 \end{pmatrix} = R^T \begin{pmatrix} a_1 \\ a_2 \\ a_3 \end{pmatrix}, \quad (\text{D.13})$$

which is equivalent to

$$a'_j = \sum_i R_{ij} a_i. \quad (\text{D.14})$$

The transformation rules for second rank tensors, such as stress and strain, can easily be found with the above-mentioned equations, keeping in mind that the result of a tensor acting on some vector  $\mathbf{a}$  must be independent of the coordinate system. When the matrices  $T'$  and  $T$ , respectively, contain the tensor elements  $T'_{ij}$  and  $T_{ij}$  for the primed and unprimed basis, the relations between these tensor elements are given in matrix form by

$$T' = R^T T R, \quad (\text{D.15})$$

with  $R$  as shown in Eq. (D.12). An intuitive proof for this result is obtained by applying the left- and right-hand side to a column vector with coefficients  $a'_i$ . As this column vector corresponds exactly to the representation of  $\mathbf{a}$  in  $\Sigma'$ , and analogously for the matrix  $T'$  representing the tensor, the left-hand side yields a column vector whose coefficients  $b'_i$  describe the result of the operation “tensor on  $\mathbf{a}$ ” in the primed basis. On the right-hand side, the matrix  $R$  transfers the coefficients  $a'_i$  of the column vector

into  $a_i$ . Next, applying  $T$  yields the resulting coefficients of “tensor on  $\mathbf{a}$ ” in the unprimed basis. Finally,  $R^T$  replaces these coefficients  $b_i$  by those in  $\Sigma'$ , i.e., by  $b'_i$ . The equality of left- and right-hand side holds for arbitrary  $a'_i$ , and so Eq. (D.15) applies. Analogously,

$$T = RT'R^T. \quad (\text{D.16})$$

We note that the results are equivalent to

$$T'_{mn} = \sum_{ij} R_{im}R_{jn}T_{ij}, \quad (\text{D.17})$$

$$T_{mn} = \sum_{ij} R_{mi}R_{nj}T'_{ij}. \quad (\text{D.18})$$

Considering the Cartesian and cylindrical coordinate systems introduced in Appendix D.2.1 as  $\Sigma$  and  $\Sigma'$ , respectively, the matrix  $R$  is

$$R = \begin{pmatrix} \cos \phi & -\sin \phi & 0 \\ \sin \phi & \cos \phi & 0 \\ 0 & 0 & 1 \end{pmatrix}. \quad (\text{D.19})$$

Thus, exploiting Eq. (D.15), the relations between the strain tensor elements in the two coordinate systems are

$$\epsilon_{rr} = \epsilon_{xx} \cos^2 \phi + \epsilon_{yy} \sin^2 \phi + \epsilon_{xy} \sin(2\phi), \quad (\text{D.20})$$

$$\epsilon_{\phi\phi} = \epsilon_{xx} \sin^2 \phi + \epsilon_{yy} \cos^2 \phi - \epsilon_{xy} \sin(2\phi), \quad (\text{D.21})$$

$$\epsilon_{r\phi} = \epsilon_{xy} \cos(2\phi) + (\epsilon_{yy} - \epsilon_{xx}) \sin \phi \cos \phi, \quad (\text{D.22})$$

$$\epsilon_{rz} = \epsilon_{xz} \cos \phi + \epsilon_{yz} \sin \phi, \quad (\text{D.23})$$

$$\epsilon_{\phi z} = \epsilon_{yz} \cos \phi - \epsilon_{xz} \sin \phi, \quad (\text{D.24})$$

where we made use of  $\epsilon_{ij} = \epsilon_{ji}$  and the trigonometric identities  $\cos(2\phi) = \cos^2 \phi - \sin^2 \phi$  and  $\sin(2\phi) = 2 \sin \phi \cos \phi$ . The element  $\epsilon_{zz}$  is the same in both coordinate systems, and the inverse relations

$$\epsilon_{xx} = \epsilon_{rr} \cos^2 \phi + \epsilon_{\phi\phi} \sin^2 \phi - \epsilon_{r\phi} \sin(2\phi), \quad (\text{D.25})$$

$$\epsilon_{yy} = \epsilon_{rr} \sin^2 \phi + \epsilon_{\phi\phi} \cos^2 \phi + \epsilon_{r\phi} \sin(2\phi), \quad (\text{D.26})$$

$$\epsilon_{xy} = \epsilon_{r\phi} \cos(2\phi) + (\epsilon_{rr} - \epsilon_{\phi\phi}) \sin \phi \cos \phi, \quad (\text{D.27})$$

$$\epsilon_{xz} = \epsilon_{rz} \cos \phi - \epsilon_{\phi z} \sin \phi, \quad (\text{D.28})$$

$$\epsilon_{yz} = \epsilon_{\phi z} \cos \phi + \epsilon_{rz} \sin \phi \quad (\text{D.29})$$

can be derived from Eq. (D.16). The above-listed equations apply analogously to the stress tensor elements  $\sigma_{ij}$ , of course.

### D.2.3 Strain in Cylindrical Coordinates

In cylindrical coordinates, the relations between the displacement field

$$\mathbf{u} = u_r \mathbf{e}_r + u_\phi \mathbf{e}_\phi + u_z \mathbf{e}_z \quad (\text{D.30})$$

and the strain tensor elements  $\epsilon_{ij}$  are nontrivial, since the basis vectors  $\mathbf{e}_r$  and  $\mathbf{e}_\phi$  depend on the angle  $\phi$ . Based on Eqs. (D.6) and (D.7), one finds

$$\partial_\phi \mathbf{e}_r = \mathbf{e}_\phi, \quad (\text{D.31})$$

$$\partial_\phi \mathbf{e}_\phi = -\mathbf{e}_r. \quad (\text{D.32})$$

Consequently,

$$\partial_r \mathbf{u} = \mathbf{e}_r \partial_r u_r + \mathbf{e}_\phi \partial_r u_\phi + \mathbf{e}_z \partial_r u_z, \quad (\text{D.33})$$

$$\frac{1}{r} \partial_\phi \mathbf{u} = \mathbf{e}_r \frac{\partial_\phi u_r - u_\phi}{r} + \mathbf{e}_\phi \frac{\partial_\phi u_\phi + u_r}{r} + \mathbf{e}_z \frac{\partial_\phi u_z}{r}, \quad (\text{D.34})$$

$$\partial_z \mathbf{u} = \mathbf{e}_r \partial_z u_r + \mathbf{e}_\phi \partial_z u_\phi + \mathbf{e}_z \partial_z u_z. \quad (\text{D.35})$$

With

$$\epsilon_{ij} = \frac{1}{2} \left( \frac{\partial u_i}{\partial x_j} + \frac{\partial u_j}{\partial x_i} \right) \quad (\text{D.36})$$

as introduced in Sec. 5.2 of Chapter 5, this yields [5]

$$\epsilon_{rr} = \partial_r u_r, \quad (\text{D.37})$$

$$\epsilon_{\phi\phi} = \frac{\partial_\phi u_\phi + u_r}{r}, \quad (\text{D.38})$$

$$\epsilon_{zz} = \partial_z u_z \quad (\text{D.39})$$

for the diagonal elements, and

$$\epsilon_{r\phi} = \frac{1}{2} \left( \frac{\partial_\phi u_r - u_\phi}{r} + \partial_r u_\phi \right), \quad (\text{D.40})$$

$$\epsilon_{rz} = \frac{1}{2} (\partial_z u_r + \partial_r u_z), \quad (\text{D.41})$$

$$\epsilon_{\phi z} = \frac{1}{2} \left( \partial_z u_\phi + \frac{\partial_\phi u_z}{r} \right) \quad (\text{D.42})$$

for the off-diagonal elements.

## D.3 Phonons in Bulk

In this appendix, we recall the theoretical description of acoustic phonons in bulk material. The formulas and results form the basis for Appendix D.4, where we derive the normalization condition for phonons in core/shell and core/multishell NWs.

### D.3.1 Plane Waves and Classical Lattice Vibrations

We start from the dynamical equation of motion in an isotropic material [3, 5, 6],

$$\rho \ddot{\mathbf{u}} = (\lambda + \mu) \nabla (\nabla \cdot \mathbf{u}) + \mu \nabla^2 \mathbf{u}, \quad (\text{D.43})$$

which is equivalent to

$$\rho \ddot{u}_i = \sum_j \frac{\partial \sigma_{ij}}{\partial x_j}. \quad (\text{D.44})$$

The introduced  $\nabla$  is the Nabla operator, and  $\nabla^2$  is the Laplacian. In bulk, where  $\rho$ ,  $\lambda$ , and  $\mu$  are constants, the elementary solutions of Eq. (D.43) are longitudinal ( $l$ ) and transverse ( $t_1, t_2$ ) plane waves

with wave vectors  $\mathbf{q}$ ,

$$\mathbf{u}_{\mathbf{q}l}^{\pm} \propto \mathbf{e}_{\mathbf{q}l} e^{i(\mathbf{q}\cdot\mathbf{r} \pm \omega_{\mathbf{q}l}\tau)}, \quad (\text{D.45})$$

$$\mathbf{u}_{\mathbf{q}t_1}^{\pm} \propto \mathbf{e}_{\mathbf{q}t_1} e^{i(\mathbf{q}\cdot\mathbf{r} \pm \omega_{\mathbf{q}t_1}\tau)}, \quad (\text{D.46})$$

$$\mathbf{u}_{\mathbf{q}t_2}^{\pm} \propto \mathbf{e}_{\mathbf{q}t_2} e^{i(\mathbf{q}\cdot\mathbf{r} \pm \omega_{\mathbf{q}t_2}\tau)}, \quad (\text{D.47})$$

where the unit vectors  $\mathbf{e}_{\mathbf{q}l} = \mathbf{q}/q$ ,  $\mathbf{e}_{\mathbf{q}t_1} \perp \mathbf{e}_{\mathbf{q}l}$ , and  $\mathbf{e}_{\mathbf{q}t_2} = \mathbf{e}_{\mathbf{q}l} \times \mathbf{e}_{\mathbf{q}t_1}$  provide the polarizations and  $\tau$  is the time. The dispersion relations between  $q = |\mathbf{q}|$  and the angular frequencies  $\omega_{\mathbf{q}l}$  and  $\omega_{\mathbf{q}t} = \omega_{\mathbf{q}t_1} = \omega_{\mathbf{q}t_2}$  are

$$\omega_{\mathbf{q}l} = \sqrt{\frac{\lambda + 2\mu}{\rho}} q = v_l q, \quad (\text{D.48})$$

$$\omega_{\mathbf{q}t} = \sqrt{\frac{\mu}{\rho}} q = v_t q, \quad (\text{D.49})$$

respectively, where  $v_l$  ( $v_t$ ) is the speed of sound for longitudinal (transverse) polarization. Assuming periodic boundary conditions and a rectangular sample of length  $L_x$ , width  $L_y$ , and height  $L_z$ , the  $N = V/a^3$  allowed values of  $\mathbf{q} = q_x \mathbf{e}_x + q_y \mathbf{e}_y + q_z \mathbf{e}_z$  within the first Brillouin zone are given by

$$q_{\kappa} \in \left\{ -\frac{\pi}{a}, -\frac{\pi}{a} + \frac{2\pi}{L_{\kappa}}, \dots, \frac{\pi}{a} - \frac{2\pi}{L_{\kappa}} \right\}, \quad (\text{D.50})$$

$$q_{\kappa} \in \left\{ -\frac{\pi}{a} + \frac{\pi}{L_{\kappa}}, -\frac{\pi}{a} + \frac{3\pi}{L_{\kappa}}, \dots, \frac{\pi}{a} - \frac{\pi}{L_{\kappa}} \right\} \quad (\text{D.51})$$

for even or odd  $L_{\kappa}/a$ , respectively, where  $\kappa \in \{x, y, z\}$ ,  $V = L_x L_y L_z$  is the sample volume, and  $a$  is the lattice constant of the material.

Classically, an arbitrary acoustic lattice vibration in bulk is described by the displacement function

$$\mathbf{u}(\mathbf{r}, \tau) = \sum_{\mathbf{q}, s} \mathbf{e}_{\mathbf{q}s} \left( c_{\mathbf{q}s} e^{i(\mathbf{q}\cdot\mathbf{r} - \omega_{\mathbf{q}s}\tau)} + \text{c.c.} \right), \quad (\text{D.52})$$

which corresponds to the most general, real-valued solution to Eq. (D.43) that fulfills the boundary conditions. The abbreviation ‘‘c.c.’’ stands for the complex conjugate, and the summation runs over all wave vectors  $\mathbf{q}$  within the first Brillouin zone and the three mode types  $s \in \{l, t_1, t_2\}$ . The real and imaginary parts of the complex coefficients  $c_{\mathbf{q}s}$  (units: length) can be chosen according to the initial conditions, and we note that the  $6V/a^3$  free parameters in Eq. (D.52) are sufficient to set the initial positions and velocities of all  $N = V/a^3$  lattice sites in the sample. Equation (D.52) yields the time derivatives

$$\dot{\mathbf{u}}(\mathbf{r}, \tau) = -i \sum_{\mathbf{q}, s} \omega_{\mathbf{q}s} \mathbf{e}_{\mathbf{q}s} \left( c_{\mathbf{q}s} e^{i(\mathbf{q}\cdot\mathbf{r} - \omega_{\mathbf{q}s}\tau)} - \text{c.c.} \right), \quad (\text{D.53})$$

$$\ddot{\mathbf{u}}(\mathbf{r}, \tau) = - \sum_{\mathbf{q}, s} \omega_{\mathbf{q}s}^2 \mathbf{e}_{\mathbf{q}s} \left( c_{\mathbf{q}s} e^{i(\mathbf{q}\cdot\mathbf{r} - \omega_{\mathbf{q}s}\tau)} + \text{c.c.} \right), \quad (\text{D.54})$$

which serve as input functions for the Hamiltonian that we discuss next.

### D.3.2 Hamiltonian

In the continuum limit, the total energy of a lattice vibration comprises the kinetic energy

$$E_{\text{kin}} = \frac{1}{2} \int_V d^3\mathbf{r} \rho \dot{\mathbf{u}}^2 \quad (\text{D.55})$$

and the elastic energy

$$U = \frac{1}{2} \sum_{i,j} \int_V d^3\mathbf{r} \sigma_{ij} \epsilon_{ij}, \quad (\text{D.56})$$

where we note that the density  $\rho$  and the Lamé parameters  $\lambda$  and  $\mu$  depend on  $\mathbf{r}$  in the general case. Integrating Eq. (D.56) by parts and exploiting  $\sigma_{ij} = \sigma_{ji}$  and Eq. (D.44), one finds that the elastic energy can be rewritten as

$$U = -\frac{1}{2} \int_V d^3\mathbf{r} \rho \mathbf{u} \cdot \dot{\mathbf{u}}. \quad (\text{D.57})$$

We omitted here the surface terms that arise from the integration by parts as these terms vanish in most cases due to the boundary conditions. For instance, considering the previously introduced, rectangular sample centered at the origin, it can directly be seen that the surface terms, which are of type

$$[\sigma_{ij} u_i]_{x_j=-L_j/2}^{x_j=L_j/2}, \quad (\text{D.58})$$

are zero both for periodic boundary conditions and for force-free sample surfaces. In the above example of the rectangular sample, the axes  $\{1,2,3\}$  correspond to  $\{x, y, z\}$ . We also verified that the surface terms vanish for the system discussed in Appendix D.4, i.e., for a cylindrically symmetric NW with a force-free surface perpendicular to the radial direction and periodic boundary conditions at the longitudinal ends. The resulting Hamiltonian

$$H = E_{\text{kin}} + U \quad (\text{D.59})$$

in the continuum limit reads

$$H = \frac{1}{2} \int_V d^3\mathbf{r} \rho (\dot{\mathbf{u}} \cdot \dot{\mathbf{u}} - \mathbf{u} \cdot \ddot{\mathbf{u}}). \quad (\text{D.60})$$

With

$$m(\mathbf{R}) = \rho a^3 |_{\mathbf{r}=\mathbf{R}} \quad (\text{D.61})$$

as the mass of the lattice site at position  $\mathbf{R}$  (comprising the masses of all atoms in the corresponding unit cell), the discretized version of  $H$  is

$$H = \frac{1}{2} \sum_{\mathbf{r}=\mathbf{R}} m (\dot{\mathbf{u}} \cdot \dot{\mathbf{u}} - \mathbf{u} \cdot \ddot{\mathbf{u}}), \quad (\text{D.62})$$

where the sum runs over all lattice vectors  $\mathbf{R}$  in the material, i.e., over all lattice sites.

We note in passing that insertion of Eqs. (D.52) to (D.54) of Appendix D.3.1 into Eq. (D.60) or (D.62) yields

$$H = 2\rho V \sum_{\mathbf{q},s} |c_{\mathbf{q}s}|^2 \omega_{\mathbf{q}s}^2, \quad (\text{D.63})$$

which corresponds to the total energy of a classical acoustic lattice vibration in bulk.

### D.3.3 Quantization

#### D.3.3.1 Generalized Coordinates and Momenta

Before quantizing the phonon field, we demonstrate that  $u_j(\mathbf{R})$  and

$$p_j(\mathbf{R}) = m(\mathbf{R}) \dot{u}_j(\mathbf{R}) \quad (\text{D.64})$$

correspond to the generalized coordinates and momenta of the lattice vibrations investigated here. The subscript  $j$  refers to the three spatial directions and, as introduced before,  $\mathbf{R}$  can be any of the  $N$  lattice vectors of the material. Using the results of Appendix D.3.2 and the Hamiltonian of Eq. (D.62), one finds

$$\mathcal{L} = \sum_{\mathbf{R},j} p_j(\mathbf{R}) \dot{u}_j(\mathbf{R}) - H = \frac{1}{2} \sum_{\mathbf{R}} m (\dot{\mathbf{u}} \cdot \dot{\mathbf{u}} + \mathbf{u} \cdot \ddot{\mathbf{u}}) = E_{\text{kin}} - U, \quad (\text{D.65})$$

and so  $\mathcal{L}$  indeed is the Lagrangian of the system. We note that

$$\frac{\partial \mathcal{L}}{\partial \dot{u}_j(\mathbf{R})} = p_j(\mathbf{R}) \quad (\text{D.66})$$

can easily be verified, since terms of type  $\mathbf{u} \cdot \ddot{\mathbf{u}}$  are independent of  $\dot{u}_j$  [see also Eqs. (D.43) and (D.44)]. Furthermore, as outlined below, one can prove that Hamilton's equations of motion are fulfilled, leaving no doubt about  $u_j(\mathbf{R})$  and  $p_j(\mathbf{R})$  being generalized coordinates and momenta.

Equations (D.43) and (D.44) illustrate that  $\ddot{\mathbf{u}}$  can be obtained from the displacement field  $\mathbf{u}$  via spatial derivatives. Due to the linear dependence, one may write [6]

$$\sum_{\mathbf{R}} \mathbf{u}(\mathbf{R}) \cdot m(\mathbf{R}) \ddot{\mathbf{u}}(\mathbf{R}) = \mathbf{U} \cdot D\mathbf{U} = \sum_{\mathbf{R},j} u_j(\mathbf{R}) \sum_{\mathbf{R}',j'} D_{\mathbf{R},j,\mathbf{R}',j'} u_{j'}(\mathbf{R}'), \quad (\text{D.67})$$

where  $\mathbf{U}$  is a  $3N$ -dimensional vector that comprises all  $u_j(\mathbf{R})$ , and  $D$  is a  $3N \times 3N$  matrix whose matrix elements  $D_{\mathbf{R},j,\mathbf{R}',j'}$  do not depend on  $\mathbf{U}$ . An important relation evident from Eq. (D.67) is

$$\sum_{\mathbf{R}',j'} D_{\mathbf{R},j,\mathbf{R}',j'} u_{j'}(\mathbf{R}') = m(\mathbf{R}) \ddot{u}_j(\mathbf{R}) = \dot{p}_j(\mathbf{R}). \quad (\text{D.68})$$

Furthermore, the matrix  $D$  must be Hermitian since  $\mathbf{U} \cdot D\mathbf{U}$  is part of the Hamiltonian, and so

$$D_{\mathbf{R},j,\mathbf{R}',j'} = D_{\mathbf{R}',j',\mathbf{R},j}, \quad (\text{D.69})$$

i.e.,  $D = D^T$ . We note in passing that the term  $\mathbf{U} \cdot D\mathbf{U}$  and the property  $D = D^T$  apply to the case of real-valued  $\mathbf{U}$  and  $D$  considered here. More generally, with the complex conjugate denoted by an asterisk ( $*$ ) and the Hermitian conjugate denoted by a dagger ( $\dagger$ ), they correspond to  $\mathbf{U}^* \cdot D\mathbf{U}$  and  $D = D^\dagger$ , respectively, and so  $D_{\mathbf{R},j,\mathbf{R}',j'} = D_{\mathbf{R}',j',\mathbf{R},j}^*$ . Inserting Eq. (D.67) into Eq. (D.62) yields the Hamiltonian

$$H = \frac{1}{2} \sum_{\mathbf{R},j} m(\mathbf{R}) \dot{u}_j^2(\mathbf{R}) - \frac{1}{2} \mathbf{U} \cdot D\mathbf{U}, \quad (\text{D.70})$$

from which one finds

$$-\frac{\partial H}{\partial u_j(\mathbf{R})} = \dot{p}_j(\mathbf{R}) \quad (\text{D.71})$$

by exploiting Eqs. (D.68) and (D.69). Similarly,

$$\frac{\partial H}{\partial p_j(\mathbf{R})} = \dot{u}_j(\mathbf{R}) \quad (\text{D.72})$$

can easily be verified with Eqs. (D.64) and (D.70).

### D.3.3.2 Operators for Phonons in Bulk

Having identified  $u_j(\mathbf{R})$  and  $p_j(\mathbf{R})$  as the generalized coordinates and momenta, we now promote them to operators and refer, e.g., to Ref. [7] for further details about the information summarized in this appendix. For the quantum mechanical description of  $u_j(\mathbf{R})$  and  $p_j(\mathbf{R})$ , we introduce the bosonic ladder



operators  $a_{\mathbf{q}s}^\dagger$  and  $a_{\mathbf{q}s}$ , which obey the commutation relations

$$\left[ a_{\mathbf{q}s}, a_{\mathbf{q}'s'}^\dagger \right] = \delta_{\mathbf{q},\mathbf{q}'} \delta_{s,s'}, \quad (\text{D.73})$$

$$\left[ a_{\mathbf{q}s}^\dagger, a_{\mathbf{q}'s'}^\dagger \right] = 0 = \left[ a_{\mathbf{q}s}, a_{\mathbf{q}'s'} \right], \quad (\text{D.74})$$

with  $\delta_{\mathbf{q},\mathbf{q}'}$  and  $\delta_{s,s'}$  as Kronecker deltas and  $[A, B] = AB - BA$ . We anticipate at this stage that the operators  $a_{\mathbf{q}s}^\dagger$  and  $a_{\mathbf{q}s}$  generate and annihilate, respectively, a phonon of mode  $s$  with wave vector  $\mathbf{q}$ . Based on Eqs. (D.52) and (D.53), a reasonable ansatz for the operators  $u_j(\mathbf{R})$  and  $p_j(\mathbf{R})$  is

$$\mathbf{u}(\mathbf{R}) = \sum_{\mathbf{q},s} \mathbf{e}_{\mathbf{q}s} (c_{\mathbf{q}s} a_{\mathbf{q}s} e^{i\mathbf{q}\cdot\mathbf{R}} + \text{H.c.}), \quad (\text{D.75})$$

$$\dot{\mathbf{u}}(\mathbf{R}) = \frac{\mathbf{p}(\mathbf{R})}{m} = -i \sum_{\mathbf{q},s} \omega_{\mathbf{q}s} \mathbf{e}_{\mathbf{q}s} (c_{\mathbf{q}s} a_{\mathbf{q}s} e^{i\mathbf{q}\cdot\mathbf{R}} - \text{H.c.}), \quad (\text{D.76})$$

where  $\mathbf{u}(\mathbf{R}) = \sum_j \mathbf{e}_j u_j(\mathbf{R})$ , and analogous for the vector operators  $\mathbf{p}(\mathbf{R})$  and  $\dot{\mathbf{u}}(\mathbf{R})$ . The Hermitian conjugate is denoted by ‘‘H.c.’’. As we analyze here the case of bulk material, the mass  $m(\mathbf{R}) = m$  is independent of the lattice site.

The introduced operators  $u_j(\mathbf{R})$  and  $p_j(\mathbf{R})$  need to meet a list of criteria. Of course, they must be Hermitian, which obviously is fulfilled. Moreover, they need to obey the canonical commutation relations

$$[u_j(\mathbf{R}), p_{j'}(\mathbf{R}')] = i\hbar \delta_{j,j'} \delta_{\mathbf{R},\mathbf{R}'}, \quad (\text{D.77})$$

$$[u_j(\mathbf{R}), u_{j'}(\mathbf{R}')] = 0 = [p_j(\mathbf{R}), p_{j'}(\mathbf{R}')]. \quad (\text{D.78})$$

Exploiting, among other things, the identity

$$\sum_{\mathbf{q}} e^{i\mathbf{q}\cdot(\mathbf{R}-\mathbf{R}')} = N \delta_{\mathbf{R},\mathbf{R}'} \quad (\text{D.79})$$

and the properties of  $\mathbf{e}_{\mathbf{q}s}$ , particularly

$$\sum_s (\mathbf{e}_{\mathbf{q}s})_j (\mathbf{e}_{\mathbf{q}s})_{j'} = \delta_{j,j'} \quad (\text{D.80})$$

due to their orthonormality, one finds that all canonical commutation relations apply when

$$|c_{\mathbf{q}s}|^2 = \frac{\hbar}{2mN\omega_{\mathbf{q}s}}. \quad (\text{D.81})$$

We note that  $mN = \rho a^3 N = \rho V$  is the mass of the sample. The above-mentioned expressions for  $u_j(\mathbf{R})$  and  $p_j(\mathbf{R})$ , however, are not the only ones that meet the criteria discussed so far. For instance, it is obvious that the canonical commutation relations also apply when  $u_j(\mathbf{R}) \rightarrow u_j(\mathbf{R}) F_j(\mathbf{R})$  and  $p_j(\mathbf{R}) \rightarrow p_j(\mathbf{R})/F_j(\mathbf{R})$ , where  $F_j(\mathbf{R})$  is an arbitrary factor that is chosen real in order to preserve Hermiticity. Thus, an important criterion remains. We can ensure that the introduced operators feature the desired physical interpretations by verifying that the Hamiltonian takes the well-known form

$$H = \sum_{\mathbf{q},s} \hbar \omega_{\mathbf{q}s} \left( a_{\mathbf{q}s}^\dagger a_{\mathbf{q}s} + \frac{1}{2} \right). \quad (\text{D.82})$$

Indeed, this requirement is satisfied for Eqs. (D.75), (D.76), and (D.81). It may easily be proven by

inserting these equations into Eq. (D.62), exploiting

$$\ddot{\mathbf{u}}(\mathbf{R}) = - \sum_{\mathbf{q},s} \omega_{\mathbf{q}s}^2 \mathbf{e}_{\mathbf{q}s} (c_{\mathbf{q}s} a_{\mathbf{q}s} e^{i\mathbf{q}\cdot\mathbf{R}} + \text{H.c.}), \quad (\text{D.83})$$

the properties of  $\mathbf{e}_{\mathbf{q}s}$  and  $\omega_{\mathbf{q}s}$ , and the identity

$$\sum_{\mathbf{R}} e^{i(\mathbf{q}-\mathbf{q}')\cdot\mathbf{R}} = N\delta_{\mathbf{q},\mathbf{q}'}. \quad (\text{D.84})$$

Equation (D.83) can readily be obtained from Eq. (D.75) because the latter is written in terms of the eigenmodes, i.e., the eigenstates of the matrix  $D$ . We conclude that Eqs. (D.75) and (D.76) are suitable operators for the canonical coordinates and momenta of acoustic lattice vibrations in bulk. The normalization condition is shown in Eq. (D.81).

Finally, we mention that the time dependence

$$O \rightarrow O(\tau) = e^{iH\tau/\hbar} O e^{-iH\tau/\hbar} \quad (\text{D.85})$$

of an operator  $O$ , where  $\tau$  is the time and  $H$  is the phonon Hamiltonian [Eq. (D.82)], can easily be obtained via

$$a_{\mathbf{q}s}^\dagger \rightarrow a_{\mathbf{q}s}^\dagger(\tau) = a_{\mathbf{q}s}^\dagger e^{i\omega_{\mathbf{q}s}\tau}, \quad (\text{D.86})$$

$$a_{\mathbf{q}s} \rightarrow a_{\mathbf{q}s}(\tau) = a_{\mathbf{q}s} e^{-i\omega_{\mathbf{q}s}\tau}. \quad (\text{D.87})$$

## D.4 Phonon Quantization in Core/Shell and Core/Multishell Wires

With the information of Appendix D.3, the normalization condition for low-energetic phonons in cylindrically symmetric core/shell and core/multishell NWs can quickly be derived. Based on Chapter 5, we consider here the four gapless phonon modes and denote the time-independent and unnormalized part of the corresponding displacement fields by

$$\mathbf{u}_{q_z s}(\mathbf{r}) = \mathbf{u}_{q_z s}(r, \phi) e^{iq_z z}. \quad (\text{D.88})$$

In contrast to Appendix D.3,  $s \in \{l, t, f_+, f_-\}$  now refers to the longitudinal ( $l$ ) and torsional ( $t$ ) modes, which fulfill

$$\mathbf{u}_{q_z l}(r, \phi) = \mathbf{u}_{q_z l}(r) = [\mathbf{u}_{q_z l}(r)]_r \mathbf{e}_r + [\mathbf{u}_{q_z l}(r)]_z \mathbf{e}_z, \quad (\text{D.89})$$

$$\mathbf{u}_{q_z t}(r, \phi) = \mathbf{u}_{q_z t}(r) = [\mathbf{u}_{q_z t}(r)]_\phi \mathbf{e}_\phi, \quad (\text{D.90})$$

and to the two flexural modes ( $f_\pm$ ), for which

$$\mathbf{u}_{q_z f_\pm}(r, \phi) = \mathbf{u}_{q_z f_\pm}(r) e^{\pm i\phi}. \quad (\text{D.91})$$

The notation  $\mathbf{u}_{q_z s}(r)$  indicates here that the components along  $\mathbf{e}_r$ ,  $\mathbf{e}_\phi$ , and  $\mathbf{e}_z$  depend solely on  $r$  in cylindrical coordinates. In Chapter 5, we explicitly show that the above-mentioned properties apply to homogeneous NWs and core/shell NWs, and we note that these features may analogously be considered for arbitrary core/multishell wires with cylindrical symmetry. The length of the NW is denoted by  $L = L_z$ , and  $N_z = L_z/a$  is the number of lattice sites along  $z$ . We mention in passing that the lattice constant  $a$  along the NW corresponds to an effective, equilibrated lattice spacing when the system is coherently strained (see, e.g.,  $a_e$  in Sec. 5.3 of Chapter 5). Assuming periodic boundary conditions along

$z$ , the  $N_z$  values of the wave number  $q_z$  in the first Brillouin zone are given by Eqs. (D.50) and (D.51). Consequently, the displacement field of an arbitrary, classical lattice vibration based on the gapless modes reads

$$\mathbf{u}(\mathbf{r}, \tau) = \sum_{q_z, s} (c_{q_z s} \mathbf{u}_{q_z s}(\mathbf{r}) e^{-i\omega_{q_z s} \tau} + \text{c.c.}), \quad (\text{D.92})$$

where  $\omega_{q_z s}$  (defined as positive) are the angular frequencies of the phonon modes,  $c_{q_z s}$  are complex coefficients (dimensionless), and the sum runs over all  $s$  and all  $q_z$  within the first Brillouin zone. The time derivative is

$$\dot{\mathbf{u}}(\mathbf{r}, \tau) = -i \sum_{q_z, s} \omega_{q_z s} (c_{q_z s} \mathbf{u}_{q_z s}(\mathbf{r}) e^{-i\omega_{q_z s} \tau} - \text{c.c.}). \quad (\text{D.93})$$

The Hamiltonian derived in Appendix D.3.2 and the discussion of the generalized coordinates and momenta in Appendix D.3.3.1 are independent of the geometry and composition of the sample. [We note in passing that additional terms of type  $\sigma_{ij}^{\text{static}} \epsilon_{ij}^{\text{phonons}}$  and  $\sigma_{ij}^{\text{phonons}} \epsilon_{ij}^{\text{static}}$  arise for the elastic energy in the Hamiltonian of NWs when both the static (see also Sec. 5.3) and the dynamical displacement are taken into account. However, these terms vanish when averaging over time and also when integrating over the NW. Contributions of type  $\sigma_{ij}^{\text{static}} \epsilon_{ij}^{\text{static}}$  only provide a constant energy shift, and so we can focus here on the terms caused solely by phonons.] For the quantum mechanical description of low-energetic phonons in NWs, we therefore proceed analogously to Appendix D.3.3.2 and define the operators

$$\mathbf{u}(\mathbf{R}) = \sum_{q_z, s} (c_{q_z s} a_{q_z s} \mathbf{u}_{q_z s}(\mathbf{R}) + \text{H.c.}), \quad (\text{D.94})$$

$$\dot{\mathbf{u}}(\mathbf{R}) = \frac{\mathbf{p}(\mathbf{R})}{m(\mathbf{R})} = -i \sum_{q_z, s} \omega_{q_z s} (c_{q_z s} a_{q_z s} \mathbf{u}_{q_z s}(\mathbf{R}) - \text{H.c.}). \quad (\text{D.95})$$

The creation ( $a_{q_z s}^\dagger$ ) and annihilation ( $a_{q_z s}$ ) operators for the respective phonons obey again the commutation relations

$$[a_{q_z s}, a_{q'_z s'}^\dagger] = \delta_{q_z, q'_z} \delta_{s, s'}, \quad (\text{D.96})$$

$$[a_{q_z s}^\dagger, a_{q'_z s'}^\dagger] = 0 = [a_{q_z s}, a_{q'_z s'}]. \quad (\text{D.97})$$

As we focus only on the four gapless modes, the canonical commutation relations shown in Eqs. (D.77) and (D.78) cannot be verified with Eqs. (D.94) and (D.95) only. The reason is simply that the  $c_{q_z s}$  introduced in Eq. (D.92) provide only  $8N_z$  free parameters, and so phonon modes of higher energy need to be included in order to reach the required  $6N$  degrees of freedom ( $N$  is the number of lattice sites). Nevertheless, Eqs. (D.94) and (D.95) can be considered consistent with the canonical commutation relations, given the formal analogy with the discussed case of bulk. The normalization condition can therefore be derived by choosing  $c_{q_z s}$  such that the resulting Hamiltonian reads

$$H = \sum_{q_z, s} \hbar \omega_{q_z s} \left( a_{q_z s}^\dagger a_{q_z s} + \frac{1}{2} \right). \quad (\text{D.98})$$

We start from the Hamiltonian in the continuum limit, Eq. (D.60), and write

$$H = \frac{a}{2} \sum_z \int_0^{R_{\text{tot}}} dr r \rho(r) \int_0^{2\pi} d\phi [\dot{\mathbf{u}}(\mathbf{r}) \cdot \dot{\mathbf{u}}(\mathbf{r}) - \mathbf{u}(\mathbf{r}) \cdot \ddot{\mathbf{u}}(\mathbf{r})], \quad (\text{D.99})$$

where  $\rho(\mathbf{r}) = \rho(r)$  because of the symmetry, and  $R_{\text{tot}}$  is the radius of the outermost shell, i.e., the total radius of the NW. The summation over the coordinate  $z$  runs over the  $N_z$  lattice positions along the  $z$  axis. That is, we consider here a discrete lattice along the NW and use the continuum limit for the

transverse directions. After insertion of [see also Eqs. (D.94) and (D.95)]

$$\mathbf{u}(\mathbf{r}) = \sum_{q_z, s} (c_{q_z s} a_{q_z s} \mathbf{u}_{q_z s}(\mathbf{r}) + \text{H.c.}), \quad (\text{D.100})$$

$$\dot{\mathbf{u}}(\mathbf{r}) = -i \sum_{q_z, s} \omega_{q_z s} (c_{q_z s} a_{q_z s} \mathbf{u}_{q_z s}(\mathbf{r}) - \text{H.c.}), \quad (\text{D.101})$$

$$\ddot{\mathbf{u}}(\mathbf{r}) = - \sum_{q_z, s} \omega_{q_z s}^2 (c_{q_z s} a_{q_z s} \mathbf{u}_{q_z s}(\mathbf{r}) + \text{H.c.}), \quad (\text{D.102})$$

and Eq. (D.88) into Eq. (D.99), the dependence on  $z$  can be removed due to [7]

$$\sum_z e^{i(q_z - q'_z)z} = N_z \delta_{q_z, q'_z}. \quad (\text{D.103})$$

It is then convenient to introduce the shorthand notation

$$\text{Int}[\mathbf{a} \cdot \mathbf{b}] = \int_0^{R_{\text{tot}}} dr r \rho(r) \int_0^{2\pi} d\phi \mathbf{a} \cdot \mathbf{b} \quad (\text{D.104})$$

with arbitrary  $\mathbf{a}$  and  $\mathbf{b}$ , and we mention that  $\text{Int}[\mathbf{a} \cdot \mathbf{b}] = \text{Int}[\mathbf{b} \cdot \mathbf{a}]$ . Exploiting the properties of the phonon modes, in particular  $\omega_{q_z s} = \omega_{-q_z s}$ ,  $\omega_{q_z f_+} = \omega_{q_z f_-}$ , and

$$\text{Int}[\mathbf{u}_{q_z s}^*(r, \phi) \cdot \mathbf{u}_{q_z s'}(r, \phi)] = \delta_{s, s'} \text{Int}[\mathbf{u}_{q_z s}^* \cdot \mathbf{u}_{q_z s}] \quad (\text{D.105})$$

due to Eqs. (D.89) to (D.91), the Hamiltonian can be reduced to

$$H = 2L_z \sum_{q_z, s} \omega_{q_z s}^2 |c_{q_z s}|^2 \text{Int}[\mathbf{u}_{q_z s}^* \cdot \mathbf{u}_{q_z s}] \left( a_{q_z s}^\dagger a_{q_z s} + \frac{1}{2} \right). \quad (\text{D.106})$$

Thus, comparison with Eq. (D.98) yields the normalization condition

$$|c_{q_z s}|^2 \text{Int}[\mathbf{u}_{q_z s}^* \cdot \mathbf{u}_{q_z s}] = \frac{\hbar}{2L_z \omega_{q_z s}}. \quad (\text{D.107})$$

For convenience, the arguments of  $\mathbf{u}_{q_z s}$  were omitted here because of

$$\mathbf{u}_{q_z s}^*(r, \phi) \cdot \mathbf{u}_{q_z s}(r, \phi) = \mathbf{u}_{q_z s}^*(r) \cdot \mathbf{u}_{q_z s}(r) = \mathbf{u}_{q_z s}^*(\mathbf{r}) \cdot \mathbf{u}_{q_z s}(\mathbf{r}) = \mathbf{u}_{q_z s}^* \cdot \mathbf{u}_{q_z s}, \quad (\text{D.108})$$

as evident from Eqs. (D.88) to (D.91). Insertion into Eq. (D.104) therefore yields

$$\text{Int}[\mathbf{u}_{q_z s}^* \cdot \mathbf{u}_{q_z s}] = 2\pi \int_0^{R_{\text{tot}}} dr r \rho(r) \mathbf{u}_{q_z s}^* \cdot \mathbf{u}_{q_z s}. \quad (\text{D.109})$$

In conclusion, the normalization condition for gapless phonon modes in cylindrically symmetric core/shell and core/multishell NWs is

$$|c_{q_z s}|^2 \int_0^{R_{\text{tot}}} dr r \rho(r) \mathbf{u}_{q_z s}^* \cdot \mathbf{u}_{q_z s} = \frac{\hbar}{4\pi L_z \omega_{q_z s}}. \quad (\text{D.110})$$

When  $\rho(r) = \rho$ , this condition matches the well-known result for homogeneous NWs [8]. In order to avoid confusion, we mention that the displacement operator  $\mathbf{u}(\mathbf{r})$  is sometimes defined with an additional prefactor of  $1/\sqrt{N}$ . A general discussion of phonon quantization in nanostructures can be found in Ref. [9]. Analogous to the case of bulk (Appendix D.3.3.2), time-dependent operators may easily be obtained through  $a_{q_z s}^\dagger \rightarrow a_{q_z s}^\dagger(\tau) = a_{q_z s}^\dagger e^{i\omega_{q_z s}\tau}$  and  $a_{q_z s} \rightarrow a_{q_z s}(\tau) = a_{q_z s} e^{-i\omega_{q_z s}\tau}$ .

# References

- [1] R. Winkler, *Spin-Orbit Coupling Effects in Two-Dimensional Electron and Hole Systems* (Springer, Berlin, 2003).
- [2] S. Adachi, *Properties of Group-IV, III-V and II-VI Semiconductors* (Wiley, Chichester, 2005).
- [3] A. N. Cleland, *Foundations of Nanomechanics: From Solid-State Theory to Device Applications* (Springer, Berlin, 2003).
- [4] V. Kornich, C. Kloeffer, and D. Loss, Phys. Rev. B **89**, 085410 (2014).  
See Chapter 6
- [5] L. D. Landau and E. M. Lifshitz, *Theory of Elasticity*, 2nd ed. (Pergamon, New York, 1970).
- [6] U. Rössler, *Solid State Theory: An Introduction*, 2nd ed. (Springer, Berlin, 2009).
- [7] N. W. Ashcroft and N. D. Mermin, *Solid State Physics* (Saunders College, Philadelphia, 1976).
- [8] M. A. Stroschio, K. W. Kim, S. Yu, and A. Ballato, J. Appl. Phys. **76**, 4670 (1994).
- [9] M. A. Stroschio and M. Dutta, *Phonons in Nanostructures* (Cambridge Univ. Press, Cambridge, 2001).



## **Appendix E**

### **Supplementary Information to Chapter 6 “Phonon-Mediated Decay of Singlet-Triplet Qubits in Double Quantum Dots”**

**Adapted from:**

Viktoriia Kornich, Christoph Kloeffel, and Daniel Loss,  
Phys. Rev. B **89**, 085410 (2014).

## E.1 Basis States

We consider a GaAs/AlGaAs heterostructure that contains a two-dimensional electron gas (2DEG). Electric gates on the top of the sample induce a double quantum dot (DQD) potential that confines electrons and enables the implementation of a singlet-triplet qubit. Assuming that this spin qubit is based on low-energy states of two electrons in the DQD, we consider the four states of lowest energy

$$|(1,1)S\rangle = |\Psi_+\rangle|S\rangle, \quad (\text{E.1})$$

$$|(1,1)T_+\rangle = |\Psi_-\rangle|T_+\rangle, \quad (\text{E.2})$$

$$|(1,1)T_0\rangle = |\Psi_-\rangle|T_0\rangle, \quad (\text{E.3})$$

$$|(1,1)T_-\rangle = |\Psi_-\rangle|T_-\rangle, \quad (\text{E.4})$$

two states with a doubly occupied quantum dot (QD)

$$|(0,2)S\rangle = |\Psi_R\rangle|S\rangle, \quad (\text{E.5})$$

$$|(2,0)S\rangle = |\Psi_L\rangle|S\rangle, \quad (\text{E.6})$$

and four additional states that feature one electron in a first excited orbital state

$$|(1^*,1)S\rangle = |\Psi_+^e\rangle|S\rangle, \quad (\text{E.7})$$

$$|(1^*,1)T_+\rangle = |\Psi_-^e\rangle|T_+\rangle, \quad (\text{E.8})$$

$$|(1^*,1)T_0\rangle = |\Psi_-^e\rangle|T_0\rangle, \quad (\text{E.9})$$

$$|(1^*,1)T_-\rangle = |\Psi_-^e\rangle|T_-\rangle \quad (\text{E.10})$$

as the basis in this problem. In the notation used above, the first and second index in parentheses corresponds to the occupation number of the left and right QD, respectively. The asterisk denotes that the electron in the QD is in the first excited state. The spin part of the wave functions consists of the singlet  $|S\rangle$  and the triplets  $|T_0\rangle$ ,  $|T_+\rangle$ , and  $|T_-\rangle$ ,

$$|S\rangle = \frac{|\uparrow\downarrow\rangle - |\downarrow\uparrow\rangle}{\sqrt{2}}, \quad (\text{E.11})$$

$$|T_0\rangle = \frac{|\uparrow\downarrow\rangle + |\downarrow\uparrow\rangle}{\sqrt{2}}, \quad (\text{E.12})$$

$$|T_+\rangle = |\uparrow\uparrow\rangle, \quad (\text{E.13})$$

$$|T_-\rangle = |\downarrow\downarrow\rangle, \quad (\text{E.14})$$

where  $\uparrow$  ( $\downarrow$ ) corresponds to an electron spin oriented along (against) the externally applied magnetic field (see Appendix E.2).

As the two minima in the DQD potential may be approximated by the confining potential of a 2D harmonic oscillator, the one-particle wave functions for ground and first excited states can be constructed from the eigenstates of the harmonic oscillators [1]. Defining the growth axis of the heterostructure as the  $z$  axis, we consider harmonic confinement potentials around  $(x, y) = (\pm a, 0)$  with  $l_c = \sqrt{\hbar/(m_{\text{eff}}\omega_0)}$  as the confinement length in the QDs. The  $x$  axis connects the two QDs, pointing from the left to the right one. The interdot distance is  $L = 2a$ ,  $m_{\text{eff}}$  is the effective mass of electrons in GaAs, and  $\hbar\omega_0$  is the orbital level spacing in each QD. With these definitions, the orbital parts of the 2D harmonic oscillator



wave functions (ground, excited along  $x$ , excited along  $y$ ) can be written as

$$\phi_{L,R}(x, y) = \frac{1}{\sqrt{\pi}l_c} e^{-[(x\pm a)^2+y^2]/(2l_c^2)}, \quad (\text{E.15})$$

$$\phi_{L,R}^x(x, y) = \sqrt{\frac{2}{\pi l_c^4}} (x \pm a) e^{-[(x\pm a)^2+y^2]/(2l_c^2)}, \quad (\text{E.16})$$

$$\phi_{L,R}^y(x, y) = \sqrt{\frac{2}{\pi l_c^4}} y e^{-[(x\pm a)^2+y^2]/(2l_c^2)}. \quad (\text{E.17})$$

The confining potential along the  $z$  axis may be considered as a triangular potential of type

$$V(z) = \begin{cases} \infty, & z < 0, \\ Cz, & z > 0, \end{cases} \quad (\text{E.18})$$

where  $C$  is a positive constant with units energy/length and  $z = 0$  corresponds to the interface between AlGaAs ( $z < 0$ ) and GaAs ( $z > 0$ ). The ground state in such a potential can be approximated by the Fang-Howard wave function [2]

$$\phi_{\text{FH}}(z) = \theta(z) \frac{z}{\sqrt{2a_z^3}} e^{-z/(2a_z)}, \quad (\text{E.19})$$

with  $a_z$  as a positive length and

$$\theta(z) = \begin{cases} 0, & z < 0, \\ 1, & z > 0, \end{cases} \quad (\text{E.20})$$

as the Heaviside step function. The Fang-Howard wave function from Eq. (E.19) is normalized and fulfills

$$\langle \phi_{\text{FH}} | z | \phi_{\text{FH}} \rangle = 3a_z, \quad (\text{E.21})$$

which may be interpreted as the width of the 2DEG.

Following Refs. [1, 3, 4] for constructing wave functions in the DQD potential, we define overlaps between the harmonic oscillator wave functions:

$$s = \langle \phi_L | \phi_R \rangle = e^{-\frac{a^2}{l_c^2}}, \quad (\text{E.22})$$

$$s_x = \langle \phi_L^x | \phi_R^x \rangle = s \left( 1 - \frac{2a^2}{l_c^2} \right), \quad (\text{E.23})$$

$$s_y = \langle \phi_L^y | \phi_R^y \rangle = s, \quad (\text{E.24})$$

and

$$g = \frac{1 - \sqrt{1 - s^2}}{s}, \quad (\text{E.25})$$

$$g_x = \frac{1 - \sqrt{1 - s_x^2}}{s_x}, \quad (\text{E.26})$$

$$g_y = \frac{1 - \sqrt{1 - s_y^2}}{s_y} = g. \quad (\text{E.27})$$

Then, the normalized orbital parts of the one-particle wave functions for the DQD are

$$\Phi_{L,R}(\mathbf{r}) = \frac{\phi_{L,R}(x,y) - g\phi_{R,L}(x,y)}{\sqrt{1-2sg+g^2}}\phi_{\text{FH}}(z), \quad (\text{E.28})$$

$$\Phi_{L,R}^{e,x}(\mathbf{r}) = \frac{\phi_{L,R}^x(x,y) - g_x\phi_{R,L}^x(x,y)}{\sqrt{1-2s_xg_x+g_x^2}}\phi_{\text{FH}}(z), \quad (\text{E.29})$$

$$\Phi_{L,R}^{e,y}(\mathbf{r}) = \frac{\phi_{L,R}^y(x,y) - g\phi_{R,L}^y(x,y)}{\sqrt{1-2sg+g^2}}\phi_{\text{FH}}(z). \quad (\text{E.30})$$

We note that these six states form an orthonormal set of basis states to a very good accuracy. The only nonzero scalar products among different states are  $\langle\Phi_L|\Phi_L^{e,x}\rangle$ ,  $\langle\Phi_R|\Phi_R^{e,x}\rangle$ ,  $\langle\Phi_L|\Phi_R^{e,x}\rangle$ , and  $\langle\Phi_R|\Phi_L^{e,x}\rangle$ . Even though there is a nonzero overlap, the absolute values of these scalar products are small ( $\sim 0.01$ – $0.1$  depending on the parameters of the DQD), which indicates that Eqs. (E.28)–(E.30) present a very good approximation for an orthonormal basis. It is, however, important to note that we set  $\langle\Phi_L|\Phi_L^{e,x}\rangle$ ,  $\langle\Phi_R|\Phi_R^{e,x}\rangle$ ,  $\langle\Phi_L|\Phi_R^{e,x}\rangle$ , and  $\langle\Phi_R|\Phi_L^{e,x}\rangle$  equal to zero when calculating the matrix elements of the effective Hamiltonian later on, in order to avoid artifacts from the finite overlap of these basis states.

Given the six basis states for the orbital part of single electrons, we can construct the two-particle wave functions [1, 4]

$$\Psi_{\pm}(\mathbf{r}_1, \mathbf{r}_2) = \frac{\Phi_L(\mathbf{r}_1)\Phi_R(\mathbf{r}_2) \pm \Phi_R(\mathbf{r}_1)\Phi_L(\mathbf{r}_2)}{\sqrt{2}}, \quad (\text{E.31})$$

$$\Psi_{\pm}^{e,\nu}(\mathbf{r}_1, \mathbf{r}_2) = \frac{\Phi_L^{e,\nu}(\mathbf{r}_1)\Phi_R(\mathbf{r}_2) \pm \Phi_R(\mathbf{r}_1)\Phi_L^{e,\nu}(\mathbf{r}_2)}{\sqrt{2}}, \quad (\text{E.32})$$

$$\Psi_{L,R}(\mathbf{r}_1, \mathbf{r}_2) = \Phi_{L,R}(\mathbf{r}_1)\Phi_{L,R}(\mathbf{r}_2), \quad (\text{E.33})$$

where  $\nu \in \{x, y\}$ . The calculations for Fig. 6.6 in Chapter 6 were done with the orbital excitation along the  $x$  axis only,  $\Psi_{\pm}^e = \Psi_{\pm}^{e,x}$ , because the rates resulting from  $\Psi_{\pm}^{e,y}$  are much smaller than those from  $\Psi_{\pm}^{e,x}$  in this setup. For some special configurations, such as  $\mathbf{B} \parallel y$  and  $x \parallel [110]$ , where  $\mathbf{B}$  is the external magnetic field, the calculations for  $\Psi_{\pm}^e = \Psi_{\pm}^{e,y}$  lead to lifetimes similar to or even shorter than those for  $\Psi_{\pm}^e = \Psi_{\pm}^{e,x}$ , and so states with the excitation along the  $y$  axis should be taken into account in these special cases. States of type  $(1, 1^*)$  with the excited electron in the right QD will change the results only by factors around 2, and therefore were not included for simplicity.

## E.2 Hamiltonian

The Hamiltonian of the considered system is

$$H = \sum_{j=1,2} \left( H_0^{(j)} + H_Z^{(j)} + H_{\text{SOI}}^{(j)} + H_{\text{hyp}}^{(j)} + H_{\text{el-ph}}^{(j)} \right) + H_C + H_{\text{ph}}, \quad (\text{E.34})$$

where the index  $j$  denotes the electron,  $H_0$  takes into account the motion of the electron in the double dot potential,  $H_Z$  is the Zeeman term,  $H_{\text{SOI}}$  is the spin-orbit interaction (SOI),  $H_{\text{hyp}}$  is the hyperfine coupling,  $H_{\text{el-ph}}$  is the electron-phonon interaction,  $H_C$  is the Coulomb repulsion, and  $H_{\text{ph}}$  is the Hamiltonian of the phonon bath. In the following, we discuss the contributions to  $H$  in further detail.

### E.2.1 Hamiltonian $H_0$

Due to  $a_z \ll l_c$ , the wave function along the  $z$  axis is the same for all basis states in our model. The one-particle Hamiltonian  $H_0$  can therefore be written as an effective 2D Hamiltonian

$$H_0 = \frac{p_x^2 + p_y^2}{2m_{\text{eff}}} + V(x, y), \quad (\text{E.35})$$

where  $p_x$  ( $p_y$ ) is the momentum along the  $x$  ( $y$ ) axis and  $V(x, y)$  is the confining potential in the transverse directions. The potential  $V(x, y)$  is provided by the electric gates and features a finite barrier between the two QDs. It also accounts for electric fields applied along the DQD axis that effectively shift the electron energy in the left QD by the detuning  $\epsilon$  compared to the right QD.

### E.2.2 Coulomb Repulsion

The Hamiltonian that describes the Coulomb interaction between the two electrons is

$$H_C = \frac{1}{4\pi\epsilon_0\epsilon_r} \frac{e^2}{|\mathbf{r}_1 - \mathbf{r}_2|}, \quad (\text{E.36})$$

where  $e$  is the elementary positive charge,  $\epsilon_0$  is the vacuum permittivity, and  $\epsilon_r$  is the relative permittivity of GaAs.

### E.2.3 Zeeman Term

We consider an in-plane magnetic field  $\mathbf{B} = |\mathbf{B}|\mathbf{e}_B = B\mathbf{e}_B$  with arbitrary orientation in the  $x$ - $y$  plane. Here and in the following,  $\mathbf{e}_k$  ( $\mathbf{e}_\eta$ ) stands for the unit vector along the direction of some vector  $\mathbf{k}$  (axis  $\eta$ ). As the 2DEG is only a few nanometers wide, orbital effects due to an in-plane magnetic field are negligible. The Hamiltonian for the Zeeman coupling reads

$$H_Z = \frac{E_Z}{2} \sigma_B, \quad (\text{E.37})$$

where  $E_Z = g\mu_B B$  is the Zeeman energy,  $g$  is the in-plane  $g$  factor,  $\mu_B$  is the Bohr magneton,  $B = |\mathbf{B}|$  is the magnetic field strength, and

$$\sigma_B = \boldsymbol{\sigma} \cdot \mathbf{e}_B, \quad (\text{E.38})$$

with  $\boldsymbol{\sigma}$  as the vector of Pauli matrices, denotes the Pauli operator for the electron spin along the magnetic field.

### E.2.4 Spin-Orbit Interaction

We assume that the heterostructure was grown along the [001] direction, referred to as both the  $z$  and  $z'$  direction. Consequently, the SOI due to Rashba and Dresselhaus SOI reads

$$H_{\text{SOI}} = \alpha (p_{x'}\sigma_{y'} - p_{y'}\sigma_{x'}) + \beta (p_{y'}\sigma_{y'} - p_{x'}\sigma_{x'}) \quad (\text{E.39})$$

for a single electron, where the axes  $x'$  and  $y'$  correspond to the main crystallographic axes [100] and [010], respectively.

Using the antihermitian operator

$$S_1 = i \frac{m_{\text{eff}}}{\hbar} [\alpha (x'\sigma_{y'} - y'\sigma_{x'}) + \beta (y'\sigma_{y'} - x'\sigma_{x'})], \quad (\text{E.40})$$

which fulfills the commutation relation

$$[S_1, H_0] = S_1 H_0 - H_0 S_1 = -H_{\text{SOI}}, \quad (\text{E.41})$$

we can remove the SOI to lowest order via a unitary (Schrieffer-Wolff) transformation [5–11],

$$\begin{aligned} \tilde{H} &= e^S H e^{-S} = e^{(\sum_j S_1^{(j)} + \dots)} H e^{-(\sum_j S_1^{(j)} + \dots)} \\ &\simeq \sum_{j=1,2} \left( H_0^{(j)} + H_Z^{(j)} + H_{\text{hyp}}^{(j)} + H_{\text{el-ph}}^{(j)} \right) + H_C + H_{\text{ph}} \\ &\quad + \sum_{j=1,2} \left( [S_1^{(j)}, H_Z^{(j)}] + \frac{1}{2} [S_1^{(j)}, H_{\text{SOI}}^{(j)}] \right). \end{aligned} \quad (\text{E.42})$$

The perturbation theory applies when both the SOI and the Zeeman coupling are weak compared to the confinement (spin-orbit length  $\gg$  confinement length; Zeeman splitting  $\ll$  orbital level splitting), which is well fulfilled in the system under study. Exploiting the commutation relations  $[\sigma_{x'}, \sigma_{y'}] = 2i\sigma_{z'}$  (and analogously for cyclic permutations) of the Pauli matrices, one finds

$$[S_1, H_Z] = g\mu_B (\mathbf{r}_{\text{SOI}} \times \mathbf{B}) \cdot \boldsymbol{\sigma}, \quad (\text{E.43})$$

where we defined the SOI-dependent vector operator

$$\mathbf{r}_{\text{SOI}} = \left( \frac{y'}{l_R} + \frac{x'}{l_D} \right) \mathbf{e}_{[100]} + \left( -\frac{x'}{l_R} - \frac{y'}{l_D} \right) \mathbf{e}_{[010]}. \quad (\text{E.44})$$

The unit vector along the [100] axis, i.e., the  $x'$  direction, is denoted by  $\mathbf{e}_{[100]} = \mathbf{e}_{x'}$ , and analogously for all other crystallographic directions. The spin-orbit lengths  $l_R$  and  $l_D$  are defined as

$$l_R = \frac{\hbar}{m_{\text{eff}}\alpha}, \quad (\text{E.45})$$

$$l_D = \frac{\hbar}{m_{\text{eff}}\beta}. \quad (\text{E.46})$$

The contribution due to  $[S_1, H_{\text{SOI}}]/2$  is less important when  $B$  is sufficiently large, and considering  $B \sim 0.7$  T [12, 13] we therefore omit it in our model. Nevertheless, we provide the result for completeness [8],

$$\frac{1}{2} [S_1, H_{\text{SOI}}] = -m_{\text{eff}} (\alpha^2 + \beta^2) + \frac{m_{\text{eff}}}{\hbar} (\beta^2 - \alpha^2) l_{z'} \sigma_{z'}. \quad (\text{E.47})$$

The operator  $l_{z'} = (x' p_{y'} - y' p_{x'})$  herein corresponds to the angular momentum along the axis of strong confinement. Again, orbital effects (canonical momentum  $\neq$  kinetic momentum) are negligible when the magnetic field is applied in plane. Finally, we mention that corrections of type  $[S_1, H_{\text{hyp}}]$  were neglected in Eq. (E.42), because  $H_Z$  is assumed to be much larger than the hyperfine coupling  $H_{\text{hyp}}$  that we discuss next.

## E.2.5 Hyperfine Interaction

The hyperfine interaction between the electron and the nuclear spins can be described in terms of an effective magnetic field. The latter can be split into a sum field, which is present in both QDs, and a gradient field, which accounts for the difference in the hyperfine field between the dots. As the sum field is usually small compared to the external magnetic field, and, moreover, may largely be accounted for by  $H_Z$ , we use  $H_{\text{hyp}}$  to quantify the gradient field between the dots. Hence, this Hamiltonian reads

$$H_{\text{hyp}} = \frac{\delta \mathbf{b} \cdot \boldsymbol{\sigma}}{4} (\mathcal{P}_L - \mathcal{P}_R), \quad (\text{E.48})$$

where  $\delta\mathbf{b}$  arises from the hyperfine field gradient between the QDs. The operators  $\mathcal{P}_L$  and  $\mathcal{P}_R$  are projectors for the left and right QD, respectively, and can be written as

$$\mathcal{P}_L = |\Phi_L\rangle\langle\Phi_L| + |\Phi_L^{e,x}\rangle\langle\Phi_L^{e,x}| + |\Phi_L^{e,y}\rangle\langle\Phi_L^{e,y}|, \quad (\text{E.49})$$

$$\mathcal{P}_R = |\Phi_R\rangle\langle\Phi_R| + |\Phi_R^{e,x}\rangle\langle\Phi_R^{e,x}| + |\Phi_R^{e,y}\rangle\langle\Phi_R^{e,y}| \quad (\text{E.50})$$

for the basis states defined in Appendix E.1.

We note that

$$\langle(1,1)S|H_{\text{hyp}}|(1,1)T_0\rangle = \frac{\delta b_B}{2}, \quad (\text{E.51})$$

where

$$\delta b_B = \delta\mathbf{b} \cdot \mathbf{e}_B \quad (\text{E.52})$$

is the component of  $\delta\mathbf{b}$  along the external magnetic field  $\mathbf{B}$ . Because it turns out that all other matrix elements of  $H_{\text{hyp}}$  within the basis of Appendix E.1 are negligible for the lifetimes of the qubit, we approximate the hyperfine coupling by

$$H_{\text{hyp}} \simeq \frac{\delta b_B}{2} |(1,1)S\rangle\langle(1,1)T_0| + \text{H.c.}, \quad (\text{E.53})$$

with the Hermitian conjugate abbreviated as ‘‘H.c.’’. We set  $\delta b_B = -0.14 \mu\text{eV}$  in our calculations, in good agreement with Refs. [12, 14].

## E.2.6 Electron-Phonon Coupling

The electron-phonon interaction

$$H_{\text{el-ph}} = H_{\text{dp}} + H_{\text{pe}} \quad (\text{E.54})$$

comprises the deformation potential coupling  $H_{\text{dp}}$  and the piezoelectric coupling  $H_{\text{pe}}$ . Both mechanisms can be derived from the displacement operator, which we therefore recall first. Most of the information summarized in this appendix on electron-phonon coupling is described in great detail in Refs. [15–21], and we refer to these for further information.

### E.2.6.1 Displacement Operator

Acoustic phonons in an isotropic crystal (bulk) lead to the displacement operator

$$\mathbf{u} = \sum_{\mathbf{q},s} \mathbf{e}_{\mathbf{q}s} (c_{\mathbf{q}s} e^{i\mathbf{q}\cdot\mathbf{r}} a_{\mathbf{q}s} + c_{\mathbf{q}s}^* e^{-i\mathbf{q}\cdot\mathbf{r}} a_{\mathbf{q}s}^\dagger), \quad (\text{E.55})$$

where  $c_{\mathbf{q}s}$  is an arbitrary coefficient with normalization condition  $|c_{\mathbf{q}s}|^2 = \hbar/(2\rho V\omega_{\mathbf{q}s})$ ,  $\rho$  and  $V$  are the density and volume of the crystal, and  $\omega_{\mathbf{q}s}$  is the angular frequency of the acoustic phonon of type  $s$  with wave vector  $\mathbf{q}$ . For the longitudinal mode  $s = l$ , the dispersion relation at small  $q = |\mathbf{q}|$  is  $\omega_{\mathbf{q}l} = q\sqrt{(\lambda + 2\mu)/\rho} = qv_l$ , while for the transverse modes  $s = t_1$  and  $s = t_2$  one finds  $\omega_{\mathbf{q}t_1} = \omega_{\mathbf{q}t_2} = \omega_{\mathbf{q}t} = q\sqrt{\mu/\rho} = qv_t$ , where  $\lambda$  and  $\mu$  are the Lamé parameters of the material and  $v_l$  ( $v_t$ ) is the speed of sound for longitudinal (transverse) waves [20]. The operators  $a_{\mathbf{q}s}^\dagger$  and  $a_{\mathbf{q}s}$  create and annihilate a corresponding phonon, and fulfill the commutation relations  $[a_{\mathbf{q}s}^\dagger, a_{\mathbf{q}'s'}^\dagger] = 0$ ,  $[a_{\mathbf{q}s}, a_{\mathbf{q}'s'}] = 0$ , and  $[a_{\mathbf{q}s}, a_{\mathbf{q}'s'}^\dagger] = \delta_{\mathbf{q},\mathbf{q}'}\delta_{s,s'}$ , with  $\delta_{\mathbf{q},\mathbf{q}'}$  and  $\delta_{s,s'}$  as Kronecker deltas. For each wave vector  $\mathbf{q}$ , the three real-valued polarization vectors  $\mathbf{e}_{\mathbf{q}s}$  form an orthonormal basis with  $\mathbf{e}_{\mathbf{q}l} \parallel \mathbf{q}$ . The summation over  $\mathbf{q}$  runs over all wave vectors within the first Brillouin zone.

With a suitable choice of the polarization vectors  $\mathbf{e}_{\mathbf{q}s}$ , the displacement operator from Eq. (E.55) can

be simplified further. We choose these vectors in such a way that the relations

$$\mathbf{e}_{-ql} = -\mathbf{e}_{ql}, \quad (\text{E.56})$$

$$\mathbf{e}_{-qt_1} = -\mathbf{e}_{qt_1}, \quad (\text{E.57})$$

$$\mathbf{e}_{-qt_2} = \mathbf{e}_{qt_2} \quad (\text{E.58})$$

are fulfilled. The advantages of this definition become obvious later on when we write the Hamiltonian for the electron-phonon coupling. In short terms, this choice allows one to define  $\mathbf{e}_{ql} = \mathbf{q}/q$  and to represent the vectors  $\mathbf{e}_{qs}$  via a simple right-handed basis. Setting  $c_{qs} = \sqrt{\hbar/(2\rho V\omega_{qs})}$ , and making use of Eqs. (E.56) to (E.58) and of the property  $\omega_{-qs} = \omega_{qs}$ , the displacement operator can be written in the convenient form

$$\mathbf{u} = \sum_{\mathbf{q},s} \sqrt{\frac{\hbar}{2\rho V\omega_{qs}}} \mathbf{e}_{qs} \left( a_{qs} \mp_s a_{-\mathbf{q}s}^\dagger \right) e^{i\mathbf{q}\cdot\mathbf{r}}, \quad (\text{E.59})$$

where

$$\mp_s = \begin{cases} - & \text{for } s = l, t_1, \\ + & \text{for } s = t_2. \end{cases} \quad (\text{E.60})$$

This representation of the displacement operator [Eq. (E.59)] will now be used to derive the Hamiltonian for the electron-phonon coupling. We note that the time dependence  $\mathbf{u} \rightarrow \mathbf{u}(\tau)$  and  $H_{\text{el-ph}} \rightarrow H_{\text{el-ph}}(\tau)$  in the interaction picture (see Appendix E.5) is simply obtained via  $a_{qs} \rightarrow a_{qs}(\tau) = a_{qs} e^{-i\omega_{qs}\tau}$  and  $a_{qs}^\dagger \rightarrow a_{qs}^\dagger(\tau) = a_{qs}^\dagger e^{i\omega_{qs}\tau}$ .

It is worth mentioning how we choose the values for the speeds of sound in GaAs. The three elastic stiffness coefficients for GaAs are  $c_{11} = 118$ ,  $c_{12} = 53.5$ , and  $c_{44} = 59.4$ , each in units of  $10^9 \text{ N/m}^2$ . These values were taken from Ref. [20] and are in very good agreement with those in, e.g., Refs. [21, 22]. It makes sense to approximate these coefficients by  $\tilde{c}_{11}$ ,  $\tilde{c}_{12}$ , and  $\tilde{c}_{44}$ , respectively, for which the condition  $\tilde{c}_{11} = \tilde{c}_{12} + 2\tilde{c}_{44}$  of an isotropic material is fulfilled. By postulating that the relative deviation for each of the three constants should be the same, we find  $\lambda = \tilde{c}_{12} = 43.5 \times 10^9 \text{ N/m}^2$  and  $\mu = \tilde{c}_{44} = 48.3 \times 10^9 \text{ N/m}^2$ , corresponding to a relative deviation of 18.7%. The resulting sound velocities in the isotropic approximation are  $v_l = \sqrt{\tilde{c}_{11}/\rho} = 5.1 \times 10^3 \text{ m/s}$  and  $v_t = \sqrt{\tilde{c}_{44}/\rho} = 3.0 \times 10^3 \text{ m/s}$ . We note that basically the same values are obtained by simply averaging over the speeds of sound along the [100], [110], and [111] directions (longitudinal or transverse waves, respectively), as listed, for instance, in Refs. [21, 22].

### E.2.6.2 Deformation Potential Coupling

The first coupling mechanism is the deformation potential coupling. In the presence of strain, the energy of the conduction band changes. For GaAs, a cubic semiconductor with the conduction band minimum at the  $\Gamma$  point, the shift of the conduction band edge is determined by the simple Hamiltonian

$$H_{\text{dp}} = \Xi \nabla \cdot \mathbf{u} = \Xi (\epsilon_{xx} + \epsilon_{yy} + \epsilon_{zz}), \quad (\text{E.61})$$

where  $\Xi$  is the hydrostatic deformation potential,  $\nabla$  is the Nabla operator, and  $\epsilon_{ij}$  are the strain tensor elements, which are related to the displacement via

$$\epsilon_{ij} = \frac{1}{2} \left( \frac{\partial u_i}{\partial x_j} + \frac{\partial u_j}{\partial x_i} \right). \quad (\text{E.62})$$

The trace of the strain tensor  $\nabla \cdot \mathbf{u} = \epsilon_{xx} + \epsilon_{yy} + \epsilon_{zz}$  corresponds to the relative change in the volume. One finds  $\Xi \approx -8 \text{ eV}$  for GaAs [19, 23], and so compression increases the energy of the conduction band

edge. Exploiting  $\nabla e^{i\mathbf{q}\cdot\mathbf{r}} = i\mathbf{q}e^{i\mathbf{q}\cdot\mathbf{r}}$  and defining  $\mathbf{e}_{ql} = \mathbf{q}/q$ , substitution of Eq. (E.59) into (E.61) yields

$$H_{\text{dp}} = i\Xi \sum_{\mathbf{q}} \sqrt{\frac{\hbar}{2\rho V \omega_{ql}}} q \left( a_{\mathbf{ql}} - a_{-\mathbf{ql}}^\dagger \right) e^{i\mathbf{q}\cdot\mathbf{r}}. \quad (\text{E.63})$$

We note that only the longitudinal mode contributes to the deformation potential coupling. This is different for the piezoelectric electron-phonon interaction that we derive next.

### E.2.6.3 Piezoelectric Coupling

In crystals without inversion symmetry, lattice vibrations (i.e., phonons) result in a finite polarization density  $\mathbf{P}_p^{\text{phon}}$  and, consequently, lead to an effective electric field  $\mathbf{E}_p$ . The latter is characterized by the equation

$$0 = \epsilon_0 \mathbf{E}_p + \mathbf{P}_p^{\text{diel}} + \mathbf{P}_p^{\text{phon}} = \epsilon_0 \epsilon_r \mathbf{E}_p + \mathbf{P}_p^{\text{phon}}, \quad (\text{E.64})$$

where we set the electric displacement on the left-hand side to zero due to the absence of free charges in this mechanism. The vector  $\mathbf{P}_p^{\text{diel}} = \epsilon_0(\epsilon_r - 1)\mathbf{E}_p$  is the polarization density induced by the field  $\mathbf{E}_p$ ,  $\epsilon_0$  is the vacuum permittivity, and  $\epsilon_r$  is the relative permittivity of the material ( $\epsilon_r \simeq 13$  in GaAs). In contrast to  $\mathbf{P}_p^{\text{diel}}$ , the term  $\mathbf{P}_p^{\text{phon}}$  results directly from the strain that is caused by the lattice vibrations. The polarization density  $\mathbf{P}_p^{\text{phon}}$  is related to the strain tensor elements via

$$P_{p,i}^{\text{phon}} = \sum_{j,k} h_{ijk} \epsilon_{jk}, \quad (\text{E.65})$$

where the  $h_{ijk}$  are the elements of the third-rank piezoelectric tensor. In zinc blende structures such as GaAs, the  $h_{ijk}$  take on a rather simple form

$$h_{ijk} = h_{14} |\varepsilon_{ijk}| = \begin{cases} h_{14} & \text{for } |\varepsilon_{ijk}| = 1, \\ 0 & \text{for } |\varepsilon_{ijk}| = 0. \end{cases} \quad (\text{E.66})$$

Here  $\varepsilon_{ijk}$  is the Levi-Civita symbol, and the  $x_i$ ,  $x_j$ , and  $x_k$  related to the indices  $i$ ,  $j$ , and  $k$ , respectively, correspond to the main crystallographic axes.

We now proceed to calculate the electric field  $\mathbf{E}_p$  via the relation [17]

$$\mathbf{E}_p = -\frac{\mathbf{P}_p^{\text{phon}}}{\epsilon_0 \epsilon_r}, \quad (\text{E.67})$$

which results directly from Eq. (E.64). In order to improve readability, we use a shorthand notation in the remainder of this subsection for convenience:  $x$ ,  $y$ , and  $z$  correspond to the coordinates along the main crystallographic axes, with  $\mathbf{e}_x$ ,  $\mathbf{e}_y$ , and  $\mathbf{e}_z$  as the unit vectors along the [100], [010], and [001] directions, respectively. Substitution of Eqs. (E.59), (E.62), (E.65), and (E.66) into Eq. (E.67) yields

$$\mathbf{E}_p = -\frac{ih_{14}}{\epsilon_0 \epsilon_r} \sum_{\mathbf{q},s} \begin{pmatrix} q_y e_{\mathbf{q}s}^z + q_z e_{\mathbf{q}s}^y \\ q_z e_{\mathbf{q}s}^x + q_x e_{\mathbf{q}s}^z \\ q_x e_{\mathbf{q}s}^y + q_y e_{\mathbf{q}s}^x \end{pmatrix} \sqrt{\frac{\hbar}{2\rho V \omega_{\mathbf{q}s}}} \left( a_{\mathbf{q}s} \mp_s a_{-\mathbf{q}s}^\dagger \right) e^{i\mathbf{q}\cdot\mathbf{r}},$$

where

$$\mathbf{q} = q_x \mathbf{e}_x + q_y \mathbf{e}_y + q_z \mathbf{e}_z, \quad (\text{E.68})$$

$$\mathbf{e}_{\mathbf{q}s} = e_{\mathbf{q}s}^x \mathbf{e}_x + e_{\mathbf{q}s}^y \mathbf{e}_y + e_{\mathbf{q}s}^z \mathbf{e}_z, \quad (\text{E.69})$$

and the three components of the vector refer to the basis  $\{\mathbf{e}_x, \mathbf{e}_y, \mathbf{e}_z\}$ . The phonon-induced electric field

$\mathbf{E}_p$  can be split into two parts,

$$\mathbf{E}_p = \mathbf{E}_p^{\parallel} + \mathbf{E}_p^{\perp}, \quad (\text{E.70})$$

where the ‘‘longitudinal’’ part

$$\mathbf{E}_p^{\parallel} = -\frac{i\hbar_{14}}{\epsilon_0\epsilon_r} \sum_{\mathbf{q},s} \frac{2(q_x q_y e_{\mathbf{q}s}^z + q_y q_z e_{\mathbf{q}s}^x + q_z q_x e_{\mathbf{q}s}^y)}{q^2} \mathbf{q} \sqrt{\frac{\hbar}{2\rho V \omega_{\mathbf{q}s}}} (a_{\mathbf{q}s} \mp_s a_{-\mathbf{q}s}^{\dagger}) e^{i\mathbf{q}\cdot\mathbf{r}} \quad (\text{E.71})$$

contains the contributions parallel to  $\mathbf{q}$  for each mode, while the ‘‘transverse’’ part  $\mathbf{E}_p^{\perp} = \mathbf{E}_p - \mathbf{E}_p^{\parallel}$  comprises the remaining components perpendicular to  $\mathbf{q}$ . The longitudinal and transverse parts fulfill

$$\nabla \times \mathbf{E}_p^{\parallel} = 0, \quad (\text{E.72})$$

$$\nabla \cdot \mathbf{E}_p^{\perp} = 0, \quad (\text{E.73})$$

respectively. As a consequence, one can write  $\mathbf{E}_p^{\parallel}$  as the gradient of a scalar potential  $\Phi_p$ , and  $\mathbf{E}_p^{\perp}$  as the curl of a vector potential  $\mathbf{A}_p$ ,

$$\mathbf{E}_p^{\parallel} = -\nabla\Phi_p, \quad (\text{E.74})$$

$$\mathbf{E}_p^{\perp} = \nabla \times \mathbf{A}_p. \quad (\text{E.75})$$

From Eqs. (E.71) and (E.74), one finds

$$\Phi_p = \frac{\hbar_{14}}{\epsilon_0\epsilon_r} \sum_{\mathbf{q},s} f_{\mathbf{q}s} \sqrt{\frac{\hbar}{2\rho V \omega_{\mathbf{q}s}}} (a_{\mathbf{q}s} \mp_s a_{-\mathbf{q}s}^{\dagger}) e^{i\mathbf{q}\cdot\mathbf{r}} \quad (\text{E.76})$$

for the scalar potential, where we introduced

$$f_{\mathbf{q}s} = \frac{2(q_x q_y e_{\mathbf{q}s}^z + q_y q_z e_{\mathbf{q}s}^x + q_z q_x e_{\mathbf{q}s}^y)}{q^2}. \quad (\text{E.77})$$

The vector potential  $\mathbf{A}_p$  and, hence, the transverse part  $\mathbf{E}_p^{\perp}$  are usually omitted for the piezoelectric electron-phonon interaction. Reasons for this omission may be inferred from Maxwell’s equations.

In accordance with common practice, we neglect the vector potential  $\mathbf{A}_p$  in the following and consider only the scalar potential  $\Phi_p$ . Using an explicit representation for the unit vectors  $\mathbf{e}_{\mathbf{q}s}$ , the result from Eq. (E.76) can be simplified further. We choose

$$\mathbf{e}_{\mathbf{q}l} = \frac{\mathbf{q}}{q} = \begin{pmatrix} \cos\phi_{\mathbf{q}} \sin\theta_{\mathbf{q}} \\ \sin\phi_{\mathbf{q}} \sin\theta_{\mathbf{q}} \\ \cos\theta_{\mathbf{q}} \end{pmatrix}, \quad \mathbf{e}_{\mathbf{q}t_1} = \begin{pmatrix} \sin\phi_{\mathbf{q}} \\ -\cos\phi_{\mathbf{q}} \\ 0 \end{pmatrix}, \quad \mathbf{e}_{\mathbf{q}t_2} = \begin{pmatrix} \cos\phi_{\mathbf{q}} \cos\theta_{\mathbf{q}} \\ \sin\phi_{\mathbf{q}} \cos\theta_{\mathbf{q}} \\ -\sin\theta_{\mathbf{q}} \end{pmatrix}, \quad (\text{E.78})$$

in agreement with Eqs. (E.56) to (E.58), where  $0 \leq \phi_{\mathbf{q}} < 2\pi$  is the azimuthal angle and  $0 \leq \theta_{\mathbf{q}} \leq \pi$  is the polar angle of  $\mathbf{q}$  in spherical coordinates. Again, the vector components in Eq. (E.78) refer to the basis  $\{\mathbf{e}_x, \mathbf{e}_y, \mathbf{e}_z\}$ , i.e., to the unit vectors for the main crystallographic directions (note the special definition of  $x$ ,  $y$ , and  $z$  in this subsection). Also, we note that the  $\{\mathbf{e}_{\mathbf{q}l}, \mathbf{e}_{\mathbf{q}t_1}, \mathbf{e}_{\mathbf{q}t_2}\}$  defined above form a right-handed, orthonormal set of basis vectors for any  $\mathbf{q}$ . With this convenient representation, which is similar to the one chosen in Ref. [18], the expression  $f_{\mathbf{q}s}$  from Eq. (E.77) simplifies to

$$f_{\mathbf{q}l} = 3 \cos\theta_{\mathbf{q}} \sin^2\theta_{\mathbf{q}} \sin(2\phi_{\mathbf{q}}), \quad (\text{E.79})$$

$$f_{\mathbf{q}t_1} = -\sin(2\theta_{\mathbf{q}}) \cos(2\phi_{\mathbf{q}}), \quad (\text{E.80})$$

$$f_{\mathbf{q}t_2} = -(3 \sin^2\theta_{\mathbf{q}} - 2) \sin\theta_{\mathbf{q}} \sin(2\phi_{\mathbf{q}}), \quad (\text{E.81})$$



where we mention that trigonometric identities allow one to rewrite the above relations in many different ways. Finally, the potential energy of an electron in the phonon-induced electric field, i.e., the Hamiltonian for the piezoelectric electron-phonon coupling, corresponds to

$$H_{\text{pe}} = -e\Phi_p, \quad (\text{E.82})$$

where  $-e$  is the charge of the electron.

## E.2.7 Phonon Bath

The Hamiltonian for the phonon bath is

$$H_{\text{ph}} = \sum_{\mathbf{q},s} \hbar\omega_{\mathbf{q}s} \left( a_{\mathbf{q}s}^\dagger a_{\mathbf{q}s} + \frac{1}{2} \right), \quad (\text{E.83})$$

where the sum runs again over all modes  $s$  and all wave vectors  $\mathbf{q}$  within the first Brillouin zone.

## E.3 Model Hamiltonian at Small Detuning

As described in detail in Chapter 6, we study the lifetimes of the singlet-triplet qubit at both small and large detuning  $\epsilon$ . In this appendix, we explain the details of our model at small detunings  $\epsilon \simeq 0$ .

### E.3.1 Exchange Energy and Orbital Level Spacing

In the unbiased DQD, the energy of  $|(0,2)S\rangle$  and  $|(2,0)S\rangle$  is much larger than that of  $(1^*,1)$ -type states with an excited orbital part. This allows us to calculate the lifetimes with an  $8 \times 8$  matrix [see Eq. (E.90)] that is based on states of type  $(1,1)$  and  $(1^*,1)$  only. Even though  $|(0,2)S\rangle$  and  $|(2,0)S\rangle$  are not part of the basis, their presence can be accounted for as described below.

Considering the basis states introduced in Appendix E.1 and shifting the energy globally by

$$\langle (1,1)T_0 | (H_0^{(1)} + H_0^{(2)} + H_C) | (1,1)T_0 \rangle,$$

the Hamiltonian  $H_0^{(1)} + H_0^{(2)} + H_C$  can be approximated via

$$H_0^{(1)} + H_0^{(2)} + H_C \approx -J_S |(1,1)S\rangle \langle (1,1)S| + \Delta E (|\Psi_+^e\rangle \langle \Psi_+^e| + |\Psi_-^e\rangle \langle \Psi_-^e|), \quad (\text{E.84})$$

where the exchange energy  $J_S$  results from admixtures with  $|(0,2)S\rangle$  and  $|(2,0)S\rangle$ . The energy gap  $\Delta E \simeq \hbar\omega_0$  is well described by the level spacing  $\hbar\omega_0$  in the left QD and corresponds to the energy difference between the four states of lowest energy in the DQD and the states with excited orbital part.

We note that  $J_S$  can be estimated [1, 3, 4] by projecting  $H_0^{(1)} + H_0^{(2)} + H_C$  onto the subspace  $\{|(2,0)S\rangle, |(0,2)S\rangle, |(1,1)S\rangle\}$  through a projector  $\mathcal{P}_{S3}$ , which yields the Hamiltonian

$$H_{S3} = \mathcal{P}_{S3} (H_0^{(1)} + H_0^{(2)} + H_C) \mathcal{P}_{S3} \quad (\text{E.85})$$

with matrix representation

$$H_{S3} = \begin{pmatrix} U - V_- & 0 & -\sqrt{2}t \\ 0 & U - V_- & -\sqrt{2}t \\ -\sqrt{2}t & -\sqrt{2}t & V_+ - V_- \end{pmatrix}. \quad (\text{E.86})$$

Here,

$$t = -\langle \Phi_L | H_0 | \Phi_R \rangle - \frac{1}{\sqrt{2}} \langle \Psi_+ | H_C | \Psi_R \rangle \quad (\text{E.87})$$

is the hopping amplitude (also referred to as the tunnel coupling),  $U = \langle \Psi_R | H_C | \Psi_R \rangle$  is the on-site repulsion,  $V_{\pm} = \langle \Psi_{\pm} | H_C | \Psi_{\pm} \rangle$ , and the energy was globally shifted as mentioned before. Diagonalization of  $H_{S3}$  results in

$$\tilde{H}_{S3} = U_{S3}^{\dagger} H_{S3} U_{S3} = \begin{pmatrix} U - 2V_- + V_+ + J_S & 0 & 0 \\ 0 & U - V_- & 0 \\ 0 & 0 & -J_S \end{pmatrix}, \quad (\text{E.88})$$

where  $U_{S3}$  is the matrix for the unitary transformation and

$$J_S = \frac{1}{2} \left( \sqrt{16t^2 + (U - V_+)^2} - U - V_+ + 2V_- \right) \quad (\text{E.89})$$

is the resulting exchange splitting between  $|(1, 1)S\rangle$  and  $|(1, 1)T_0\rangle$ . Considering  $\epsilon \simeq 0$ , the formulas for  $J_S$  and  $U_{S3}$  from this estimate allow us to account for admixtures of  $|(2, 0)S\rangle$  and  $|(0, 2)S\rangle$  to the qubit state of type  $|(1, 1)S\rangle$  and, consequently, to study the effects of these admixtures on the phonon-induced lifetimes of the qubit.

### E.3.2 Matrix Representation

We analyze the qubit lifetimes in an unbiased DQD by projecting the Hamiltonian  $\tilde{H}$ , Eq. (E.42), onto the basis  $\{|(1, 1)S\rangle, |(1, 1)T_0\rangle, |(1, 1)T_+\rangle, |(1, 1)T_-\rangle, |(1^*, 1)S\rangle, |(1^*, 1)T_+\rangle, |(1^*, 1)T_0\rangle, |(1^*, 1)T_-\rangle\}$ . The basis states are described in detail in Appendix E.1, and the projection yields

$$\tilde{H} = \begin{pmatrix} -J_S + P_{SS} & \frac{\delta b_B}{2} & \frac{\Omega}{\sqrt{2}} & -\frac{\Omega}{\sqrt{2}} & P_{cr}^e & \frac{\Omega_1}{\sqrt{2}} & 0 & -\frac{\Omega_1}{\sqrt{2}} \\ \frac{\delta b_B}{2} & P_T & 0 & 0 & 0 & -\frac{\Omega_1}{\sqrt{2}} & P_{cr}^e & -\frac{\Omega_1}{\sqrt{2}} \\ \frac{\Omega}{\sqrt{2}} & 0 & E_Z + P_T & 0 & \frac{\Omega_1}{\sqrt{2}} & P_{cr}^e & -\frac{\Omega_1}{\sqrt{2}} & 0 \\ -\frac{\Omega}{\sqrt{2}} & 0 & 0 & -E_Z + P_T & -\frac{\Omega_1}{\sqrt{2}} & 0 & -\frac{\Omega_1}{\sqrt{2}} & P_{cr}^e \\ P_{cr}^{e\dagger} & 0 & \frac{\Omega_1}{\sqrt{2}} & -\frac{\Omega_1}{\sqrt{2}} & \Delta E + P^e & \frac{\Omega_2}{\sqrt{2}} & 0 & -\frac{\Omega_2}{\sqrt{2}} \\ \frac{\Omega_1}{\sqrt{2}} & -\frac{\Omega_1}{\sqrt{2}} & P_{cr}^{e\dagger} & 0 & \frac{\Omega_2}{\sqrt{2}} & \Delta E + E_Z + P^e & -\frac{\Omega_3}{\sqrt{2}} & 0 \\ 0 & P_{cr}^{e\dagger} & -\frac{\Omega_1}{\sqrt{2}} & -\frac{\Omega_1}{\sqrt{2}} & 0 & -\frac{\Omega_3}{\sqrt{2}} & \Delta E + P^e & -\frac{\Omega_3}{\sqrt{2}} \\ -\frac{\Omega_1}{\sqrt{2}} & -\frac{\Omega_1}{\sqrt{2}} & 0 & P_{cr}^{e\dagger} & -\frac{\Omega_2}{\sqrt{2}} & 0 & -\frac{\Omega_3}{\sqrt{2}} & \Delta E - E_Z + P^e \end{pmatrix} + H_{\text{ph}}. \quad (\text{E.90})$$

Here the  $\Omega$  with different indices quantify the matrix elements resulting from the SOI. Defining

$$R_{\text{SOI}} = (\mathbf{r}_{\text{SOI}} \times \mathbf{e}_B)_z, \quad (\text{E.91})$$

one obtains

$$\Omega = E_Z (\langle \Phi_L | R_{\text{SOI}} | \Phi_L \rangle - \langle \Phi_R | R_{\text{SOI}} | \Phi_R \rangle), \quad (\text{E.92})$$

$$\Omega_1 = E_Z \langle \Phi_L | R_{\text{SOI}} | \Phi_L^{e,\nu} \rangle, \quad (\text{E.93})$$

$$\Omega_2 = E_Z (\langle \Phi_L^{e,\nu} | R_{\text{SOI}} | \Phi_L^{e,\nu} \rangle - \langle \Phi_R | R_{\text{SOI}} | \Phi_R \rangle), \quad (\text{E.94})$$

$$\Omega_3 = E_Z (\langle \Phi_L^{e,\nu} | R_{\text{SOI}} | \Phi_L^{e,\nu} \rangle + \langle \Phi_R | R_{\text{SOI}} | \Phi_R \rangle). \quad (\text{E.95})$$

Analogously, the electron-phonon coupling is denoted by  $P$  with different labels,

$$P_T = \langle \Phi_R | H_{\text{el-ph}} | \Phi_R \rangle + \langle \Phi_L | H_{\text{el-ph}} | \Phi_L \rangle, \quad (\text{E.96})$$

$$P^e = \langle \Phi_L^{e,\nu} | H_{\text{el-ph}} | \Phi_L^{e,\nu} \rangle + \langle \Phi_R | H_{\text{el-ph}} | \Phi_R \rangle, \quad (\text{E.97})$$

$$P_{cr}^e = \langle \Phi_L | H_{\text{el-ph}} | \Phi_L^{e,\nu} \rangle. \quad (\text{E.98})$$

The above expressions for  $\Omega_1$ ,  $\Omega_2$ ,  $\Omega_3$ ,  $P^e$ , and  $P_{cr}^e$  correspond to  $\Psi_{\pm}^e = \Psi_{\pm}^{e,\nu}$ , for which the orbital excitation is chosen along the axis  $\nu \in \{x, y\}$ .

In order to account for the finite admixtures from the states  $|(0, 2)S\rangle$  and  $|(2, 0)S\rangle$ , we set the matrix element  $\langle (1, 1)S | (H_{\text{el-ph}}^{(1)} + H_{\text{el-ph}}^{(2)}) | (1, 1)S \rangle$  of the electron-phonon interaction to  $P_{SS}$ . The latter is a linear combination of  $P_{SL}$ ,  $P_{SR}$ ,  $P_S$ , and  $P_S^\dagger$ , where

$$P_{SL} = 2\langle \Phi_L | H_{\text{el-ph}} | \Phi_L \rangle, \quad (\text{E.99})$$

$$P_{SR} = 2\langle \Phi_R | H_{\text{el-ph}} | \Phi_R \rangle, \quad (\text{E.100})$$

$$P_S = \sqrt{2}\langle \Phi_R | H_{\text{el-ph}} | \Phi_L \rangle. \quad (\text{E.101})$$

The coefficients of the linear combination depend on  $U$ ,  $V_+$ ,  $V_-$ , and  $t$ . We find these coefficients by projecting  $H_{\text{el-ph}}^{(1)} + H_{\text{el-ph}}^{(2)}$  onto the subspace  $\{|(2, 0)S\rangle, |(0, 2)S\rangle, |(1, 1)S\rangle\}$ ,

$$\mathcal{P}_{S3}(H_{\text{el-ph}}^{(1)} + H_{\text{el-ph}}^{(2)})\mathcal{P}_{S3} = \begin{pmatrix} P_{SL} & 0 & P_S^\dagger \\ 0 & P_{SR} & P_S \\ P_S & P_S^\dagger & P_T \end{pmatrix}, \quad (\text{E.102})$$

which allows calculation of  $P_{SS}$  via

$$P_{SS} = \left( U_{S3}^\dagger \mathcal{P}_{S3} (H_{\text{el-ph}}^{(1)} + H_{\text{el-ph}}^{(2)}) \mathcal{P}_{S3} U_{S3} \right)_{33}. \quad (\text{E.103})$$

For further information on the transformation matrix  $U_{S3}$ , see Appendix E.3.1.

We note, however, that the above-mentioned contributions from  $|(2, 0)S\rangle$  and  $|(0, 2)S\rangle$  to  $P_{SS}$  turn out to be negligibly small, because setting  $P_{SS} = P_T$  does not affect the lifetimes in our calculations. Furthermore, two-phonon processes based on admixtures from  $|(2, 0)S\rangle$  and  $|(0, 2)S\rangle$  are strongly suppressed at  $\epsilon \simeq 0$  and can be omitted, as we explain in detail in Appendix E.8. In conclusion, we find for the parameters in this work that the qubit lifetimes in unbiased DQDs are determined by the basis states with excited orbital parts. The corrections from  $|(2, 0)S\rangle$  and  $|(0, 2)S\rangle$  are negligible.

## E.4 Model Hamiltonian at Large Detuning

When  $|\epsilon| \sim U - V_{\pm}$  such that the energy gap between the qubit and either  $|(2, 0)S\rangle$  (negative  $\epsilon$ ) or  $|(0, 2)S\rangle$  (positive  $\epsilon$ ) is smaller than the orbital level spacing,  $0 < U - V_{\pm} - |\epsilon| < \hbar\omega_0$ , the effects of higher orbitals on the lifetimes are negligible. In the regime of large detuning, we therefore project  $\tilde{H}$ , Eq. (E.42), onto the basis  $\{|(1, 1)T_0\rangle, |(1, 1)S\rangle, |(1, 1)T_+\rangle, |(1, 1)T_-\rangle, |(0, 2)S\rangle, |(2, 0)S\rangle\}$  and investigate the lifetimes via this  $6 \times 6$  matrix. The explicit form of the matrix is shown in Eq. (6.12) of Chapter 6, and details for all its matrix elements are provided in Appendix E.3.

## E.5 Bloch-Redfield Theory

Having identified a suitable matrix representation for small and large detunings, we apply a unitary transformation to  $\tilde{H}$  that diagonalizes  $\tilde{H} - \sum_{j=1,2} H_{\text{el-ph}}^{(j)}$  exactly. In order to decouple the qubit subspace

$\{|(1,1)S\rangle, |(1,1)T_0\rangle\}$  perturbatively from the remaining states, we then perform a third-order Schrieffer-Wolff transformation, leading to corrections up to the third power in the electron-phonon coupling. The perturbation theory applies when the matrix elements for the electron-phonon coupling are smaller than the energy separation between the qubit and the other states.

The resulting effective Hamiltonian  $H_{\text{eff}} = H_{\text{q}} + H_{\text{q-ph}} + H_{\text{ph}}$  for the  $S$ - $T_0$  qubit, its interaction with the phonon bath, and the bath itself can be described in terms of a coupled spin-1/2 system and allows application of the Bloch-Redfield theory [7, 24, 25]. Introducing the effective magnetic fields  $\mathbf{B}_{\text{eff}}$  and  $\delta\mathbf{B}$ , we write the Hamiltonian of the qubit as

$$H_{\text{q}} = \frac{1}{2}g\mu_B\mathbf{B}_{\text{eff}} \cdot \boldsymbol{\sigma}', \quad (\text{E.104})$$

and the Hamiltonian for the interaction between the qubit and the phonon bath reads

$$H_{\text{q-ph}}(\tau) = \frac{1}{2}g\mu_B\delta\mathbf{B}(\tau) \cdot \boldsymbol{\sigma}'. \quad (\text{E.105})$$

Here  $\boldsymbol{\sigma}'$  is the vector of spin-1/2 Pauli matrices for the  $S$ - $T_0$  qubit,  $\tau$  is the time, and the time-dependent  $H_{\text{q-ph}}(\tau)$  is written in the interaction representation,

$$H_{\text{q-ph}}(\tau) = e^{iH_{\text{ph}}\tau/\hbar}H_{\text{q-ph}}e^{-iH_{\text{ph}}\tau/\hbar}. \quad (\text{E.106})$$

Next, following Refs. [7, 25], we define the spectral functions

$$J_{ij}(\omega) = \frac{g^2\mu_B^2}{2\hbar^2} \int_0^\infty e^{-i\omega\tau} \langle \delta B_i(0)\delta B_j(\tau) \rangle d\tau, \quad (\text{E.107})$$

where the temperature-dependent correlators  $\langle \delta B_i(0)\delta B_j(\tau) \rangle$  with  $i, j \in \{x, y, z\}$  are calculated for a phonon bath in thermal equilibrium. More precisely, we assume that the density matrix  $\rho_{\text{ph}}$  that describes the mixed state of the phonon bath is diagonal when represented via standard Fock states for the phonons considered here (i.e., occupation numbers referring to acoustic phonons classified by the wave vectors  $\mathbf{q}$  and modes  $s$ ), with the probabilities on the diagonal provided by Boltzmann statistics. The correlator  $\langle \delta B_i(0)\delta B_j(\tau) \rangle$  corresponds to the expectation value of the operator  $\delta B_i(0)\delta B_j(\tau)$  and, thus, is equal to the trace of  $\rho_{\text{ph}}\delta B_i(0)\delta B_j(\tau)$ . In particular, one obtains  $\langle a_{\mathbf{q}s}^\dagger a_{\mathbf{q}'s'} \rangle = \delta_{\mathbf{q},\mathbf{q}'}\delta_{s,s'}n_B(\omega_{\mathbf{q}s})$ , where

$$n_B(\omega) = \frac{1}{e^{\hbar\omega/(k_B T)} - 1} \quad (\text{E.108})$$

is the Bose-Einstein distribution,  $k_B$  is the Boltzmann constant, and  $T$  is the temperature.

Using the formulas (C16) and (C25)–(C27) from Ref. [25], it is possible to express the lifetimes of the qubit in terms of the above-mentioned spectral functions. For convenience, we define the basis of  $\boldsymbol{\sigma}'$  such that only the  $z$  component of the effective magnetic field  $\mathbf{B}_{\text{eff}}$  is nonzero. In this case, the lifetimes depend solely on the quantities

$$J_{ii}^+(\omega) = \text{Re}[J_{ii}(\omega) + J_{ii}(-\omega)] = \frac{g^2\mu_B^2}{2\hbar^2} \int_{-\infty}^\infty \cos(\omega\tau) \langle \delta B_i(0)\delta B_i(\tau) \rangle d\tau. \quad (\text{E.109})$$

The last equality holds because the  $\delta B_i(\tau)$  are Hermitian and the correlators are time-translational invariant. We finally calculate the relaxation time  $T_1$  of the qubit via

$$\frac{1}{T_1} = J_{xx}^+(\omega_Z) + J_{yy}^+(\omega_Z), \quad (\text{E.110})$$

where  $\hbar\omega_Z = |g\mu_B\mathbf{B}_{\text{eff}}|$  is the effective Zeeman splitting. The time  $T_\phi$  that accounts for pure dephasing

is obtained through

$$\frac{1}{T_\varphi} = J_{zz}^+(0), \quad (\text{E.111})$$

and the decoherence time  $T_2$  can then be expressed in terms of  $T_1$  and  $T_\varphi$ ,

$$\frac{1}{T_2} = \frac{1}{2T_1} + \frac{1}{T_\varphi}. \quad (\text{E.112})$$

Considering one- and two-phonon processes in our calculations, the third-order contribution to  $\delta B_i(0)$  [ $\delta B_i(\tau)$ ] enters the correlator  $\langle \delta B_i(0)\delta B_i(\tau) \rangle$  in Eq. (E.109) together with the first-order contribution to  $\delta B_i(\tau)$  [ $\delta B_i(0)$ ]. As a consequence, the third-order terms in  $\delta \mathbf{B}$  cannot contribute to the dephasing rate  $1/T_\varphi$  (see also Appendix E.7). Furthermore, we expect only a negligible effect on the relaxation rate  $1/T_1$ , as the rates that arise from third-order corrections can be considered small compared to those from single-phonon processes that are based solely on the first-order terms. For simplicity, the third-order contributions to  $\delta \mathbf{B}$  are therefore omitted in the calculations for Figs. 6.2 to 6.6 in Chapter 6.

## E.6 Continuum Limit

For the investigation of the phonon-induced lifetimes of the qubit, we consider the continuum limit and replace the summation over the phonon wave vectors  $\mathbf{q}$  by an integral. Furthermore, the low temperatures discussed here allow integration up to infinite  $q$ , because the effects resulting from terms with wave vectors outside the first Brillouin zone are clearly negligible. We therefore substitute

$$\sum_{\mathbf{q}} \rightarrow \frac{V}{(2\pi)^3} \int_0^\infty dq q^2 \int_0^\pi d\theta_{\mathbf{q}} \sin \theta_{\mathbf{q}} \int_0^{2\pi} d\phi_{\mathbf{q}} \quad (\text{E.113})$$

in our calculations. For details of the electron-phonon interaction, see Appendix E.2.6.

## E.7 Simple Model for Dephasing at Large Detuning

As discussed in Sec. 6.3.4 of Chapter 6, the relevant dynamics at  $0 < U - V_\pm - \epsilon < \hbar\omega_0$  and  $\Omega = 0$  is very well described by the Hamiltonian

$$\tilde{H} = \begin{pmatrix} 0 & \frac{\delta b_B}{2} & 0 \\ \frac{\delta b_B}{2} & V_+ - V_- & -\sqrt{2}t + P_S^\dagger \\ 0 & -\sqrt{2}t + P_S & V_+ - V_- + \Delta_S + \tilde{P} \end{pmatrix} + H_{\text{ph}} \quad (\text{E.114})$$

with basis states  $|(1, 1)T_0\rangle$ ,  $|(1, 1)S\rangle$ , and  $|(0, 2)S\rangle$ . Compared to Eq. (6.12), we omitted here the decoupled states  $|(1, 1)T_+\rangle$ ,  $|(1, 1)T_-\rangle$ , and  $|(2, 0)S\rangle$ , subtracted  $P_T$  from the diagonal (global shift, no effect on the lifetimes), and introduced

$$\tilde{P} = P_{SR} - P_T \quad (\text{E.115})$$

as a matrix element for the electron-phonon coupling and

$$\Delta_S = U - V_+ - \epsilon \quad (\text{E.116})$$

as the bare splitting between  $|(1, 1)S\rangle$  and  $|(0, 2)S\rangle$ .

The hyperfine coupling ( $\delta_B$ ) is the only mechanism in Eq. (E.114) that couples the spin states and, hence, is crucial for the relaxation of the  $S$ - $T_0$  qubit. In fact, we find for the parameters in this work that the relaxation times  $T_1$  are mainly determined by the hyperfine coupling rather than the SOI. In

order to derive a simple model for the short decoherence times [ $T_2 \ll T_1$ , Fig. 6.2a], we neglect  $\delta_B$  in the following, resulting in pure dephasing, and so  $T_2 = T_\varphi$ . Furthermore, we find that the matrix element  $P_S$  is negligible for our parameter range. Defining

$$\tilde{H} = H_s + H_{s\text{-ph}} + H_{\text{ph}} \quad (\text{E.117})$$

and omitting  $\delta_B$  and  $P_S$ , one obtains

$$H_s = \begin{pmatrix} 0 & 0 & 0 \\ 0 & V_+ - V_- & -\sqrt{2}t \\ 0 & -\sqrt{2}t & V_+ - V_- + \Delta_S \end{pmatrix} \quad (\text{E.118})$$

for the part that describes the electronic system, and

$$H_{s\text{-ph}} = \begin{pmatrix} 0 & 0 & 0 \\ 0 & 0 & 0 \\ 0 & 0 & \tilde{P} \end{pmatrix} \quad (\text{E.119})$$

for the interaction with the phonon bath.

The Hamiltonians  $H_s$  and  $H_{s\text{-ph}}$  can be rewritten in a different basis  $\{|(1,1)T_0\rangle, |(1,1)S'\rangle, |(0,2)S'\rangle\}$  as

$$H_s = \begin{pmatrix} 0 & 0 & 0 \\ 0 & -J_{\text{tot}} & 0 \\ 0 & 0 & -J_{\text{tot}} + \Delta'_S \end{pmatrix} \quad (\text{E.120})$$

and

$$H_{s\text{-ph}} = \tilde{P} \begin{pmatrix} 0 & 0 & 0 \\ 0 & v_{s'd}^2 & v_{s'd}v_{d'd} \\ 0 & v_{s'd}v_{d'd} & v_{d'd}^2 \end{pmatrix}, \quad (\text{E.121})$$

where

$$\Delta'_S = \sqrt{\Delta_S^2 + 8t^2} \quad (\text{E.122})$$

and

$$J_{\text{tot}} = V_- - V_+ + \frac{\Delta'_S - \Delta_S}{2}. \quad (\text{E.123})$$

The basis states

$$|(1,1)S'\rangle = v_{s's} |(1,1)S\rangle + v_{s'd} |(0,2)S\rangle, \quad (\text{E.124})$$

$$|(0,2)S'\rangle = v_{d's} |(1,1)S\rangle + v_{d'd} |(0,2)S\rangle \quad (\text{E.125})$$

are normalized eigenstates of  $H_s$ . The notation  $|(1,1)S'\rangle$  and  $|(0,2)S'\rangle$  is justified because we consider  $\Delta_S > 0$ , and so  $|v_{s's}|^2 > 1/2$  and  $|v_{d'd}|^2 > 1/2$ . In Eq. (E.121),  $v_{s'd}$  and  $v_{d'd}$  are assumed to be real. A suitable choice for the coefficients is, e.g.,

$$v_{s's} = \frac{\Delta_S + \Delta'_S}{D_+}, \quad (\text{E.126})$$

$$v_{s'd} = \frac{2\sqrt{2}t}{D_+}, \quad (\text{E.127})$$

$$v_{d's} = \frac{\Delta_S - \Delta'_S}{D_-}, \quad (\text{E.128})$$

$$v_{d'd} = \frac{2\sqrt{2}t}{D_-}, \quad (\text{E.129})$$

where the denominator

$$D_{\pm} = \sqrt{(\Delta_S \pm \Delta'_S)^2 + 8t^2} \quad (\text{E.130})$$

ensures normalization.

Following the steps explained in Appendix E.5, one finds

$$g\mu_B B_{\text{eff},z} = J_{\text{tot}} \quad (\text{E.131})$$

and

$$g\mu_B \delta B_z = -v_{s'd}^2 \tilde{P} + \frac{v_{s'd}^2 v_{d'd}^2}{\Delta'_S} \tilde{P}^2 + \frac{v_{s'd}^2 v_{d'd}^2 (v_{s'd}^2 - v_{d'd}^2)}{(\Delta'_S)^2} \tilde{P}^3 \quad (\text{E.132})$$

from the third-order Schrieffer-Wolff transformation. We recall that  $\delta B_x = 0 = \delta B_y$  due to omission of the hyperfine coupling, and so  $T_2 = T_{\varphi}$  (pure dephasing). Furthermore, we note that the Bloch-Redfield theory requires  $\langle \delta \mathbf{B}(\tau) \rangle$  to vanish [24]. Therefore, terms of type  $a_{\mathbf{q}s}^{\dagger} a_{\mathbf{q}s}$  and  $a_{\mathbf{q}s} a_{\mathbf{q}s}^{\dagger}$  must be removed from the second-order contributions to  $\delta \mathbf{B}$  and, consequently, from the part  $\propto \tilde{P}^2$  in Eq. (E.132). The terms removed from  $\delta \mathbf{B}$  can be considered as minor corrections to  $\mathbf{B}_{\text{eff}}$ , with  $a_{\mathbf{q}s}^{\dagger} a_{\mathbf{q}s} \rightarrow n_B(\omega_{\mathbf{q}s})$  and  $a_{\mathbf{q}s} a_{\mathbf{q}s}^{\dagger} \rightarrow n_B(\omega_{\mathbf{q}s}) + 1$ , where  $n_B(\omega)$  is the Bose-Einstein distribution [Eq. (E.108)]. In this work, we simply neglect these corrections to  $\mathbf{B}_{\text{eff}}$  because of their smallness.

The decoherence time  $T_2 = T_{\varphi}$  is calculated via

$$\frac{1}{T_2} = \frac{g^2 \mu_B^2}{2\hbar^2} \int_{-\infty}^{\infty} \langle \delta B_z(0) \delta B_z(\tau) \rangle d\tau, \quad (\text{E.133})$$

see Appendix E.5. Remarkably, the only nonzero contribution after insertion of Eq. (E.132) into Eq. (E.133) is

$$\frac{1}{T_2} = \frac{v_{s'd}^4 v_{d'd}^4}{2\hbar^2 (\Delta'_S)^2} \int_{-\infty}^{\infty} \langle \tilde{P}^2(0) \tilde{P}^2(\tau) \rangle d\tau. \quad (\text{E.134})$$

In particular, one finds that single-phonon processes cannot lead to dephasing,

$$\int_{-\infty}^{\infty} \langle \tilde{P}(0) \tilde{P}(\tau) \rangle d\tau = 0. \quad (\text{E.135})$$

As there is no energy transfer between the electrons and the phonon bath [evaluation of  $J_{zz}^+(\omega)$  at  $\omega = 0$ ], the left-hand side of Eq. (E.135) can only be nonzero for a phonon with  $\omega_{\mathbf{q}s} = 0 = q$ , for which, however, the expression vanishes as well. An analogous explanation applies to

$$\int_{-\infty}^{\infty} \langle \tilde{P}^3(0) \tilde{P}(\tau) \rangle d\tau = 0 = \int_{-\infty}^{\infty} \langle \tilde{P}(0) \tilde{P}^3(\tau) \rangle d\tau. \quad (\text{E.136})$$

Consequently, the dephasing in our model results purely from two-phonon processes that are based on the second-order contributions to  $\delta B_z$ .

Finally, using Eqs. (E.127) and (E.129) in Eq. (E.134) yields

$$\frac{1}{T_2} = \frac{2t^4}{\hbar^2 (\Delta'_S)^6} \int_{-\infty}^{\infty} \langle \tilde{P}^2(0) \tilde{P}^2(\tau) \rangle d\tau. \quad (\text{E.137})$$

We note that in the case of  $|t| \ll \Delta_S$  and negligibly small  $V_+ - V_-$ , one finds  $J_{\text{tot}} \simeq 2t^2/\Delta'_S$  in this model and

$$\frac{2t^4}{\hbar^2 (\Delta'_S)^6} \simeq \frac{J_{\text{tot}}^2}{2\hbar^2 (\Delta'_S)^4} \quad (\text{E.138})$$

for the prefactor.

## E.8 Dephasing via Singlet States at Small Detuning

In order to estimate the dephasing due to the states  $|(2, 0)S\rangle$  and  $|(0, 2)S\rangle$  in an unbiased DQD,  $\epsilon \simeq 0$ , we study a model similar to that of Appendix E.7. Using  $|(2, 0)S\rangle$ ,  $|(0, 2)S\rangle$ ,  $|(1, 1)S\rangle$ , and  $|(1, 1)T_0\rangle$  as the basis states, we consider

$$H_s = \begin{pmatrix} U - V_- & 0 & -\sqrt{2}t & 0 \\ 0 & U - V_- & -\sqrt{2}t & 0 \\ -\sqrt{2}t & -\sqrt{2}t & V_+ - V_- & 0 \\ 0 & 0 & 0 & 0 \end{pmatrix} \quad (\text{E.139})$$

as the Hamiltonian for the electronic system and

$$H_{s\text{-ph}} = \begin{pmatrix} -\tilde{P} & 0 & 0 & 0 \\ 0 & \tilde{P} & 0 & 0 \\ 0 & 0 & 0 & 0 \\ 0 & 0 & 0 & 0 \end{pmatrix} \quad (\text{E.140})$$

as the electron-phonon interaction. Again, we removed here  $P_T$  from the diagonal and neglected the off-diagonal matrix elements  $P_S$  and  $P_S^\dagger$ . Furthermore, we exploited the relation

$$P_{SL} - P_T = -(P_{SR} - P_T) = -\tilde{P}. \quad (\text{E.141})$$

This relation is based on the properties

$$\langle \Phi_L | \cos(\mathbf{q} \cdot \mathbf{r}) | \Phi_L \rangle = \langle \Phi_R | \cos(\mathbf{q} \cdot \mathbf{r}) | \Phi_R \rangle, \quad (\text{E.142})$$

$$\langle \Phi_L | \sin(\mathbf{q} \cdot \mathbf{r}) | \Phi_L \rangle = -\langle \Phi_R | \sin(\mathbf{q} \cdot \mathbf{r}) | \Phi_R \rangle. \quad (\text{E.143})$$

Using the states  $|\Phi_{L,R}\rangle$  defined in Appendix E.1 [Eq. (E.28)], it is straightforward to show that these equations apply to our calculations (at least in very good approximation, given the small width of the 2DEG). Proceeding analogously to Appendix E.7 and exploiting  $|t| \ll U - V_+$ , the calculation of  $T_2 = T_\varphi$  with Eqs. (E.139) and (E.140) yields

$$\frac{1}{T_2} = \frac{8t^4}{\hbar^2(U - V_+)^6} \int_{-\infty}^{\infty} \langle \tilde{P}^2(0) \tilde{P}^2(\tau) \rangle d\tau, \quad (\text{E.144})$$

which is formally equivalent to Eq. (E.137).

Operation of the qubit at  $\epsilon \simeq 0$  requires control over the tunnel coupling  $t$ , which can be achieved by changing the tunnel barrier of the DQD with electric gates [26]. Consequently, the value of  $t$  at  $\epsilon \simeq 0$  is usually different from that at large  $\epsilon$ . As a simple estimate, using  $|t| \ll U - V_+$  and assuming that  $V_+ - V_-$  and  $\delta_B$  are negligible, one finds  $J_{\text{tot}} \simeq 4t^2/(U - V_+)$  through Taylor expansion of  $J_S$  [Eq. (E.89)]. Analogously, one obtains

$$\frac{8t^4}{\hbar^2(U - V_+)^6} \simeq \frac{J_{\text{tot}}^2}{2\hbar^2(U - V_+)^4} \quad (\text{E.145})$$

for the prefactor in Eq. (E.144). Considering  $J_{\text{tot}}$  to be the same in the biased and unbiased DQD, comparison with Eq. (E.138) yields a suppression factor on the order of  $(\Delta'_S)^4/(U - V_+)^4$ . For the parameters in this work, the associated dephasing times at  $\epsilon \simeq 0$  are therefore several orders of magnitude longer than those at large  $\epsilon$ . The strong suppression allows omission of this mechanism in our model for an unbiased DQD described in Appendix E.3.

The matrix elements  $P_S$  and  $P_S^\dagger$  of the electron-phonon interaction provide a direct coupling between



Table E.1. Input parameters used for the calculations in Chapter 6.

Parameter	Value	References
$\epsilon_r$	13	
$\rho$	5.32 g/cm <sup>3</sup>	
$v_l$	$5.1 \times 10^3$ m/s	[20–22], Appendix E.2.6.1
$v_t$	$3.0 \times 10^3$ m/s	[20–22], Appendix E.2.6.1
$\Xi$	–8 eV	[19, 23]
$h_{14}$	–0.16 As/m <sup>2</sup>	[21, 22, 31]
$g$	–0.4	
$B$	0.7 T	[12, 13]
$m_{\text{eff}}$	$6.1 \times 10^{-32}$ kg	
$\Delta E = \hbar\omega_0$	124 $\mu\text{eV}$	[14]
$l_D$	1, 0.8, 0.5 $\mu\text{m}$	[27–29], Appendix E.9
$l_R$	2, 1.6, 1 $\mu\text{m}$	
$3a_z$	6 nm	Appendix E.9
$L = 2a$	400 nm	
$\delta b_B$	–0.14 $\mu\text{eV}$	[12, 14]
$U$	1 meV	[4]
$V_+$	40, 50 $\mu\text{eV}$	[4]
$V_-$	39.78, 49.5 $\mu\text{eV}$	[4], Appendix E.9
$t$	7.25, 24 $\mu\text{eV}$	[4], Appendix E.9

the state  $|(1,1)S\rangle$  and the states  $|(0,2)S\rangle$  and  $|(2,0)S\rangle$ . Consequently, these matrix elements enable dephasing via two-phonon processes even at  $t = 0$ . In the case of large detuning  $\epsilon$ , the effect of  $P_S$  and  $P_S^\dagger$  on the dephasing time  $T_\varphi$  (and on the lifetimes in general) turns out to be negligible. At  $\epsilon \simeq 0$ , this two-phonon-based contribution to  $T_\varphi$  is suppressed even further, by a factor on the order of  $4\Delta_S^2/(U - V_+)^2$ , and can therefore be neglected in the calculation with excited orbital states (Appendix E.3).

## E.9 Summary of Input Parameters

Table E.1 lists the values that were used for the results discussed in Chapter 6. We note that the results are independent of the sample volume  $V$  because the volume cancels out in the calculation.

It is worth mentioning that the values  $l_D \sim 0.5\text{--}1 \mu\text{m}$  [27–29] for the Dresselhaus SOI are consistent with the assumed width of the 2DEG. Neglecting orbital effects, the general form of the Dresselhaus SOI for an electron in GaAs is

$$H_D = b_{41}^{6c6c} [(k_{y'}^2 - k_{z'}^2) k_{x'} \sigma_{x'} + \text{c.p.}], \quad (\text{E.146})$$

where  $\hbar k_i$  is the momentum along the  $i$  axis,  $\sigma_i$  is the corresponding Pauli operator for spin 1/2, the axes  $x'$ ,  $y'$ , and  $z'$  are the main crystallographic axes [100], [010], and [001], respectively, “c.p.” stands for cyclic permutations, and  $b_{41}^{6c6c} \simeq 28 \text{ \AA}^3 \text{eV}$  [29]. For our 2DEG with strong confinement along the [001] direction ( $z$  axis), the Dresselhaus SOI can be well approximated by

$$H_D \simeq b_{41}^{6c6c} \langle \phi_{\text{FH}} | k_z^2 | \phi_{\text{FH}} \rangle (k_{y'} \sigma_{y'} - k_{x'} \sigma_{x'}), \quad (\text{E.147})$$

where  $z' = z$  and  $\phi_{\text{FH}}(z)$  is the Fang-Howard wave function of Eq. (E.19). Using  $\langle \phi_{\text{FH}} | k_z^2 | \phi_{\text{FH}} \rangle = 1/(4a_z^2)$ , one finds

$$l_D \simeq \frac{4\hbar^2 a_z^2}{m_{\text{eff}} b_{41}^{6c6c}} \quad (\text{E.148})$$

from comparison with Eqs. (E.39) and (E.46). With  $m_{\text{eff}} = 0.067 m_{\text{el}}$  [29] as the effective electron mass in GaAs and  $m_{\text{el}}$  as the bare electron mass, evaluation of Eq. (E.148) with  $3a_z = 6 \text{ nm}$  yields  $l_D \simeq 0.65 \mu\text{m}$ ,

in good agreement with the values used in the calculation.

The splitting between the eigenstates of type  $|(1, 1)S\rangle$  and  $|(1, 1)T_0\rangle$  after diagonalization is denoted by  $J_{\text{tot}} = \hbar\omega_Z$ . When  $J_{\text{tot}} \gg |\delta b_B|$ , the spin states of these eigenstates are  $|S\rangle$  and  $|T_0\rangle$  with high accuracy, and the state of the  $S$ - $T_0$  qubit precesses around the  $z$  axis of the Bloch sphere. When the splitting is provided by the hyperfine coupling  $\delta b_B$  instead of the exchange interaction, the eigenstates are of type  $|\uparrow\downarrow\rangle$  and  $|\downarrow\uparrow\rangle$ , leading to precessions around the  $x$  axis. In experiments,  $J_{\text{tot}} \gg |\delta b_B|$  is commonly realized for a biased DQD (large detuning) and the hyperfine coupling dominates in the unbiased case [14, 30]. In order to account for this feature, we set the parameters in Sec. 6.3 such that  $J_{\text{tot}}$  at  $\epsilon \simeq 0$  would be largely provided by  $\delta b_B$ . Using  $U$ ,  $V_+$ ,  $V_-$ , and  $t$  approximately as in Ref. [4], we do this by adapting  $t$  (or  $V_-$ ) such that  $J_S \ll |\delta b_B|$ , where  $J_S$  is the bare exchange splitting at  $\epsilon = 0$  [Eq. (E.89)]. The lifetimes in Figs. 6.2 to 6.5 were calculated with  $U = 1$  meV,  $V_+ = 40$   $\mu$ eV,  $V_- = 39.78$   $\mu$ eV, and  $t = 7.25$   $\mu$ eV, for which  $J_S \ll |\delta b_B|$  is fulfilled. The detuning  $\epsilon \sim 0.9$  meV in these calculations was chosen such that  $J_{\text{tot}} = 1.43$   $\mu$ eV, and we note that the excited states are negligible due to  $0 < U - V_{\pm} - \epsilon < \hbar\omega_0$ . In Fig. 6.6, where we consider operation at small detuning, the parameters  $U = 1$  meV,  $V_+ = 50$   $\mu$ eV, and  $V_- = 49.5$   $\mu$ eV are similar to before. However, in order to achieve  $J_{\text{tot}} = 1.41$   $\mu$ eV at  $\epsilon \simeq 0$ , we use a larger tunnel coupling  $t = 24$   $\mu$ eV. Experimentally, this can be realized by tuning the tunnel barrier of the DQD electrically [26].

# References

- [1] G. Burkard, D. Loss, and D. P. DiVincenzo, Phys. Rev. B **59**, 2070 (1999).
- [2] F. F. Fang and W. E. Howard, Phys. Rev. Lett. **16**, 797 (1966).
- [3] D. Stepanenko, N. E. Bonesteel, D. P. DiVincenzo, G. Burkard, and D. Loss, Phys. Rev. B **68**, 115306 (2003).
- [4] D. Stepanenko, M. Rudner, B. I. Halperin, and D. Loss, Phys. Rev. B **85**, 075416 (2012).
- [5] A. V. Khaetskii and Y. V. Nazarov, Phys. Rev. B **61**, 12639 (2000).
- [6] I. L. Aleiner and V. I. Fal'ko, Phys. Rev. Lett. **87**, 256801 (2001).
- [7] V. N. Golovach, A. V. Khaetskii, and D. Loss, Phys. Rev. Lett. **93**, 016601 (2004).
- [8] P. Stano and J. Fabian, Phys. Rev. B **72**, 155410 (2005).
- [9] P. Stano and J. Fabian, Phys. Rev. Lett. **96**, 186602 (2006).
- [10] V. N. Golovach, A. V. Khaetskii, and D. Loss, Phys. Rev. B **77**, 045328 (2008).
- [11] M. Raith, P. Stano, F. Baruffa, and J. Fabian, Phys. Rev. Lett. **108**, 246602 (2012).
- [12] H. Bluhm, S. Foletti, D. Mahalu, V. Umansky, and A. Yacoby, Phys. Rev. Lett. **105**, 216803 (2010).
- [13] M. D. Shulman, O. E. Dial, S. P. Harvey, H. Bluhm, V. Umansky, A. Yacoby, Science **336**, 202 (2012).
- [14] O. E. Dial, M. D. Shulman, S. P. Harvey, H. Bluhm, V. Umansky, and A. Yacoby, Phys. Rev. Lett. **110**, 146804 (2013).
- [15] V. F. Gantmakher and Y. B. Levinson, *Carrier Scattering in Metals and Semiconductors* (North-Holland, Amsterdam, 1987).
- [16] U. Rössler, *Solid State Theory: An Introduction*, 2nd ed. (Springer, Berlin, 2009).
- [17] P. Y. Yu and M. Cardona, *Fundamentals of Semiconductors: Physics and Materials Properties*, 4th ed. (Springer, Berlin, 2010).
- [18] K. A. Benedict, R. K. Hills, and C. J. Mellor, Phys. Rev. B **60**, 10984 (1999).
- [19] S. Adachi, *GaAs and Related Materials: Bulk Semiconducting and Superlattice Properties* (World Scientific, Singapore, 1994).
- [20] A. N. Cleland, *Foundations of Nanomechanics: From Solid-State Theory to Device Applications* (Springer, Berlin, 2003).
- [21] S. Adachi, *Properties of Group-IV, III-V and II-VI Semiconductors* (Wiley, Chichester, 2005).
- [22] <http://www.ioffe.ru/SVA/NSM/Semicond/GaAs>.

- [23] C. G. Van de Walle, Phys. Rev. B **39**, 1871 (1989).
- [24] C. P. Slichter, *Principles of Magnetic Resonance* (Springer, Berlin, 1980).
- [25] M. Borhani, V. N. Golovach, and D. Loss, Phys. Rev. B **73**, 155311 (2006).
- [26] D. Loss and D. P. DiVincenzo, Phys. Rev. A **57**, 120 (1998).
- [27] A. V. Khaetskii and Y. V. Nazarov, Phys. Rev. B **64**, 125316 (2001).
- [28] R. Hanson, L. P. Kouwenhoven, J. R. Petta, S. Tarucha, and L. M. K. Vandersypen, Rev. Mod. Phys. **79**, 1217 (2007).
- [29] R. Winkler, *Spin-Orbit Coupling Effects in Two-Dimensional Electron and Hole Systems* (Springer, Berlin, 2003).
- [30] J. R. Petta, A. C. Johnson, J. M. Taylor, E. A. Laird, A. Yacoby, M. D. Lukin, C. M. Marcus, M. P. Hanson, and A. C. Gossard, Science **309**, 2180 (2005).
- [31] K. Hübner, Phys. Status Solidi B **57**, 627 (1973).

## Appendix F

# Supplementary Information to Chapter 7 “Controlling the Interaction of Electron and Nuclear Spins in a Tunnel-Coupled Quantum Dot”

**Adapted from:**

Christoph Kloeffel, Paul A. Dalgarno, Bernhard Urbaszek, Brian D. Gerardot, Daniel Brunner,  
Pierre M. Petroff, Daniel Loss, and Richard J. Warburton,  
*Phys. Rev. Lett.* **106**, 046802 (2011).

## F.1 Outline

In Chapter 7 we report a technique for manipulating the nuclear spins and the emission polarization of a single optically active quantum dot. In order to describe this system theoretically, we divide the calculation into two interlinked parts. Process I: the laser field induces dynamics in a five-level electronic system. The final event is  $X^{1-}$  recombination. Process II: nuclear spin polarization builds up via electron-nuclear-spin flip-flop processes. Process I provides an unpaired electron spin as input to process II. Conversely, process II creates an Overhauser field which is an input to process I. In the presence of nuclear spin leakage, a master equation for the nuclear spin polarization  $\langle I_z \rangle$  has stable solutions where  $\frac{d}{dt}\langle I_z \rangle = 0$ . Associated with the stable solutions for  $\langle I_z \rangle$  are particular values of the Overhauser field and, hence, particular values of the photoluminescence energies and intensities for the two light polarizations  $\sigma^+$  and  $\sigma^-$ . The details of this calculation are described here along with the input parameters. The results of the calculation can be compared directly with the experiment (Fig. 7.2 of Chapter 7). Based on our model, we also discuss consequences on the fluctuations of the nuclear spin ensemble.

## F.2 Coherent Evolution of Five-Level System

The dynamics of the five-level quantum system induced by the laser field are calculated with the density matrix. The ground state is the empty dot,  $|0\rangle$ . There are two neutral exciton states,  $|\uparrow\downarrow\rangle$  (hole spin up, electron spin down) and  $|\downarrow\uparrow\rangle$  (hole spin down, electron spin up). Defining the ground state energy as zero, the diagonal terms of the Hamiltonian matrix  $\hat{H}$  are

$$\langle\uparrow\downarrow|\hat{H}|\uparrow\downarrow\rangle = \hbar\omega_0 + \frac{1}{2}(g_X\mu_B B_z - A\langle I_z\rangle), \quad (\text{F.1})$$

$$\langle\downarrow\uparrow|\hat{H}|\downarrow\uparrow\rangle = \hbar\omega_0 - \frac{1}{2}(g_X\mu_B B_z - A\langle I_z\rangle), \quad (\text{F.2})$$

where  $\hbar\omega_0$  is the eigenenergy of  $|\uparrow\downarrow\rangle$  and  $|\downarrow\uparrow\rangle$  in the absence of a magnetic field. Coupling to the external magnetic field  $B_z$  is determined by the exciton  $g$  factor  $g_X$ . The electron also interacts with the internal (Overhauser) magnetic field, given by the expectation value of the nuclear spin  $z$  projection  $\langle I_z \rangle$  (in units of  $\hbar$ ) and the averaged effective coupling constant  $A$ . The  $\sigma^+$  polarized laser of angular frequency  $\omega = \omega_0 + \delta$ , with  $\hbar\delta$  as detuning, drives the  $|0\rangle \leftrightarrow |\uparrow\downarrow\rangle$  but not the  $|0\rangle \leftrightarrow |\downarrow\uparrow\rangle$  transition on account of the selection rules. As the laser is always close to the resonance, the rotating wave approximation applies. The off-diagonal elements in the Hamiltonian are

$$\langle 0|\hat{H}|\uparrow\downarrow\rangle = \frac{\hbar\Omega}{2}e^{i\omega t}, \quad (\text{F.3})$$

$$\langle\downarrow\uparrow|\hat{H}|\uparrow\downarrow\rangle = \frac{\hbar\omega_{\text{fs}}}{2}, \quad (\text{F.4})$$

where  $\hbar\Omega$  is the optical Rabi energy and  $\hbar\omega_{\text{fs}}$  is the fine structure splitting arising from the anisotropic part of the electron-hole exchange [1]. The two neutral exciton states can decay either to the ground state by spontaneous emission at rate  $\tau_0^{-1}$ , or to a negatively charged trion  $X^{1-}$  by tunneling of an electron into the quantum dot at rate  $\tau_{\text{in}}^{-1}$ . Tunneling converts  $|\uparrow\downarrow\rangle$  into the  $X^{1-}$  state  $|\uparrow\downarrow\uparrow\rangle$ , and  $|\downarrow\uparrow\rangle$  into the other  $X^{1-}$  state  $|\downarrow\uparrow\downarrow\rangle$ . The trion states decay by spontaneous recombination, at rate  $\tau_1^{-1}$ , to states  $|\uparrow\rangle$  and  $|\downarrow\rangle$ , respectively. Figure 7.4 (top) of Chapter 7 summarizes all the decay processes and coherent couplings.

At time  $t = 0$ , the entire population resides in the ground state. The probability of finding the system in state  $|s\rangle$  at a time  $t > 0$  corresponds to the element  $\langle s|\hat{\rho}|s\rangle$  of the density matrix  $\hat{\rho}$ , and we use the

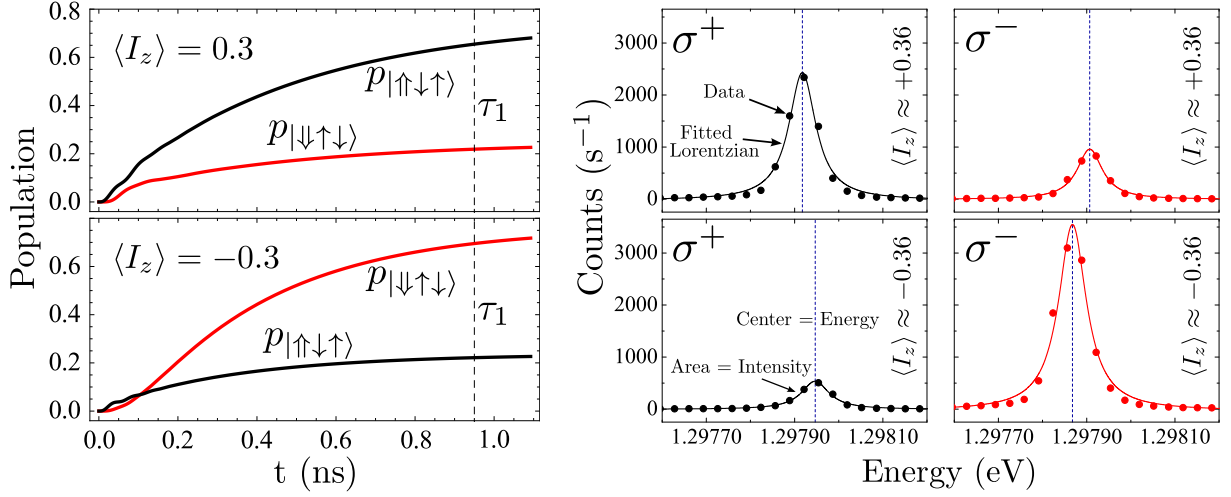


Figure F.1. Left: Simulation of the trion occupation probabilities  $p_{|\uparrow\downarrow\uparrow\rangle}$  and  $p_{|\downarrow\uparrow\downarrow\rangle}$  in the five-level system formed by  $|0\rangle$ ,  $|\uparrow\downarrow\rangle$ ,  $|\downarrow\uparrow\rangle$ ,  $|\uparrow\downarrow\uparrow\rangle$ , and  $|\downarrow\uparrow\downarrow\rangle$ , considering the entire population in the ground state  $|0\rangle$  at time  $t = 0$ . The parameters, summarized in detail in Appendix F.6, are the same as used in Chapter 7, with the detuning  $\hbar\delta$  fixed in the region of bistability. Depending on the value of  $\langle I_z \rangle$ , either  $|\uparrow\downarrow\uparrow\rangle$  or  $|\downarrow\uparrow\downarrow\rangle$  is preferentially occupied after the  $X^{1-}$  recombination time  $\tau_1$ , resulting in different rates for the emission of  $\sigma^+$  and  $\sigma^-$  photons and, thus, for the creation of  $\uparrow$  and  $\downarrow$  electrons. Right: Measured counts-energy spectra with the laser tuned to the region of bistability. The dot, at 4.2 K, is the same as in Figs. 7.1 to 7.3 of Chapter 7, and the energy of the detected signal corresponds to  $X^{1-}$ . The experimental data are fitted to Lorentzians, yielding both the energies  $E(\sigma^\pm)$  (center of curve) and the signal intensities  $S(\sigma^\pm)$  (area under curve). A clear shift in the energies is observed, arising from different nuclear spin polarizations  $\langle I_z \rangle$ . As expected from the theory (left), the  $\sigma^+$  signal is pronounced when  $\langle I_z \rangle$  is positive, and vice versa. Both theory and experiment use a  $\sigma^+$  pump and an external field of  $B_z = +0.5$  T.

master equation with the decay processes in Lindblad form,

$$\frac{d}{dt}\hat{\rho} = -\frac{i}{\hbar}[\hat{H}, \hat{\rho}] + D\hat{\rho}, \quad (\text{F.5})$$

$$D\hat{\rho} = \sum_{m,n} \Gamma_{|m\rangle \rightarrow |n\rangle} \left( |n\rangle \langle m| \hat{\rho} |m\rangle \langle n| - \frac{1}{2} |m\rangle \langle m| \hat{\rho} - \frac{1}{2} \hat{\rho} |m\rangle \langle m| \right), \quad (\text{F.6})$$

to calculate its coherent evolution [2]. The dissipator  $D\hat{\rho}$  accounts for the decay processes, where  $\Gamma_{|m\rangle \rightarrow |n\rangle}$  is the transition rate from state  $|m\rangle$  to state  $|n\rangle$ .

Of particular interest are the trion populations  $p_{|\uparrow\downarrow\uparrow\rangle} = \langle \uparrow\downarrow\uparrow | \hat{\rho} | \uparrow\downarrow\uparrow \rangle$  and  $p_{|\downarrow\uparrow\downarrow\rangle} = \langle \downarrow\uparrow\downarrow | \hat{\rho} | \downarrow\uparrow\downarrow \rangle$ , since they determine both the  $X^{1-}$  emission intensity and the probability of creating a conduction band electron with spin up (down) after trion recombination. The spontaneous  $X^{1-}$  recombination time is  $\tau_1$ , and we therefore take  $(p_{|\uparrow\downarrow\uparrow\rangle}/\tau_1)|_{t=\tau_1}$  and  $(p_{|\downarrow\uparrow\downarrow\rangle}/\tau_1)|_{t=\tau_1}$  as the rates of creating an electron  $\uparrow$  and  $\downarrow$ , respectively. This approximation, assuming essentially that the dynamics approach the steady state (population distributed among trions) before  $X^{1-}$  recombines, is well justified for laser energies near resonance. At large detunings, the approximation works less well, but going beyond this approximation would greatly complicate the calculation at the expense of transparency. Figure F.1 (left) shows the evolution of the trion population as calculated in the five-level system for a laser energy in the region of the bistability. The parameters are the same as used in Chapter 7 and are summarized in detail in Appendix F.6. For positive (negative) nuclear spin polarization, the  $|\uparrow\downarrow\uparrow\rangle$  ( $|\downarrow\uparrow\downarrow\rangle$ ) state is preferentially occupied, leading to  $\sigma^+$  ( $\sigma^-$ ) emission and dynamic nuclear spin polarization in positive (negative)  $z$  direction.

### F.3 Flip-Flop of Electron and Nuclear Spin

At time  $t = \tau_1$ , after  $X^{1-}$  recombination, the quantum dot is in the  $|e\rangle$  state and contains a free electron. This electron interacts with the  $N$  nuclear spins in the quantum dot before it tunnels into the Fermi sea at rate  $\tau_{\text{out}}^{-1}$ . Since the conduction band electron has an  $s$ -type Bloch function, its coupling to the nuclear spins is well described by the contact hyperfine interaction with effective Hamiltonian

$$\hat{H}_{\text{hf}} = \nu_0 \sum_k A_k^j |\psi(\mathbf{R}_k)|^2 \mathbf{I}_k \cdot \mathbf{S}. \quad (\text{F.7})$$

Here  $\psi(\mathbf{R}_k)$  is the electron wave function at the  $k$ th nucleus,  $A_k^j = A^j$  are the effective hyperfine coupling constants for atoms of type  $j$ ,  $\nu_0$  denotes the volume per atom, and  $\mathbf{I}_k$  and  $\mathbf{S}$ , respectively, are the nuclear and electron spins in units of  $\hbar$  [3]. We assume homogeneous coupling, which yields

$$\hat{H}_{\text{hf}} \simeq \frac{A}{N} \sum_k \mathbf{I}_k \cdot \mathbf{S} \equiv A \langle \mathbf{I} \rangle \cdot \mathbf{S}, \quad (\text{F.8})$$

a result used in the diagonal elements of the five-level system [Eqs. (F.1) and (F.2)]. Based on  $\text{In}_{0.5}\text{Ga}_{0.5}\text{As}$ , we take  $A \approx 90 \mu\text{eV}$  as the averaged effective coupling constant [3] and  $I = 0.75 \cdot 3/2 + 0.25 \cdot 9/2 = 2.25$  as averaged nuclear spin quantum number. Adding the Zeeman term  $\hat{H}_{\text{ext}}$ , with  $g_e$  as electron  $g$  factor, the total Hamiltonian reads

$$\hat{H}_{\text{ext}} + \hat{H}_{\text{hf}} = g_e \mu_B B_z S_z + A \langle I_z \rangle S_z + \frac{A}{2N} \sum_k (I_k^+ S^- + I_k^- S^+), \quad (\text{F.9})$$

where  $I_k^\pm = I_k^x \pm i I_k^y$  and  $S^\pm = S_x \pm i S_y$  are ladder operators, so that the final term describes a flip-flop of electron and nuclear spin. In the following it is assumed that the electron has spin up; the calculation for spin down is analogous.

In order to estimate the flip-flop probability as a function of net nuclear polarization, we calculate the time evolution of the effective two-level system formed by  $|M, \uparrow\rangle$  and  $|M+1, \downarrow\rangle$ , where  $|M\rangle$  represents the ensemble of nuclear spin states with  $z$  projection  $M = N \langle I_z \rangle$ . With the system in state  $|M, \uparrow\rangle$  at time  $t' = t - \tau_1 = 0$ , one finds from the von Neumann equation [2] that the population of  $|M+1, \downarrow\rangle$  oscillates in time according to

$$p_{|M+1, \downarrow\rangle} = \frac{4\gamma}{4\gamma + \xi} \sin^2 \left( \frac{\sqrt{4\gamma + \xi}}{2\hbar} t' \right), \quad (\text{F.10})$$

where

$$\gamma = \left| \langle M+1, \downarrow | \hat{H}_{\text{hf}} | M, \uparrow \rangle \right|^2, \quad (\text{F.11})$$

$$\xi = \left| \langle M+1, \downarrow | \hat{H}_{\text{ext}} + \hat{H}_{\text{hf}} | M+1, \downarrow \rangle - \langle M, \uparrow | \hat{H}_{\text{ext}} + \hat{H}_{\text{hf}} | M, \uparrow \rangle \right|^2. \quad (\text{F.12})$$

From Eq. (F.9), one finds

$$\xi = (g_e \mu_B B_z + A \langle I_z \rangle)^2. \quad (\text{F.13})$$

Simple results for  $\gamma$  only exist when the nuclear spins are either fully correlated or fully uncorrelated, neither of which is the case here. With

$$\gamma = \frac{A^2}{4N} (I - |\langle I_z \rangle|) \quad (\text{F.14})$$

we take an average of the two extremes, as derived in Appendix F.7. Integrating Eq. (F.10) over the



survival distribution, characterized by the tunneling time  $\tau_{\text{out}}$ , finally yields the flip-flop probability

$$p_{\text{ff}} = \int_{t'=0}^{\infty} dt' \frac{e^{-t'/\tau_{\text{out}}}}{\tau_{\text{out}}} p_{|M+1, \downarrow\rangle} = \frac{2\gamma\tau_{\text{out}}^2}{(4\gamma + \xi)\tau_{\text{out}}^2 + \hbar^2}. \quad (\text{F.15})$$

Referring to previous work on dynamic nuclear polarization, the result is of a rather standard form, with  $\tau_{\text{out}}$  as correlation time [4, 5]. Since we operate at relatively low magnetic fields, where the “bright”  $X^0$  states  $|\uparrow\downarrow\rangle$  and  $|\downarrow\uparrow\rangle$  are split from the “dark”  $X^0$  states  $|\uparrow\uparrow\rangle$  and  $|\downarrow\downarrow\rangle$  by far more than a hundred  $\mu\text{eV}$  [1, 6], spin flip-flops among electron and nuclei are negligible in the presence of a hole.

## F.4 Nuclear Spin Dynamics and Stable Solutions

The combination of the electron spin creation rate and the flip-flop probability results in a dynamic equation for the nuclear spin polarization  $\langle I_z \rangle$ . The latter is driven up depending on  $p_{|\uparrow\downarrow\uparrow\rangle}$ , down depending on  $p_{|\downarrow\uparrow\downarrow\rangle}$ , and decays in the absence of driving with rate  $\Gamma_{\text{leak}}$ . With  $\tau_1$  ( $\sim\text{ns}$ )  $\gg \tau_{\text{out}}$  ( $\sim\text{ps}$ ), the cycle round-trip time is simply  $\tau_1$  and the dynamic equation reads

$$\frac{d}{dt} \langle I_z \rangle \simeq \frac{p_{\text{ff}}}{N\tau_1} [p_{|\uparrow\downarrow\uparrow\rangle} - p_{|\downarrow\uparrow\downarrow\rangle}]_{t=\tau_1} - \Gamma_{\text{leak}} \langle I_z \rangle. \quad (\text{F.16})$$

The flip-flop probability  $p_{\text{ff}}$  is a function of  $\langle I_z \rangle$ ; the populations  $p_{|\uparrow\downarrow\uparrow\rangle}$  and  $p_{|\downarrow\uparrow\downarrow\rangle}$  are functions of both  $\langle I_z \rangle$  and laser detuning  $\hbar\delta$ . We solve Eq. (F.16) numerically to find stable values of  $\langle I_z \rangle$  as a function of  $\hbar\delta$ . Figure F.2 shows  $\frac{d}{dt} \langle I_z \rangle$  from Eq. (F.16) as a function of  $\langle I_z \rangle$  as the laser is tuned through the bistability (parameters as in Chapter 7 and Appendix F.6). Stable nuclear spin polarizations are found where  $\frac{d}{dt} \langle I_z \rangle$  crosses zero with negative slope. These stable values of  $\langle I_z \rangle$  are directly related to the Overhauser shift  $\Delta_n$  observed in the experiment. For the difference between the  $X^{1-}$  emission energies  $E(\sigma^+)$  and  $E(\sigma^-)$  measured for photons with  $\sigma^+$  and  $\sigma^-$  polarization, respectively, one obtains

$$E(\sigma^+) - E(\sigma^-) = g_X \mu_B B_z + \Delta_n \equiv g_X^{\text{eff}} \mu_B B_z, \quad (\text{F.17})$$

where we use  $\Delta_n = -A \langle I_z \rangle$  based on Eq. (F.8). Figure F.1 (right) shows four counts-energy spectra measured in the region of bistability and fitted to Lorentzian curves, with  $E(\sigma^\pm)$  given by the centers of the respective fit functions. The figure illustrates a key feature of the presented scheme, i.e., the tuning of resonance energies via control over the net polarization of the nuclear spin bath. In Chapter 7, a change from  $-45 \mu\text{eV}$  to  $+20 \mu\text{eV}$  in the total electron Zeeman splitting  $g_e^{\text{eff}} \mu_B B_z = g_e \mu_B B_z + A \langle I_z \rangle$  is observed. That is, the sign of the effective electron  $g$  factor  $g_e^{\text{eff}}$  can be inverted and, using the continuous change in  $\langle I_z \rangle$  at more positive laser energies,  $g_e^{\text{eff}}$  can be tuned precisely to zero. Accordingly, the effective exciton  $g$  factor  $g_X^{\text{eff}}$  is tuned from 2.6 to 0.3, and tuning  $g_X^{\text{eff}}$  through zero should easily be possible with an optimized cycle.

The Lorentzians fitted to the experimental data not only yield the line energies (center), but also the line intensities (area under the curve) denoted by  $S(\sigma^\pm)$ . In terms of the theoretical model, the  $\sigma^+$  ( $\sigma^-$ ) intensity corresponds to the rate of creating an  $\uparrow$  ( $\downarrow$ ) electron via  $X^{1-}$  recombination. For each stable solution of  $\frac{d}{dt} \langle I_z \rangle = 0$  we can hence calculate the  $\sigma^\pm$  emission intensity and the associated degree of polarization,

$$P = \frac{S(\sigma^+) - S(\sigma^-)}{S(\sigma^+) + S(\sigma^-)} = \left. \frac{p_{|\uparrow\downarrow\uparrow\rangle} - p_{|\downarrow\uparrow\downarrow\rangle}}{p_{|\uparrow\downarrow\uparrow\rangle} + p_{|\downarrow\uparrow\downarrow\rangle}} \right|_{t=\tau_1}. \quad (\text{F.18})$$

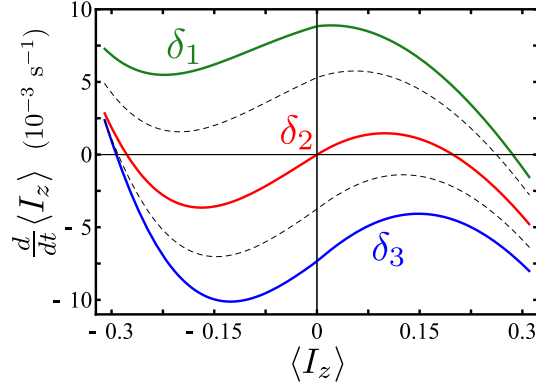


Figure F.2. Simulation of  $\frac{d}{dt}\langle I_z \rangle$ , Eq. (F.16), with  $B_z = +0.5$  T and the parameters summarized in Appendix F.6. Stable nuclear spin polarizations are found where the horizontal axis is crossed with negative slope. For  $\hbar\delta_1 = -42$   $\mu\text{eV}$  (green), one solution exists at positive  $\langle I_z \rangle$ . For  $\hbar\delta_2 = -38.5$   $\mu\text{eV}$  (red), an additional stable solution exists at negative nuclear spin polarization, leading to a bistability. The solution at positive  $\langle I_z \rangle$  disappears when the laser detuning is increased further,  $\hbar\delta_3 = -36$   $\mu\text{eV}$  (blue). The theoretical width of the bistable region is 2  $\mu\text{eV}$  and generally depends on the various input parameters. Widths  $> 10$   $\mu\text{eV}$  are achievable.

## F.5 Calculation of Nuclear Spin Distribution Width

The model also provides insight into the width of the nuclear spin distribution. Typical fluctuations of the nuclear magnetic field seen by the electron spin via the hyperfine interaction are of the order of  $A/(|g_e|\mu_B\sqrt{N})$  [7, 8]. This corresponds to fluctuations of the nuclear spin polarization  $\langle I_z \rangle$  by  $\sim 1/\sqrt{N}$  and, in terms of the associated Gaussian distribution function, to a variance of  $\sigma^2 \sim 1/N$ . In order to calculate the nuclear spin distribution in the presence of the laser field, we follow the steps summarized in the supplementary information of Ref. [9]. Starting from a basic rate equation, reformulation in the continuum limit results in a Fokker-Planck equation that is solved for stable nuclear spin distributions. These solutions are of type  $e^{F(\langle I_z \rangle)}$ , and expansion of the function  $F(\langle I_z \rangle)$  around the stable nuclear spin polarization  $I_{z,0}$  to the second power of  $\langle I_z \rangle - I_{z,0}$  yields the variance of the distribution. One finds

$$\sigma^2 = \frac{1}{2N} \frac{\Gamma_{\text{tot}}}{\frac{\partial}{\partial \langle I_z \rangle} \left( -\frac{d}{dt} \langle I_z \rangle \right)} \Big|_{\langle I_z \rangle = I_{z,0}}, \quad (\text{F.19})$$

where  $\Gamma_{\text{tot}}$  is the total spin-flip rate divided by  $N$ ,

$$\Gamma_{\text{tot}} = \frac{p_{\text{ff}}}{N\tau_1} [p_{|\uparrow\uparrow\uparrow} + p_{|\downarrow\downarrow\downarrow}]_t = \tau_1 + \Gamma_{\text{leak}}|\langle I_z \rangle| + 2\Gamma_{\text{leak}}. \quad (\text{F.20})$$

The additional  $2\Gamma_{\text{leak}}$  accounts for intrinsic diffusion and ensures that  $\sigma^2 = 1/N$  in the absence of a laser field. The simulation shows that our cycle results in a reduction of the variance by a small factor  $\sim 1.7$  in the experiment of Chapter 7. However, by increasing the tunneling times slightly, the scheme is capable of narrowing the variance of the nuclear spin distribution by factors  $\sim 5$ . Similar numbers have been reported in Ref. [10].

## F.6 Input Parameters

The parameters for the simulation are set by in situ characterization of the quantum dot, by comparison with previous experiments on the same sample, and by making small tweaks to fit the experimental data in Fig. 7.2 of Chapter 7. The main features – an abrupt inversion in the polarization of both photoluminescence (PL) and nuclear spins, followed by continuous tuning through zero – are not sensitive to the parameters in the calculation. Reproducing the exact experimental results is however sensitive to

the exact parameters, in particular to  $\hbar\omega_{\text{fs}}$ ,  $\tau_{\text{in}}$ ,  $\tau_{\text{out}}$ , and  $\Gamma_{\text{leak}}$ .

- The Rabi energy  $\hbar\Omega$  is proportional to the amplitude of the oscillating electric field and can therefore be estimated from the power density at the quantum dot, which gives us a rough estimate of  $\hbar\Omega$ . A more precise determination is taken from Ref. [11] in which the Rabi energy is measured directly from the Autler-Townes splitting in a pump-probe experiment. This experiment used the same microscope and a sample from the same wafer as the present experiment. Given a laser power of  $13 \text{ kW/cm}^2$  and the values reported in Ref. [11], we determine  $\hbar\Omega = 23 \text{ } \mu\text{eV}$ .
- The fine structure splitting  $\hbar\omega_{\text{fs}}$  is highly scattered from dot to dot in this sample [12];  $40 \text{ } \mu\text{eV}$  is taken here, largely by fitting the results of the model to the experimental data.
- For the exciton recombination times  $\tau_0$  ( $X^0$ ) and  $\tau_1$  ( $X^{1-}$ ), we take  $\tau_0 = 0.75 \text{ ns}$  and  $\tau_1 = 0.95 \text{ ns}$  from lifetime measurements of quantum dots in this wafer [13]. There is a systematic increase in the recombination lifetimes on going from  $X^0$  to  $X^{1-}$ , and a systematic dependence on the  $X^0$  exciton energy. Both these factors are included.
- The time  $\tau_{\text{in}} = 35 \text{ ps}$  for tunneling into the dot is estimated from  $\tau_0$  and the ratio of  $X^0$  and  $X^{1-}$  PL intensities in the hybridization region. The time  $\tau_{\text{out}}$  for tunneling out of the dot is smaller as the electron is now above rather than below the Fermi energy (where the energy barrier is thinner). Experiments probing the spin cotunneling rate [14] and the PL in the hybridization region [15] on dots similar to the one used here point to a time  $\tau_{\text{out}} \sim 10 \text{ ps}$ . Fine tuning by fitting the experimental data gives  $\tau_{\text{out}} = 5 \text{ ps}$ .
- $N$ , the number of quantum dot nuclear spins, is estimated from the extent of the electron wave function. For this, the ground state wave function for harmonic confinement,

$$\psi_0 = C_0 e^{-\frac{1}{2} \left( \frac{x^2}{l_x^2} + \frac{y^2}{l_y^2} + \frac{z^2}{l_z^2} \right)}, \quad (\text{F.21})$$

is replaced by a box-like function  $\psi_b$  with constant amplitude  $\psi_b = C_0/\sqrt{e} = 1/\sqrt{V}$  in the volume  $V$  and with  $\psi_b = 0$  outside of  $V$ . We note that, in the simple case of spherical symmetry,  $C_0/\sqrt{e}$  is the value of  $\psi_0$  at the radius  $r = \sqrt{x^2 + y^2 + z^2}$  where  $|\psi_0|^2 4\pi r^2 dr$  peaks. From the normalization condition one obtains  $V = l_x l_y l_z \pi^{3/2} e$ , and the effective number of nuclear spins in the quantum dot corresponds to  $N = 8V/a^3$  (zinc blende), where  $a$  is the lattice constant. The confinement lengths  $l_i$  are related to the level spacings  $\hbar\omega_i$  and the effective electron mass  $m^*$  via  $l_i = \sqrt{\hbar/(m^*\omega_i)}$ . With  $\hbar\omega_{x,y} = 30 \text{ meV}$  [16] and  $\hbar\omega_z = 95 \text{ meV}$  [17], we calculate  $N = 8.5 \times 10^4$  as the number of nuclear spins covered by  $\psi_b$ . This result is consistent with a measurement of the fluctuations in the Overhauser field [18] (see also Appendix F.5).

- The electron  $g$  factor is  $g_e = -0.5$ , as determined by optically detected single electron spin resonance performed on a dot in a very similar sample to the one used here [18]. For the exciton,  $g_X = 1.55$  was measured by assuming that at large detunings, where  $E(\sigma^+) - E(\sigma^-)$  takes on a constant value,  $\Delta_n$  changes sign but not magnitude on switching the pump polarization,

$$g_X \simeq \frac{1}{2\mu_B B_z} \left( [E(\sigma^+) - E(\sigma^-)]_{\sigma^+ \text{ pump}} + [E(\sigma^+) - E(\sigma^-)]_{\sigma^- \text{ pump}} \right). \quad (\text{F.22})$$

- The order of magnitude of the spin depolarization rate  $\Gamma_{\text{leak}}$  results from direct experimental observations. As demonstrated in Chapter 7, the system always preserves its state when the laser, tuned to the region of bistability, is turned off and back on after  $\sim 30 \text{ s}$ . For times  $> 1 \text{ min}$  this is no longer true, pointing towards leakage rates of  $\sim 0.01\text{--}0.1 \text{ s}^{-1}$ . This measures the decay of the nuclear spin

polarization with the dot in the vacuum state  $|0\rangle$ . Optical pumping in the hybridization region causes the dot, averaged over time, to be partially occupied such that the relevant value of  $\Gamma_{\text{leak}}$  is likely to be larger. We take  $\Gamma_{\text{leak}} = 0.1 \text{ s}^{-1}$  here as it gives the best fit to the experimental data.

## F.7 Flip-Flop Term in an Effective Two-Level System

In this appendix we provide details for the derivation of the electron-nuclear-spin flip-flop probability in Appendix F.3. Since  $\langle I_z \rangle$  is observed via the Overhauser shift  $\Delta_n = -A\langle I_z \rangle$ , we calculate the flip-flop probability as a function of the nuclear spin polarization. Defining

$$M = \sum_k I_k^z = N\langle I_z \rangle \quad (\text{F.23})$$

as the total nuclear spin  $z$  projection in units of  $\hbar$ , the state of the nuclear spin bath is a linear superposition of states  $|J, M, \lambda_M^J\rangle$  with fixed  $M$ . Here  $J$  is the quantum number for the size of the total spin,  $|M| \leq J \leq NI$ , and  $\lambda_M^J$  is an additional quantum number whose range depends on  $M$  and  $J$  such that

$$\sum_{J=0(\frac{1}{2})}^{NI} \sum_{M'=-J}^J \sum_{\lambda} |J, M', \lambda_{M'}^J\rangle \langle J, M', \lambda_{M'}^J| = \mathbb{1}. \quad (\text{F.24})$$

Assuming that the free electron in the quantum dot has initially spin up (Appendix F.3), the Hamiltonian  $\hat{H}_{\text{ext}} + \hat{H}_{\text{hf}}$  shown in Eq. (F.9) couples the states  $|J, M, \lambda_M^J, \uparrow\rangle$  with states  $|J, M+1, \lambda_{M+1}^J, \downarrow\rangle$ , where the electron spin was simply added in the notation. For given  $M$ , considering the large number of  $\sim 10^5$  nuclear spins, the system of interest is therefore high-dimensional. However, it can be reduced to an effective two-level system.

Since the energy depends only on the electron spin and the nuclear spin  $z$  projection, all states  $|J, M, \lambda_M^J, \uparrow\rangle$  and  $|J, M+1, \lambda_{M+1}^J, \downarrow\rangle$  have the same eigenenergy  $E_1$  and  $E_2$ , respectively. The population at time  $t' = 0$  is distributed among the states  $|J, M, \lambda_M^J, \uparrow\rangle$ , which we formally replace by a state  $|M, \uparrow\rangle$  with 100% occupation probability and eigenenergy  $E_1$ . This state  $|M, \uparrow\rangle$  is coupled to the states with electron spin down and nuclear spin  $z$  projection  $M+1$  via the flip-flop term in the contact hyperfine interaction [Eqs. (F.8) and (F.9)]. For the estimate of the flip-flop probability it only matters whether the system occupies state  $|M, \uparrow\rangle$  or any of the other states  $|J, M+1, \lambda_{M+1}^J, \downarrow\rangle$ . Therefore, the dynamics can equivalently be calculated in a reduced system, where the  $|J, M+1, \lambda_{M+1}^J, \downarrow\rangle$  are replaced by the effective state  $|M+1, \downarrow\rangle$  of energy  $E_2$ . The effective coupling between  $|M, \uparrow\rangle$  and  $|M+1, \downarrow\rangle$  is given by

$$\gamma = \left| \langle M+1, \downarrow | \hat{H}_{\text{hf}} | M, \uparrow \rangle \right|^2 = \sum_{J=|M+1|}^{NI} \sum_{\lambda} \left| \langle J, M+1, \lambda_{M+1}^J, \downarrow | \hat{H}_{\text{hf}} | M, \uparrow \rangle \right|^2. \quad (\text{F.25})$$

The value of  $\gamma$  strongly depends on the system. In the following, the two extremes of a strongly correlated and a fully uncorrelated nuclear spin bath will be considered.

### F.7.1 Strong Correlation

As a first limit, we assume a highly coherent system free of further interactions, so that transitions  $J \leftrightarrow J+1$  are impossible. The relevant flip-flop term in the Hamiltonian  $\hat{H}_{\text{hf}}$  is

$$\frac{A}{2N} \sum_k I_k^+ S^- = \frac{A}{2N} J^+ S^-, \quad (\text{F.26})$$

where  $J^+ = \sum_k I_k^+$  acts as a raising operator for the total spin. Its effect on a state  $|J, M, \uparrow\rangle$  ( $\lambda$  irrelevant) within  $|M, \uparrow\rangle$  is

$$\frac{A}{2N} J^+ S^- |J, M, \uparrow\rangle = \frac{A}{2N} \sqrt{(J-M)(J+M+1)} |J, M+1, \downarrow\rangle, \quad (\text{F.27})$$

which breaks down as soon as the expression under the square root is zero. Starting from an unpolarized system, the typical order of magnitude for the starting value of  $J$  can be estimated from the infinite temperature limit,

$$\bar{J}(\bar{J}+1) = \langle \mathbf{J} \cdot \mathbf{J} \rangle = \sum_{k \neq k'} \langle \mathbf{I}_k \cdot \mathbf{I}_{k'} \rangle + \sum_k \langle \mathbf{I}_k \cdot \mathbf{I}_k \rangle = \sum_k \langle \mathbf{I}_k \cdot \mathbf{I}_k \rangle = NI(I+1), \quad (\text{F.28})$$

which yields

$$\bar{J} \simeq \sqrt{N} \sqrt{I(I+1)}. \quad (\text{F.29})$$

Given this value,  $J \sim \bar{J}$ , the square root in Eq. (F.27) typically approaches zero at  $|\langle I_z \rangle| \sim \sqrt{I(I+1)}/N$ . For  $N = 8.5 \times 10^4$  and  $I = 2.25$ , these so-called dark states would therefore be reached at nuclear spin polarizations  $|\langle I_z \rangle|/I$  of less than 1% in both positive and negative  $z$  direction. This is in clear contradiction with the experiment, where polarizations of  $\sim 20\%$  were measured and dark states were not observed.

## F.7.2 No Correlation

In the other extreme, we take an uncorrelated system without transverse spin coherence, so that there is no correlation among the  $x, y$  components of the nuclear spins. Starting from Eq. (F.25), we find

$$\begin{aligned} \gamma &= \sum_{J=|M+1|}^{NI} \sum_{\lambda} \left| \langle J, M+1, \lambda_{M+1}^J, \downarrow | \hat{H}_{\text{hf}} | M, \uparrow \rangle \right|^2 = \frac{A^2}{4N^2} \sum_{J=|M+1|}^{NI} \sum_{\lambda} \left| \langle J, M+1, \lambda_{M+1}^J | \sum_k I_k^+ | M \rangle \right|^2 \\ &= \frac{A^2}{4N^2} \sum_{k, k'} \langle M | I_k^- \underbrace{\sum_{J=|M+1|}^{NI} \sum_{\lambda} |J, M+1, \lambda_{M+1}^J\rangle \langle J, M+1, \lambda_{M+1}^J |}_{\text{equivalent to } \mathbb{1}, \text{ only nonzero contribution}} I_{k'}^+ | M \rangle \\ &= \frac{A^2}{4N^2} \underbrace{\sum_{k \neq k'} \langle M | I_k^- I_{k'}^+ | M \rangle}_{=0} + \frac{A^2}{4N^2} \sum_k \langle M | I_k^- I_k^+ | M \rangle \\ &= \frac{A^2}{4N^2} \sum_k \langle M | (I^2 + I - (I_k^z)^2 - I_k^z) | M \rangle \simeq \frac{A^2}{4N} (I^2 + I - \langle I_z \rangle^2 - \langle I_z \rangle). \end{aligned} \quad (\text{F.30})$$

This calculation represents the nuclear spin system when coherence in the nuclear spin bath is lost between two cycles via various mechanisms such as the dipole-dipole interaction among the nuclear spins. However, these interactions are weak and the cycle round-trip time is very short,  $\sim 1$  ns, and so this limit is not realistic either.

Considering  $I = 2.25$ , we therefore take  $\gamma = \frac{A^2}{4N} (I - |\langle I_z \rangle|)$  as a compromise of the two extremes. An analogous calculation can be carried out when the electron spin is initially down. It is clear that  $\gamma$  must decrease as  $|\langle I_z \rangle|$  increases. The exact functional form of  $\gamma$  is not crucial to describe theoretically the main experimental phenomena but it is important to describe the experimental results quantitatively.



# References

- [1] M. Bayer, G. Ortner, O. Stern, A. Kuther, A. A. Gorbunov, A. Forchel, P. Hawrylak, S. Fafard, K. Hinzer, T. L. Reinecke, S. N. Walck, J. P. Reithmaier, F. Klopff and F. Schäfer, *Phys. Rev. B* **65**, 195315 (2002).
- [2] H. P. Breuer and F. Petruccione, *The Theory of Open Quantum Systems* (Oxford Univ. Press, Oxford, 2002), Chapter 3.
- [3] W. A. Coish and J. Baugh, *Phys. Status Solidi B* **246**, 2203 (2009).
- [4] B. Eble, O. Krebs, A. Lemaitre, K. Kowalik, A. Kudelski, P. Voisin, B. Urbaszek, X. Marie, and T. Amand, *Phys. Rev. B* **74**, 081306(R) (2006).
- [5] A. Abragam, *Principles of Nuclear Magnetism* (Oxford Univ. Press, Oxford, 1961), Chapter 8.
- [6] F. Klotz, V. Jovanov, J. Kierig, E. C. Clark, M. Bichler, G. Abstreiter, M. S. Brandt, J. J. Finley, H. Schwager, and G. Giedke, *Phys. Rev. B* **82**, 121307(R) (2010).
- [7] A. V. Khaetskii, D. Loss, and L. Glazman, *Phys. Rev. Lett.* **88**, 186802 (2002).
- [8] M. I. Dyakonov and V. I. Perel, in *Optical Orientation* (North-Holland, Amsterdam, 1984), p. 11.
- [9] I. T. Vink, K. C. Nowack, F. H. L. Koppens, J. Danon, Y. V. Nazarov, and L. M. K. Vandersypen, *Nat. Phys.* **5**, 764 (2009).
- [10] C. Latta, A. Högele, Y. Zhao, A. N. Vamivakas, P. Maletinsky, M. Kroner, J. Dreiser, I. Carusotto, A. Badolato, D. Schuh, W. Wegscheider, M. Atature, and A. Imamoglu, *Nat. Phys.* **5**, 758 (2009).
- [11] B. D. Gerardot, D. Brunner, P. A. Dalgarno, K. Karrai, A. Badolato, P. M. Petroff, and R. J. Warburton, *New J. Phys.* **11**, 013028 (2009).
- [12] S. Seidl, B. D. Gerardot, P. A. Dalgarno, K. Kowalik, A. W. Holleitner, P. M. Petroff, K. Karrai, and R. J. Warburton, *Physica E* **40**, 2153 (2008).
- [13] P. A. Dalgarno, J. M. Smith, J. McFarlane, B. D. Gerardot, K. Karrai, A. Badolato, P. M. Petroff, and R. J. Warburton, *Phys. Rev. B* **77**, 245311 (2008).
- [14] J. M. Smith, P. A. Dalgarno, R. J. Warburton, A. O. Govorov, K. Karrai, B. D. Gerardot, and P. M. Petroff, *Phys. Rev. Lett.* **94**, 197402 (2005).
- [15] P. A. Dalgarno, M. Ediger, B. D. Gerardot, J. M. Smith, S. Seidl, M. Kroner, K. Karrai, P. M. Petroff, A. O. Govorov, and R. J. Warburton, *Phys. Rev. Lett.* **100**, 176801 (2008).
- [16] C. Schulhauser, D. Haft, R. J. Warburton, K. Karrai, A. O. Govorov, A. V. Kalameitsev, A. Chaplik, W. Schoenfeld, J. M. Garcia, and P. M. Petroff, *Phys. Rev. B* **66**, 193303 (2002).
- [17] R. J. Warburton, C. Schulhauser, D. Haft, C. Schäfflein, K. Karrai, J. M. Garcia, W. Schoenfeld, and P. M. Petroff, *Phys. Rev. B* **65**, 113303 (2002).
- [18] M. Kroner, K. M. Weiss, B. Biedermann, S. Seidl, S. Manus, A. W. Holleitner, A. Badolato, P. M. Petroff, B. D. Gerardot, R. J. Warburton, and K. Karrai, *Phys. Rev. Lett.* **100**, 156803 (2008).





# Curriculum Vitae

## Christoph Kloeffel

Date of Birth     September 26, 1983  
Place of Birth    Schweinfurt, Germany  
Citizenship      German

## Education

- 2014     PhD in Theoretical Physics  
          Group of Prof. Dr. Daniel Loss  
          University of Basel, Switzerland  
          Summa Cum Laude
- 2009     MPhys in Physical Science  
          Heriot-Watt University, Edinburgh, UK  
          Watt Club Medal (Best Final Year Student), Honors of the First Class
- 2007     Prediploma in Physics  
          University of Würzburg, Germany  
          With Distinction (“mit Auszeichnung, 1.0”)
- 2003     Abitur (Bavaria)  
          Jack-Steinberger-Gymnasium Bad Kissingen, Germany



# List of Publications

1. *Acoustic Phonons and Strain in Core/Shell Nanowires*,  
Christoph Kloeffel, Mircea Trif, and Daniel Loss,  
Phys. Rev. B **90**, 115419 (2014).
2. *Phonon-Mediated Decay of Singlet-Triplet Qubits in Double Quantum Dots*,  
Viktoriia Kornich, Christoph Kloeffel, and Daniel Loss,  
Phys. Rev. B **89**, 085410 (2014).
3. *Circuit QED with Hole-Spin Qubits in Ge/Si Nanowire Quantum Dots*,  
Christoph Kloeffel, Mircea Trif, Peter Stano, and Daniel Loss,  
Phys. Rev. B **88**, 241405(R) (2013).
4. *Tunable  $g$  Factor and Phonon-Mediated Hole Spin Relaxation in Ge/Si Nanowire Quantum Dots*,  
Franziska Maier, Christoph Kloeffel, and Daniel Loss,  
Phys. Rev. B **87**, 161305(R) (2013).
5. *Prospects for Spin-Based Quantum Computing in Quantum Dots*,  
Christoph Kloeffel and Daniel Loss,  
Annu. Rev. Condens. Matter Phys. **4**, 51 (2013).
6. *Strong Spin-Orbit Interaction and Helical Hole States in Ge/Si Nanowires*,  
Christoph Kloeffel, Mircea Trif, and Daniel Loss,  
Phys. Rev. B **84**, 195314 (2011).
7. *Controlling the Interaction of Electron and Nuclear Spins in a Tunnel-Coupled Quantum Dot*,  
Christoph Kloeffel, Paul A. Dalgarno, Bernhard Urbaszek, Brian D. Gerardot, Daniel Brunner,  
Pierre M. Petroff, Daniel Loss, and Richard J. Warburton,  
Phys. Rev. Lett. **106**, 046802 (2011).